

Mitigating Size Related Limitations in Wind Turbine Control

A thesis presented in fulfilment of the
requirements for the degree of Doctor of Philosophy

David William Thompson

Supergen Wind Energy Technologies Consortium
Department of Electronic and Electrical Engineering
University of Strathclyde, Glasgow

August 2018

This thesis is the result of the author's original research. It has been composed by the author and has not been previously submitted for examination which has led to the award of a degree.

The copyright of this thesis belongs to the author under the terms of the United Kingdom Copyright Acts as qualified by University of Strathclyde Regulation 3.50. Due acknowledgement must always be made of the use of any material contained in, or derived from, this thesis.

Abstract

As the size of wind turbines steadily increase, a control system which can manage the loads and dynamics becomes more important. In this thesis, the effects of turbine scale on the control system are examined and designs which mitigate the arising problems are presented and discussed.

In this thesis, a set of three wind turbines is developed using a method to scale a mathematical model of a wind turbine while maintaining similarity in the dynamics. This framework for producing the scaled wind turbines is presented and discussed.

The performance of the controller for a very large wind turbine is limited by the dynamics of the tower. By accounting for the non-minimum-phase dynamics present in the wind turbine, previous work has reduced loads in the tower. In this thesis, this framework is developed to improve speed and power control and recover some of the performance lost as turbine size increases.

As well as the effect of the tower, non-linear dynamics present in the pitch control loop adversely effect performance. Previous work has developed a framework for a controller for non-linear plants which satisfies a criteria called extended local linear equivalence (ELLE). A novel controller which satisfies the ELLE criteria is presented which counters the non-linear dynamics present in the wind turbine and reduces fluctuations in speed and power.

A comparison of a baseline controller and a controller which incorporates the two designs described above shows significant reductions in the fluctuations of ro-

tor and generator speed as well as power output. These changes to the controller also show greater improvements to performance in larger turbines. The influence of the tower and the non-linear dynamics present in the aerodynamics both become more severe as the size of the wind turbine increases. Therefore, a controller design which mitigates these effects has greater value as the wind energy industry continues on its path and develops ever larger wind turbines.

Acknowledgements

Firstly I would like to thank my supervisor Professor Bill Leithead for his patient advice, without which I would have no hope of completing this work.

I cannot thank my parents enough for their love and support. When this work took longer than planned, their help ensured that I could complete it.

I am extremely grateful for the help of Julia and Mike in editing and correcting this work.

Finally, and in no particular order, I would like to thank all of my colleagues from the University of Strathclyde, particularly Adam Stock, Hong Yue, Sung Ho Hur, Charlie Plumley, Sheila Campbell, Saman Poushpas, Julian Feuchtwang and Alex Giles.

I would also like to acknowledge the support of the EPSRC for the Supergen Wind Energy Technology Consortium, grant number EP/H018662/1.

Contents

Acknowledgements	iv
Contents	viii
Nomenclature	ix
List of Figures	xiii
List of Tables	xxi
1 Introduction	1
1.1 Overview of Thesis	1
1.2 Contribution to Knowledge	3
1.3 Publication	3
2 Wind Energy and Wind Turbine Control	5
2.1 Wind Energy	6
2.1.1 Wind Turbine Components and Nomenclature	8
2.2 Wind Turbine Control	10
2.2.1 Pitch Regulated, Variable Speed Control	11
2.3 Simulation Environments	16
2.3.1 DNV GL Bladed	17
2.3.2 MATLAB Simulink	17

2.4	Linearised Models	18
3	Baseline Models and the Up-Scaling of Wind Turbines	21
3.1	Wind Turbine Model Scaling	22
3.1.1	Power	23
3.1.2	Mass and Inertia	23
3.1.3	Stiffness & Natural Frequency	24
3.2	Controller Design	25
3.2.1	Operating Strategy	25
3.2.2	Gain-Scheduling	29
3.2.3	Linear Control Design	33
3.2.4	Drivetrain Filter	38
3.2.5	Discretisation and the Anti-windup Loop	39
3.3	Controller Implementation and Architecture	40
3.3.1	Below-rated Switching	41
3.4	Simulations	43
3.4.1	Comparison of Simulation Environments	43
3.4.2	Comparison of Turbine Size	47
3.5	Concluding Remarks	54
4	Development of a Coordinated Controller for Improved Control of Very Large Wind Turbines	56
4.1	The Right-Half-Plane Zero in Wind Turbine Dynamics	57
4.2	Coordinated Controller Design	60
4.2.1	Implementation and Simulations	62
4.3	Power Coordinated Controller	70
4.3.1	Implementation and Simulations	72
4.4	Improved Control of Very Large Wind Turbines	78
4.4.1	Controller Design	79

4.4.2	Simulations	85
4.5	Concluding Remarks	108
5	Development of a Linear Parameter-varying Wind Turbine Con-	
	troller	110
5.1	Non-linearity in the Wind Turbine Plant Dynamics	111
5.2	Simple Gain-scheduled Controller	113
5.2.1	Implementation and Simulations	115
5.3	Extended Local Linear Equivalence	120
5.4	An Extended Local Linear Equivalence Controller	125
5.4.1	Implementation	128
5.4.2	Simulations	141
5.5	Comparison of Turbine Size	145
5.5.1	Simulations	148
5.6	Concluding Remarks	155
6	Mitigating the Restrictions of Wind Turbine Size	157
6.1	Controller Design	158
6.2	Simulations	163
6.2.1	Performance	164
6.2.2	Structural Loads	171
6.2.3	Switching Between Operating Modes	180
6.2.4	Actuator Saturation	182
6.3	Concluding Remarks	183
7	Conclusion	186
	References	191

A Parameters for Upscaled Wind Turbines	196
A.1 Plant Transfer Functions	197
A.2 Plant Parameters	197
A.3 Controller Transfer Functions	198
A.4 Controller Parameters	199
B State Space Model	202
B.1 Rotor Dynamics	203
B.2 Drivetrain Dynamics	204
C Calculation of Damage Equivalent Loads	206
D Formulation of Transfer Functions for the Anti-windup Loop	208

Nomenclature

Symbol	Description
A	Rotor swept area
$A(s)$	Transmittance from blade pitch angle to generator speed
$a(y); b(y); c(y)$	Linear functions which vary with the output of the gain-scheduled compensator
B	Drivetrain damping
$B(s)$	Transmittance from generator torque demand to generator speed
$b_1; b_2; b_3$	Static gains; part of the gain-scheduled compensator
B_{TS}	Tower side-to-side damping
$C(s)$	Transmittance from generator torque demand to generator torque
$C_{AR}(s)$	Above rated controller
$C_{BR}(s)$	Below rated controller
$C_i(s)$	Inner controller
$C_o(s)$	Outer controller
C_p	Power coefficient
$C_{p_{\max}}$	Maximum power coefficient
D	Scale factor

D	Total damage
d	Cantilever deflection
E	Young's Modulus
E	Controller error
E_e	Estimated controller error
$F(s)$	Filter to correct gain response of the PCC
F_1	In-plane aerodynamic torque
F_2	Out-of-plane aerodynamic torque
$G_{pre}(s)$	Transfer function which precedes gain-scheduled compensator
$GS(s)$	Function representing the gain-scheduled compensator
$H(s)$	Transfer function representing part of the controller
I	2nd moment of inertia
I_{HS}	High-speed shaft inertia
I_{LS}	Low-speed shaft inertia
I_x	2nd moment of area
J	Rotor or inertia
J_c	Cross coupling inertia
J_T	Tower fore-aft inertia
J_{TS}	Tower side-to-side inertia
k	Miscellaneous gain
K_{cc}	Extra gain applied to the IPCC
K_{cp}	Gain related to below-rated switching
K_{LS}	Low-speed shaft stiffness
K_o	Gain related to below-rated switching
K_{opt}	Gain relating to max power tracking control
K_p	Above-rated controller gain
K_{TS}	Tower side-to-side stiffness
L	Characteristic length

M	Bending moment
m	Wholer exponent
n	Gearbox ratio
N	Load case
n_i	Number of cycles
N_i	Number of cycles to failure
P	Power
P_{bl}	Baseline parameter
P_{ex}	Extrapolated parameter
Q	Blade torque
R	Rotor radius
r	Radius
S	Stresses
SP	Scale factor power
T_0	Torque defining the control strategy
T_1	Torque defining the control strategy
T_d	Torque demand
T_g	Generator torque
T_h	Hub torque
T_m	Intermediate variable in the controller
T_{set}	Above-rated generator torque
v	Wind speed
W	Force
$X(s)$	Coordinating transfer function for the CCD
$X'(s)$	Coordinating transfer function for the PCC & IPCC
$Y(s)$	Notch filter for coordinated control
β	Blade pitch angle
β_d	Blade pitch angle demand

γ_1^*	Low-speed shaft material damping
γ_2^*	High-speed shaft material damping
γ_{LS}	Low-speed shaft damping
ζ	Damping ratio
$\dot{\theta}_H$	Hub speed
θ_R	Out-of-plane rotor angular deflection
θ_T	Tower fore-aft angular deflection
Ω	Rotor speed
ω_1	Generator speed defining the controller strategy
ω_2	Generator speed defining the controller strategy
ω_e	Blade edgewise natural frequency
ω_f	Blade flapwise natural frequency
ω_g	Generator speed
ω_n	Miscellaneous natural frequency
ω_{set}	Above-rated generator speed
ω_t	Tower fore-aft natural frequency

List of Figures

2.1	James Blyth’s turbine, Marykirk, Scotland [1]	7
2.2	Charles F. Brush’s wind turbine, Cleveland, Ohio [2]	7
2.3	Wind turbines of the Danish three-bladed concept at Sheringham Shoal [3]	9
2.4	Major components of a large, modern wind turbine	9
2.5	$C_p - \lambda$ curve for a 5MW wind turbine at minimum blade pitch angle	12
2.6	A typical control strategy for a 5MW HAWT shown on a torque- speed diagram	14
2.7	Power curve for a 5MW wind turbine	15
2.8	Wind spectrum based on work by van der Hoven	16
2.9	Comparison of Bladed and algebraic linearisations	20
3.1	5MW control strategy	27
3.2	7.5MW control strategy	28
3.3	10MW control strategy	28
3.4	Dynamics of torque, pitch angle, rotor speed and effective wind speed	30
3.5	Separated dynamics of pitch demand and generator torque	30
3.6	Structure for implementing gain-scheduling	31
3.7	Partial derivative of torque with respect to pitch angle for the 5MW wind turbine	31

3.8	Open loop Bode plot without gain-scheduling	32
3.9	Open loop Bode plot with gain-scheduling	33
3.10	Van der Hoven spectrum	34
3.11	Open loop Bode plots for the controller and plant at 14m/s of three differently sized turbines	36
3.12	Sensitivity functions of the controller and plant for three differently sized turbines	37
3.13	Location of the drivetrain filter in the system	38
3.14	Switching structure	40
3.15	Below-rated switching structure	42
3.16	HSS power for 16m/s mean wind speed, 15% turbulence - compar- ison of simulation environments	45
3.17	Generator speed for 16m/s mean wind speed, 15% turbulence - comparison of simulation environments	46
3.18	Blade pitch angle for 16m/s mean wind speed, 15% turbulence - comparison of simulation environments	47
3.19	Comparison of HSS power for different sizes of turbine operating below rated power (6m/s mean wind speed)	48
3.20	Comparison of generator speeds for different sizes of turbine sizes operating below rated power (6m/s mean wind speed)	49
3.21	Comparison of blade pitch angle for different sizes of turbine op- erating at above-rated power (18m/s mean wind speed)	50
3.22	Comparison of generator speed for different sizes of turbine oper- ating at above-rated power (18m/s mean wind speed)	51
3.23	Comparison of power spectral densities of nacelle fore-aft velocity in above-rated operation (16m/s mean wind speed)	52
3.24	Comparison of generator speeds for different sizes of turbine switch- ing between controller modes (11m/s mean wind speed)	53

3.25	Comparison of blade pitch angles for different sizes of turbine switching between controller modes (11m/s mean wind speed) . . .	54
4.1	Bode plot of pitch angle demand to generator speed indicating the phase loss due to the presence of RHPZs	59
4.2	Implementation of the coordinated control design	60
4.3	Internal view of the wind turbine plant dynamics	61
4.4	Bode plot of the notch filter for the 5MW turbine	63
4.5	Bode plot showing the approximation of the coordinating function	64
4.6	Bode plot showing open loop system in Figure 4.2 of the baseline controller and the CCD	65
4.7	Power spectral density of fore-aft bending moment at the tower base	66
4.8	Power spectral density of blade pitch angle	67
4.9	Power spectral density of generator torque	67
4.10	Comparison of generator speed for baseline and CCD	68
4.11	Comparison of generator torque for baseline and CCD	69
4.12	Comparison of generator power for baseline and CCD	70
4.13	Implementation of the power coordinated controller	71
4.14	Bode plot showing the approximation of the coordinating function	72
4.15	Bode plot showing the open loop system in Figure 4.13 of the baseline controller and the PCC	73
4.16	Power spectral density of fore-aft bending moment at the tower base	74
4.17	Power spectral density of blade pitch angle	74
4.18	Power spectral density of generator torque	75
4.19	Comparison of generator torque for baseline and CCD	76
4.20	Comparison of generator power for baseline and CCD	77
4.21	Comparison of generator speed for baseline and CCD	78
4.22	Bode plots of notch filters for use with three differently sized turbines	80

4.23	Bode plots showing the approximation of the coordinating function for the 5MW turbine	81
4.24	Bode plots showing the controller and 5MW plant for the baseline controller, PCC and IPCC	82
4.25	Bode plots showing the controller and 7.5MW plant for the baseline controller, PCC and IPCC	83
4.26	Bode plots showing the controller and 10MW plant for the baseline controller, PCC and IPCC	84
4.27	Generator speeds for the baseline controller and IPCC for different sizes of turbine	86
4.28	Power spectral densities of fore-aft the moment at the tower base for the baseline controller, PCC and IPCC (5MW)	87
4.29	Power spectral densities of blade pitch angle for the baseline controller, PCC and IPCC (5MW)	88
4.30	Power spectral densities of generator torque for the baseline controller, PCC and IPCC (5MW)	89
4.31	Generator torque for the baseline controller, PCC and IPCC (5MW)	90
4.32	HSS power for the baseline controller, PCC and IPCC (5MW) . .	91
4.33	Generator speed for the baseline controller, PCC and IPCC (5MW)	92
4.34	HSS power for the baseline controller and the IPCC (7.5MW) . .	93
4.35	HSS power for the baseline controller and the IPCC (10MW) . . .	94
4.36	Generator speed for the baseline controller and the IPCC (7.5MW)	95
4.37	Generator speed for the baseline controller and the IPCC (10MW)	96
4.38	Power spectral densities of fore-aft the moment at the tower base for the baseline controller and IPCC (7.5MW)	97
4.39	Power spectral densities of fore-aft the moment at the tower base for the baseline controller and IPCC (10MW)	98

4.40	Damage equivalent loads at the tower base for the baseline controller and IPCC operating in a turbulent wind with a mean wind speed of 18m/s	99
4.41	Bode plots showing the baseline, PCC and provisional controllers	101
4.42	Bode plot showing the filter to correct the gain response of the PCC	102
4.43	Bode plots showing the baseline, PCC and provisional controllers	103
4.44	Comparison of generator speed for the baseline, PCC and provisional controllers	104
4.45	Comparison of mechanical power for the baseline, PCC and provisional controllers	105
4.46	Comparison of power spectral densities of blade pitch angle for the baseline, PCC and provisional controllers	106
4.47	Comparison of power spectral densities of tower fore-aft moment for the baseline, PCC and provisional controllers	107
5.1	Pole-zero map of the open loop system showing a pole on the real axis with a frequency which is a function of wind speed	112
5.2	Open loop Bode plots of the open loop system showing non-linearity at a low frequency	113
5.3	Frequencies of the variable pole and polynomial approximation . .	116
5.4	Open loop Bode plots of the open loop system with the simple gain-scheduling implementation	117
5.5	Comparison of generator speed for baseline and simple gain-scheduled realisation	118
5.6	Comparison of HSS power for baseline and simple gain-scheduled realisation	119
5.7	LLE condition illustrating locus of equilibrium points	121
5.8	ELLE condition illustrating lines of constant β_d	122
5.9	A first order realisation of the ELLE condition	122

5.10	A first order realisation of the ELLE condition with an integrator on the input line	124
5.11	A first order realisation of the ELLE condition with an integrator moved to the output	124
5.12	Continuous-time implementation of the ELLE condition compensator	127
5.13	Implementation of the ELLE controller in the baseline switching configuration	129
5.14	Discrete-time implementation of the ELLE condition compensator	131
5.15	Linear approximations for $a(y)$, $b(y)$ and $c(y)$	133
5.16	quadratic approximations for $a(y)$, $b(y)$ and $c(y)$	134
5.17	Generator speed for the baseline controller and linear and quadratic implementations of the ELLE controller	135
5.18	HSS power for the baseline controller and linear and quadratic implementations of the ELLE controller	136
5.19	Bode plot for the baseline controller at a selection of wind speeds	139
5.20	Bode plot for the ELLE controller at a selection of wind speeds .	140
5.21	Sensitivity functions for the baseline controller and ELLE controller at 24m/s	141
5.22	Comparison of generator speeds for the baseline controller, the ELLE controller and the simple gain-scheduling realisation	142
5.23	Comparison of HSS power for the baseline controller, the ELLE controller and the simple gain-scheduling realisation	143
5.24	Comparison of blade pitch angle for the baseline controller and the ELLE controller	144
5.25	Comparison of power spectral densities of the tower base fore-aft bending moment for the baseline controller and the ELLE controller	145
5.26	Bode plot for the baseline controller at a selection of wind speeds for a 7.5MW turbine	147

5.27	Bode plot for the baseline controller at a selection of wind speeds for a 10MW turbine	147
5.28	Comparison of generator speed for the baseline controller and the ELLE controller for a 7.5MW turbine	148
5.29	Comparison of generator speed for the baseline controller and the ELLE controller for a 10MW turbine	149
5.30	Comparison of HSS power for the baseline controller and the ELLE controller for a 7.5MW turbine	150
5.31	Comparison of HSS power for the baseline controller and the ELLE controller for a 10MW turbine	151
5.32	Comparison of power spectral densities of the tower base fore-aft bending moment for the baseline controller and the ELLE controller for the 7.5MW turbine	153
5.33	Comparison of power spectral densities of the tower base fore-aft bending moment for the baseline controller and the ELLE controller for the 10MW turbine	154
5.34	Damage equivalent loads at the tower base for the baseline and ELLE controller operating in a turbulent wind with a mean wind speed of 18m/s	155
6.1	Block diagram of the baseline controller structure with the IPCC and ELLE controller implemented	158
6.2	Bode plot showing the baseline controller with the IPCC, ELLE controller, and the IPCC & ELLE combined	159
6.3	Sensitivity function of the baseline controller with the IPCC, ELLE controller, and the IPCC & ELLE combined	160
6.4	Sensitivity function of the baseline controller with the IPCC, ELLE controller, and the IPCC & ELLE combined for the 5MW turbine	161

6.5	Sensitivity function of the baseline controller with the IPCC, ELLE controller, and the IPCC & ELLE combined for the 7.5MW turbine	162
6.6	Sensitivity function of the baseline controller with the IPCC, ELLE controller, and the IPCC & ELLE combined for the 10MW turbine	163
6.7	Generator speed for the 5MW turbine with the baseline controller and combined controller in 16m/s mean wind speed	165
6.8	Generator speed for the 7.5MW turbine with the baseline controller and combined controller in 16m/s mean wind speed	166
6.9	Generator speed for the 10MW with the baseline controller and combined controller in 16m/s mean wind speed	167
6.10	Mechanical power at the generator for the 5MW turbine with the baseline controller and combined controller in 16m/s mean wind speed	168
6.11	Mechanical power at the generator for the 7.5MW turbine with the baseline controller and combined controller in 16m/s mean wind speed	169
6.12	Mechanical power at the generator for the 10MW turbine with the baseline controller and combined controller in 16m/s mean wind speed	170
6.13	Damage equivalent loads at the tower base with the baseline and combined controllers operating in a turbulent wind with a mean wind speed of 18m/s	171
6.14	Comparison of power spectral densities of the tower base fore-aft bending moment with the baseline and combined controllers for the 5MW turbine in 18m/s mean wind speed	173
6.15	Comparison of power spectral densities of the tower base fore-aft bending moment with the ELLE and combined controllers for the 5MW turbine in 18m/s mean wind speed	174

6.16	Comparison of power spectral densities of the tower base fore-aft bending moment with the baseline and combined controllers for the 7.5MW turbine in 18m/s mean wind speed	175
6.17	Comparison of power spectral densities of the tower base fore-aft bending moment with the baseline and combined controllers for the 10MW turbine in 18m/s mean wind speed	176
6.18	Damage equivalent loads at the blade root with the baseline and combined controllers operating in a turbulent wind with a mean wind speed of 18m/s	177
6.19	Comparison of power spectral densities of the blade root bending moment with the baseline and combined controllers for the 5MW turbine in 18m/s mean wind speed	178
6.20	Comparison of power spectral densities of the blade root bending moment with the baseline and combined controllers for the 7.5MW turbine in 18m/s mean wind speed	179
6.21	Comparison of power spectral densities of the blade root bending moment with the baseline and combined controllers for the 10MW turbine in 18m/s mean wind speed	180
6.22	Comparison of generator speed with the baseline and combined controllers for the 5MW turbine in 11m/s mean wind speed	181
6.23	Comparison of blade pitch angle with the baseline and combined controllers for the 5MW turbine in 11m/s mean wind speed	182
6.24	Comparison of blade pitch angle rates with and without the anti-windup loop applied and the rate limit restricted to 1.5deg/s	183
B.1	Rotor dynamics and drivetrain dynamics in the state space model	202

List of Tables

3.1	Radii for the baseline 5MW model and the two large models . . .	23
3.2	Primary natural frequencies (rad/s)	25
3.3	Control strategy rotor speeds (rad/s)	27
3.4	Stability margins and crossover frequencies for the above-rated controllers at a wind speed of 14m/s	35
3.5	Transfer functions of the above-rated controllers	35
3.6	Transfer functions for the below-rated controllers	38
3.7	Transfer functions for inner and outer controllers	41
3.8	Logic for switches in below-rated control	42
3.9	Comparison of the standard deviation of generator speeds for above- rated operation	51
4.1	Gains to increase crossover frequencies as applied to three sizes of wind turbine	84
4.2	Crossover frequencies for the baseline controller and IPCC	85
4.3	Standard deviations of HSS power	94
4.4	Standard deviations of generator speed	96
4.5	Averages of damage equivalent loads across three simulations for the baseline and IPCC	100

5.1	Frequencies of the variable pole for a selection of wind speeds and blade pitch angles	115
5.2	Values of $\psi(\beta_d)$ at pitch angle demand values of β_{di} ($i = 1, 2, 3, 4$)	126
5.3	Standard deviations of generator speed for the baseline controller and linear and quadratic implementations of the ELLE controller	136
5.4	Standard deviations of HSS power for the baseline controller and linear and quadratic implementations of the ELLE controller . . .	137
5.5	Values for α at various wind speeds	138
5.6	Polynomials for the variable components of the compensator . . .	138
5.7	Standard deviations of generator speed for the baseline controller, the ELLE controller and the simple gain-scheduled controller . . .	142
5.8	Standard deviations of HSS power for the baseline controller, the ELLE controller and the simple gain-scheduled controller	143
5.9	Values for α for three turbines at various wind speeds	146
5.10	Standard deviations of generator speed for the baseline controller and the ELLE controller for different sizes of wind turbine at 16m/s	149
5.11	Standard deviations of HSS power for the baseline controller and the ELLE controller for different sizes of wind turbine at 16m/s .	151
5.12	Standard deviations of generator speed for the baseline controller and the ELLE controller for different sizes of wind turbine at 18m/s	152
5.13	Standard deviations of HSS power for the baseline controller and the ELLE controller for different sizes of wind turbine at 18m/s .	152
5.14	Averages of damage equivalent loads across three simulations for the baseline and ELLE controllers	155
6.1	Standard deviations of generator speed for the baseline controller and the combined controller for different sizes of wind turbine at 16m/s	167

LIST OF TABLES

6.2	Standard deviations of mechanical power at the generator for the baseline controller and the combined controller for different sizes of wind turbine at 16m/s	170
6.3	Averages of damage equivalent loads at the tower base across three simulations for the baseline and combined controllers	172
6.4	Comparison of percentage changes in damage equivalent loads for different controller configurations	172
6.5	Averages of damage equivalent loads at the blade root across three simulations for the baseline and combined controllers	177

Chapter 1

Introduction

The need for new, renewable sources of energy is clear and wind power is highly likely to play a significant part in the future energy mix. It is a trend in the wind energy industry that turbines increase in size in order to deliver a lower cost of energy. For this reason research into the potential problems associated with upscaling is vital.

This thesis presents a controller design which improves the performance of the control systems of very large wind turbines. Two significant problems are identified when a wind turbine is scaled up and a control solution is provided for each. These two solutions are combined to provide a controller framework which is more robust to the constraints of ever increasing turbine size.

1.1 Overview of Thesis

In Chapter 1 (this chapter), a brief introduction is made. This is followed by an outline of the contribution to knowledge made by this research as well as publications which resulted from it.

In Chapter 2, the motivation behind the research is presented along with an

introduction to the principals of wind energy and wind turbine control. The software packages and simulation environments used in conducting this research and producing the data are also outlined.

In Chapter 3, a method is presented which is used to upscale a baseline wind turbine and controller in a way where similarity in all relevant dynamics is maintained. This is followed by wind turbine models and controllers of three different sizes, scaled using the previously defined method. The structure and configuration of these controllers, which are referred to as a ‘baseline’, prior to the modifications outlined in the subsequent chapters, are described in detail. Finally, results from simulations of the three sizes of wind turbine are analysed and discussed.

In Chapter 4, a controller previously developed to decrease loads in the wind turbine tower is presented. This design is modified to mitigate the restriction a low frequency fore-aft tower mode imposes on controller design. Simulations of the three wind turbines developed in Chapter 3 are conducted with this new controller and the results are analysed. The effect of turbine size on the improvements offered by this new controller are discussed.

In Chapter 5, a new controller design is developed which counters a non-linearity present when the turbine speed is controlled by pitching the blades. The performance of this new controller is tested and, using the wind turbines and baseline controller models developed in Chapter 3, the relative improvements to different sizes of wind turbine are analysed.

In Chapter 6, the two controller designs presented in Chapter 4 and Chapter 5 are combined to make a controller structure which is less sensitive to the restrictions of turbine size. The combined controller is tested using the three previously developed wind turbine models and compared to the baseline. Finally, the ability of this controller to mitigate the limitations of wind turbine size are discussed.

Chapter 7 summarises the results and points of discussion presented in this thesis and draws conclusions. Finally potential future work is discussed.

1.2 Contribution to Knowledge

The contribution to knowledge made by the research in this thesis is as follows:

- A family of dynamically similar wind turbine models of increasing size, complete with controllers, has been developed, scaled up to 7.5MW and 10MW from the Supergen 5MW exemplar wind turbine. Since the focus of this thesis is on control, scaling has been done in a manner which keeps the dynamic behaviour similar so that any differences in performance can be attributed to size increases and not other controller issues.
- A novel wind turbine controller has been developed which mitigates the restriction the wind turbine tower imposes on controller design whilst also reducing loads on the tower.
- A novel wind turbine controller has been developed which improves control of power and rotor speed by countering a non-linearity present in the dynamics. Improvements seen by the application of this controller become greater as turbine size increases.
- A controller combining the two points outlined above has been developed to provide a controller which is not as negatively influenced by size as an equivalent baseline. By combining these two controllers, two restrictions imposed by increasing the size of a wind turbine are mitigated and control performance is increased.

1.3 Publication

The following paper is the result of the research presented in this thesis.

- D. W. Thompson and W. E. Leithead, “A gain-scheduled controller for improved power regulation of very large wind turbines,” in *EWEA, Barcelona*, 2014

Chapter 2

Wind Energy and Wind Turbine Control

Climate change is predominantly caused by the emission of greenhouse gasses through electricity generation, agriculture, industry, and transportation [4]. Given that continued burning of fossil fuels to generate electricity will lead to further, accelerated global warming [5], clean sources of energy are therefore an essential component in what needs to be a global strategy for tackling climate change. As well as environmental concerns, moving away from fossil fuels reduces the requirement to import resources from other countries and regions where the political situation may be relatively unstable or unfriendly. As a result of the environmental implications of the continued use of fossil fuels and the associated political consequences, several agreements and targets have been set at national, European, and global levels. The most notable of these in recent times is the Paris Agreement, which states that the signatories [6] [7]:

“Notes with concern that the estimated aggregate greenhouse gas emission levels in 2025 and 2030 resulting from the intended nationally determined contributions do not fall within least-cost 2°C scenarios but rather lead to a projected level of 55 gigatonnes in 2030, and also notes that much greater emission reduction efforts will be required than those associated with the intended nationally determined contributions in order to hold the increase in the global average temperature to below 2°C above pre-industrial levels by reducing emissions to 40 gigatonnes or to 1.5°C above pre-industrial levels”

Each signatory country determines which policies it follows to achieve or work towards achieving this goal and, for most, it is highly likely that wind energy will be a part of the solution.

2.1 Wind Energy

The wind has been harnessed as an energy source for thousands of years, from powering sailing ships to grinding grain and pumping water. In 1887, James Blyth, the Scottish academic of Anderson’s College in Glasgow (later to become the University of Strathclyde), became the first person to use a wind powered machine to generate electricity [8]. This first wind turbine powered the lights in Blyth’s holiday home in Marykirk, Aberdeenshire.

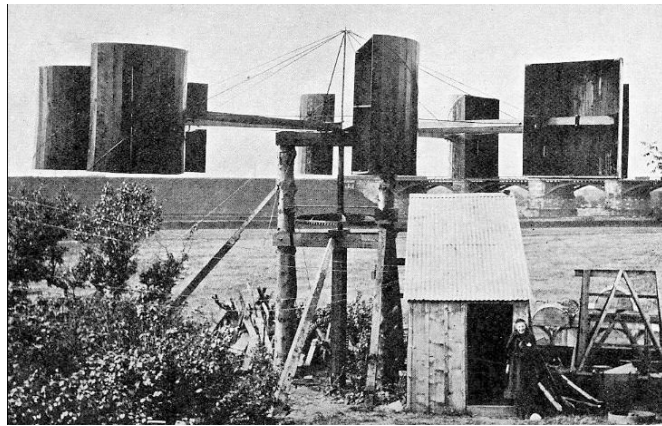


Figure 2.1: James Blyth's turbine, Marykirk, Scotland [1]

The following year, Charles F. Brush built a 12kW wind turbine at his home in Cleveland, Ohio [2]. Brush's machine had a rotor which spun on a horizontal axis and was much larger than the one built by Blyth. From the machines of Blyth and Brush in the late 19th century, wind turbines have been steadily increasing in size to the multi-megawatt scale machines available today.

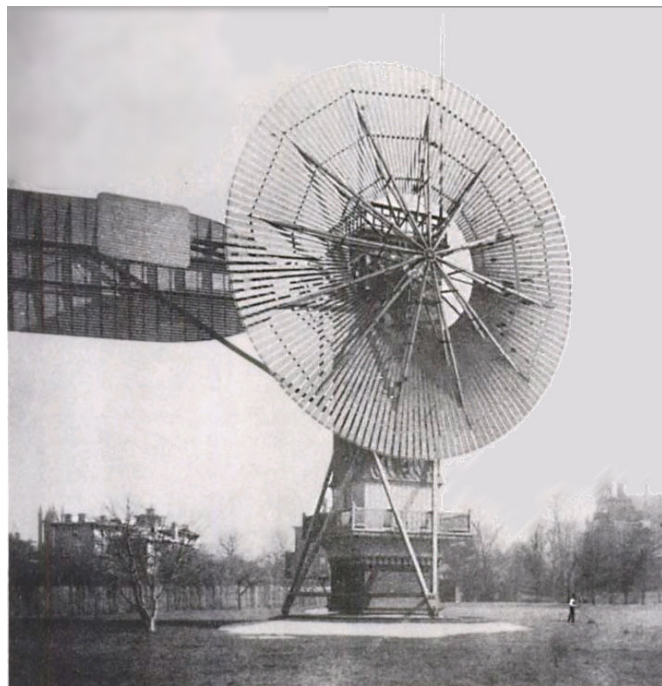


Figure 2.2: Charles F. Brush's wind turbine, Cleveland, Ohio [2]

The European Wind Energy Association (EWEA) states a key objective of the wind industry is for onshore wind to be “the most competitive energy source” by 2020 and offshore by 2030 [9]. It also states that, to meet these demands, a significant portion of future capacity will be offshore. In 2017, the governments of Germany, Denmark and Belgium — leading offshore wind markets — signed a joint statement reaffirming a commitment to a significant deployment of new offshore wind power [10]. The push to increase the capacity of wind power offshore also contributes to the drive to increase the size of individual wind turbines. There are several reasons for this; one of the most significant for offshore installations is that fewer, larger infrastructure items generally deliver lower costs of energy for the same capacity [11]. Larger wind turbines can also have a greater proportion of the rotor further from the ground or water surface, are therefore exposed to a higher average wind speed across the rotor disc and can therefore capture more energy.

2.1.1 Wind Turbine Components and Nomenclature

Although there are several alternative configurations available, notably direct-drive, the majority of installed wind turbines use a gearbox and conform the Danish three-bladed concept shown in Figure 2.3. The vast majority of modern, large wind turbines have three blades connected to a central hub which transmits torque via a low-speed shaft, a gearbox and a high speed shaft, which are contained within a nacelle. Figure 2.4 depicts where these components are located in relation to each other.



Figure 2.3: Wind turbines of the Danish three-bladed concept at Sheringham Shoal [3]

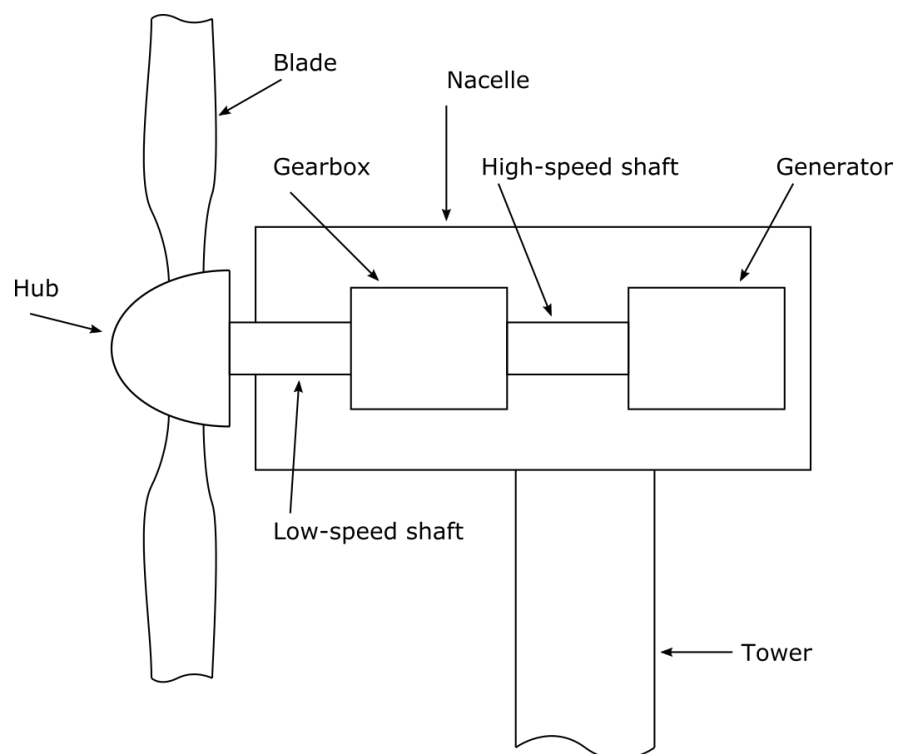


Figure 2.4: Major components of a large, modern wind turbine

2.2 Wind Turbine Control

The primary purpose of the wind turbine control system is to maintain the speed of the rotor at a desired set-point, generally determined by the wind speed. As wind turbines increase in size, the demands on the control system are often increased with the requirement to reduce loads on the tower, blades, and drive-train [12].

The control objectives of a large, modern wind turbine can be split into two groups:

- **Supervisory control:** Includes tasks such as system startup and shut-down, condition monitoring, fault handling, and data collection [13]. Also included in this category is power production which refers to the connection of the generator to the grid. [14]
- **Operational control:** Automatic adjustment of the state of the wind turbine based on pre-determined objectives such as power output or generator speed.

A control strategy dictates how the operational controller keeps the wind turbines operating in a state where it generates the most possible power in lower wind speeds and protects the wind turbine structure in high wind speeds. For horizontal axis wind turbines (HAWTs), there are four common types of control strategy:

- Stall regulated, constant speed
- Stall regulated, variable speed
- Pitch regulated, constant speed
- Pitch regulated, variable speed

Stall regulated wind turbines have blades which are designed to stall to limit the rotor speed when the wind speed becomes too great. This configuration removes the requirement for blade pitch actuators. For constant speed machines, the generator torque is controlled to maintain a rotor speed which is constant across all wind speeds. For variable speed machines, the generator torque is controlled to allow different rotor speeds, depending on the wind speed. For the vast majority of multi-megawatt scale horizontal axis wind turbines, a pitch regulated, variable speed control strategy is used. This has the advantage of increased power capture from varying the rotor speed to maintain an optimum value and reduced structural loads by operating the blades further away from the point of stall.

2.2.1 Pitch Regulated, Variable Speed Control

Operational control of a pitch regulated, variable speed wind turbine can be split into two categories: ‘below-rated’ and ‘above-rated’. Up to a certain operating point, the wind turbine should be controlled to generate as much power as possible within appropriate rotor speed limits. At a pre-determined operating point, ‘rated power’, the controller switches to maintaining a constant rotor speed and power output by actively pitching the blades. Capping the rotor speed in this way mitigates the loads experienced by the wind turbine structure in high wind speeds.

Below-rated

A typical control strategy for a below-rated controller comprises of three modes. From the cut-in wind speed there is a mode where the rotor is held at a constant speed by varying the generator torque. At slightly higher wind speeds the generator speed is controlled to produce the maximum possible power. This is achieved by tracking the maximum value of the power coefficient, $C_{p_{\max}}$. The power coefficient, C_p is a function of the blade pitch angle, β and the tip speed

ratio, λ and is part of the equation to determine the power output of a wind turbine - (2.1) where P is the power output, ρ is the air mass density, A is the rotor area and v is the wind speed.

$$P = \frac{1}{2} C_p \rho A v^3 \quad (2.1)$$

In below-rated operation, the blade pitch angle is held constant at its minimum value because this is generally where $C_{p_{\max}}$ is. For the controller to track $C_{p_{\max}}$, it must maintain a constant tip speed ratio. The tip speed ratio which represents this maximum power coefficient is shown by the $C_p - \lambda$ curve in Figure 2.5. The shape of this curve is determined by the physical attributes of the rotor. In the case of Figure 2.5, $C_{p_{\max}}$ is about 0.48 and occurs at a tip speed ratio of about 7.8.

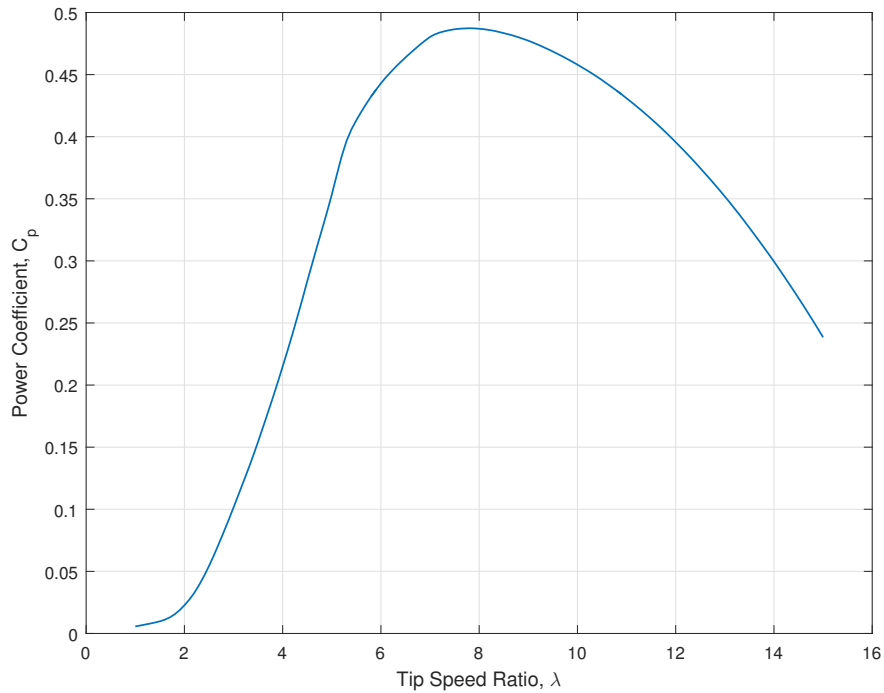


Figure 2.5: $C_p - \lambda$ curve for a 5MW wind turbine at minimum blade pitch angle

To track the maximum power coefficient, the generator torque is controlled

using equation (2.2), where T is the generator torque, K_{opt} is a constant chosen so that power output is at a maximum for a given wind speed and ω_g is the generator speed.

$$T = K_{opt}\omega_g^2 \tag{2.2}$$

At higher wind speeds, the third below-rated mode is another constant speed mode where the generator torque is controlled to maintain a constant speed. This generator speed is the same as the generator speed for above-rated operation.

The below-rated control strategy is therefore defined by the generator speeds of the two constant speed sections and the torques which represent where these speeds intersect the $C_{p_{max}}$ curve defined by (2.2). The torque-speed diagram in Figure 2.6 shows the two constant speed modes as vertical lines and the $C_{p_{max}}$ tracking mode as a curve between them. The dashed lines show the torque-speed curve for a series of constant wind speeds from lower at the bottom left to higher at the top right.

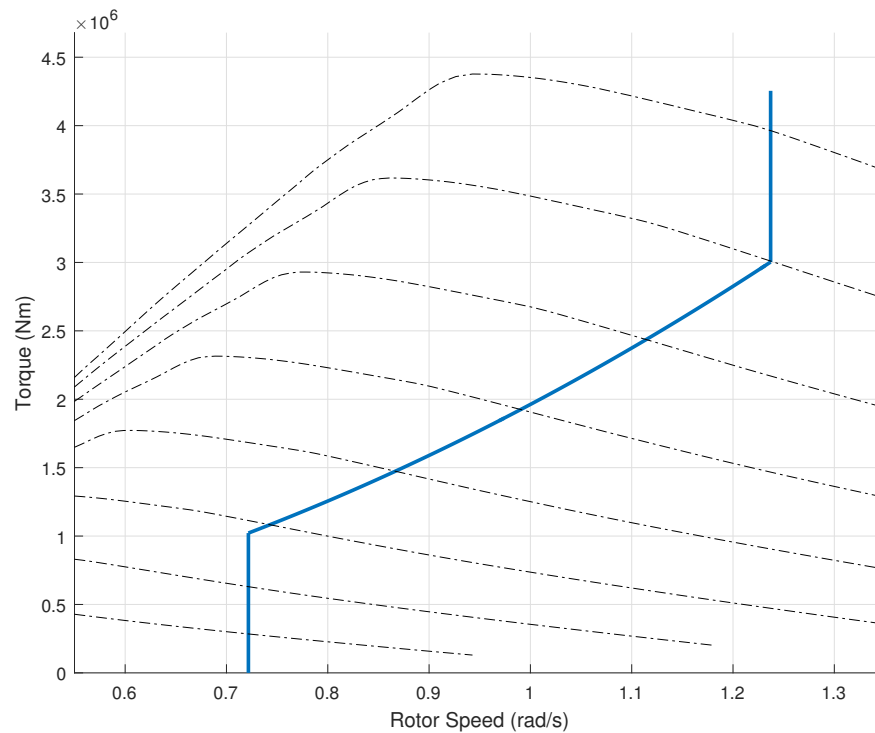


Figure 2.6: A typical control strategy for a 5MW HAWT shown on a torque-speed diagram

Above-rated

When operating above-rated, the torque and speed are held constant at the point at the top of the higher constant speed section shown in Figure 2.6. The power output of the wind turbine is therefore constant for all above-rated wind speeds. Figure 2.7 shows a the power output for a range of wind speeds for a wind turbine with a rated power of 5MW. The three below-rated modes are marked by the vertical dotted lines along with cut-in and cut-out wind speeds at 4m/s and 25m/s respectively. In these modes the power output steadily increases with wind speed. In above-rated operation, the power output is constant because the generator torque is also constant and the blade pitch angle is controlled to maintain a constant generator speed. The power output shown in Figure 2.7 is mechanical power at the hub. It is therefore slightly greater than the nameplate

rating of 5MW to account for mechanical and electrical losses further down the power-train.

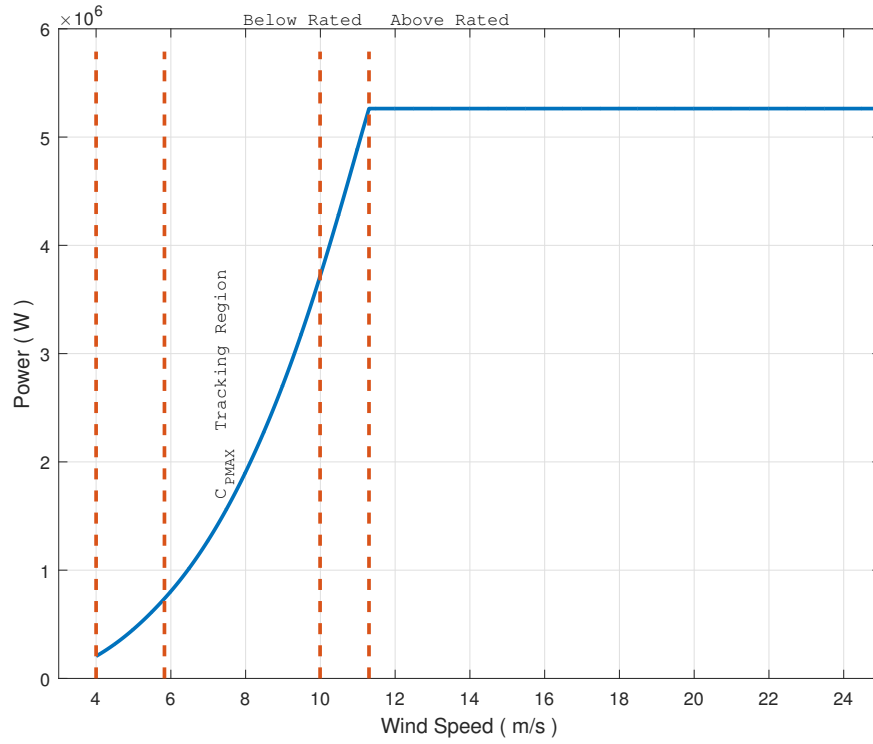


Figure 2.7: Power curve for a 5MW wind turbine

The fundamental design objective for the above-rated controller of a large pitch actuated, variable speed HAWT is to balance the gain crossover frequency with appropriate gain and phase margins. Work by van der Hoven [15], states that a turbulent peak exists in the spectrum of the wind centred around a period of about 1 minute. The wind spectrum showing this turbulent peak along with a diurnal peak, a synoptic peak and a seasonal peak is shown in Figure 2.8. The controller design task is a disturbance rejection problem where the disturbance is the wind. Specifically, the controller must be designed so that the system rejects the disturbance of the turbulent spectral peak in the wind speed depicted by the van der Hoven spectrum.

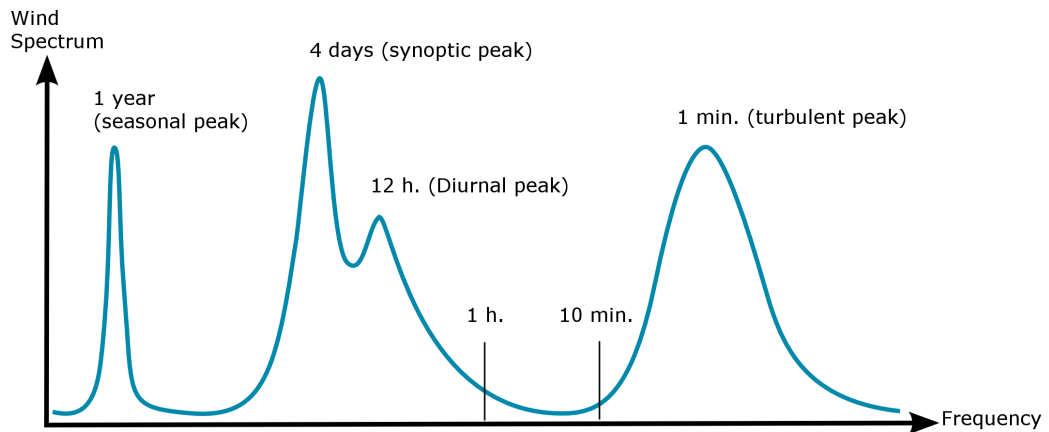


Figure 2.8: Wind spectrum based on work by van der Hoven

The focus of this thesis is on operational control. The following chapters make comparisons between various controller designs and overall wind turbine sizes and use the definition of operational control at the start of this section as a measure of performance. When the wind turbine is operating above-rated power, smaller fluctuations in generator speed and power output are desirable because this is better for the electrical hardware and the grid. Lower loads in the blades, tower, and drivetrain are also desirable because this increases component lifetime and reduces the cost of the mechanical design which will consequently reduce the cost of energy.

2.3 Simulation Environments

Two simulation environments have been used to produce the data presented in this thesis: Simulink and Bladed. MATLAB and Simulink provides an environment to easily modify and develop the controller design and wind turbine model. Bladed, developed by DNV GL, previously Garrad Hassan, is a proprietary wind turbine simulation package widely used by the wind energy industry. It offers

a much more complex simulation of the wind turbine and is used to produce the majority of the data in this thesis. The key differences between these two simulation environments are highlighted in the following sections.

2.3.1 DNV GL Bladed

Bladed is a widely used and well validated aero-elastic wind turbine design tool. It uses blade element momentum theory to model the rotor aerodynamics in a three-dimensional turbulent wind field [16]. Blade element momentum (BEM) theory considers the rotor to be an ‘actuator disk’ [17]. As air flows through the swept area of the rotor, its velocity and static pressure changes resulting in a change in momentum. This change in momentum is used to calculate forces on the blades. The simulated wind field includes spatial characteristics such as wind shear, where the wind speed varies with height, and tower shadow, where the flow around the blade is distorted by the presence of the tower.

Controllers used for Bladed simulations are written as discrete-time routines in either Fortran or the C programming language. All Bladed simulations referred to in this thesis use controllers written in C. The nature of this implementation means that controller code must be written so that it is executable without the use of a numerical solver. This means that, unlike with Simulink which has a built-in numerical solver, the controller algorithm must not contain any algebraic loops.

2.3.2 MATLAB Simulink

The Simulink model of the Supergen Exemplar turbine [14] is much simpler than Bladed but offers an environment where changes can be made and tested much more easily and without the constraints of designing for a discrete-time implementation. It also avoids the need to write code for the controller in C until the

control algorithm has been fully designed and tested.

In-plane and out-of-plane torques on the rotor are calculated by using the values of blade pitch angle and tip-speed ratio and values for the power coefficient, C_p , from a look-up table. These rotor torques, along with a model of the drivetrain, are used to calculate the torques and speed at the generator.

The most significant simplification is that the wind is modelled as an effective wind speed, uniform across the whole rotor rather than a full turbulent wind field.

An effective wind speed is a scalar, time-varying wind speed, applied uniformly over the rotor that produces a scalar torque or force induced by the spatially and time-varying wind field. It includes components that represent the stochastic and deterministic effects seen in a full wind field model [18]. It, therefore, essentially represents an average of the wind speed across the rotor. Rotational sampling of the turbulent wind field, wind shear, and tower shadow are all accounted for. Compared to a wind speed measured at a single point, this results in the power spectrum of wind speed having peaks at frequencies of integer multiples of the rotor speed (particularly three and six times the rotor speed) and being decreased elsewhere.

A model for calculating an effective wind speed in a continuous-time simulation is presented by Neilson [13] and is used here for all simulations in Simulink.

2.4 Linearised Models

A linearised model of the wind turbine is an approximation of the dynamics of the system at a set operating point. Here, linear models of the wind turbine are used to assess the stability of the controlled system and the characteristics of the dynamics. In the context of wind turbine controller design, this operating point is normally set by a wind speed. Accurate linearised models are therefore

important for the design of the controllers discussed here.

There are several methods available to produce such a linearisation of the wind turbine. Both Simulink and Bladed have modules or toolboxes available to linearise the system and they work in similar ways. Perturbations are applied to the full dynamic model, the outputs are measured, and a representative state space model is produced. Alternatively a state space model of the wind turbine can be constructed algebraically. In Leithead and Rogers [19] [20] and subsequently Chatzopoulos [14], a state space model is produced which includes aerodynamics and dynamics of the rotor, drivetrain, and tower. A MATLAB toolbox has also been developed by SgurrControl [21] which provides a tool for easily producing linearised models of the wind turbine. The algebraic state space model of the wind turbine is presented in detail in Appendix B.

Figure 2.9 shows a comparison of the two linearisation methods described above for the transmittance from blade pitch angle demand to generator speed for a wind speed of 14m/s. The two methods generally agree on the frequencies of important dynamics like the natural frequency of the tower at just less than 2rad/s and the first drivetrain mode at about 9rad/s but there are small differences in the level of damping. This difference can be attributed to the different levels of complexity in the dynamic models. Also, the Bladed linearisation includes a second drivetrain mode at just over 20rad/s. The algebraic linearisation provided by the SgurrControl MATLAB toolbox is used to generate all linear models used in this thesis because of its convenience and because it does not include dynamics superfluous to the requirements of controller design like the second drivetrain mode visible in Figure 2.9. For this reason, there is no peak showing a second drivetrain mode in the bode plot of the algebraic linearisation.

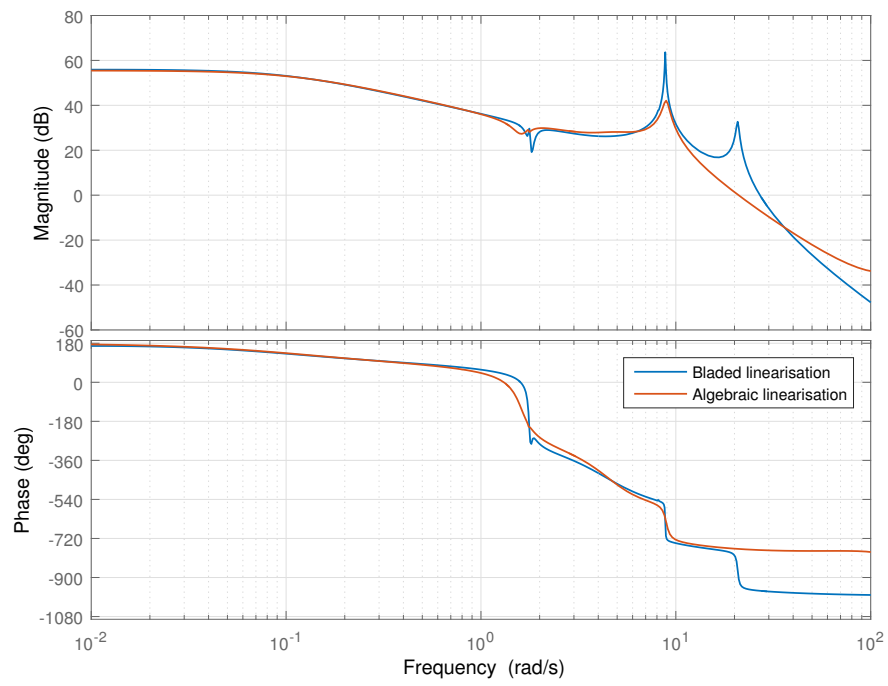


Figure 2.9: Comparison of Bladed and algebraic linearisations

Chapter 3

Baseline Models and the Up-Scaling of Wind Turbines

As wind turbines increase in size, their dynamics and behaviour change. This chapter discusses how two very large wind turbines and controllers are designed by extrapolation of the parameters of an existing model. These models are tested, and behavioural changes resulting from the increased scale are discussed. The existing model from which the larger machines are extrapolated is a 5MW wind turbine developed by the Supergen Wind Energy Technologies Consortium.

If a sample of real wind turbines of varying sizes was taken, it is likely that the larger ones would be newer and would include newer technology. Consequently, it is also likely that the performance of the wind turbines in the sample would perform differently for reasons other than physical size. The method for extrapolating the parameters of the up-scaled wind turbine models is described in the following section. This method maintains similarity between the models by ensuring that, in simulations, the only differences that can be seen are due to size.

The controllers for the up-scaled wind turbines are also scaled so that only the

effect of the physical size of the wind turbine is evident in simulation results. This is achieved by designing the up-scaled controllers to switch operating modes at the same wind speeds, track the same tip-speed ratios and have the same stability margins as each other.

Models of all three turbine sizes have been constructed in both MATLAB Simulink and DNV GL Bladed and compared with each other. Where appropriate, linear models are derived using the SgurrControl MATLAB toolbox (SgurrControlBox). Tables of parameters describing the relevant major components of the upscaled models used in the Bladed simulations are shown in Appendix A.

3.1 Wind Turbine Model Scaling

If a homogeneous three-dimensional object is considered with a characteristic length L , then the object's surface area and volume would scale as L^2 and L^3 respectively. The physical parameters of the wind turbine discussed in the following sections use this method of considering scale-factor powers. For the purpose of extrapolating parameters for a wind turbine, the characteristic length used is the radius of the rotor. With the scale-factor power and the value of the parameter from the baseline model, an extrapolated value can be calculated as in (3.1) where P_{ex} is some parameter of the extrapolated model, P_{bl} is the equivalent parameter in the baseline model, D is the scale factor and SP is the scale factor power.

$$P_{ex} = P_{bl}D^{SP} \tag{3.1}$$

The scaling rules set out in the sections below are used with the baseline 5MW machine to construct models of two wind turbines with rated power outputs of 7.5MW and 10MW.

3.1.1 Power

The aerodynamic power at the rotor is given by equation (3.2) [17] where ρ is the fluid density, R is the radius of the rotor, v is the wind speed and C_P is the power coefficient.

$$P = \frac{1}{2}\rho\pi R^2 v^3 C_P \quad (3.2)$$

The density of air ρ and the wind speed v are unrelated to the size of the wind turbine. The Reynolds number will increase with turbine size, but for multi-megawatt scales the effect of this is negligible [11]. If the Reynolds number and the tip speed are maintained constant in similarly scaled models then the flow geometry is also unchanged and therefore the power coefficient does not change with turbine size. The relationship between C_P , the blade pitch angle β , and the tip speed ratio λ also remains unchanged. It follows, then, that the power output scales with the square of blade length.

With this method, the rotor radius of similarly scaled wind turbines with power outputs of 7.5MW and 10MW can therefore be calculated from a baseline 5MW model. The radii for the three machines are shown in Table 3.1.

Rated Power (MW)	Rotor Radius (m)
5.0	63.0
7.5	75.9
10.0	87.6

Table 3.1: Radii for the baseline 5MW model and the two large models

3.1.2 Mass and Inertia

Given that volume scales cubically with characteristic length, mass also has a scaling power of 3. However, if a selection of real wind turbines were to be gathered and the masses of various components compared, then the empirical

value would be lower than this [11]. The primary reason for this is that larger wind turbines tend to be more modern and more advanced materials and manufacturing processes have been used to reduce mass. However, these factors are outwith the scope of this thesis and therefore not considered.

The moment of inertia is the product of the mass and the square of the radius of gyration. Therefore, if the mass scales cubically and the radius linearly, the moment of inertia scales with the power of 5.

All masses and inertias used for the scaled wind turbine models discussed in this thesis are obtained using the above scaling factors.

3.1.3 Stiffness & Natural Frequency

The end deflection, d , of a cantilever beam with a point load at the tip is shown in (3.3), where W is the load, L is length of the beam, E is the Young's modulus of the beam material and I is the second moment of area of the beam.

$$d = \frac{WL^3}{3EI} \quad (3.3)$$

If the load and material properties remain constant, the maximum deflection of the tip of this beam would then scale with the power of -1. Therefore, if the stiffness of the beam is the ratio of the load to the displacement, W/d , it will scale linearly.

The natural frequencies of the first fore-aft mode of the tower and first edge-wise and flapwise modes of the blade are calculated using the modal analysis feature of Bladed. All masses, inertias and stiffness are defined using the scaling factors as described above. The resulting frequencies are shown in Table 3.2.

	5MW	7.5MW	10MW
Tower fore-aft mode, ω_t	1.7467	1.3258	1.0681
Blade flap mode, ω_f	4.2726	3.2358	2.6075
Blade edge mode, ω_e	6.7984	5.1459	4.1407

Table 3.2: Primary natural frequencies (rad/s)

3.2 Controller Design

Baseline controller designs are produced for the two upscaled turbines. These controllers use the same basic structure and switching design as the 5MW machine [14] but have different parameters and transfer functions to suit the different dynamics of the larger turbines. The following sections describe the design of the control strategy, which defines a set of operating modes where the relationship between torque and speed is set. A global gain-scheduling design is used to counter non-linearities which exist between torque and blade pitch angle and rotor speed. In addition, a drivetrain filter is used to increase the damping of the system around the frequency of the first drivetrain structural mode. Finally, transfer functions of the above-rated and below-rated controllers are defined.

3.2.1 Operating Strategy

The control strategy is designed to allow the wind turbine to achieve the greatest power capture whilst avoiding operating at rotor speeds which will excite primary structural modes. As well as this, the rotor speed may also be limited to avoid excessive noise. Historically, blade tip speed has been limited to 75–80m/s for land-based wind turbines [22]. In this thesis, however, the priority is that the controllers of three machines are similar. For this reason, the tip speed in above-rated operation has been kept the same, at 77.94m/s.

When operating below rated power, the control strategy defines the relationship between generator torque and generator speed. The designs discussed here

have four operating modes. In mode 0, for wind speeds at the lowest end of the operating range, the speed is maintained at a constant value, ω_0 , as torque varies between cut-in and a value of T_0 where the maximum value of the power coefficient C_{Pmax} is reached. Mode 1 tracks this maximum by controlling generator speed to maintain a constant tip speed ratio. The resulting curve is described by equation (3.4). In mode 2 the speed is kept constant in the same way as in mode 0 and the torque varies up to T_{set} where rated power is reached. Mode 3 is also called above-rated where generator torque is constant at T_{set} and the blade pitch angle is controlled to maintain a constant generator speed.

$$T = K_{opt}\omega^2 \quad (3.4)$$

The rotor speeds of the first and second constant speed sections are chosen to ensure that the rotor sampling frequencies, 1P, 3P and 6P, do not coincide with the primary natural frequencies of the blades and tower shown in Table 3.2.

In addition, constant speed sections of the strategy are also chosen to provide as large maximum power tracking region as possible. This mode of operation, where the tip speed ratio is kept at the level which delivers the maximum power coefficient, must cover as wide a range of speeds as possible to deliver the greatest possible power capture.

The strategies of the up-scaled controllers are designed to have the same tip speed at both upper and lower constant speed sections and the same generator speeds. The turbines have different gearbox ratios to achieve this. The rotor speeds for the lower (Ω_0) and upper (Ω_1) constant speeds are shown in Table 3.3. Each turbine has a different value for K_{opt} as a result of having different upper and lower constant speeds but the controller is tracking the same maximum power coefficient at the same tip-speed ratio in mode 1.

	5MW	7.5MW	10MW
Ω_0	0.72	0.60	0.52
Ω_1	1.24	1.03	0.89

Table 3.3: Control strategy rotor speeds (rad/s)

Complete torque-speed diagrams showing the strategy for the 5MW, 7.5MW, and 10MW designs are shown in Figures 3.1, 3.2, and 3.3 respectively.

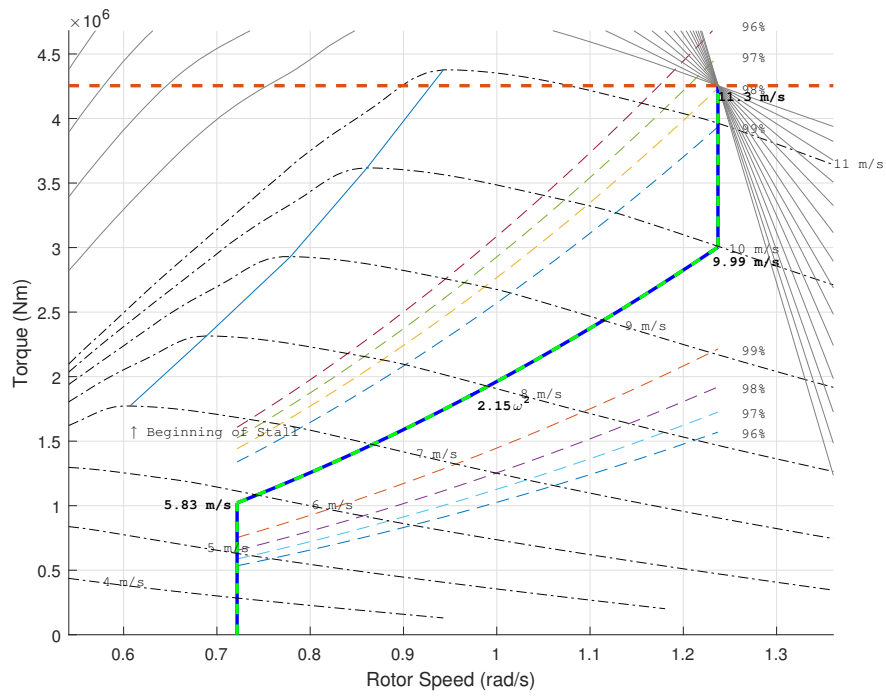


Figure 3.1: 5MW control strategy

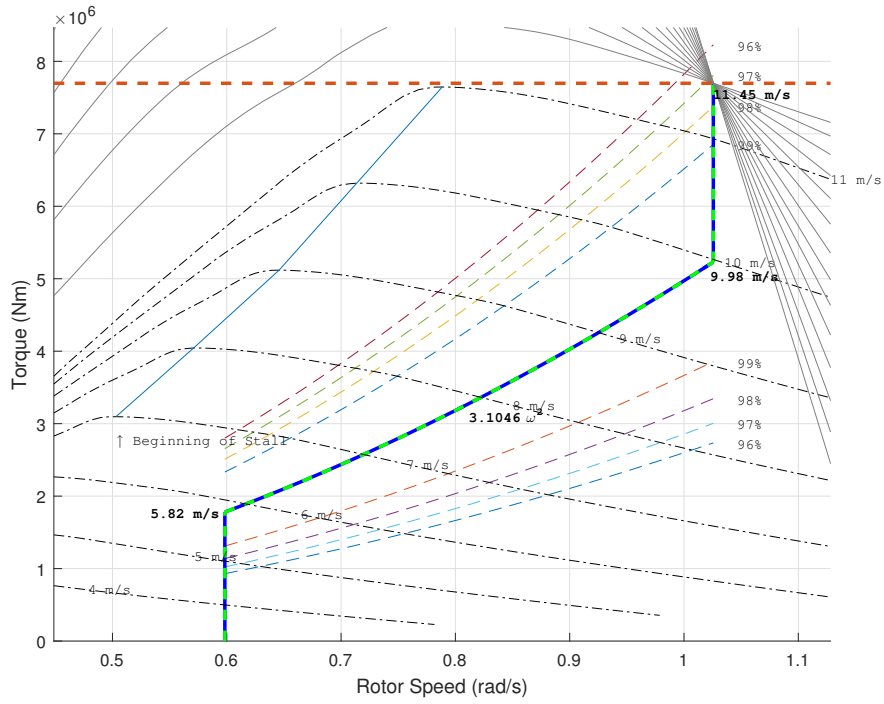


Figure 3.2: 7.5MW control strategy

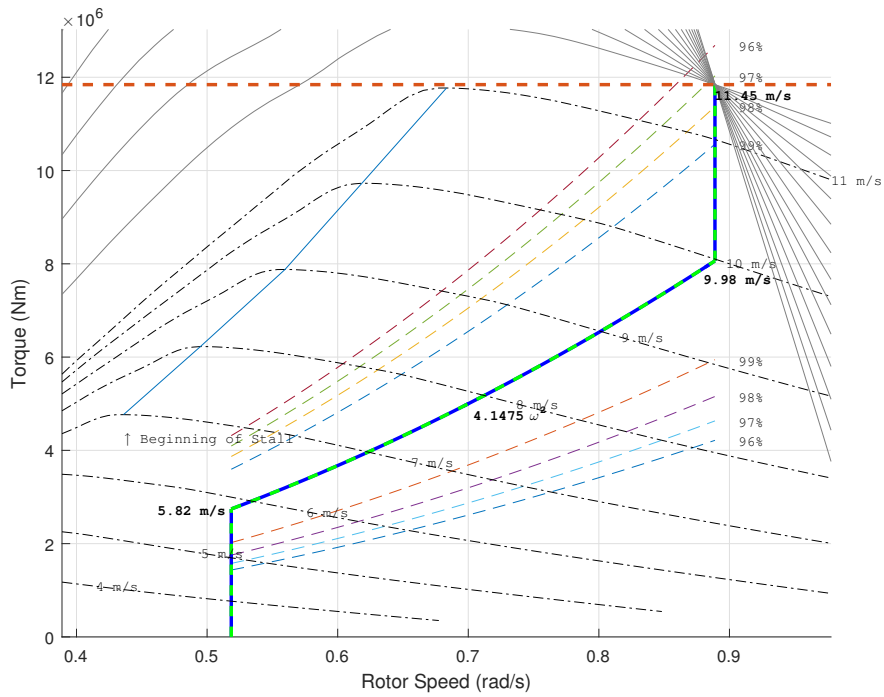


Figure 3.3: 10MW control strategy

3.2.2 Gain-Scheduling

Gain-scheduling is a type of non-linear control design that allows linear control techniques to be applied to a system which exhibits non-linear behaviour. Traditional gain-scheduling uses a set of linearisations at equilibrium operating points to enable the design a set of linear controllers. A gain-scheduled controller is designed by selecting structures for the set of linear controllers which can be easily interpolated between [23].

For pitch regulated wind turbines, a non-linearity exists between the aerodynamic torque generated and the blade pitch angle [24]. The traditional gain-scheduling approach is not appropriate for this application so, instead, the system is globally linearised exploiting separability. An implementation of global gain-scheduling which allows linear control design methods to be used with a globally linearised system is described below.

Separability

The aerodynamics of a pitch regulated wind turbine is highly non-linear. Separability allows a linear control design approach to be applied to the non-linear system [25]. Figure 3.4 shows the non-linear plant dynamics where torque (T) is a function of pitch angle β , rotor speed (Ω) and effective wind speed (v). Separability determines that this function can be separated into two components as in (3.5) with one function dependent on pitch angle and rotor speed and one function dependent solely on effective wind speed [25]. This is achieved by linearising the system locally to an equilibrium point defined by the pitch angle, rotor speed and effective wind speed. The resulting block diagram is shown in Figure 3.5.

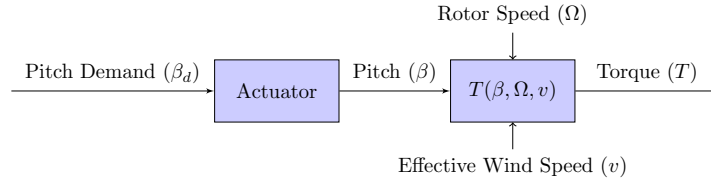


Figure 3.4: Dynamics of torque, pitch angle, rotor speed and effective wind speed

$$T(\beta, \Omega, v) = h(\beta, \Omega) - g(v) \quad (3.5)$$

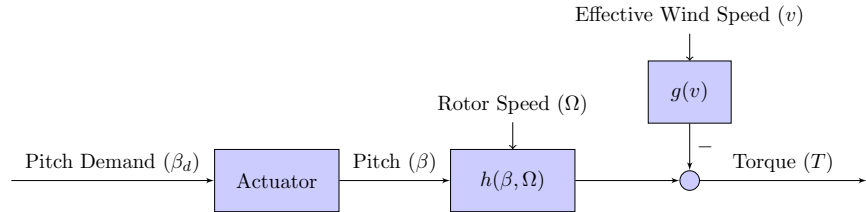


Figure 3.5: Separated dynamics of pitch demand and generator torque

The result of this is that the dynamics of the wind turbine which are relevant to the design of the controller are not dependant on wind speed.

Global Gain-scheduling Implementation

For pitch regulated wind turbines the rotor speed is constant when operating above-rated. The function $h(\beta, \Omega)$ as described in Figure 3.5 can therefore be considered to be a function dependent solely on pitch angle, $h(\beta)$. Figure 3.6 shows the structure of the non-linear controller, where β_{d0} is the unscheduled pitch demand, β_d is the gain-scheduled pitch demand, $A(s)$ is a transfer function describing the pitch actuator and h is the non-linear dynamics, as in (3.5) [23].

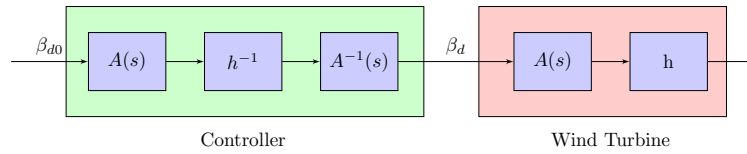


Figure 3.6: Structure for implementing gain-scheduling

The function h^{-1} in the controller, as shown in Figure 3.6, can be implemented by taking a normalised linear fit of the partial derivative of torque with respect to pitch angle, $\partial Q/\partial\beta$, then integrating and inverting. Figure 3.7 illustrates the partial derivative $\partial Q/\partial\beta$ and the linear fit.

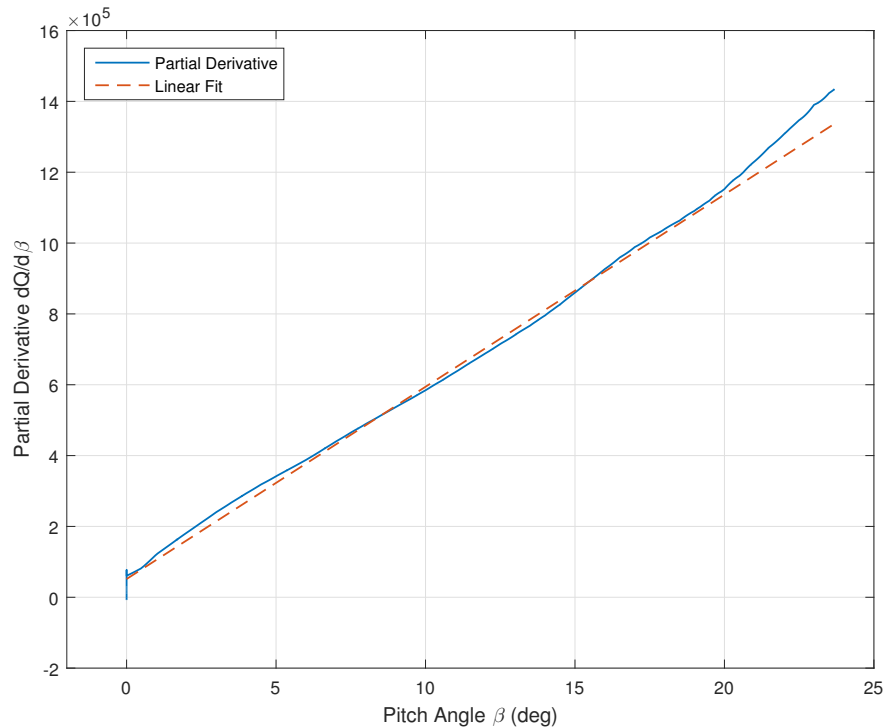


Figure 3.7: Partial derivative of torque with respect to pitch angle for the 5MW wind turbine

The aerodynamic non-linearity that this global gain-scheduling implementation is intended to eliminate can be seen in Figure 3.8, where different wind speeds exhibit a different gain response around the critical frequency range about

1rad/s and below. This frequency range is important because it coincides with a spectral peak in the wind speed which represents turbulence. This is discussed in more detail in the next section. With the global linearisation implementation as described above, this aspect of aerodynamic non-linearity is removed and the wind turbine exhibits the same gain response around the crossover frequency just below 1rad/s for all wind speeds. This effect is shown in Figure 3.9, where the gain response for different wind speeds appears to be ‘pinched’ together at these frequencies. A linearised gain response at the crossover frequency allows design techniques for linear control to be applied for the main controller. Although the gain response shows linear behaviour at frequencies in the region of around 0.5–1rad/s, a significant non-linearity is still evident at lower frequencies. This can be seen in Figure 3.9 as a ‘fanning’ of the gain response for different wind speeds. This will be discussed further in Chapter 5. In both Figures 3.8 and 3.9 a drivetrain filter is present as described in Section 3.2.4.

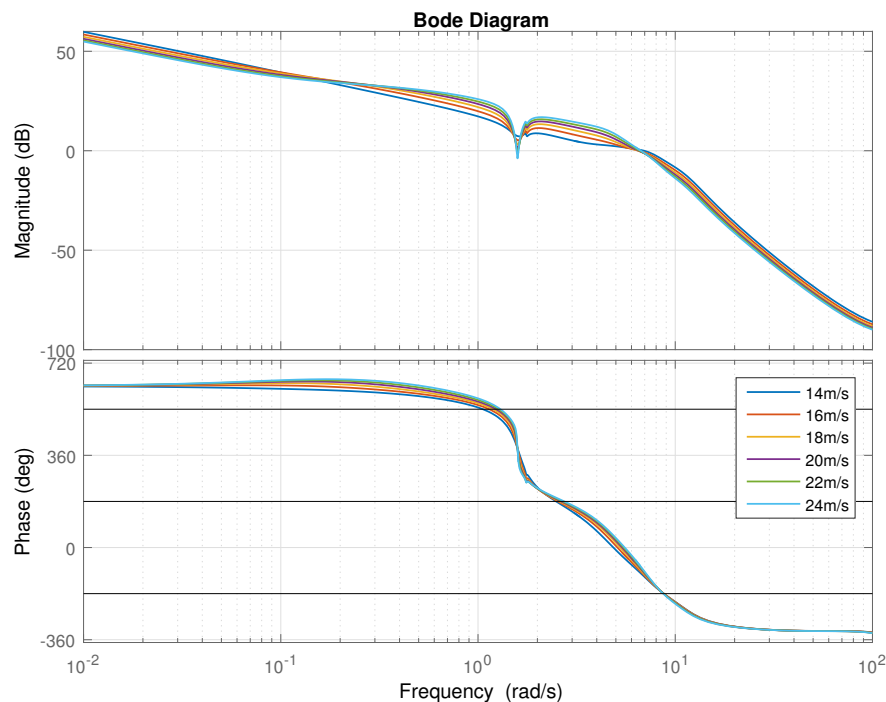


Figure 3.8: Open loop Bode plot without gain-scheduling

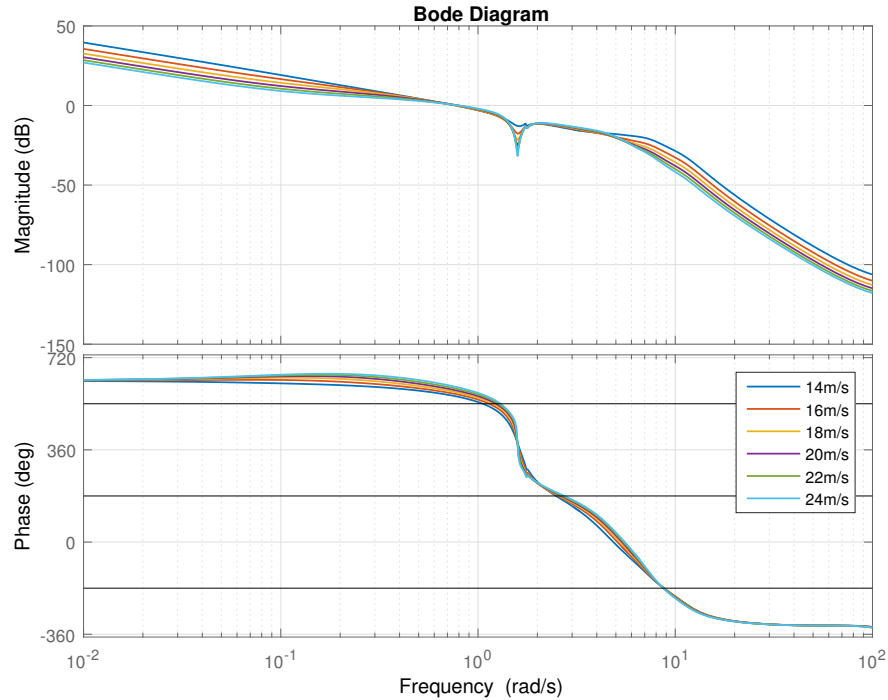


Figure 3.9: Open loop Bode plot with gain-scheduling

3.2.3 Linear Control Design

Above-Rated Controller

The above-rated controllers for the upscaled machines are structurally the same as in the 5MW baseline model. They comprise static gain, an integrator, a real zero and a real pole to provide zero-offset set-point tracking, good disturbance rejection at low frequencies and high-frequency roll-off.

The van der Hoven spectrum describes how peaks in the power spectrum of wind speed are present in two distinct frequency ranges separated by a spectral gap [15]. Figure 3.10 shows these two spectral peaks as well as a third, seasonal peak. The first peak occurs at a period of around 4 days and constitutes changes in wind speed due to passing synoptic pressure systems. The second peak is centred at a period of around 1 minute and is due to more local turbulence. For a controller to provide good disturbance rejection, it is therefore important for

the bandwidth of the controller to span the frequency range of the high frequency peak in the Van der Hoven spectrum. For this reason, it is desirable to have a gain crossover frequency as close to 1rad/s as possible.

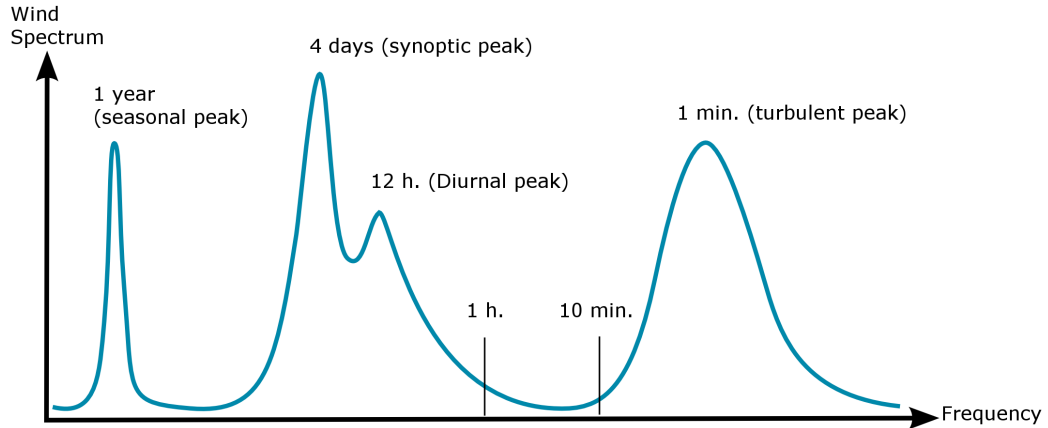


Figure 3.10: Van der Hoven spectrum

With the 5MW baseline machine, a crossover frequency of 0.8rad/s is achievable. However, as the size of the wind turbine increases and the natural frequency of the tower decreases, it becomes more difficult to design a controller with a suitably high crossover frequency and appropriate margins of stability. The controllers for the upscaled wind turbines have therefore been designed with lower gain crossover frequencies and similar gain and phase margins. The crossover frequencies and stability margins for the above-rated controllers at a wind speed of 14m/s are shown in Table 3.4. The transfer functions of the above-rated controllers for the 7.5MW and 10MW turbines are given in Table 3.5. The locations of the poles and zeros in the upscaled controllers have been adjusted to maintain similarity in the dynamics of the series of controllers.

	5MW	7.5MW	10MW
Gain Margin	3.97dB	3.63dB	3.87dB
Phase Margin	31.0°	29.6°	31.2°
Crossover Frequency	0.751rad/s	0.575rad/s	0.451rad/s

Table 3.4: Stability margins and crossover frequencies for the above-rated controllers at a wind speed of 14m/s

5MW	7.5MW	10MW
$-0.17238 \frac{(s+0.12024)}{s(s+1.8)}$	$-0.16527 \frac{(s+0.08766)}{s(s+1.5)}$	$-0.13933 \frac{(s+0.07249)}{s(s+1.3)}$

Table 3.5: Transfer functions of the above-rated controllers

Figure 3.11 shows the open loop Bode plots of the controller and plant for the three different sizes of turbine. The rapid phase loss due to right-half-plane zeros at the tower first mode natural frequency is visible between 1rad/s and 2rad/s. As wind turbines increase in size and the tower frequency reduces, the rapid phase loss necessitates a lower crossover frequency. This constriction of the available bandwidth inhibits the ability of a controller to reject disturbances from the wind. Therefore, as the size of a wind turbine increases, this reduced ability would be expected to contribute to a reduction in effectiveness of speed control.

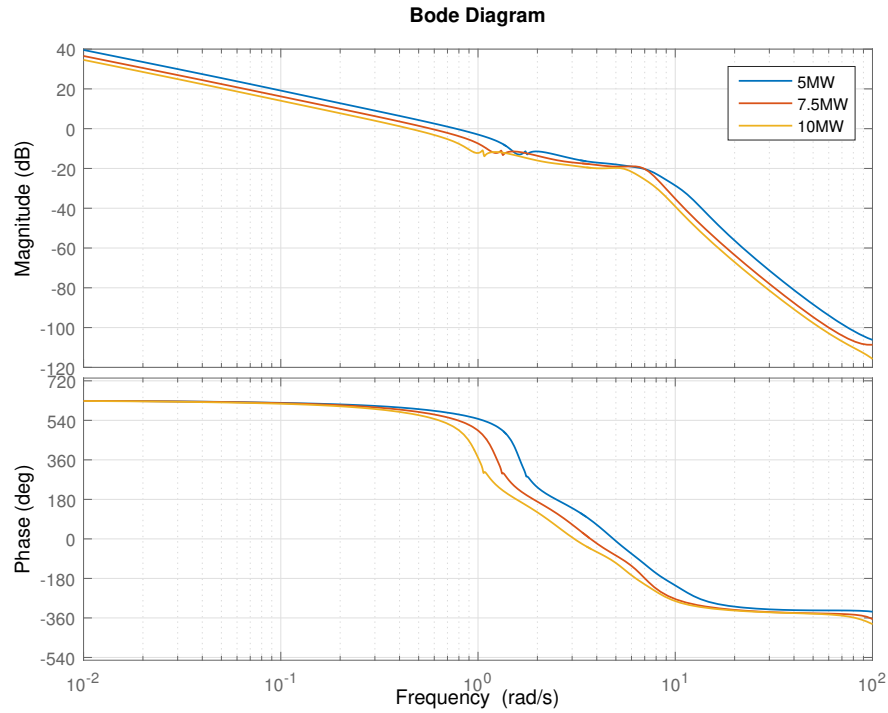


Figure 3.11: Open loop Bode plots for the controller and plant at 14m/s of three differently sized turbines

Sensitivity functions are compared in Figure 3.12. The ability of the controller to reject the disturbance of the wind is indicated by the area at low frequency between 0dB and the magnitude of the sensitivity function. Since the gain crossover frequency is reduced, the larger turbines have a smaller area and therefore would have relatively poorer speed control.

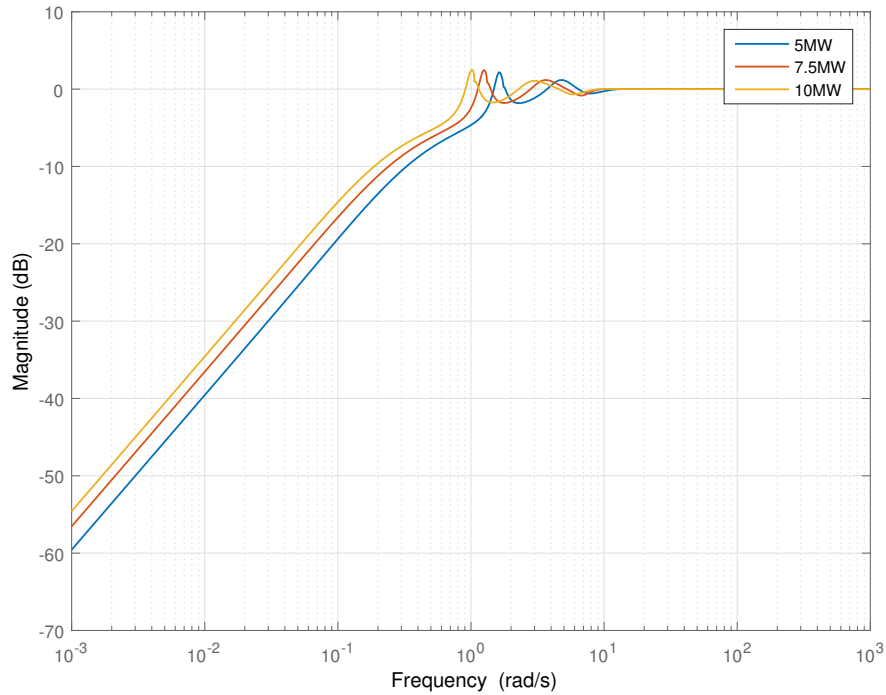


Figure 3.12: Sensitivity functions of the controller and plant for three differently sized turbines

Below-Rated Controller

The below-rated controllers have poles and zeros in the same locations as their corresponding above-rated controllers. The gain is adjusted so that the crossover frequency is the same as for the above-rated controller. This is to ensure that there is no transients in the control signal when changing between above and below-rated operating modes. The nature of the dynamics of below-rated control means that any limiting factors on crossover frequency tend to be more restrictive in above-rated control. For this reason it is generally not a problem to design a below-rated controller with the same crossover frequency as the above-rated controller. The transfer functions of the below-rated controllers for all three turbines are shown in Table 3.6. Note that only the gain has changed from the transfer functions in Table 3.5.

5MW	7.5MW	10MW
$-11743.2 \frac{(s+0.12024)}{s(s+1.8)}$	$-9310.38 \frac{(s+0.08766)}{s(s+1.5)}$	$-9789.71 \frac{(s+0.07249)}{s(s+1.3)}$

Table 3.6: Transfer functions for the below-rated controllers

3.2.4 Drivetrain Filter

The first drivetrain mode is lightly damped and highly resonant. If left unchecked it can cause unacceptable loads and even controller instability. By adding a feedback loop with a signal proportional to the rate of change of the generator speed to the torque controller, damping can be increased. To achieve this, a band pass filter is used to ensure that only the frequencies close to the first drivetrain mode are affected to avoid influencing generator speed control. The transfer function for the drivetrain filter is shown in (3.6) and a block diagram illustrating its place in the system is shown in Figure 3.13. T_d is the generator torque demand from the controller, ω is the generator speed, ζ is the damping ratio and k is a gain.

$$G_{dtr}(s) = \frac{k\omega s}{s^2 + 2\zeta\omega_n s + \omega_n^2} \quad (3.6)$$

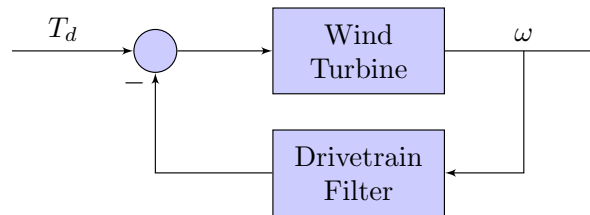


Figure 3.13: Location of the drivetrain filter in the system

3.2.5 Discretisation and the Anti-windup Loop

The anti-windup loop is a mechanism built into the controller to prevent it from requesting a blade pitch rate which is out of the range of the actuator. The estimated demanded pitch rate is compared to pre-set upper and lower limits which, if passed, closes the anti-windup loop. Such a situation may arise when a controller set-point is changed, for example, creating a step change in the error. In this situation the actuator can't keep up with the demanded values and the integrator term in the controller 'winds up' and becomes irregularly large [14].

To accommodate the anti-windup loop, all transfer functions in the path from the measured generator speed to pitch demand are formulated so that, in their discrete-time form, their outputs are not dependent on their inputs at the current time step. The result is that each transfer function is replaced by a transfer function the output of which is added to the current input multiplied by a constant. The details of this formulation is in Appendix D. This change allows the input to be back calculated at the current time step if the output is known.

In the continuous-time implementation, the anti-windup loop is applied as a feedback loop with the feedback signal proportional to the difference between the demanded pitch rate and the pre-set limit. The feedback loop is such that, if closed, the input of the controller is modified so that the demanded pitch rate is exactly that of the pitch rate limit. In the discrete time implementation, this is achieved by calculating back through the controller using the new formulation [25] [26].

When the output would saturate the actuator, the states of the actuator are back-calculated and the input error is modified to that which would cause the controller output to just cause the actuator to saturate.

3.3 Controller Implementation and Architecture

This section outlines the implementation of switching structure presented by Leithead and, subsequently, Chatzopoulos [27] [14]. The low frequency dynamics of both the above-rated and below-rated controllers are similar. It is therefore only necessary for the difference to be a change in gain. This relationship is described by (3.7), where $C_{AR}(s)$ is the above rated controller, $C_{BR}(s)$ is the below rated controller and K_p is the gain which relates the two.

$$C_{AR}(s) = C_{BR}(s)K_p \quad (3.7)$$

The switching structure is as follows:

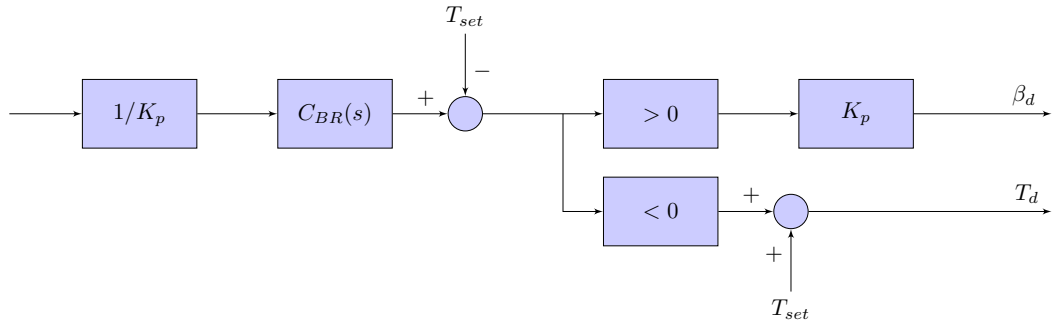


Figure 3.14: Switching structure

Switching between the two paths shown in Figure 3.14 occurs on the change of sign. Since K_p is just a gain, it does not alter the low frequency dynamics of the system and there are therefore no significant transients when switching occurs. Additionally, for the torque loop, $1/K_p$ and K_p cancel meaning there is no rescaling of the offset.

The below rated controller $C_{BR}(s)$ is split into two components: the outer controller, $C_o(s)$ and the inner controller, $C_i(s)$. The components are split so

that:

$$K_p^{-1}C_{BR}(s) = C_o(s)C_i(s) \quad (3.8)$$

The outer and inner controllers are split such that the outer controller contains no low frequency dynamics and $\frac{C_o(s)C_i(s)}{1-C_i(s)}$ is a low pass filter. The transfer functions for the inner and outer controllers for the 5MW, 7.5MW and 10MW turbines are shown in Table 3.7.

	5MW	7.5MW	10MW
Outer controller	$\frac{117.432}{(s+1.8)}$	$\frac{165.270}{(s+1.5)}$	$\frac{139.330}{(s+1.3)}$
Inner controller	$\frac{-100(s+0.12024)}{s}$	$\frac{-100(s+0.08766)}{s}$	$\frac{-100(s+0.07249)}{s}$

Table 3.7: Transfer functions for inner and outer controllers

3.3.1 Below-rated Switching

In below-rated operation, there are three operating regions which are defined by the control strategy. The first (mode 0) is a constant speed section. In the second region (mode 1), the rotor speed varies to track the maximum power coefficient. The third region (mode 2) is another constant speed section. Torque-speed diagrams depicting these operating modes are shown in Section 3.2.1. Figure 3.15 shows the configuration of the switching for below-rated control. The logic for the switches, S1, S2, S3, and S4 are shown in Table 3.8. Where present, u refers to the input of the block. The configuration shown in Figure 3.15 assumes there are no damping losses in the drivetrain. To account for damping losses and ensure the the controller tracks the maximum possible power coefficient, $K_{opt}(u)^2$ should be replaced with $K_{opt}(u)^2 + Bu$, where B is the drivetrain damping. At time of writing, and for all of the simulation results presented in this thesis, damping losses are not accounted for in the controller in this way.

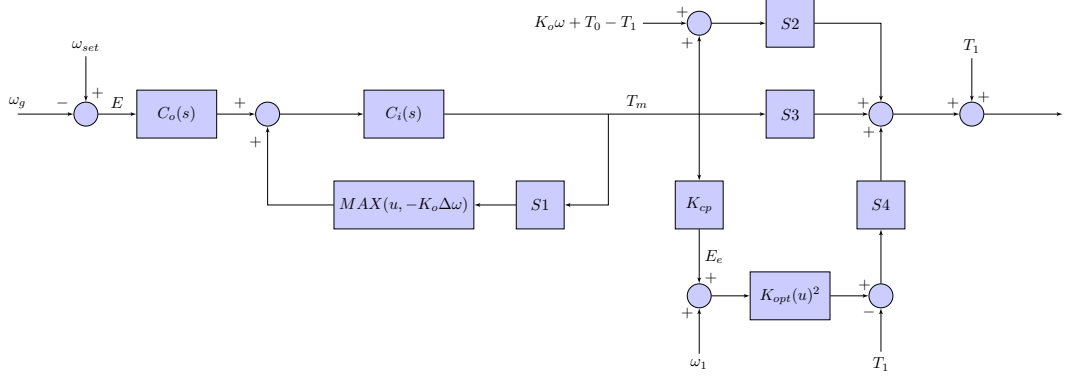


Figure 3.15: Below-rated switching structure

Switch	Logic
$S1$	< 0
$S2$	$< (T_0 - T_1)$
$S3$	> 0
$S4$	$> (T_0 - T_1) AND < 0$

Table 3.8: Logic for switches in below-rated control

Switching between the three below-rated operating modes is based on the demanded generator torque, represented in Figure 3.15 by T_m .

In mode 1, where the rotor speed varies to track the maximum power coefficient, the generator speed ω_g is less than the set point ω_{set} and E (in Figure 3.15) is less than 0. $C_i(s)$ has a negative gain so T_m will be less than 0. This closes the switch $S1$ and opens $S2$ and $S3$. With the loop containing $S1$ closed, the equation for T_m is as follows:

$$T_m = \frac{C_o(s)C_i(s)}{1 - C_i(s)} E \quad (3.9)$$

The gain, K_{cp} , is chosen so that E_e is an estimate of the error, E , with high frequency components of the signal removed. To achieve this $K_{cp} = 1/H(0)$ where:

$$H(s) = \frac{C_o(s)C_i(s)}{1 - C_i(s)} \quad (3.10)$$

The error estimation E_e is squared and multiplied by K_{opt} to give the torque demand. If the controller is to also account for losses due to drivetrain damping, the torque demand is equal to $E_e^2 K_{opt} + E_e B$. The torque demand, calculated in this way should be less than $T1$ so $T1$ is subtracted and the switch S4 closes when the signal is less than 0 and greater than $T_0 - T1$.

When $\omega_g > \omega_{set}$, T_m is positive so switch S3 closes and S2 and S4 open. Now, $T_m = E C_o(s)C_i(s)$

Switching to the lower constant speed section, mode 0, the speed is controlled on $\omega_g - \omega_{set}$ by introducing an offset of $-K_o \Delta\omega$ where $K_o = H(0)$ and $\Delta\omega = \omega_{set} - \omega_0$. Switching between modes 0 and 1 therefore occurs when $T_m = -K_o \Delta\omega$.

3.4 Simulations

In this section, simulation results for a baseline wind turbine and two upscaled wind turbines are presented. The simulations are conducted in both Simulink and Bladed and compared to demonstrate agreement in behaviour. Further simulation results from Bladed are presented to show the effect of up-scaling on generator speed, power output and pitch activity. All simulations in this section use a turbulent wind with Class B intensity as described by the IEC international standard 61400-1 (third edition) [28]. This usually results in a turbulence intensity of 10% to 20%, calculated over 10 minute intervals.

3.4.1 Comparison of Simulation Environments

The figures in this section show a comparison of the Simulink and Bladed simulation environments. The results are for simulations of 600 seconds with a 16m/s

mean wind speed and a turbulence intensity of about 15%. As discussed in the preceding chapter, the Simulink simulation uses an effective wind speed whereas the Bladed simulation uses a more comprehensive, three-dimensional turbulent wind field model. For these Simulink tests, the effective wind speed was derived using the hub point wind speed from the Bladed tests. This allows a reasonable comparison between the two simulation environments. Figures 3.16, 3.17 and 3.18 show comparisons of the two simulation environments for high-speed shaft (HSS) power, generator speed and blade pitch angle respectively. The plots show largely similar results, with some discrepancies which can be attributed to the much more simplistic approach of the Simulink wind model. In figures 3.16 and 3.18, a drop can be seen at about 650s. This is the result of a drop in the wind speed. Both HSS power and blade pitch angle drop because the controller switches from above-rated to below-rated operation. A drop in generator speed is not seen in Figure 3.17 because the controller is still in the upper constant speed section of the below-rated control strategy.

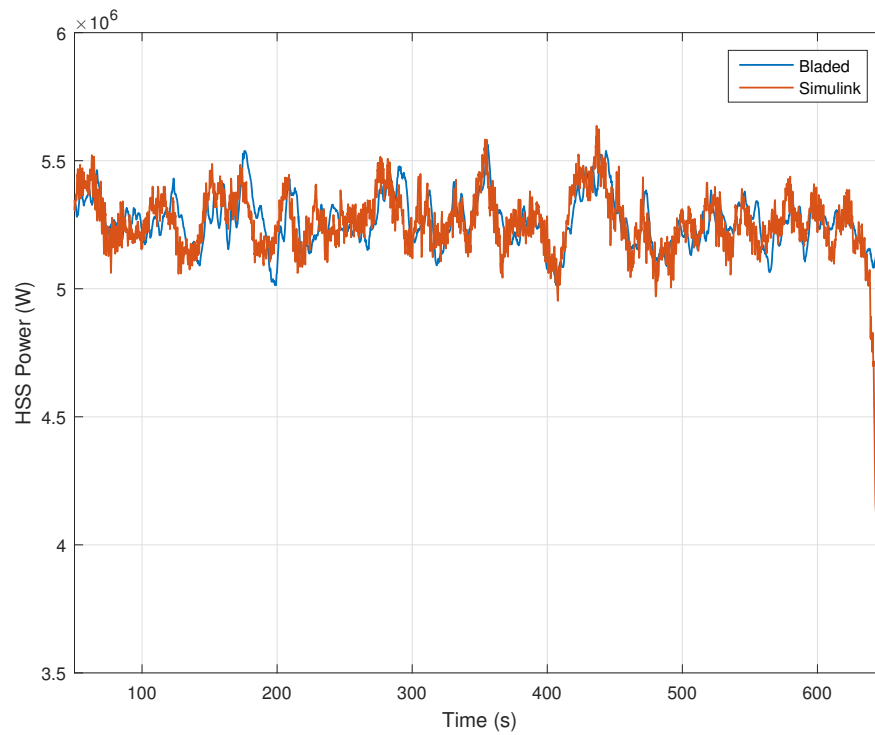


Figure 3.16: HSS power for 16m/s mean wind speed, 15% turbulence - comparison of simulation environments

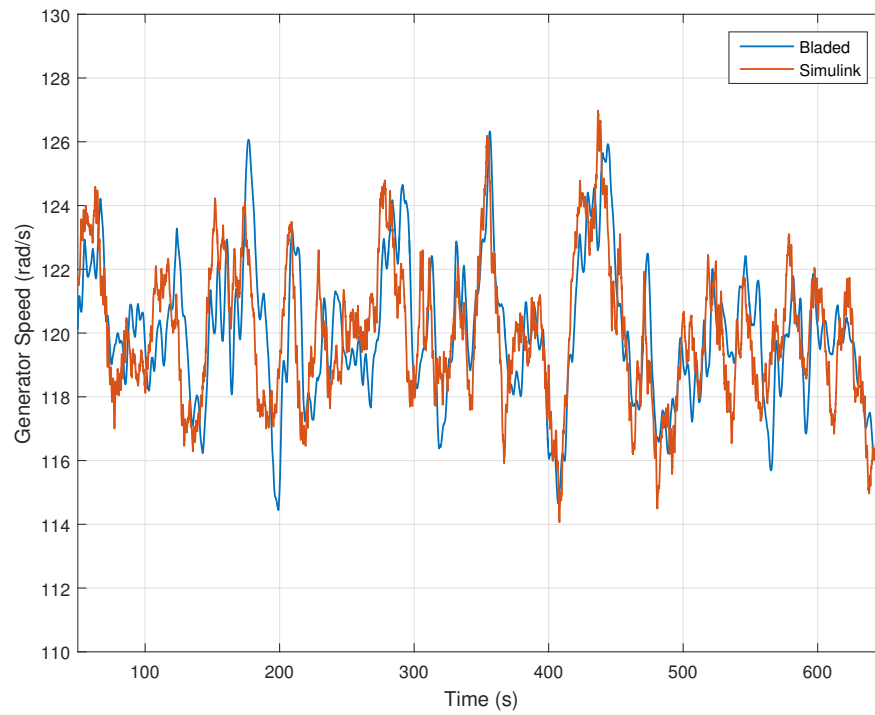


Figure 3.17: Generator speed for 16m/s mean wind speed, 15% turbulence - comparison of simulation environments

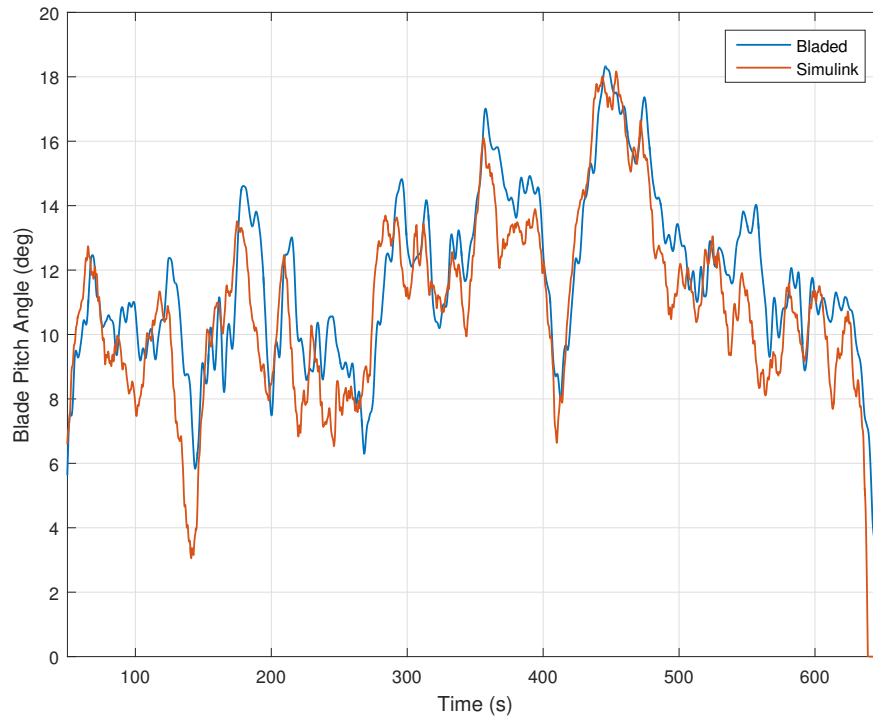


Figure 3.18: Blade pitch angle for 16m/s mean wind speed, 15% turbulence - comparison of simulation environments

3.4.2 Comparison of Turbine Size

Simulations to compare the baseline upscaled turbines were conducted in Bladed. Mean wind speeds of 6m/s, 8m/s, 11m/s and 18m/s were used each with IEC edition 3, Class B turbulence [28]. These wind speeds were chosen to demonstrate and compare below-rated operation, above-rated operation and switching between these two modes.

Below-Rated

In below-rated operation the wind turbine controller is varying the generator torque to maintain a constant tip speed ratio and therefore maximise power capture. Given that the similarly scaled machines have the same maximum power coefficient, differences in power output are dictated by rotor size and wind speed.

In the same wind field, a larger wind turbine will therefore generate more power, as shown in Figure 3.19. In the simulation shown in Figure 3.19, the controller is operating in mode 1 except for times from about 170-250s, 460-520s, and 600-610s, where it is in mode 0.

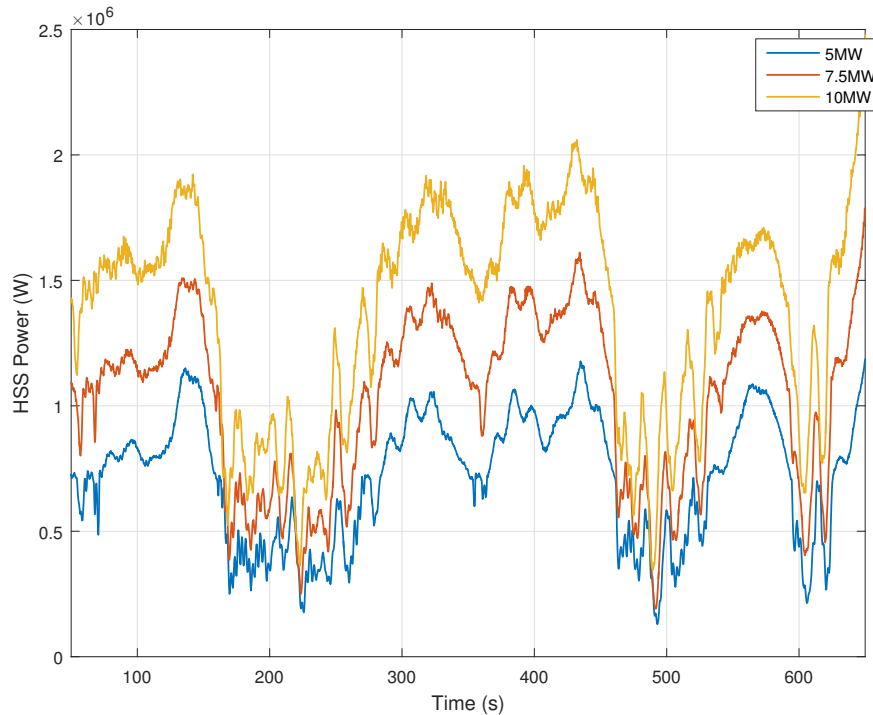


Figure 3.19: Comparison of HSS power for different sizes of turbine operating below rated power (6m/s mean wind speed)

Figure 3.20 compares the generator speed for the three turbines operating below rated power. In these simulations the controller is operating in the first constant speed section, mode 0, where the generator speed is 70rad/s, and in the C_{Pmax} tracking region, mode 1, where the generator speed increases to maintain a constant tip speed ratio. All three controllers have been designed to switch between modes at the same wind speeds so that the points at which the generator speed changes (at about 280 seconds and 540 seconds) are the same for all three turbines.

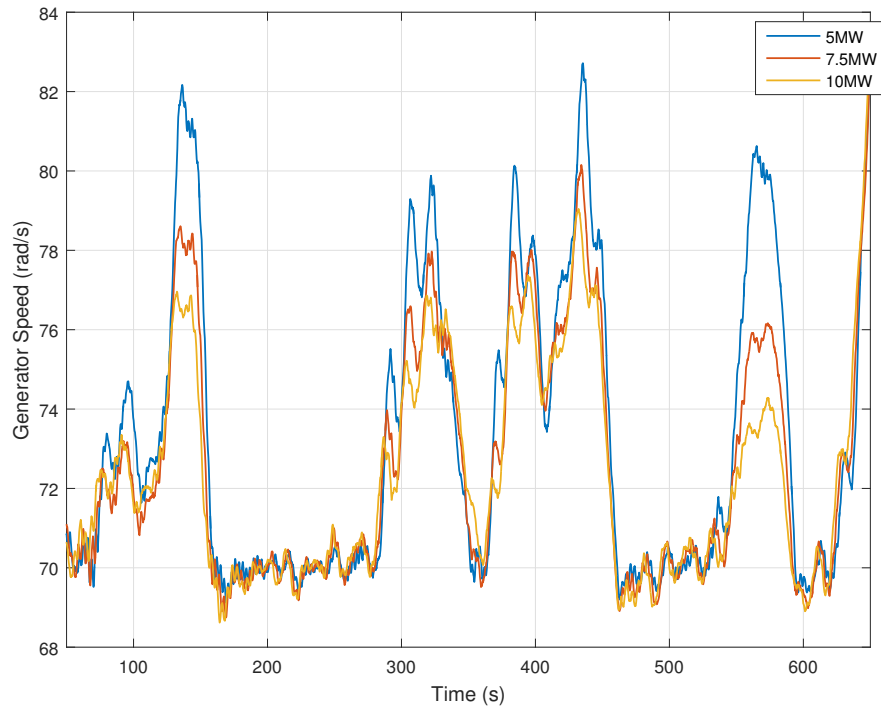


Figure 3.20: Comparison of generator speeds for different sizes of turbine sizes operating below rated power (6m/s mean wind speed)

Above-Rated

When operating at above-rated power, the blade pitch angle is controlled to maintain a constant generator speed. Figure 3.21 shows how the blade pitch angle changes for the three different sizes of turbine experiencing the same wind field. Although all three machines have closely similar pitch angles at the same time, the variance decreases with turbine size. Two factors contributing to this are the gain crossover frequency and the averaging of the wind speed over the rotor.

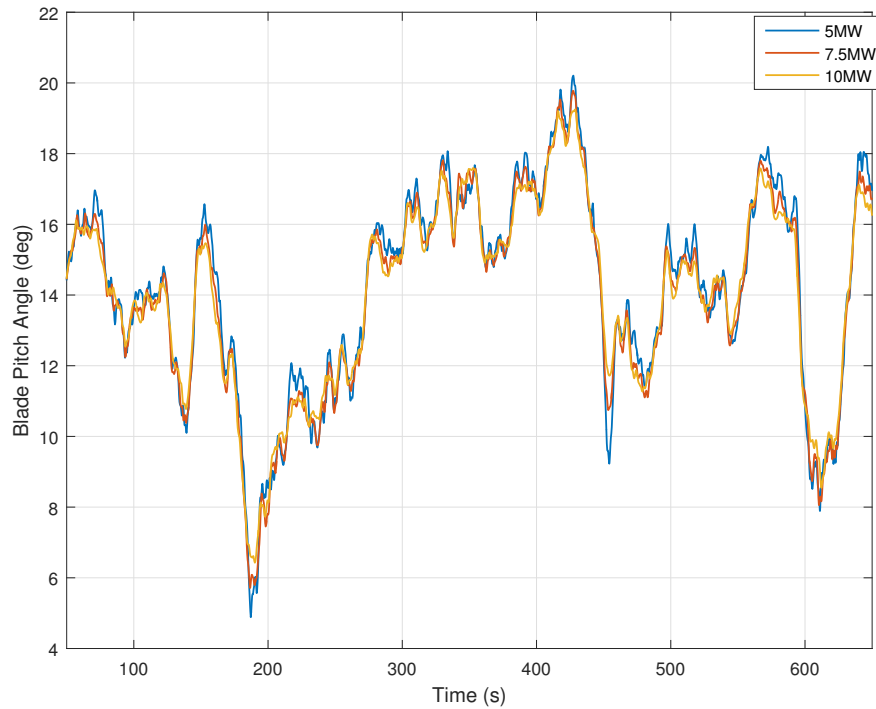


Figure 3.21: Comparison of blade pitch angle for different sizes of turbine operating at above-rated power (18m/s mean wind speed)

Likewise, the generator speed plots shown in Figure 3.22 are largely the same, with slightly more variation as turbine size increases. While the reduction in gain crossover frequency leads to an increase in variation; the averaging of wind speed across the rotor leads to a reduction. The standard deviations for each plot in Table 3.9 show a statistical representation of this increase in variation.

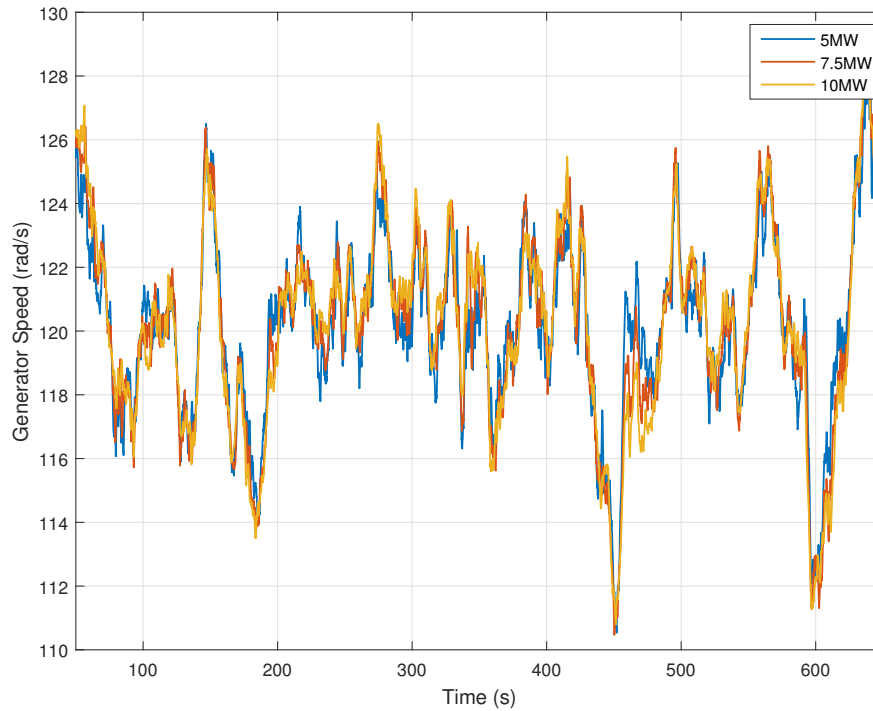


Figure 3.22: Comparison of generator speed for different sizes of turbine operating at above-rated power (18m/s mean wind speed)

Rated Power (MW)	Standard deviation of generator speed
5.0	2.7170
7.5	2.9973
10.0	3.1139

Table 3.9: Comparison of the standard deviation of generator speeds for above-rated operation

A frequency analysis of certain simulation outputs allows further insight into how the dynamics of the wind turbine changes as size is increased. Of particular interest for this thesis is the dynamics of the tower and the change in frequency of the first fore-aft mode. Figure 3.23 shows the peaks representing this dynamic mode for each machine at just above 1rad/s, where increasing the size results in a lower frequency.

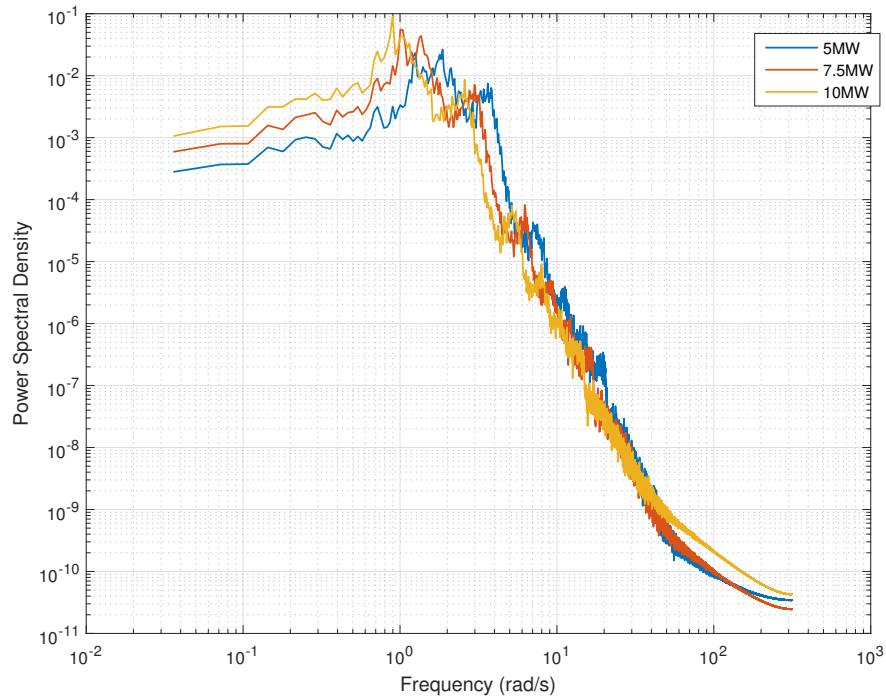


Figure 3.23: Comparison of power spectral densities of nacelle fore-aft velocity in above-rated operation (16m/s mean wind speed)

Switching Between Modes

The controllers for all three wind turbines are designed to have similar control strategies. The wind speeds at which they switch modes are therefore the same. The simulation results in this section demonstrate that the three controllers switch smoothly at the same wind speeds.

Figure 3.20 shows the controller switching between the first constant speed section at 70rad/s and the $C_{P_{max}}$ tracking region, where the generator speed is allowed to increase. This plot shows that the controllers for each machine are switching between these two modes at the same wind speed. Similarly, Figure 3.24 shows the controller switching from the $C_{P_{max}}$ tracking region to the second constant speed section.

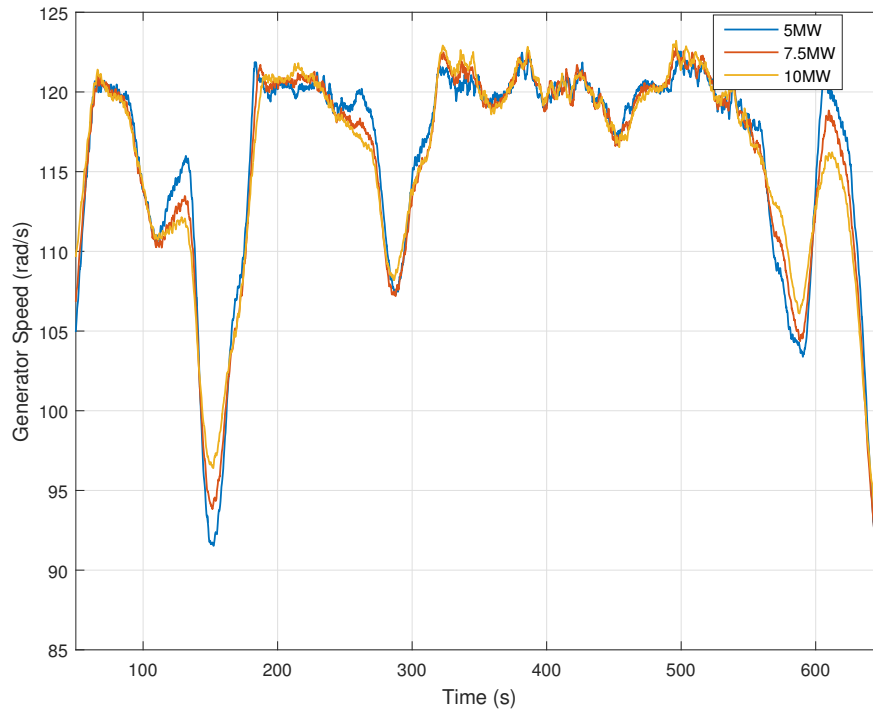


Figure 3.24: Comparison of generator speeds for different sizes of turbine switching between controller modes (11m/s mean wind speed)

A time series plot of the blade pitch angle confirms that the three wind turbines switch from below-rated to above-rated modes at the same wind speed. Figure 3.25 shows several points where the controllers are operating below rated power, where the pitch angle is zero, switching to above-rated operation. At around 370s and 490s all three machines start pitching at the same time; given that the rated wind speed for each machine is the same, this is the expected behaviour. However, there are several events where the smallest wind turbine starts pitching and the others do not. Averaging of the wind speed across the larger rotors acts as a low-pass filter on the wind field. As the rotor size increases the bandwidth of this filter decreases.

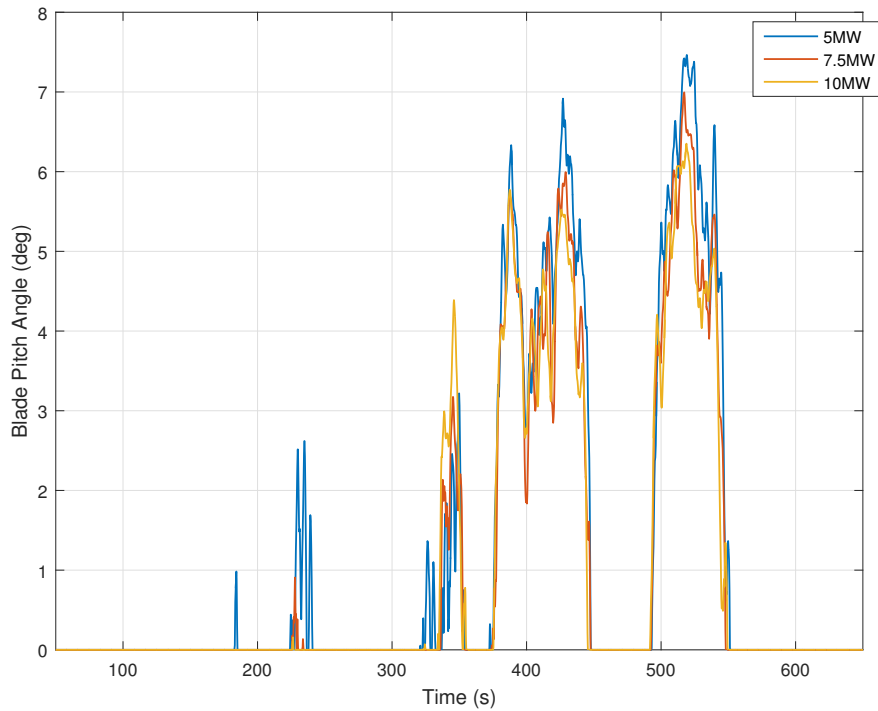


Figure 3.25: Comparison of blade pitch angles for different sizes of turbine switching between controller modes (11m/s mean wind speed)

3.5 Concluding Remarks

This chapter outlines the principles of up-scaling a wind turbine model and described the design of three wind turbines with rated power outputs of 5MW, 7.5MW and 10MW. Simulations of these wind turbines show that the wind turbine plant and the controller have been scaled in a way that they remain comparable. They are also shown to behave in a way that is expected of three wind turbines of increasing size.

By developing a method for scaling each parameter of the wind turbine, a framework for producing similarly scaled plant models for simulation in DNV GL Bladed and MATLAB Simulink can be constructed. These models are physically similar in that all lengths are scaled by the same factor, which is then used to scale masses, inertias, and other dynamic properties. This process results in the

wind turbines being aerodynamically similar in that the power coefficient has the same relationship with pitch angle and tip speed ratio.

The controllers presented in this chapter are designed to be similar. ‘Similar’ in the context of the controller means that they switch operating modes at the same wind speeds and have the same stability margins. However, to achieve the same stability margins across all sizes of wind turbine, concessions have to be made to the gain crossover frequency as size increases. The result of a reduced gain crossover frequency is relatively poorer speed control, the effect of which is predicted by the system’s sensitivity function and seen in the simulation results.

When tested, the baseline wind turbine and two upscaled machines show the behaviour expected of the similarly scaled machines. The larger machines also exhibit the following changes in behaviour due to their size:

- Larger rotors increase the effect of wind speed averaging, resulting in less variation in the wind speed ‘seen’ by the rotor as a whole.
- A lower gain crossover frequency in the above-rated controller results in poorer speed control.

Of particular interest in this thesis and the subject of the following chapter is the constraints that the frequency of the first fore-aft mode of the tower impose on the controller. This natural frequency is a function of the height of the tower and mass at the top and therefore the rated power output. It is also the primary constraint on the achievable crossover frequency of the above-rated controller.

Chapter 4

Development of a Coordinated Controller for Improved Control of Very Large Wind Turbines

This chapter presents a coordinated controller design (CCD) which has previously been used [14] to decrease tower loads by reducing pitch activity at frequencies close to the frequency of the first tower fore-aft structural mode and using generator torque to maintain adequate speed control. Whilst reducing tower loads, the CCD also introduces fluctuations to the generator torque, and therefore power output. An extension to the CCD, the power coordinated controller (PCC), uses power as a set point for regulation of the wind turbine rather than generator speed. This reduces the power fluctuations introduced by the CCD at the expense of slightly greater fluctuation in generator speed.

The interaction of the wind turbine tower and the drivetrain dynamics introduces a pair of right-half-plane zeros (RHPZs) to the dynamics of above-rated control, which can restrict the capability of the controller to regulate speed and power [29]. The frequency of these RHPZs is linked to the first fore-aft mode

of the tower and will therefore reduce as turbine size increases. As a result, the presence of RHPZs can limit the controller design for ever larger wind turbines.

In this chapter, the structure of the PCC is exploited as a means of neutralising the RHPZs present in the above-rated wind turbine dynamics. The properties of the system with the RHPZs removed then enables an increase in the overall gain of the controller and increase in the gain crossover frequency of the open loop system. This is especially useful with very large wind wind turbines where the gain crossover frequency would otherwise be restricted by the low tower frequency.

The three configurations of controller presented in this chapter are summarised below.

- **Baseline Controller:** The baseline controller described in Chapter 3
- **Coordinated Controller Design (CCD):** A controller design which reduces tower loads at the expense of increased fluctuations in power output.
- **Power Coordinated Controller (PCC):** A development of the CCD which also reduces tower loads but does not increase fluctuations in power output. Fluctuations in generator speed are introduced, however.
- **Improved Power Coordinated Controller (IPCC):** A controller design which uses the structure of the PCC to increase the gain crossover frequency.

4.1 The Right-Half-Plane Zero in Wind Turbine Dynamics

A zero located in the left half of the s-plane is characterised by a 20dB/decade rising gain magnitude and a 90° phase lead. A zero located in the right-half of the s-plane exhibits the same rising gain magnitude but with a 90° phase lag. The phase loss due to a right-half-plane zero (RHPZ) in a plant cannot be

compensated for in the same way that a left-half-plane zero can be. For this reason, the loop gain is reduced to appropriate stability margins, resulting in a lower gain crossover frequency than could otherwise be achieved.

A pair of RHPZs can be present in the transmittance from blade pitch angle demand to generator speed at the frequency of the first fore-aft mode of the tower. This dynamic property is evident in the way the controller increases the blade pitch angle in order to decrease the generator speed. The reduced pitch angle causes a decrease in thrust force across the rotor, which in turn causes the nacelle and tower to move forward. The motion of the tower causes the effective wind speed across the rotor to increase and therefore the generator speed to increase. The increase in blade pitch angle that was intended to reduce generator speed has therefore caused it to transiently increase instead [30]. This is a characteristic signature of non-minimum phase behaviour. A Bode plot of the transmittance from pitch angle demand to generator speed is shown in Figure 4.1, with the phase loss of 360° at the frequency of the tower due to the presence of RHPZs indicated.

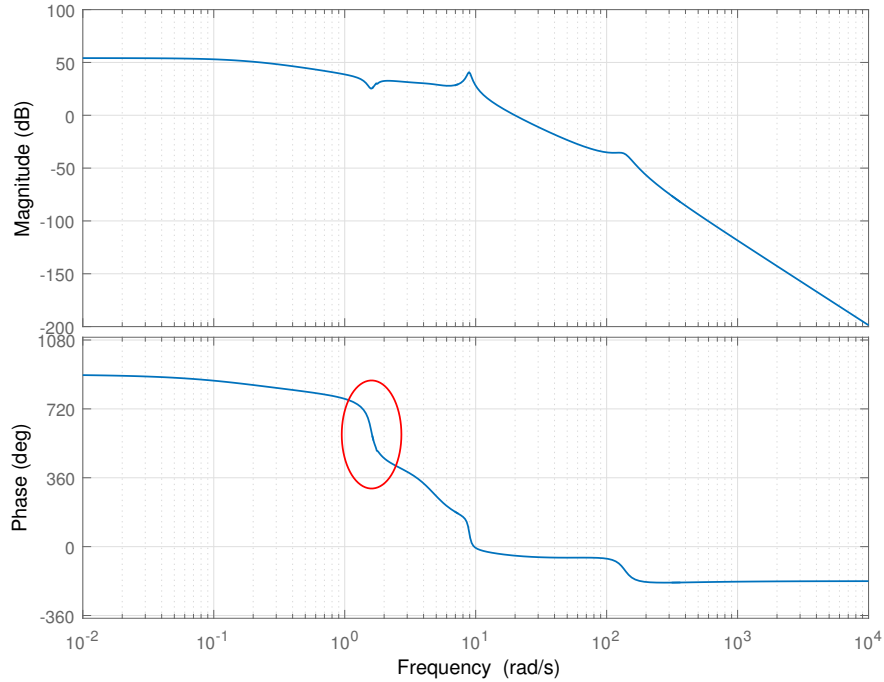


Figure 4.1: Bode plot of pitch angle demand to generator speed indicating the phase loss due to the presence of RHPZs

The presence of RHPZs in the physical system has the effect of introducing an upper limit on the open-loop gain crossover frequency of the controlled system [31].

As wind turbines increase in size, the mass of components such as the tower, blades and nacelle increases, causing natural frequencies to decrease. As discussed in Chapter 3, a gain crossover frequency of 1rad/s is desirable in the open-loop dynamics of the wind turbine controller. In larger machines it becomes increasingly difficult to achieve this target as the phase drop at the tower frequency restricts the controller's available bandwidth. By eliminating the phase loss, a higher gain crossover frequency is achievable within suitable stability margins and therefore a greater bandwidth is available.

4.2 Coordinated Controller Design

The CCD [14] uses a notch filter, $Y(s)$, to remove a band of frequencies, centred on the tower frequency, from the pitch angle demand, and adds the missing signal to the torque loop through a coordinating transfer function, $X(s)$. By reducing pitch activity at the tower frequency, tower loads are reduced. Figure 4.2 shows the implementation of the CCD, where C is the controller, β_d and T_d are pitch and torque demands, ω_{set} is the generator speed set-point and T_{set} is the unmodified above-rated generator torque. The coordinating function is designed so that the following paths are equivalent:

$$X(\beta) \longrightarrow \text{Torque} \longrightarrow \text{Wind turbine dynamics} \longrightarrow \omega_g$$

and:

$$\beta \longrightarrow \text{Wind turbine dynamics} \longrightarrow \omega_g$$

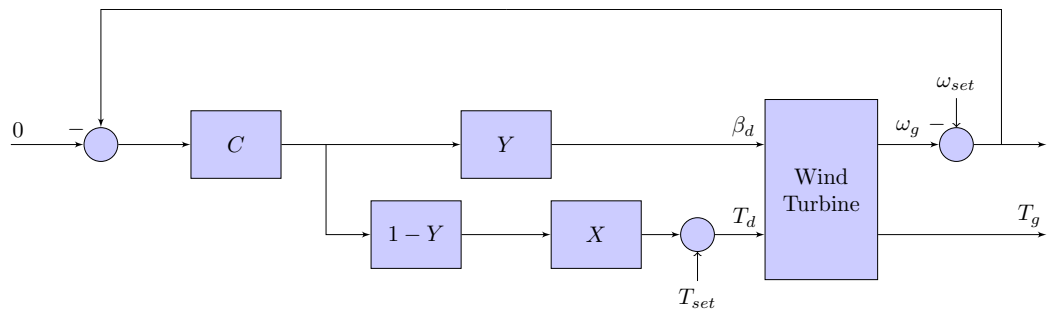


Figure 4.2: Implementation of the coordinated control design

The dynamics of the wind turbine consists of three transmittances, see Figure 4.3 which shows an internal view of the wind turbine block in Figure 4.2.

In Figure 4.3:

- $A(s)$ is the transmittance from blade pitch angle demand (β_d) to generator speed (ω_g).

- $B(s)$ is the transmittance from generator torque demand (T_d) to generator speed.
- $C(s)$ is the transmittance from generator torque demand to actual generator torque (T_g).

These three linear transfer functions are derived for the wind turbine operating at a given wind speed. A wind speed above the rated wind speed is chosen as the CCD is only applicable above-rated.

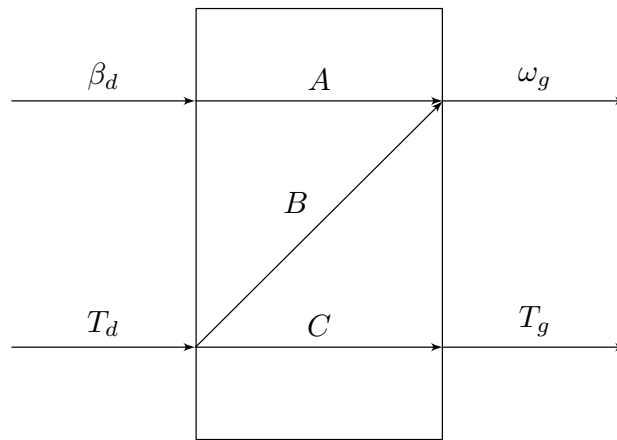


Figure 4.3: Internal view of the wind turbine plant dynamics

The controller must be designed so that the dynamics of the overall system remain unchanged — in this case, equation (4.1) must be satisfied.

$$C_{AR} \cdot Y \cdot A + C_{AR} \cdot (1 - Y) \cdot X \cdot B \equiv C_{AR} \cdot A \quad (4.1)$$

Therefore:

$$X \equiv \frac{A}{B} \quad (4.2)$$

This procedure results in the coordinating function, X , being of very high order. It is therefore appropriate to reduce the order, taking care to maintain

accuracy around the frequency of the tower. Because Y is a notch filter, X only has to be accurate at frequencies close to the notch frequency.

Since the left-hand side of (4.1) can be rearranged to give:

$$C_{AR} \cdot Y \cdot A(1 + X(1 - Y)/Y(B/A)) \equiv C_{AR} \cdot A \quad (4.3)$$

X can be considered as a controller for the plant $(1 - Y)/Y(B/A)$ with right-half-plane poles at the tower frequency. The design task for X is now to obtain a controller for which the closed loop is stable.

Gain-scheduling

With regard to the order of components in the implementation of the controller, the CCD is applied before the gain-scheduling described in Chapter 3. It is therefore important to account for this when designing the coordinating function.

4.2.1 Implementation and Simulations

The notch filter must be designed so that it successfully removes a band of frequencies from the pitch control signal without adversely affecting the performance of speed control or introducing instability, particularly when switching between operating modes. If the notch is too narrow or too shallow, tower loads will not be reduced. If the notch is too wide, generator speed is overly compromised. A wider notch can also introduce unacceptable transients when switching between operating modes. The notch filters for use with the 5MW wind turbine is shown in (4.4). The Bode plot is shown in Figure 4.4.

$$Y(s) = \frac{s^2 + 0.3s + 3.051}{s^2 + 0.9s + 3.051} \quad (4.4)$$

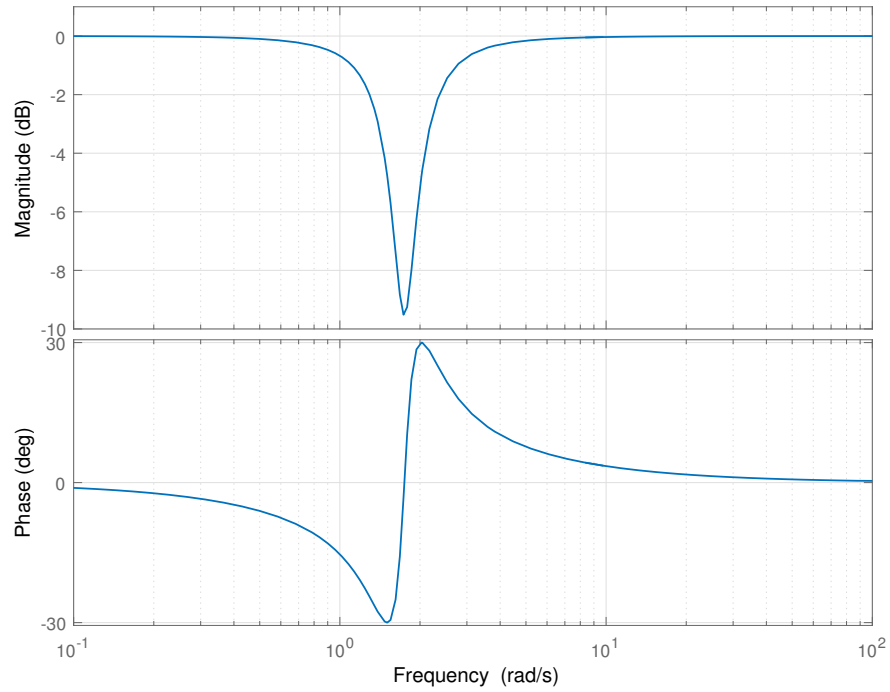


Figure 4.4: Bode plot of the notch filter for the 5MW turbine

The coordinating function for the 5MW turbine is shown in (4.5) and the corresponding Bode plot in Figure 4.5. This consists of only three poles and a gain and only needs to be accurate across the frequencies which are passed to it by $(1 - Y)$.

$$X(s) = \frac{3.5 \times 10^8}{(s + 2)(s + 10)(s + 200)} \quad (4.5)$$

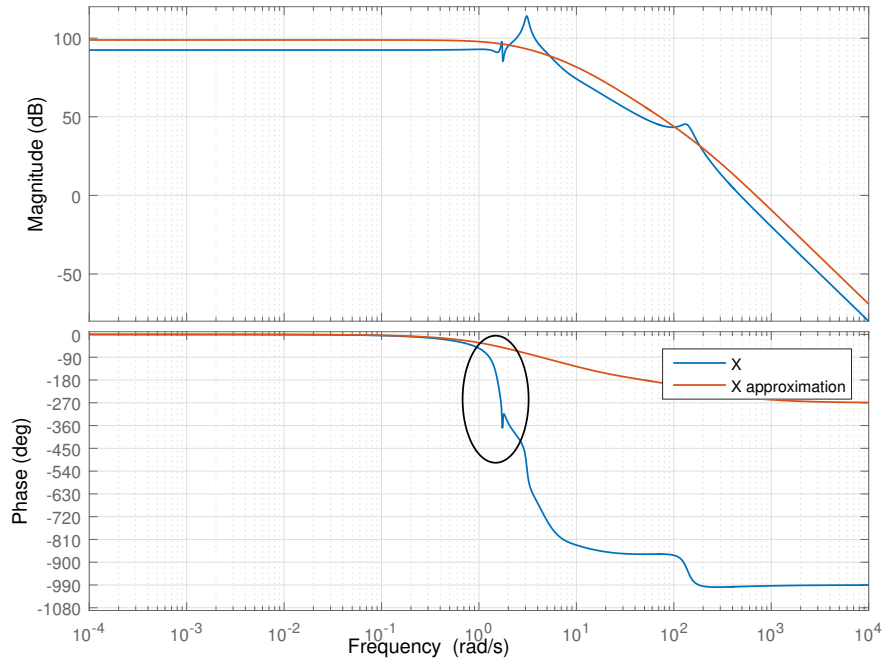


Figure 4.5: Bode plot showing the approximation of the coordinating function

In Figure 4.5, the line representing (4.2) shows a feature in the gain response at about 100rad/s which is not present in the approximation as well as an overall difference in gain. These differences, however, are not relevant because signals at these frequencies are not passed by the notch filter, (4.4). The major change in phase in Figure 4.5 is the removal of the 360° step down in phase at the tower frequency of just over 1rad/s. Figure 4.6 shows Bode plots for both sides of equation (4.1). Other than the frequencies close to the tower frequency which are covered by the notch filter, Y , the dynamics of both systems are very similar. Improvements in the phase properties of the system with the CCD controller are also evident. This change could be exploited to increase the bandwidth of the controller. Although this is not discussed in this section, it is explored later in this chapter. The changes visible in Figures 4.5 and 4.6 show that the RHPZs have been removed.

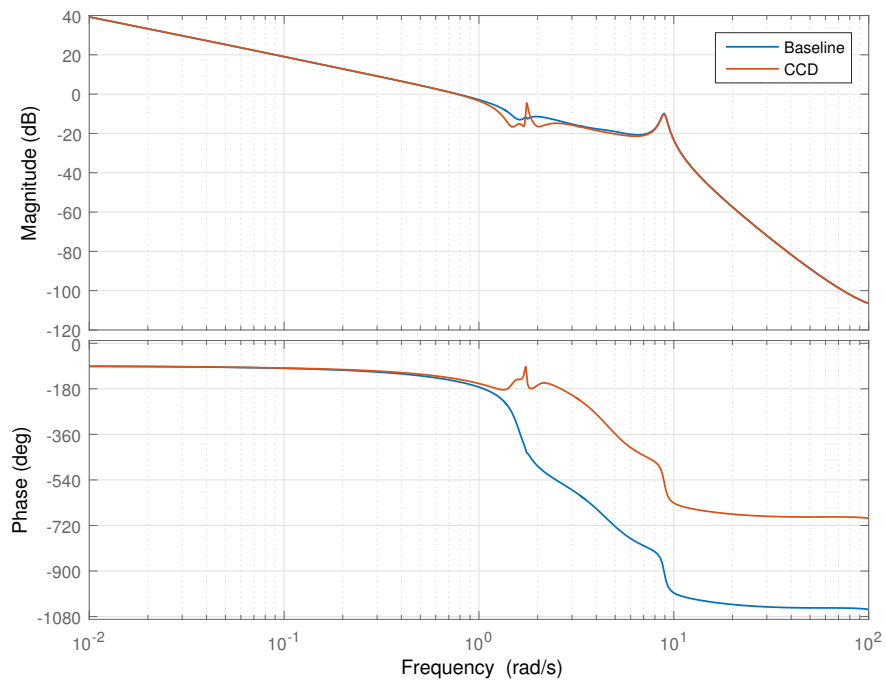


Figure 4.6: Bode plot showing open loop system in Figure 4.2 of the baseline controller and the CCD

The effect of the CCD on tower loads can be seen by comparing the power spectral density (PSD) to the baseline. The peak in the PSD is reduced at the tower frequency of around 1.7rad/s.

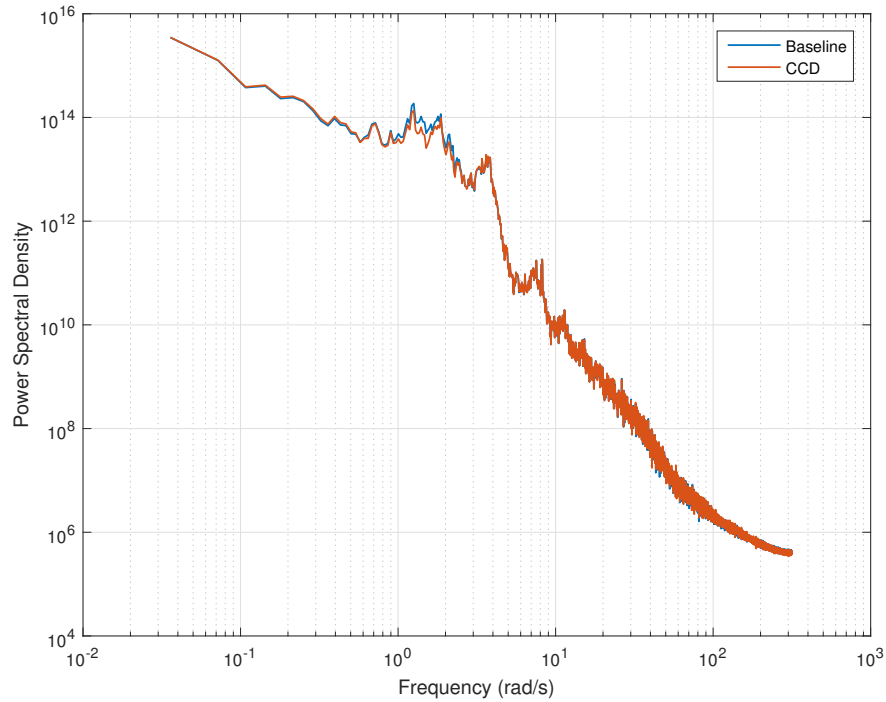


Figure 4.7: Power spectral density of fore-aft bending moment at the tower base

The change in pitch angle demand and generator torque demand can also be seen in their respective power spectral density plots. The notch filter has removed pitch activity from around the tower frequency so a reduction in the PSD is seen, as shown in Figure 4.8. The generator torque demand is augmented with the signal removed from the pitch loop to maintain speed control. There is therefore an increase in the PSD of generator torque around these frequencies, as shown in Figure 4.9.

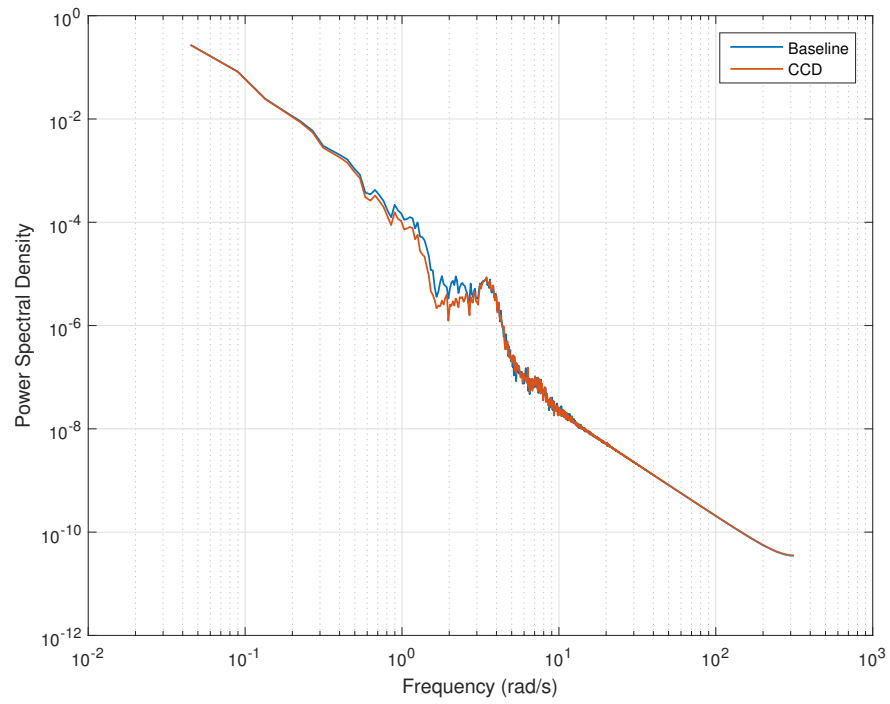


Figure 4.8: Power spectral density of blade pitch angle

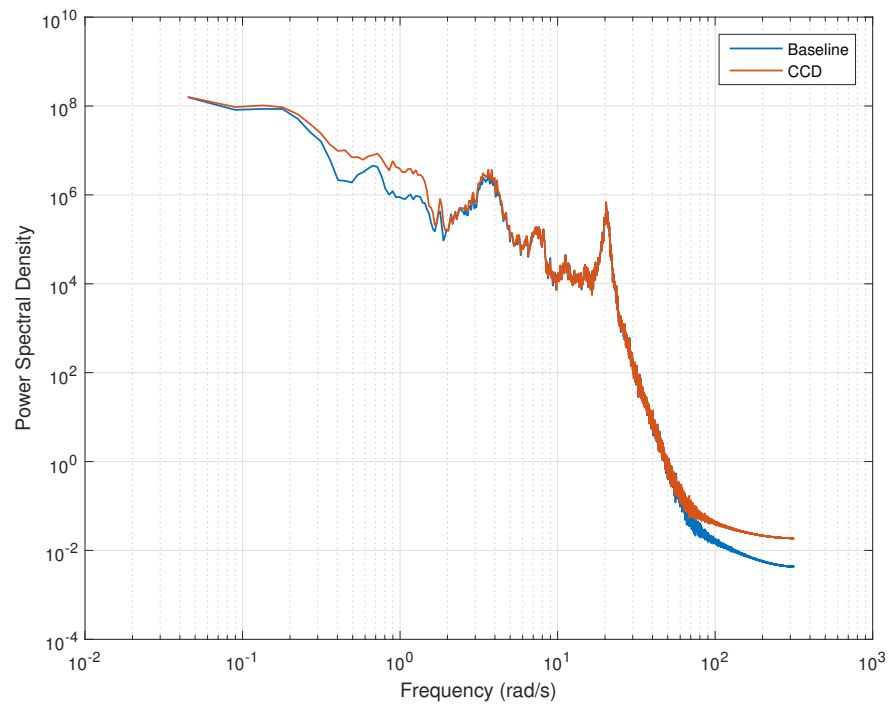


Figure 4.9: Power spectral density of generator torque

One of the requirements of the CCD is that it does not adversely effect speed control. Figure 4.10 shows no significant changes in this respect.

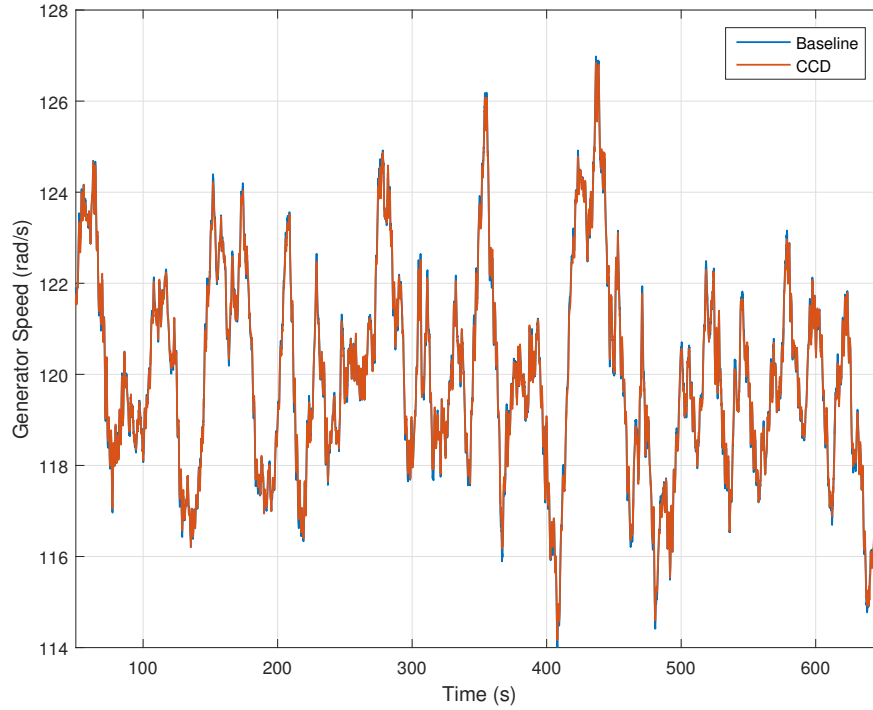


Figure 4.10: Comparison of generator speed for baseline and CCD

Due to the augmentation of generator torque demand, fluctuations in power output is also increased. Figure 4.11 shows significantly greater variations in generator torque from the baseline and this change is evident in the power output as shown in Figure 4.12.

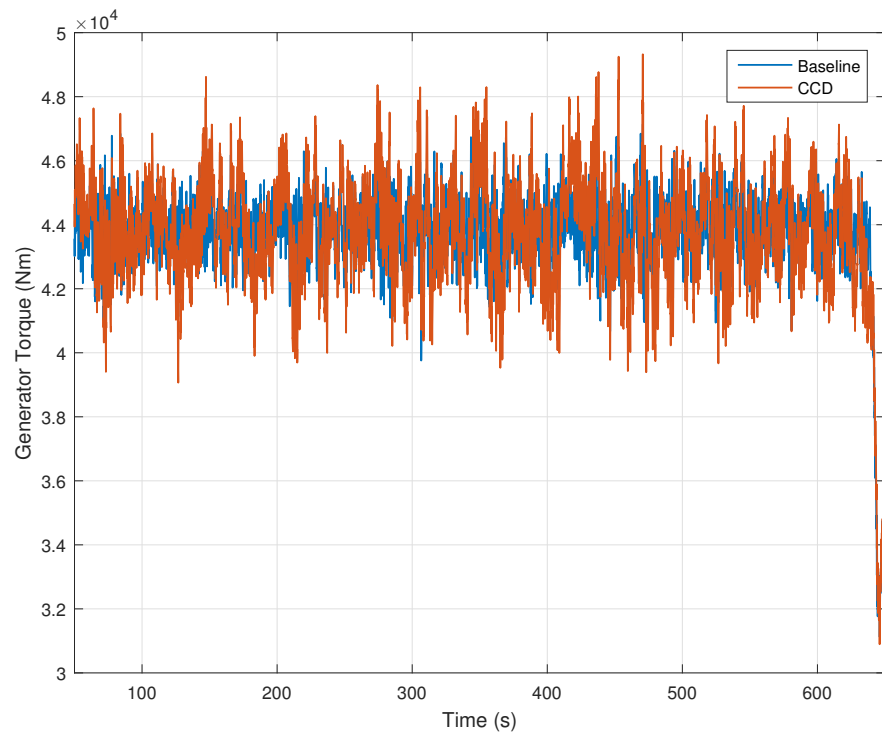


Figure 4.11: Comparison of generator torque for baseline and CCD

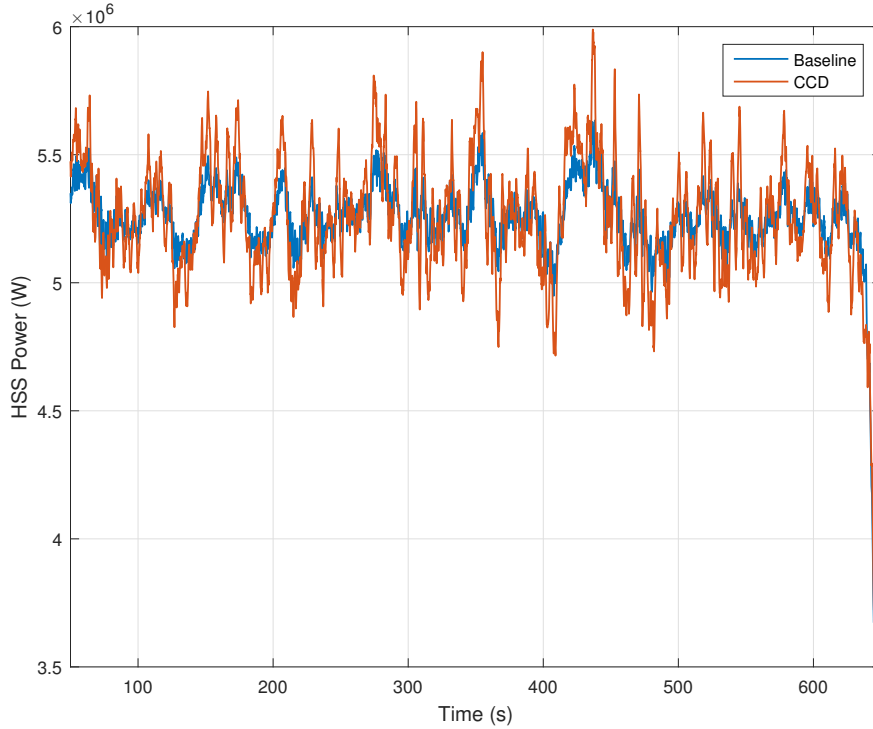


Figure 4.12: Comparison of generator power for baseline and CCD

4.3 Power Coordinated Controller

The coordinated controller can successfully reduce tower loads but in doing so also introduces greater fluctuations in power output. To avoid fluctuations in power output and the resulting increased load on drivetrain components, the controller is reconfigured with power as a target rather than speed [14].

Fluctuations in power output relative to the rated power are almost entirely due to fluctuations in generator speed ω_g . This is because the response of generator torque to perturbations in blade pitch angle demand is very weak. Therefore, if power is well controlled then so too is generator speed.

Therefore, the output of the plant (4.6) becomes (4.7).

$$P - P_0 = \omega_g T_g \quad (4.6)$$

$$P = \omega_{g0} * T_{g0} + T_{g0}(\omega_g - \omega_{g0}) + \omega_{g0}(T_g - T_{g0}) \quad (4.7)$$

This can then be reformulated as (4.8).

$$P = \omega_{g0} + (\omega_g - \omega_{g0}) + (T_g - T_{g0})(\omega_{g0}/T_{g0}) \quad (4.8)$$

The power coordinated controller (PCC) is implemented as in Figure 4.13 using the formulation in (4.8).

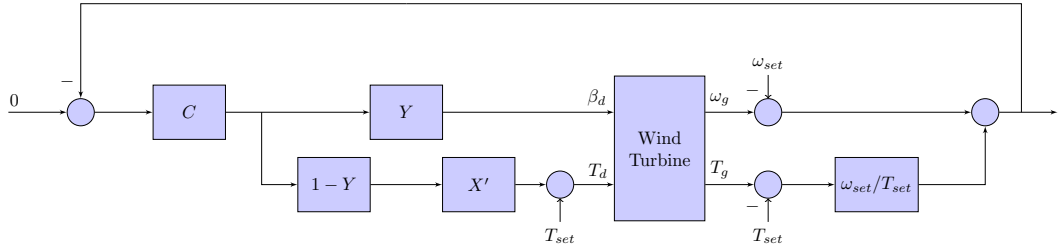


Figure 4.13: Implementation of the power coordinated controller

As with the CCD, the coordinating function must be designed so that the dynamics of the whole system remain unchanged from the baseline. Due to the changes made in the extension to the PCC, the coordinating function, X' is different from the CCD. The formulation of X' is shown in (4.9). As before, X' , as described by (4.10), needs to be reduced from a very high order function when implemented.

$$C_{AR} \cdot Y \cdot A + C_{AR} \cdot (1 - Y) \cdot X' \cdot \left(B + \frac{\omega_{set}}{T_{set}}\right) \equiv C_{AR} \cdot A \quad (4.9)$$

Therefore:

$$X' \equiv \frac{A}{B + \frac{\omega_{set}}{T_{set}}} \quad (4.10)$$

Similarly to the design of X in Section 4.2, X' has to be designed to stabilise $(1 - Y)/Y(B + \omega_{set}/T_{set})/A$.

4.3.1 Implementation and Simulations

For the PCC, there is no need to change to notch filter from the design used in the CCD. Y , therefore, remains as shown in (4.4). X' is designed to reflect the changes made by adding the power loop as in (4.10). The resulting transfer function is shown in (4.11). Bode plots of X' and the approximation used are shown in Figure 4.14.

$$X'(s) = \frac{-1 \times 10^8}{(s + 0.035)(s + 5)(s + 50)(s + 120)} \quad (4.11)$$

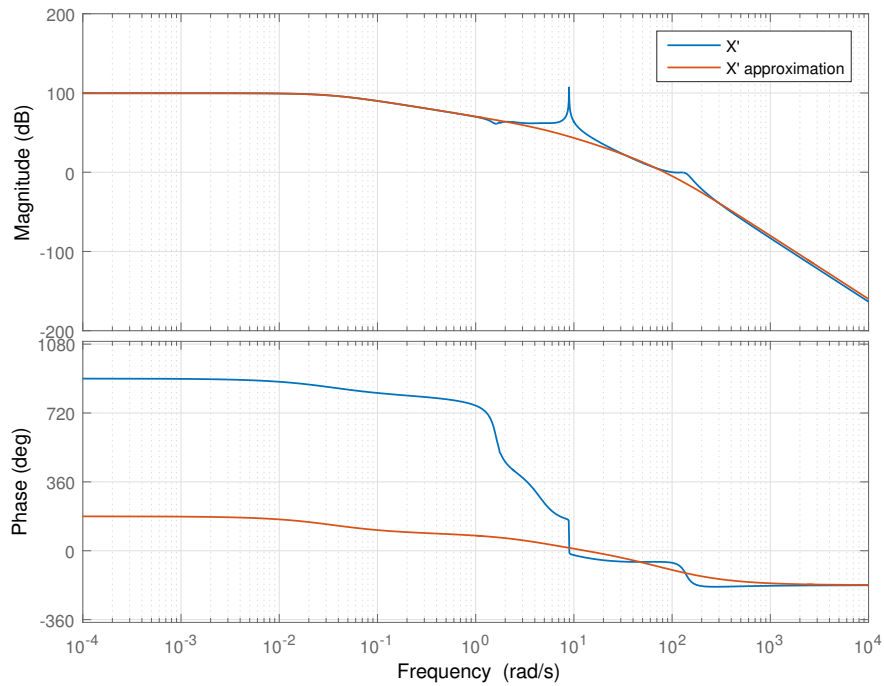


Figure 4.14: Bode plot showing the approximation of the coordinating function

Figure 4.15 shows a comparison of the open loop system with the baseline controller and the PCC. As with the CCD and Figure 4.6, the dynamics outwith the band of frequencies covered by the notch filter are unaffected and the RHPZs at the tower frequency have been removed.

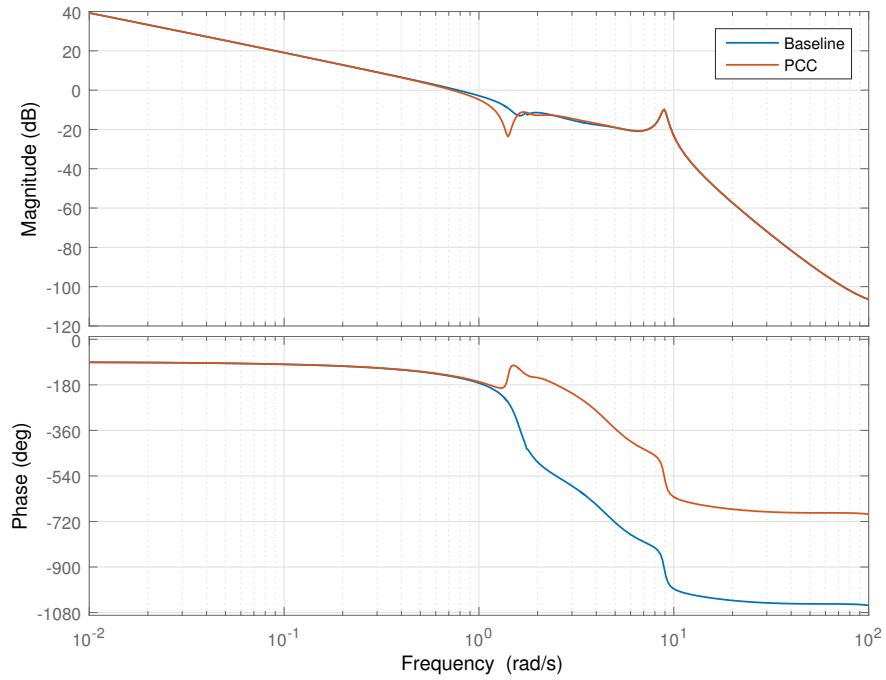


Figure 4.15: Bode plot showing the open loop system in Figure 4.13 of the baseline controller and the PCC

With the PCC, pitch activity around the tower frequency is still removed by the notch filter resulting in reduced tower loads. Figure 4.16 shows the PCC achieves a similar reduction in tower loads as the CCD does. Figure 4.17 shows the reduced pitch activity from the baseline, similar to the CCD.

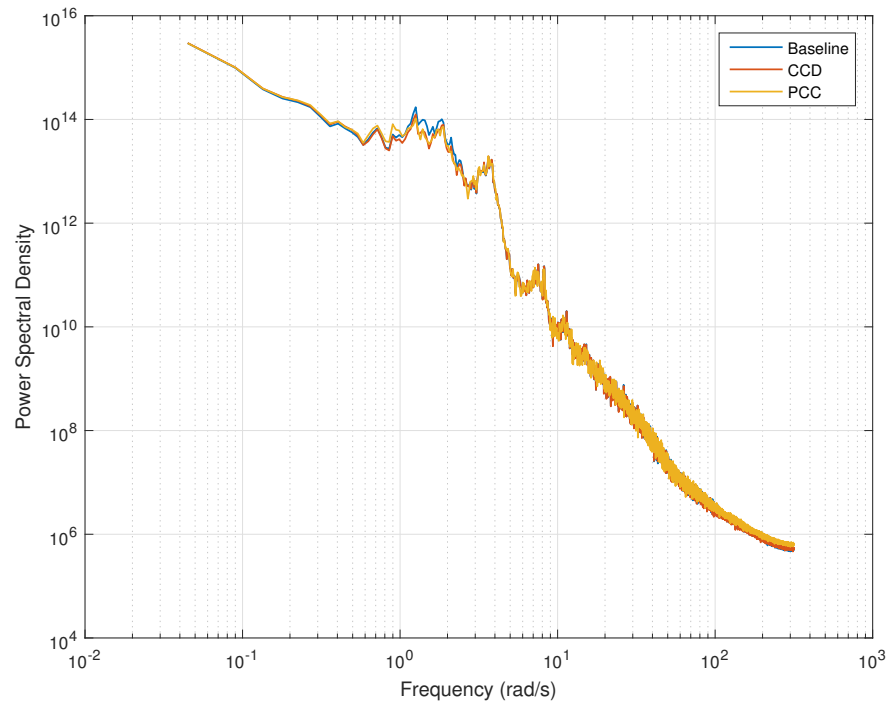


Figure 4.16: Power spectral density of fore-aft bending moment at the tower base

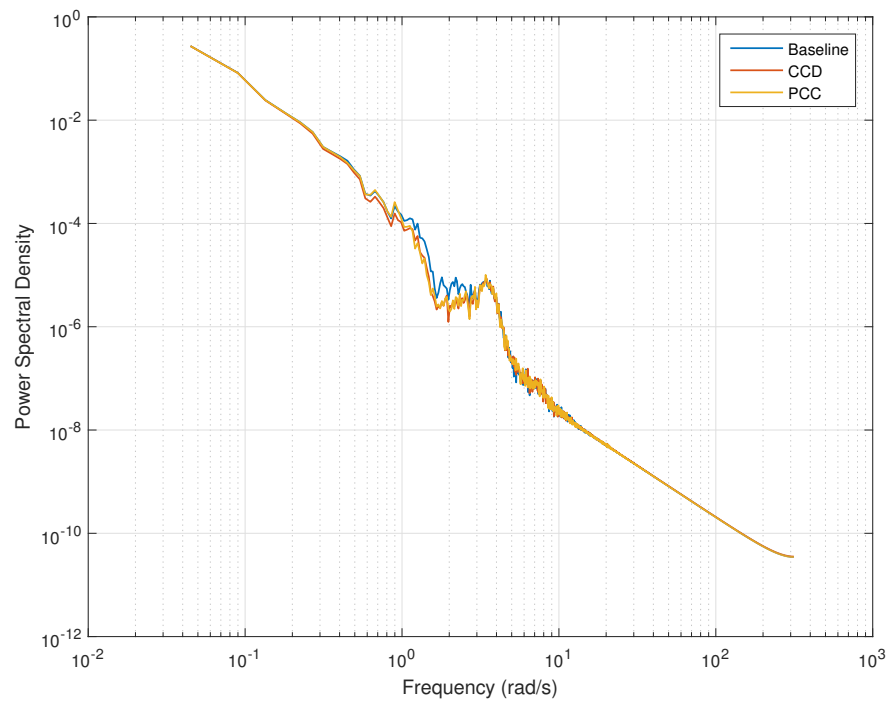


Figure 4.17: Power spectral density of blade pitch angle

The spectra for torque in Figure 4.18, however, shows that the PCC is more similar to the baseline than the CCD. This reduction is also visible in Figure 4.19. This reduction in the variation of generator torque means that variations in the power output is reduced from the levels seen in the CCD. Figure 4.20 shows the PCC with similar levels of variation to the baseline and the CCD with much greater excursions from the set point.

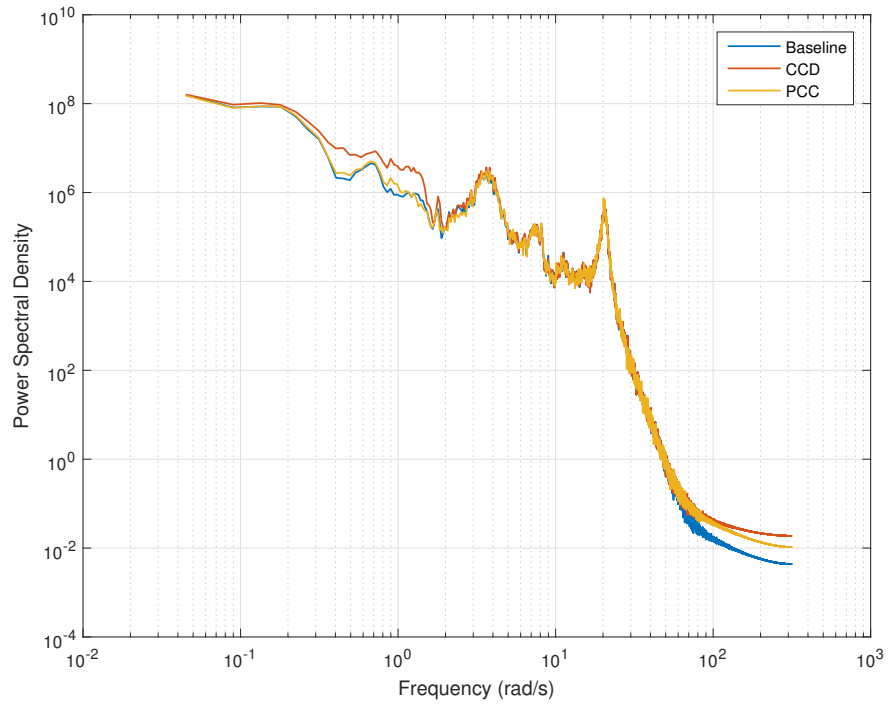


Figure 4.18: Power spectral density of generator torque

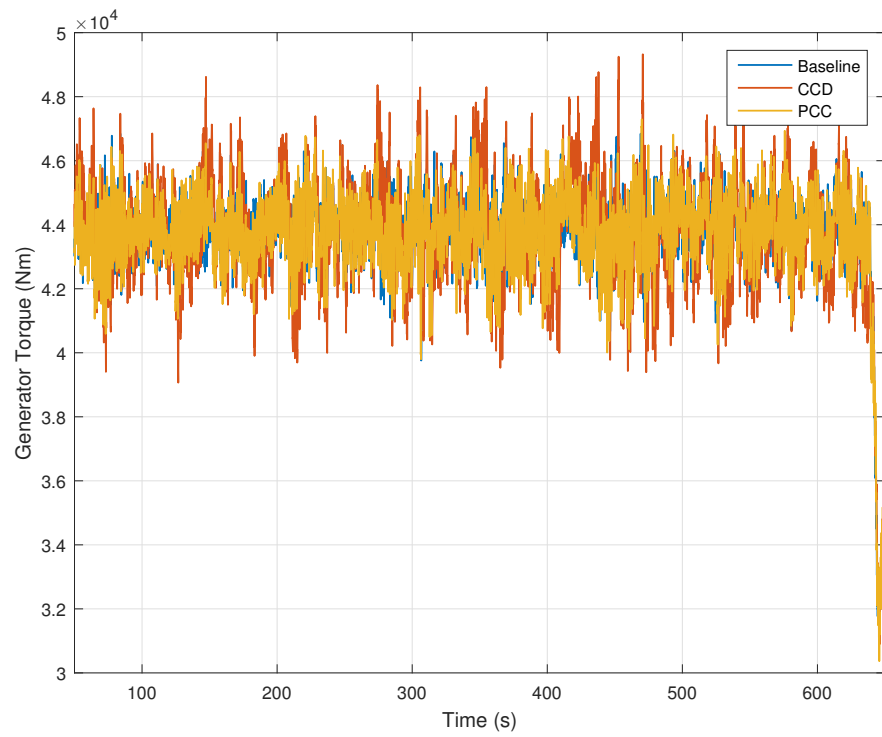


Figure 4.19: Comparison of generator torque for baseline and CCD

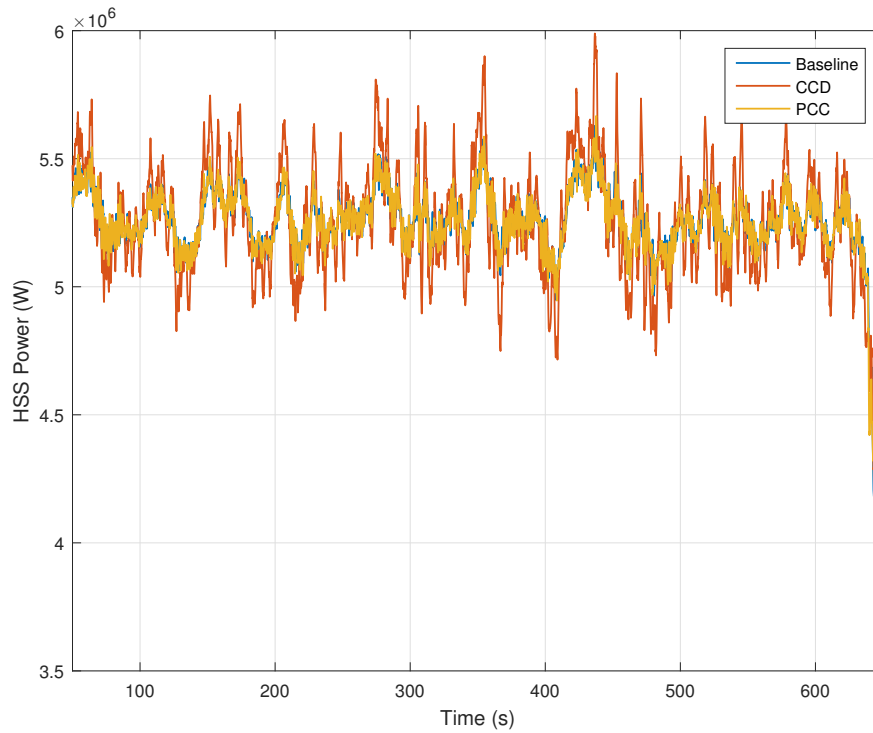


Figure 4.20: Comparison of generator power for baseline and CCD

Figure 4.21 shows slightly greater fluctuation in generator speed with the PCC than with the baseline and the CCD. This is a result of changing the control target from speed to power. The structure of the CCD and PCC may be exploited to improve speed control, however. The method and implementation of this is explored later in this chapter.

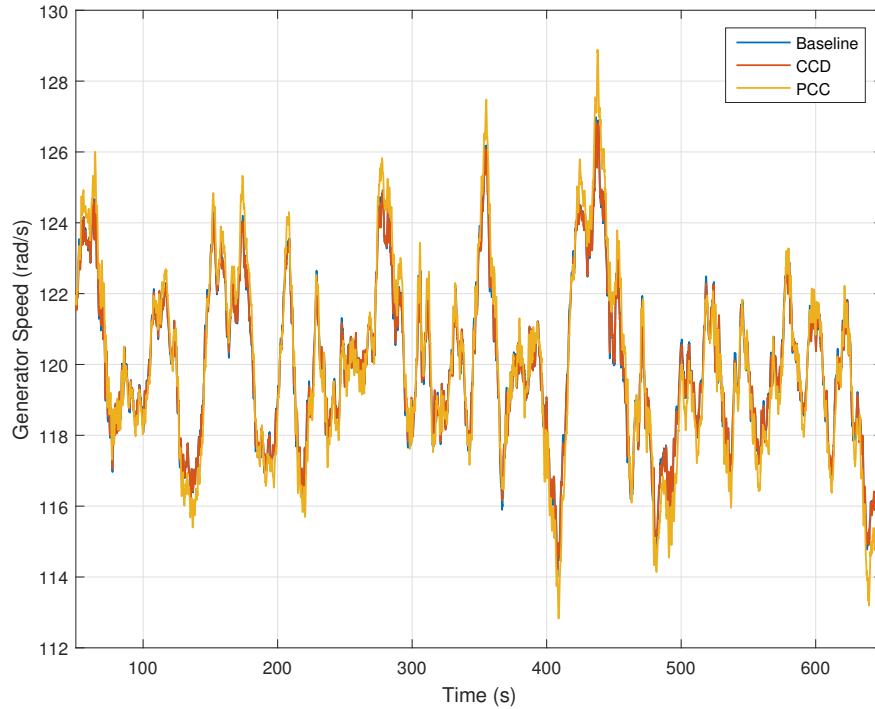


Figure 4.21: Comparison of generator speed for baseline and CCD

4.4 Improved Control of Very Large Wind Turbines

The PCC is able to successfully reduce tower loads by reducing pitch activity at the tower frequency. Another result of implementing the PCC is neutralising the RHPZs in the pitch control loop and removing the non-minimum phase behaviour from above-rated control. Removal of the RHPZs allows a controller to be designed which is less restricted by a low tower frequency.

As wind turbines increase in size, it can be beneficial to use the coordinated controller to increase the overall controller gain while maintaining stability margins that are similar to those for the baseline controller. Increasing the overall gain in this way increases the gain crossover frequency and bandwidth of the controller, which is constricted in larger machines.

This section presents a configuration of the power coordinated controller for eliminating the effect of RHPZs related to the first fore-aft mode of the tower, and therefore allowing an increased overall gain which increases the gain crossover frequency and available bandwidth of larger wind turbines. Simulations of three sizes of wind turbine are presented to compare the behaviour of this design with that of the baseline controllers described in Chapter 3.

4.4.1 Controller Design

There are three elements in the design of the PCC which is used to extend bandwidth in larger wind turbines. The notch filter, Y , and the coordinating function X' are identical to those used in the original configuration of the PCC described in the previous section. The difference between the PCC and the improved power coordinated controller (IPCC) is a gain, K_{cc} , which is now included as part of the main controller (C in Figure 4.13).

As the structure of the IPCC is identical to that of the PCC, the same criteria for the design of the notch filter Y and the coordinating function X' stands. Additionally, the phase loss due to the RHPZs must be removed from the dynamics of open loop system in order to provide the scope to increase the gain crossover frequency. For example, if the notch is too narrow, the phase loss remains and so the gain, K_{cc} , cannot be applied to increase the crossover frequency. If the notch is too wide, the same consequences are seen as with the PCC and the CCD: poorer speed control and transients when switching between operating modes. The notch filters for use with the 5MW, 7.5MW and 10MW wind turbines are shown in (4.12), (4.13) and (4.14) and the corresponding Bode diagrams are shown in Figure 4.22. The notch filter for the 5MW is the same in the IPCC as in the PCC.

$$Y_5(s) = \frac{s^2 + 0.3s + 3.051}{s^2 + 0.9s + 3.051} \quad (4.12)$$

$$Y_{7.5}(s) = \frac{s^2 + 0.3s + 1.758}{s^2 + 0.9s + 1.758} \quad (4.13)$$

$$Y_{10}(s) = \frac{s^2 + 0.3s + 1.141}{s^2 + 0.9s + 1.141} \quad (4.14)$$

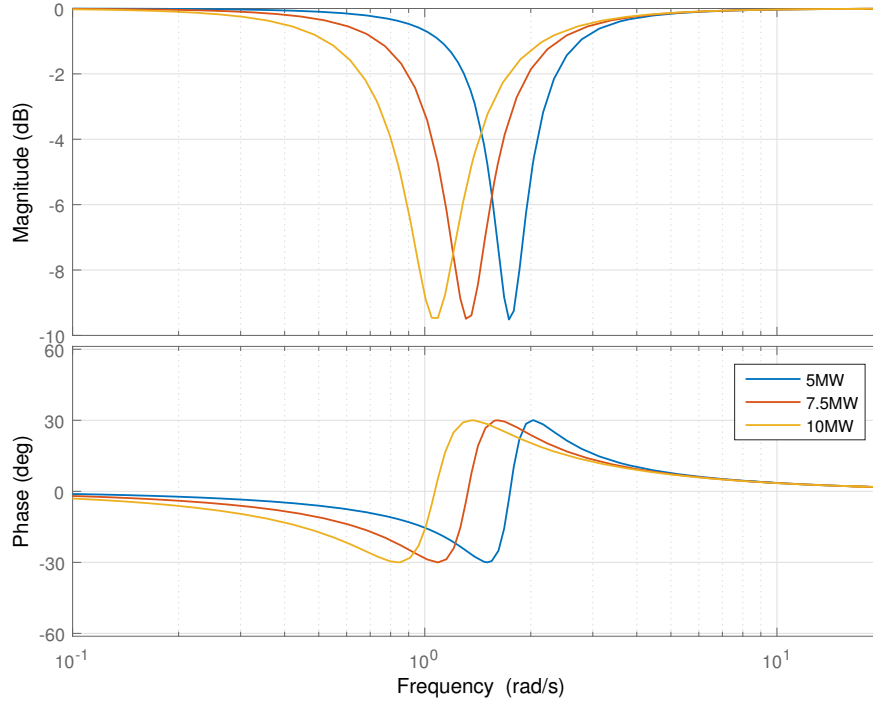


Figure 4.22: Bode plots of notch filters for use with three differently sized turbines

The coordinating functions for the IPCC for three sizes of wind turbines are designed as with the PCC. As before, the function calculated as in (4.10) is reduced for practicality of implementation. The approximated transfer functions for the three sizes of wind turbine are shown in (4.15), (4.16) and (4.17).

$$X'_5(s) = \frac{-1 \times 10^8}{(s + 0.035)(s + 5)(s + 50)(s + 120)} \quad (4.15)$$

$$X'_{7.5}(s) = \frac{-3.7 \times 10^7}{(s + 0.0245)(s + 3.5)(s + 35)(s + 84)} \quad (4.16)$$

$$X'_{10}(s) = \frac{-1.3 \times 10^7}{(s + 0.0175)(s + 2.5)(s + 25)(s + 60)} \quad (4.17)$$

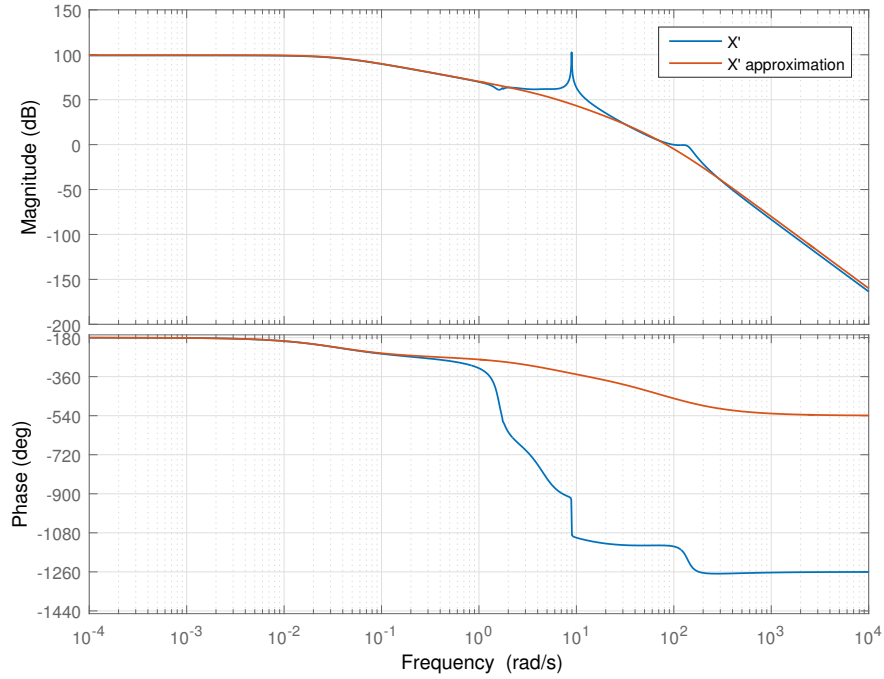


Figure 4.23: Bode plots showing the approximation of the coordinating function for the 5MW turbine

Inspection of the open-loop Bode plot of the controller and plant shows the characteristics of the system with the RHPZs removed. With this information, particularly the shape of the phase response, the extra gain (K_{cc}) can be adjusted, balancing the changes to stability margins and the improvement in the gain crossover frequency. Figures 4.24, 4.25 and 4.26 show the Bode plots for the 5MW, 7.5MW and 10MW turbines respectively.

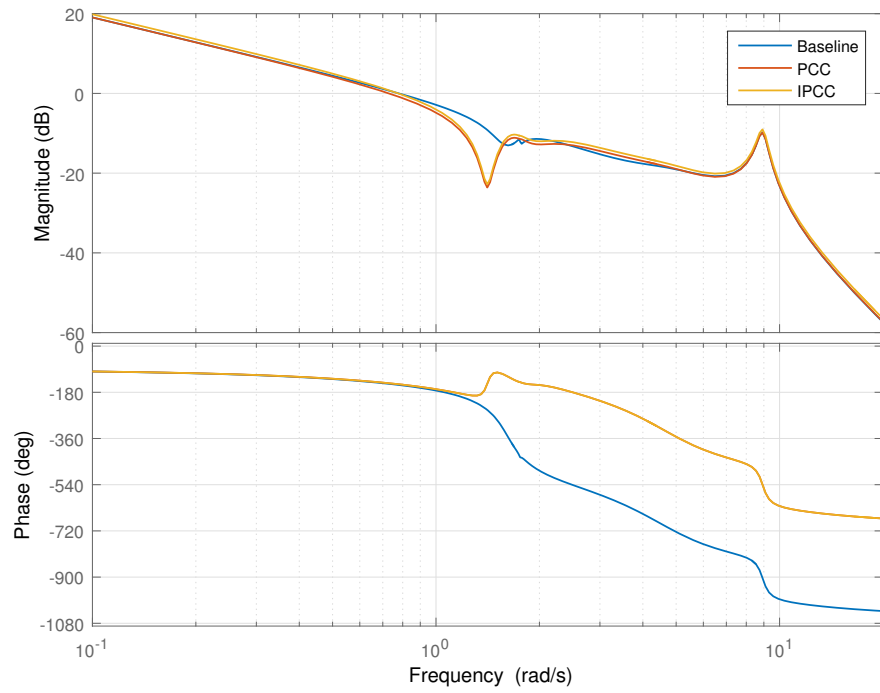


Figure 4.24: Bode plots showing the controller and 5MW plant for the baseline controller, PCC and IPCC

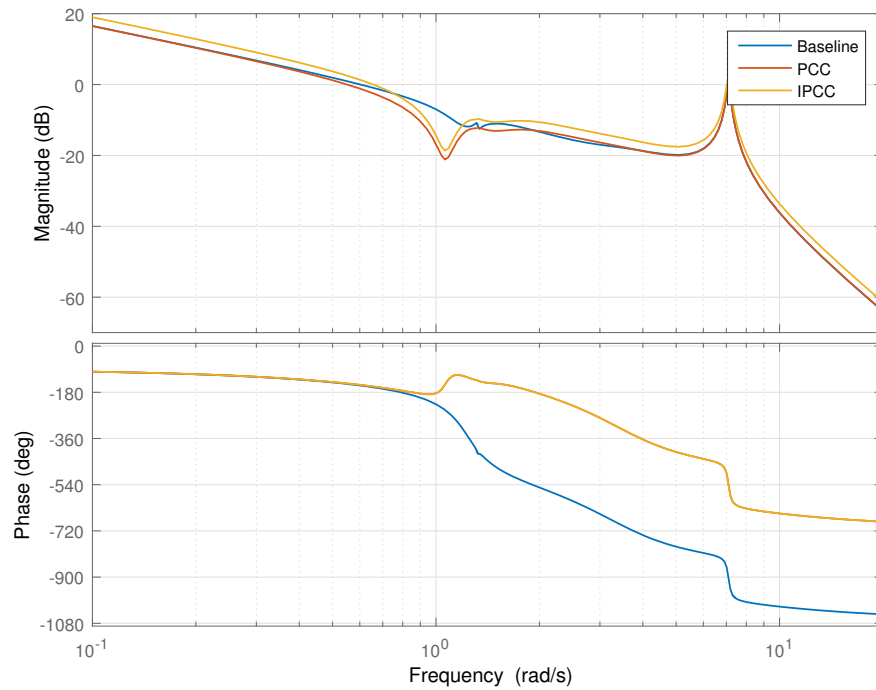


Figure 4.25: Bode plots showing the controller and 7.5MW plant for the baseline controller, PCC and IPCC

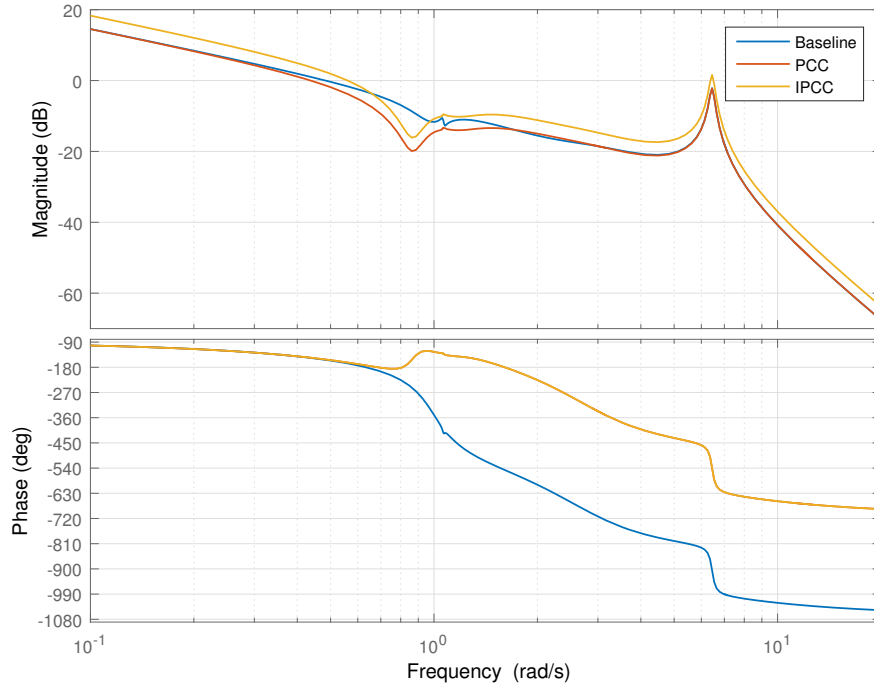


Figure 4.26: Bode plots showing the controller and 10MW plant for the baseline controller, PCC and IPCC

Table 4.1 shows the gains applied to the IPCC for the three different sizes of wind turbine to increase the gain crossover frequency. These values are chosen to maintain gain and phase margins similar to those of the corresponding baseline controllers presented in Chapter 3.

Rated Power (MW)	K_{cc} (dB)
5.0	0.8
7.5	2.5
10.0	4.0

Table 4.1: Gains to increase crossover frequencies as applied to three sizes of wind turbine

As discussed in Chapter 3, the first fore-aft structural mode of the tower is the primary factor which limits the gain crossover frequency. It follows then, that a larger turbine with a lower tower frequency will benefit more from removal of this effect. The IPCC designs presented here support this statement

as the value of gain which can be added whilst maintaining the same stability margins as the equivalent baseline is greater for larger turbines. Table 4.2 shows the gain crossover frequencies of the baseline models and the IPCC. The 10MW machine has the greatest difference at 0.078rad/s and the 5MW has the smallest at 0.004rad/s.

Rated Power (MW)	Baseline Crossover (rad/s)	Improved Crossover (rad/s)	Difference (rad/s)
5.0	0.753	0.757	0.004
7.5	0.575	0.641	0.066
10.0	0.483	0.561	0.078

Table 4.2: Crossover frequencies for the baseline controller and IPCC

4.4.2 Simulations

This section presents simulation results demonstrating the function of the IPCC. Because the IPCC only changes pitch control, the behaviour of below-rated operation remains unchanged. Simulations to demonstrate that the IPCC switches between operating modes properly are presented, followed by simulations at higher wind speeds to show the improvement in control through less variation in power output. These simulations are presented as comparisons between the baseline controller, the PCC and the IPCC for the 5MW turbine, followed by comparisons of the IPCC with the baseline for three sizes of turbine. All simulation results presented and discussed in this chapter are from the DNV GL Bladed simulation environment.

Switching Between Modes

Figure 4.27 shows the generator speeds for a 5MW, 7.5MW and 10MW wind turbine with the baseline controller and IPCC operating in a turbulent wind with an 11m/s mean wind speed. For all sizes of wind turbine tested here, the rated

wind speed is about 11.4m/s so the wind turbine frequently switches between the below-rated and above-rated operating modes. From Figure 4.27 it can be seen that no instability is introduced by the new controller and the points at which the controller switches modes are unchanged. At just about 180s, the generator speed increases rapidly and stabilises at the set point of 120rad/s without any major overshoot. Also, from about 320s to 550s, the wind speed stays at around the rated wind speed, sometimes dropping into the C_{Pmax} tracking region without the turbine showing any signs of instability.

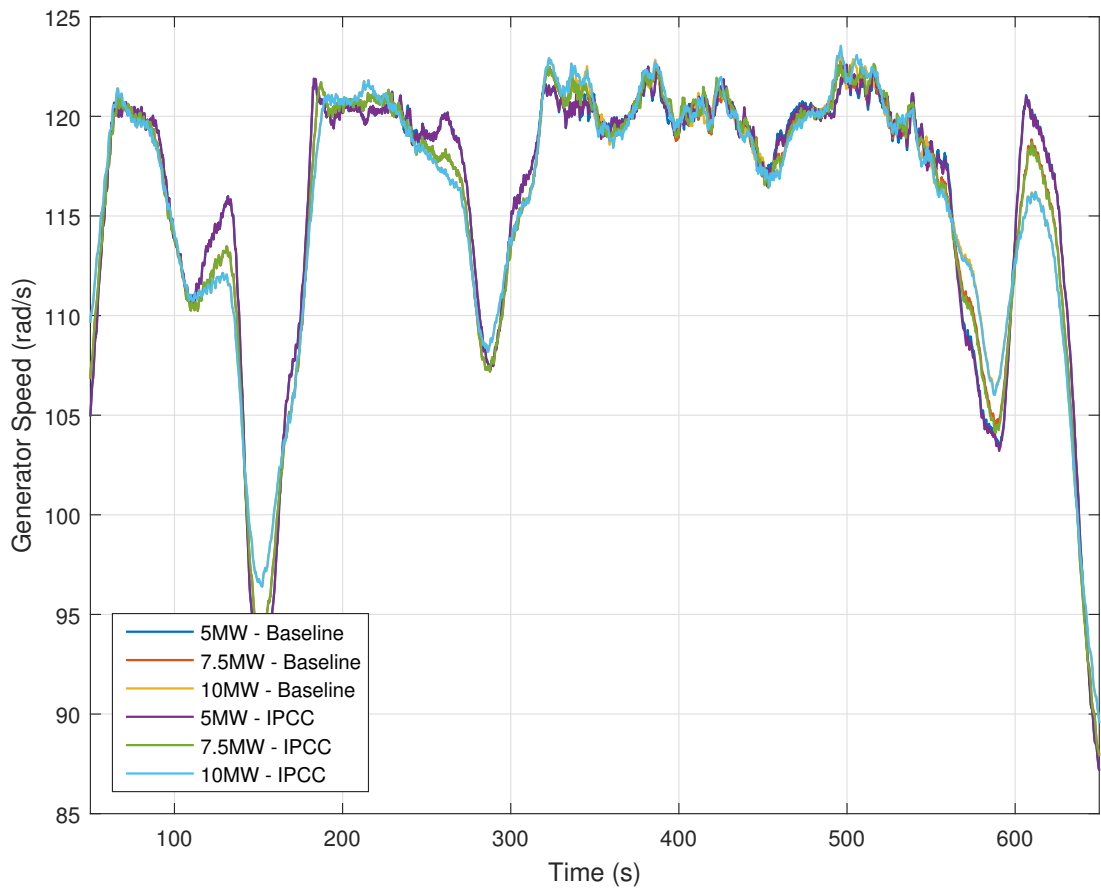


Figure 4.27: Generator speeds for the baseline controller and IPCC for different sizes of turbine

Above-rated

The differences between PCC and IPCC implementations for the 5MW turbine are actually only very slight. The overall gain of the controller is increased by 0.8dB. This has the effect of increasing pitch activity across the spectrum over which the controller operates, as well as extending the frequency range at the lower end. The result of this is a slight increase in the the primary peak of the power spectral density of the tower fore-aft moment seen in Figure 4.28. Although the peak is higher for the IPCC than for the PCC, it is still lower than that of the baseline controller. All simulations in this section are for a 16m/s mean wind speed with IEC class B turbulence unless otherwise stated.

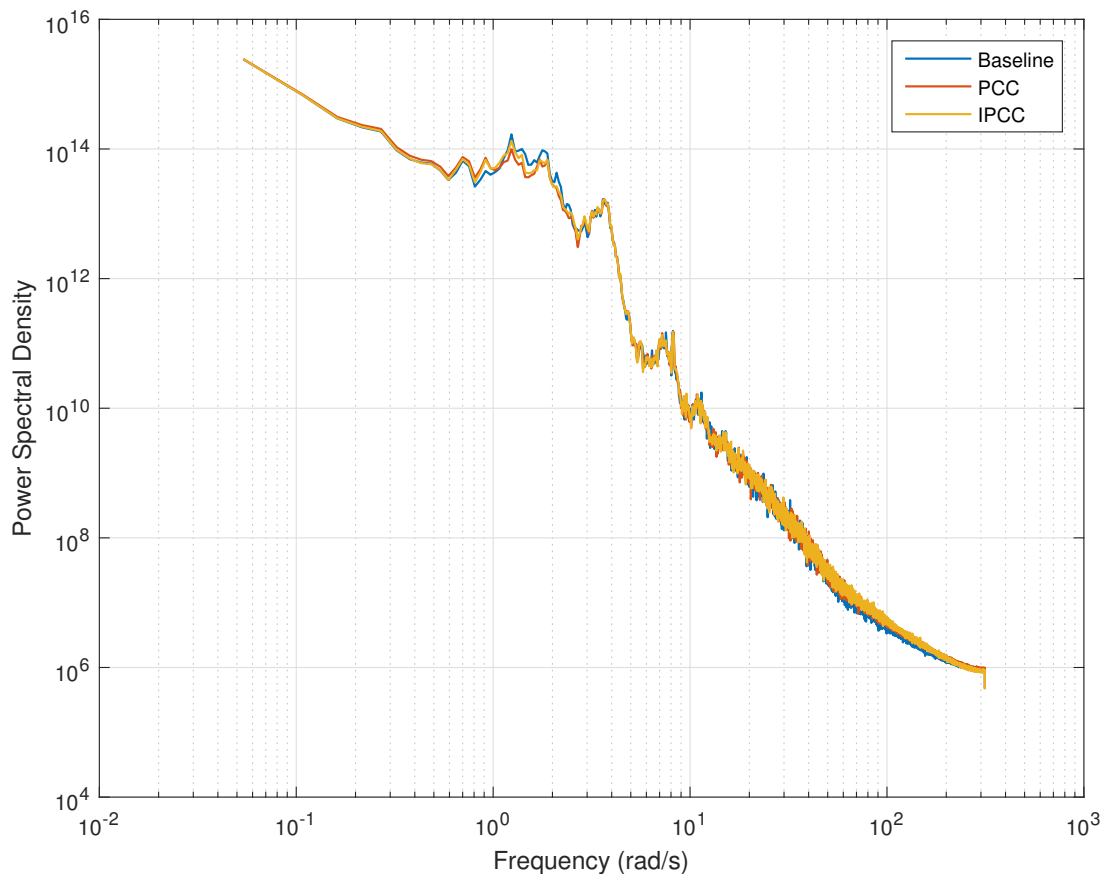


Figure 4.28: Power spectral densities of fore-aft the moment at the tower base for the baseline controller, PCC and IPCC (5MW)

The effect of increasing the gain can be seen in the power spectral densities of blade pitch angle and generator torque: Figure 4.29 and Figure 4.30 respectively. The reduction across the range of frequencies covered by the notch filter which is visible between the baseline controller and the PCC is somewhat reduced by the IPCC. There is also slightly more activity in the torque spectrum with the IPCC than with the PCC. Both of these results are a consequence of increasing the overall controller gain.

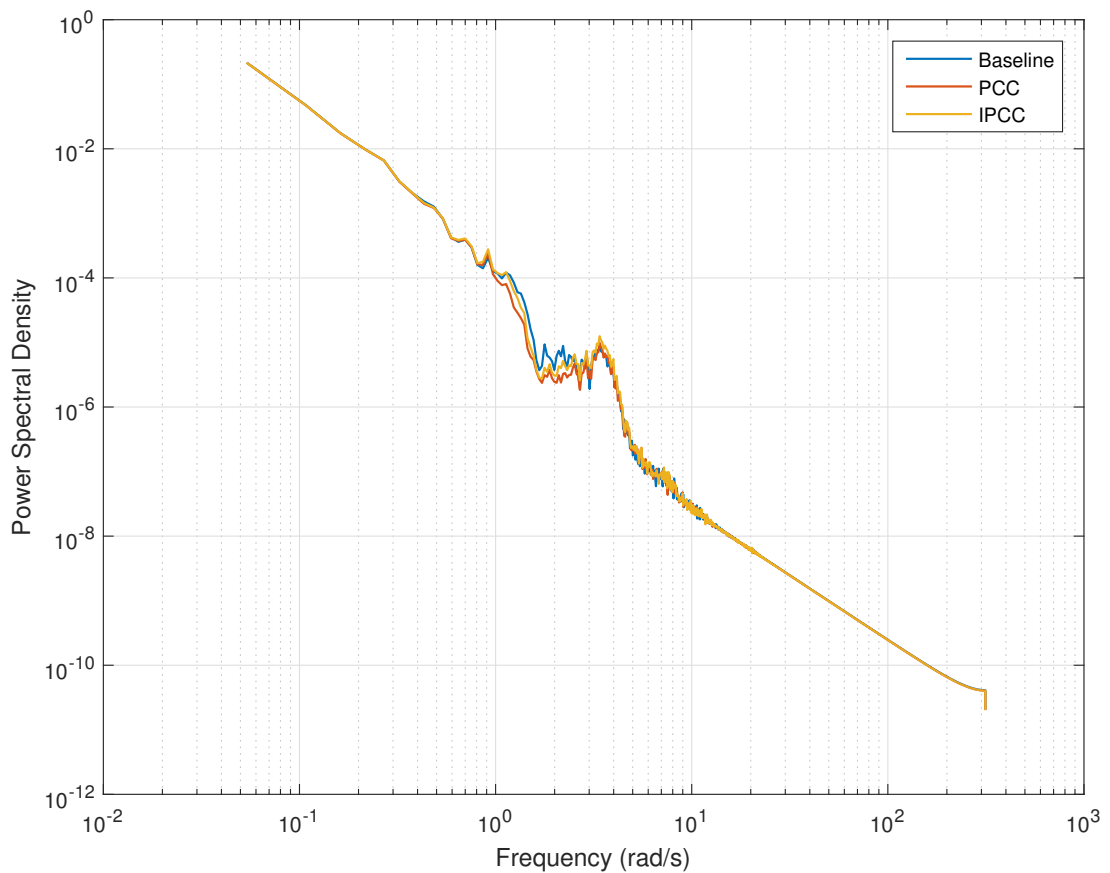


Figure 4.29: Power spectral densities of blade pitch angle for the baseline controller, PCC and IPCC (5MW)

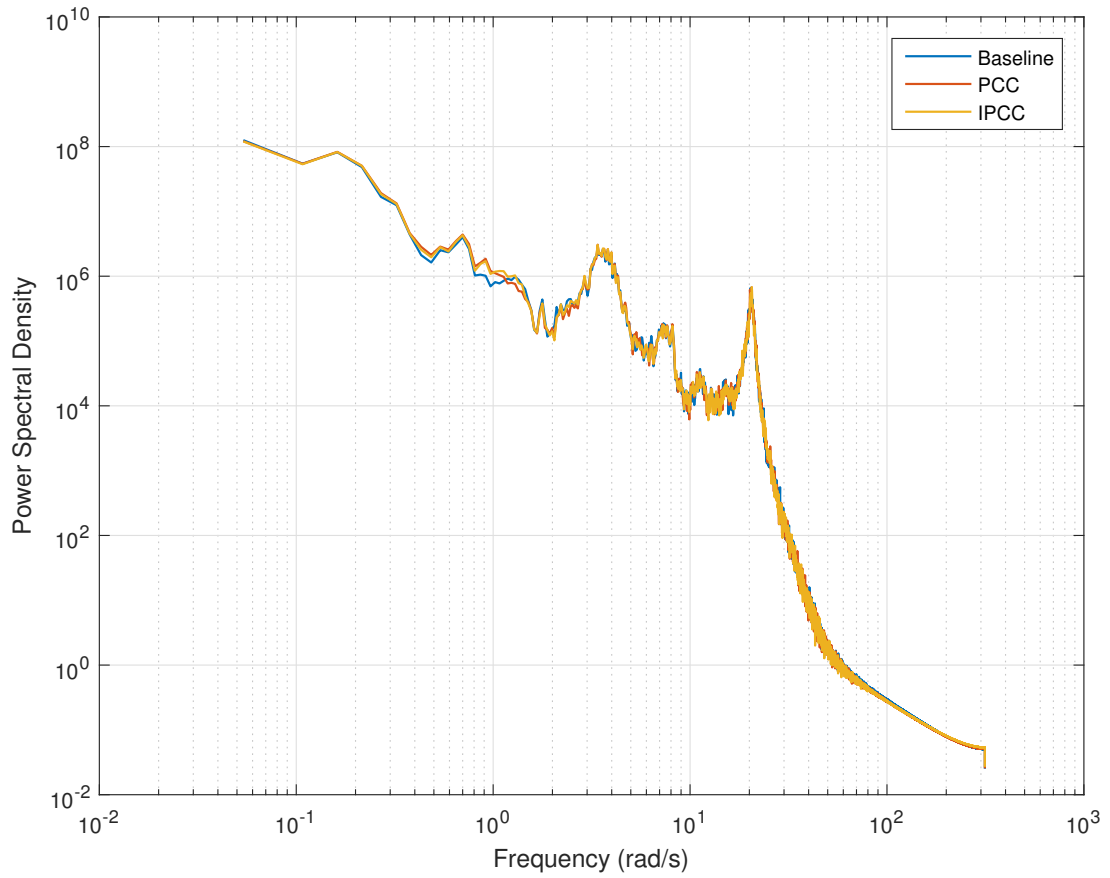


Figure 4.30: Power spectral densities of generator torque for the baseline controller, PCC and IPCC (5MW)

The changes introduced by the PCC mean that the time series of generator torque looks very similar to that of the baseline. For the IPCC, consistent with Figure 4.30, the time series for the IPCC, shown in Figure 4.31 is also very similar.

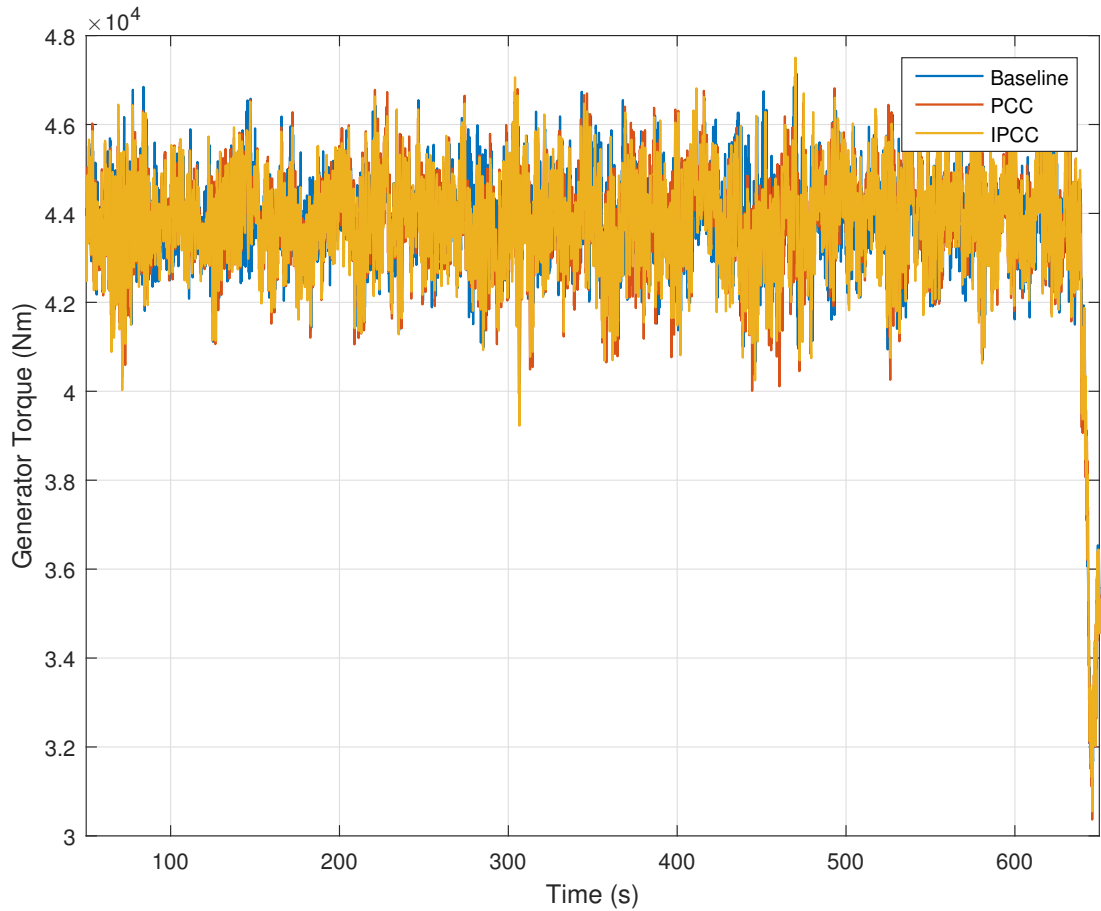


Figure 4.31: Generator torque for the baseline controller, PCC and IPCC (5MW)

The purpose of the IPCC is to increase the gain crossover frequency of the open loop system. The result of doing this is improved power and speed control. Figure 4.32 and Figure 4.33 show slightly smaller fluctuations in power and speed for the IPCC than the PCC and the baseline. The improvement is small but this is consistent with the small change to the overall gain which constitutes the difference between the PCC and the IPCC.

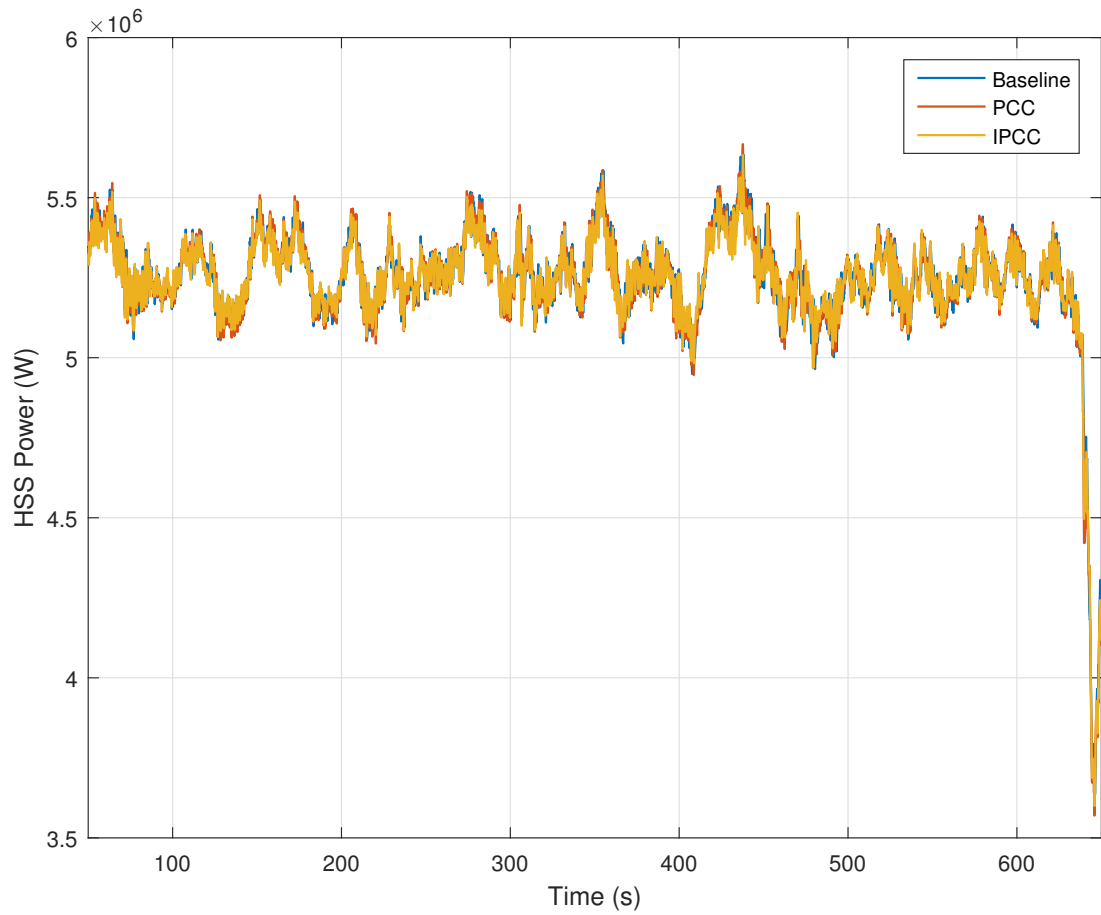


Figure 4.32: HSS power for the baseline controller, PCC and IPCC (5MW)

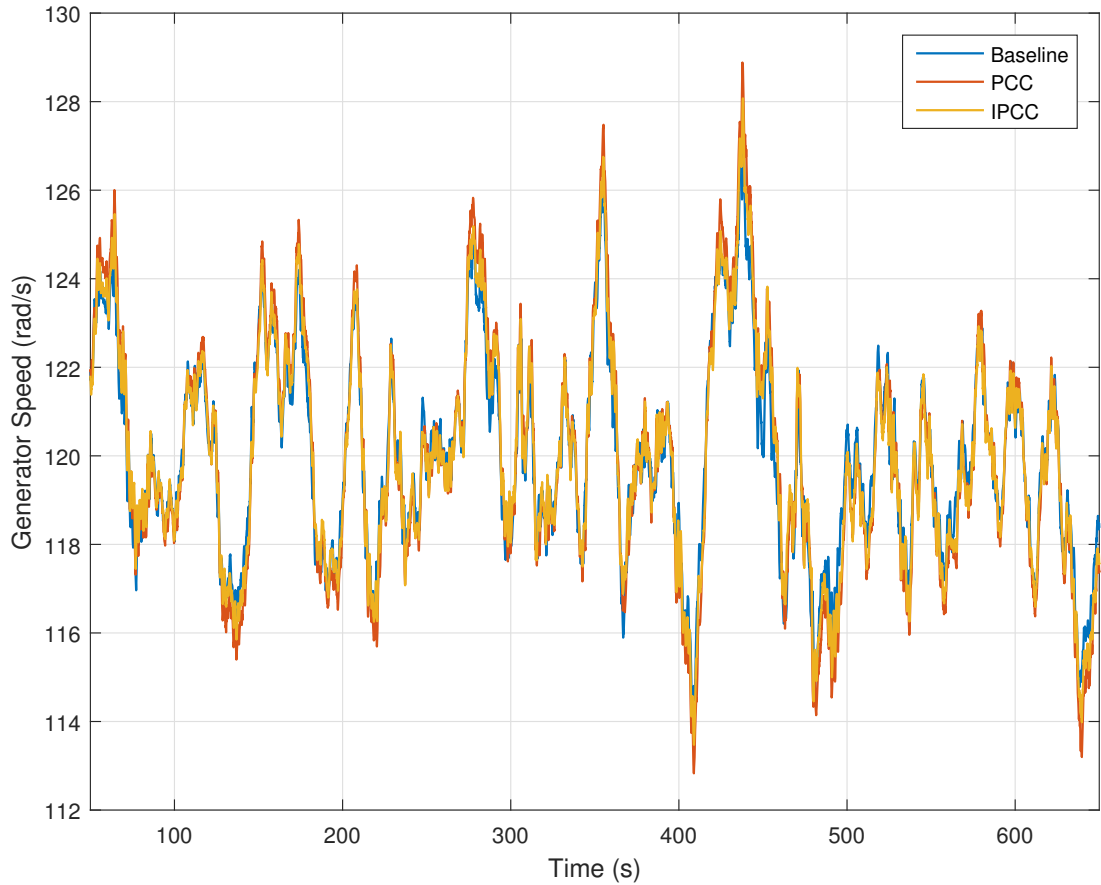


Figure 4.33: Generator speed for the baseline controller, PCC and IPCC (5MW)

Removing the effect of the RHPZs from the controller allows the gain of the controller for the 5MW turbine to be increased by just 0.8dB. However, for larger 7.5MW and 10MW turbines, which have lower tower fore-aft natural frequencies, the overall gain, and therefore the gain crossover frequency can be increased by much more. This means that the improvements of the IPCC over the PCC are more apparent as turbine size increases.

Figure 4.34 and Figure 4.35 show the power at the high speed shaft for the 7.5MW and 10MW respectively. These figures and Figure 4.32 show that the IPCC achieves greater reductions in the fluctuations in power output as turbine size increases. The standard deviations of data shown in these figures is displayed in Table 4.3. A 11.38% reduction in the standard deviation of HSS power is

achieved for the 10MW turbine.

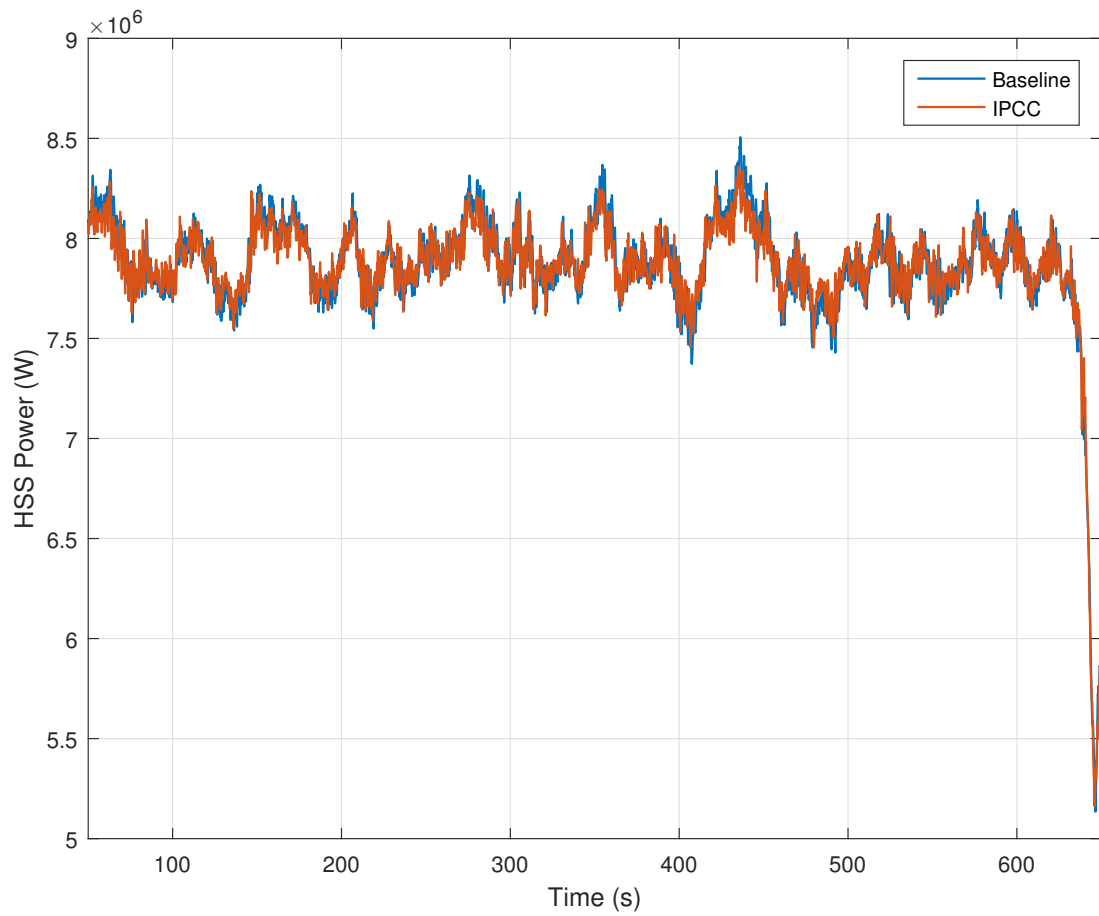


Figure 4.34: HSS power for the baseline controller and the IPCC (7.5MW)

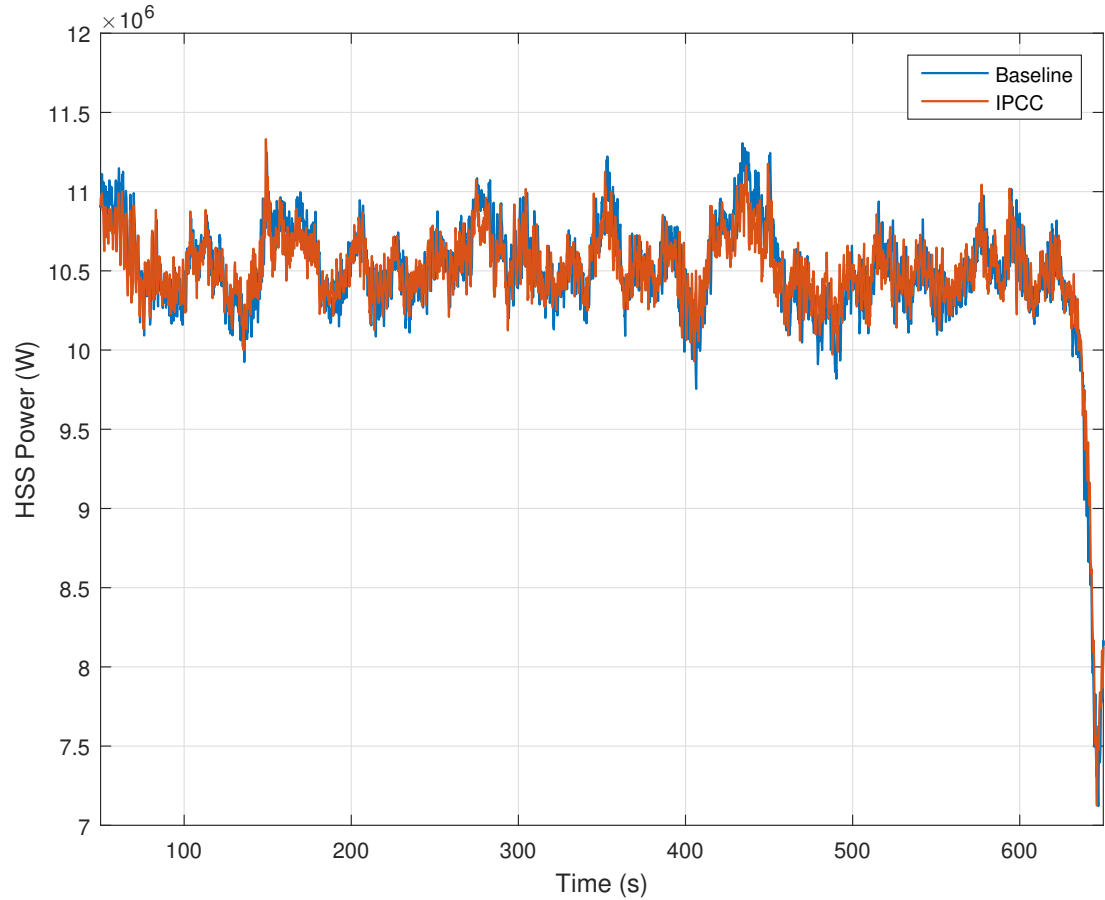


Figure 4.35: HSS power for the baseline controller and the IPCC (10MW)

Rated Power (MW)	Std. Dev. of HSS Power Baseline	Std. Dev. of HSS Power IPCC	Difference (%)
5.0	1.8443	1.8163	1.52
7.5	3.1033	2.9701	4.29
10.0	4.1845	3.7085	11.38

Table 4.3: Standard deviations of HSS power

With the PCC, changing the control target from generator speed to power resulted in a slight increase in generator speed fluctuations over the baseline controller. With the IPCC, Figure 4.33 shows this increase is still present. However, with the larger turbines, the gain has been increased by much more than the

5MW and the deterioration in speed control starts to disappear. The 10MW turbine even shows smaller fluctuations in generator speed with the IPCC than with the baseline controller. Figure 4.36 and Figure 4.37 show the generator speed for the 7.5MW and 10MW turbines. Table 4.4 shows the standard deviations of the data from these figures and Figure 4.33.

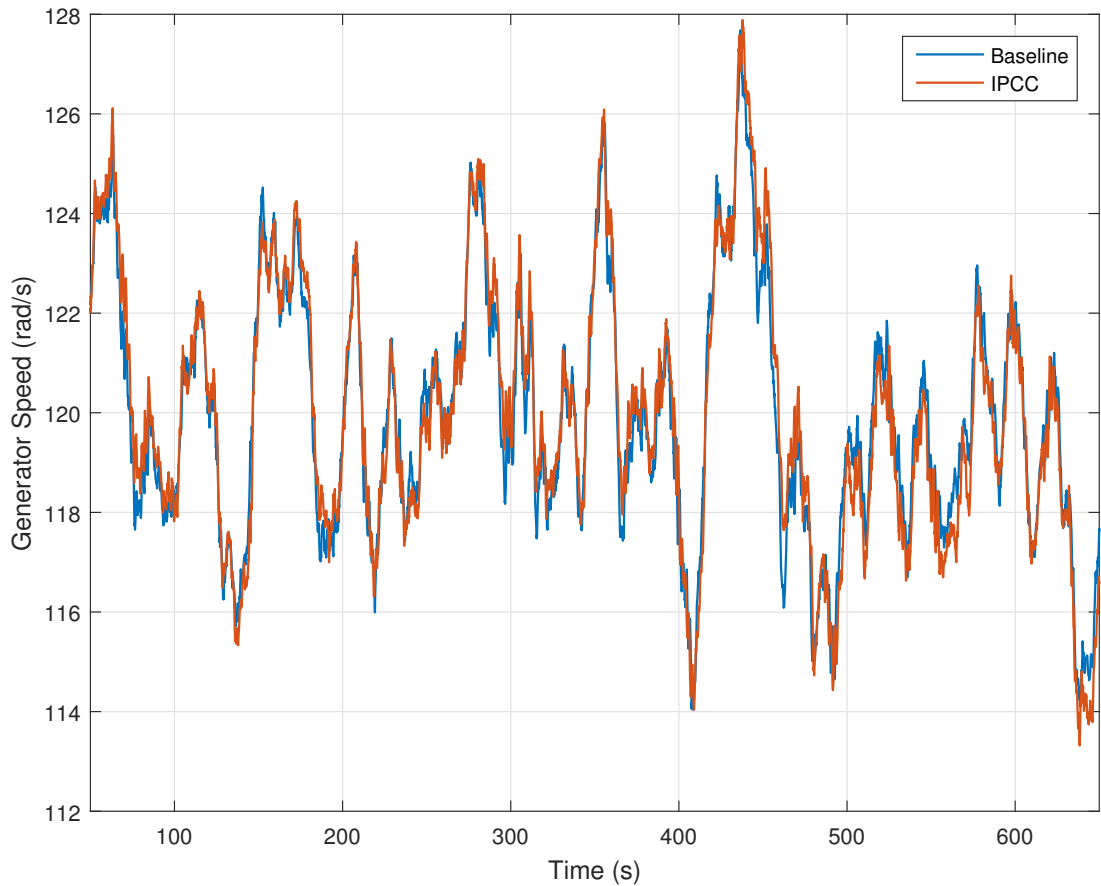


Figure 4.36: Generator speed for the baseline controller and the IPCC (7.5MW)

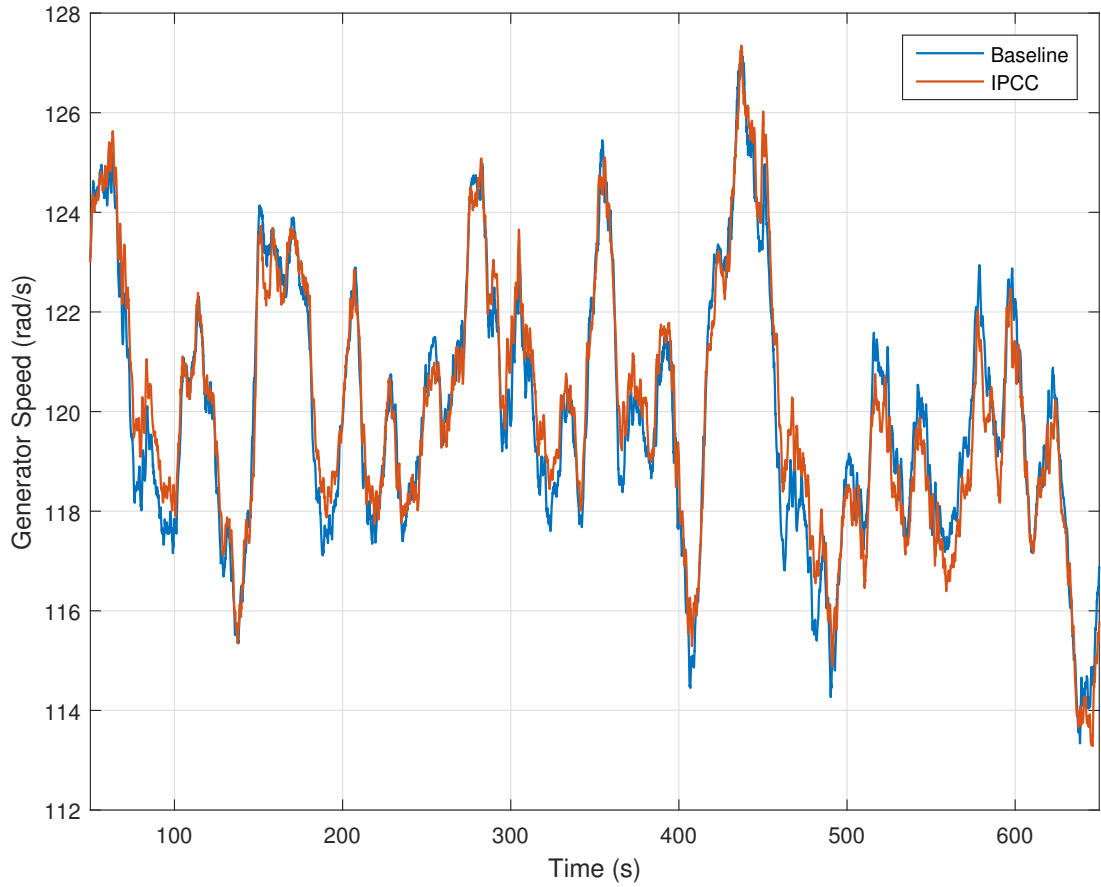


Figure 4.37: Generator speed for the baseline controller and the IPCC (10MW)

Rated Power (MW)	Std. Dev. of Generator Speed Baseline	Std. Dev. of Generator Speed IPCC	Difference (%)
5.0	2.2370	2.4141	-7.92
7.5	2.4559	2.6129	-6.39
10.0	2.5499	2.5171	1.29

Table 4.4: Standard deviations of generator speed

As with the 5MW, the 7.5MW turbine shows very little difference in the power spectral density of the tower fore-aft moment, shown in Figure 4.38, with the IPCC when compared to the baseline. Where, with the 5MW turbine, the IPCC plot was closer to that of the PCC, the 7.5MW turbine is a little higher

and close to the baseline controller. The 10MW turbine, however, has a peak slightly higher than that of the baseline. This reflects the comparatively greater gain added with the implementation of the IPCC. Figure 4.38 and Figure 4.39 show plots of the power spectral density of the tower fore-aft moment for the baseline controller and IPCC for the 7.5MW and 10MW turbines.

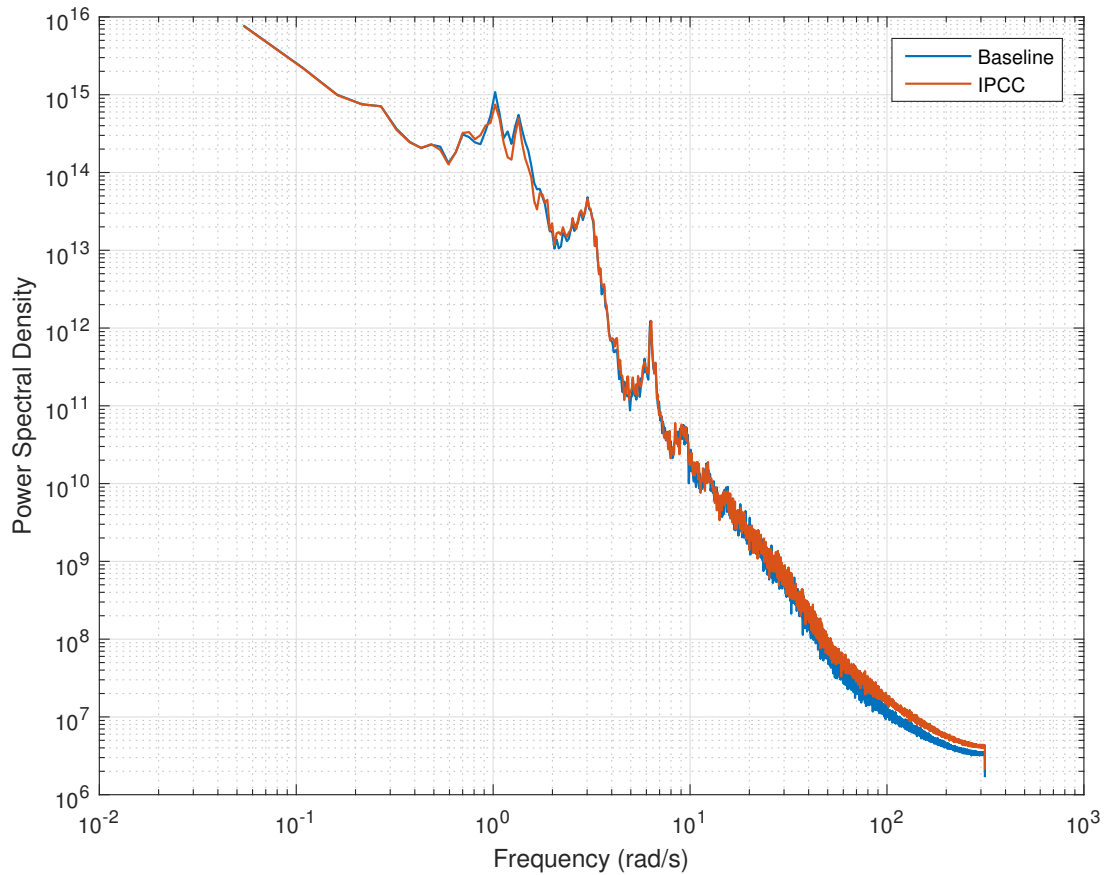


Figure 4.38: Power spectral densities of fore-aft the moment at the tower base for the baseline controller and IPCC (7.5MW)

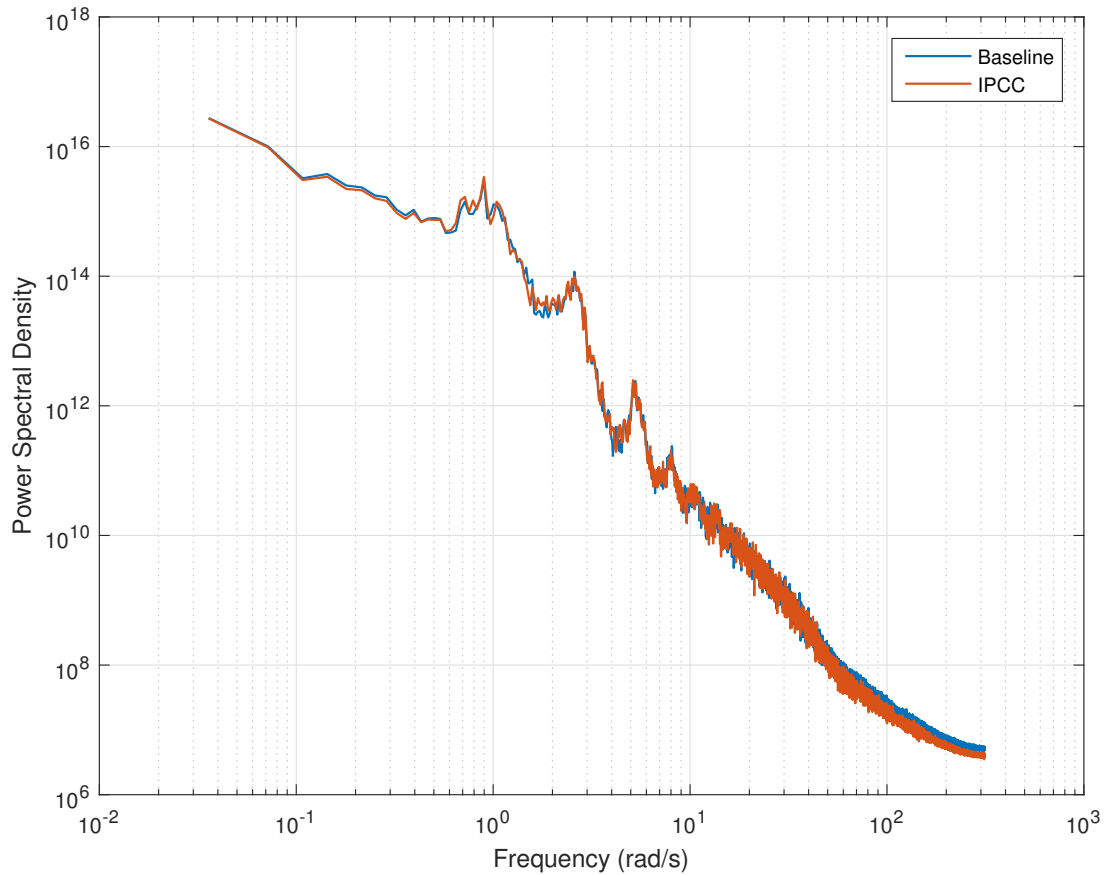


Figure 4.39: Power spectral densities of fore-aft the moment at the tower base for the baseline controller and IPCC (10MW)

Further to looking at the frequency analyses of the tower loads, damage equivalent loads can give an indication of the effect of a change to the controller on the fatigue life of major components. Figure 4.40 shows the damage equivalent loads at the base of the tower for all three turbines. The details of these calculations are described in Appendix C.

The baseline controller and the improved PCC are compared for three different wind fields, all with a mean wind speed of 18m/s, designated ‘Run 1’, ‘Run 2’ and ‘Run 3’ in the plot legend of Figure 4.40. Results from simulations with this mean wind speed are presented here because they contain long, continuous periods of continuous data where the wind turbine is operating at above-rated

power.

This data shows that the improved controller has a minimal effect on fatigue damage of the tower for the 5MW machine, but a with greater effect as size increases. The average damage equivalent loads across the three wind fields are shown in Table 4.5.

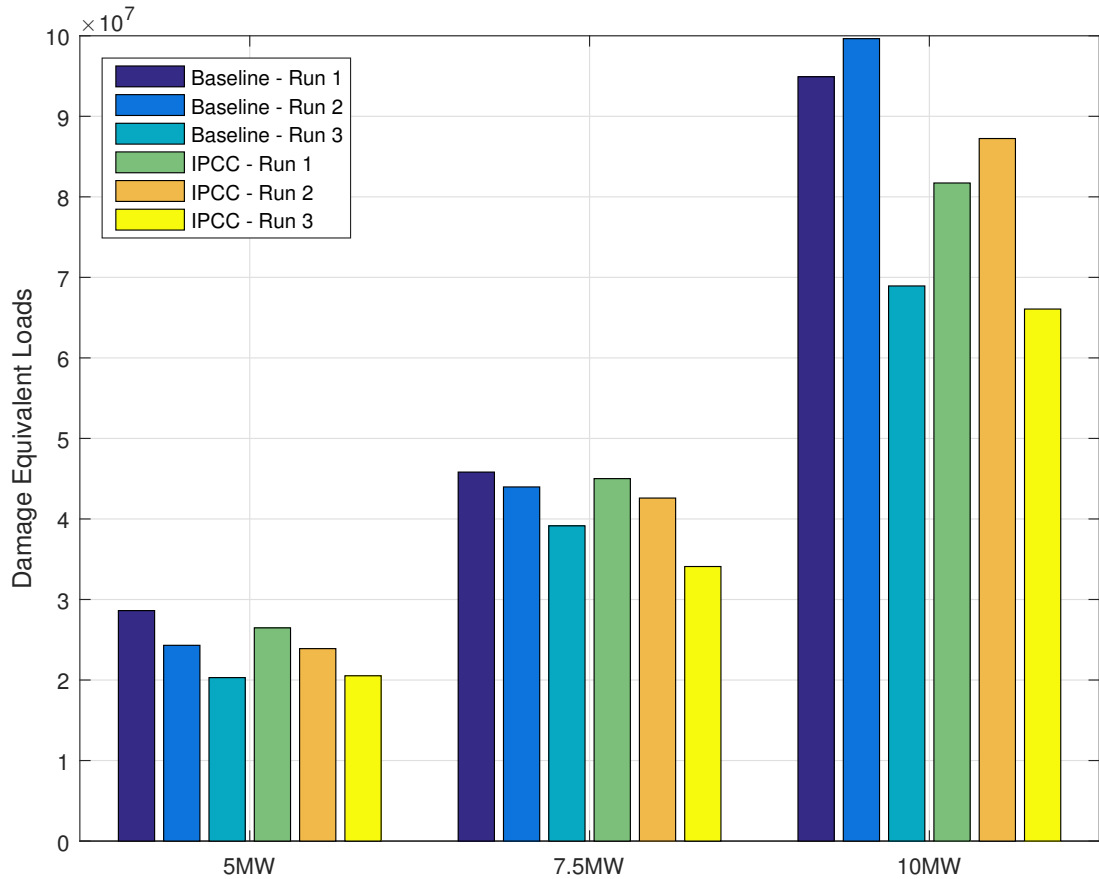


Figure 4.40: Damage equivalent loads at the tower base for the baseline controller and IPCC operating in a turbulent wind with a mean wind speed of 18m/s

Rated Power (MW)	Baseline Controller	IPCC	Difference (%)
5.0	2.4411×10^7	2.3634×10^7	3.18%
7.5	4.2982×10^7	4.0567×10^7	5.62%
10.0	8.7831×10^7	7.8344×10^7	10.80%

Table 4.5: Averages of damage equivalent loads across three simulations for the baseline and IPCC

A Notch in the Gain Response

While the IPCC shows improvements as outlined above, a notch, visible in Figure 4.15 is introduced in the gain. The position of this notch means that the gain which can be applied to increase the gain crossover frequency is limited. To correct this and attempt to return to a gain response similar to the baseline controller, a filter, $F(s)$, can be added immediately to the right of the notch filter, Y , in Figure 4.13. The stability margins of the system are especially sensitive to changes made in this range of frequencies so it may not be possible to completely restore the gain response to be the same as the baseline.

For the 5MW turbine a filter which gives as similar gain response to the baseline as possible is (4.18). Figure 4.41 shows the removal of the notch in the gain response introduced by the PCC. With this filter, however, unstable behaviour is observed during simulations. This instability is due to non-linear dynamic issues, resulting in the size and shape of the notch changing as the wind speed and blade pitch angle changes. As stated above, the system is very sensitive to changes in this frequency range; small changes to the transfer function can result in large changes to the stability margins.

$$F_1(s) = \frac{s^2 + 0.45s + 2.045}{s^2 + 0.04s + 2.045} \quad (4.18)$$

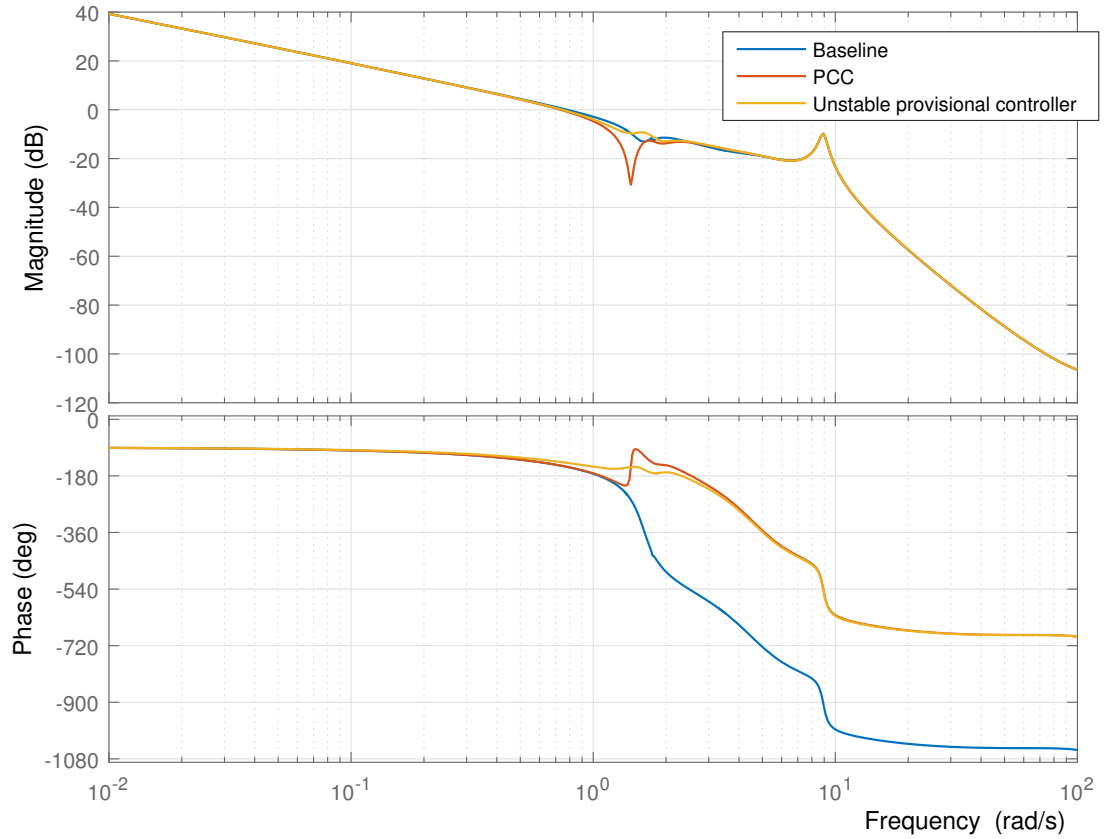


Figure 4.41: Bode plots showing the baseline, PCC and provisional controllers

A stable solution for the 5MW turbine is the transfer function (4.19). A Bode plot of the filter alongside the one used in Figure 4.41 is shown in Figure 4.42. A Bode plot showing a comparison of this provisional controller design with the baseline controller and the PCC is shown in Figure 4.43.

$$F_2(s) = \frac{s^2 + 0.1s + 2.045}{s^2 + 0.05s + 2.045} \quad (4.19)$$

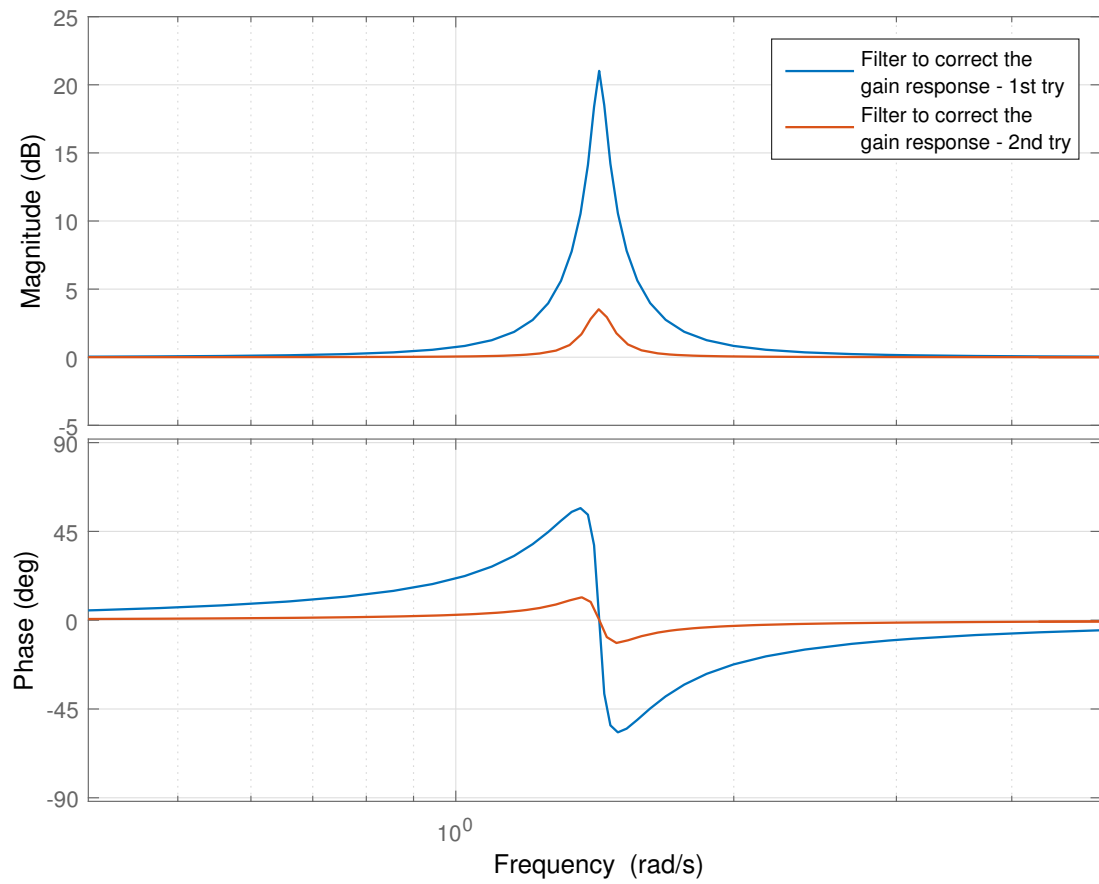


Figure 4.42: Bode plot showing the filter to correct the gain response of the PCC

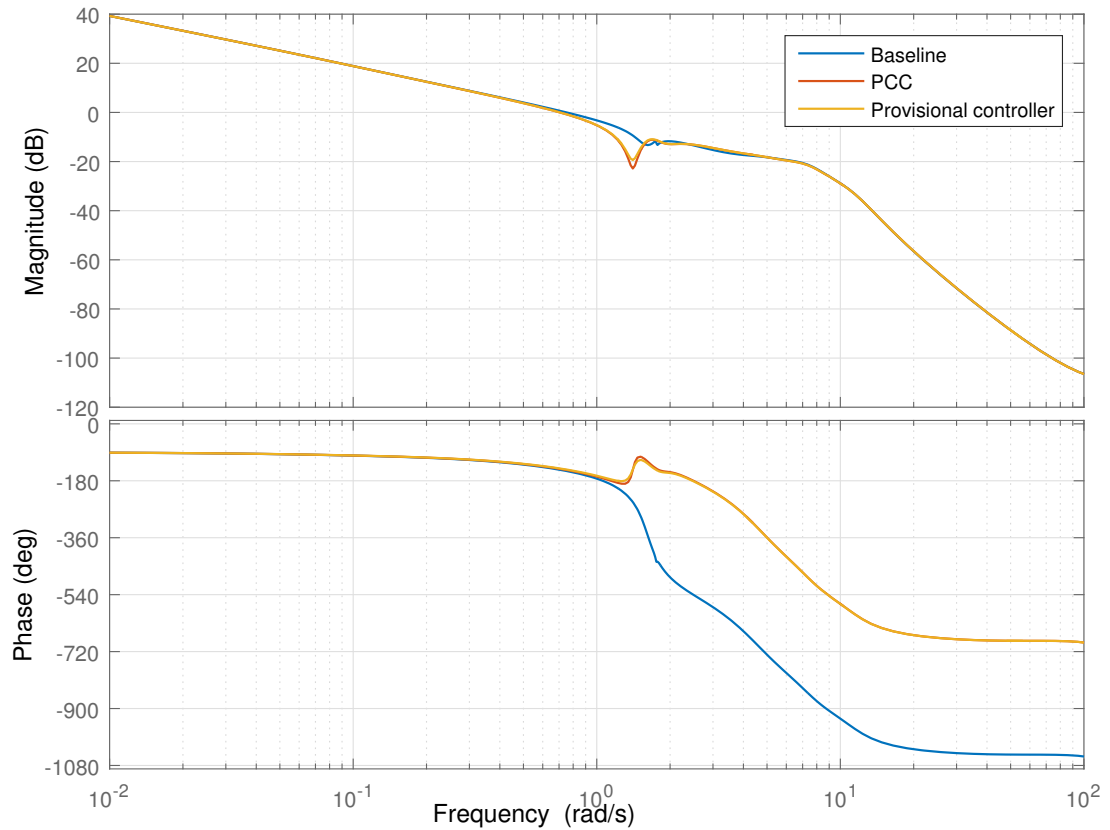


Figure 4.43: Bode plots showing the baseline, PCC and provisional controllers

Figure 4.43 shows a slight reduction in the depth of the notch introduced by the PCC. When a filter is introduced which attempts to fill the notch to a greater extent than this, unstable behaviour is observed during simulations.

Figure 4.44 shows the generator speed from simulations of the three controllers (baseline, PCC and provisional) operating with a mean wind speed of 16m/s and 15% turbulence intensity. These simulations show that the effect of the provisional controller on speed control is negligible.

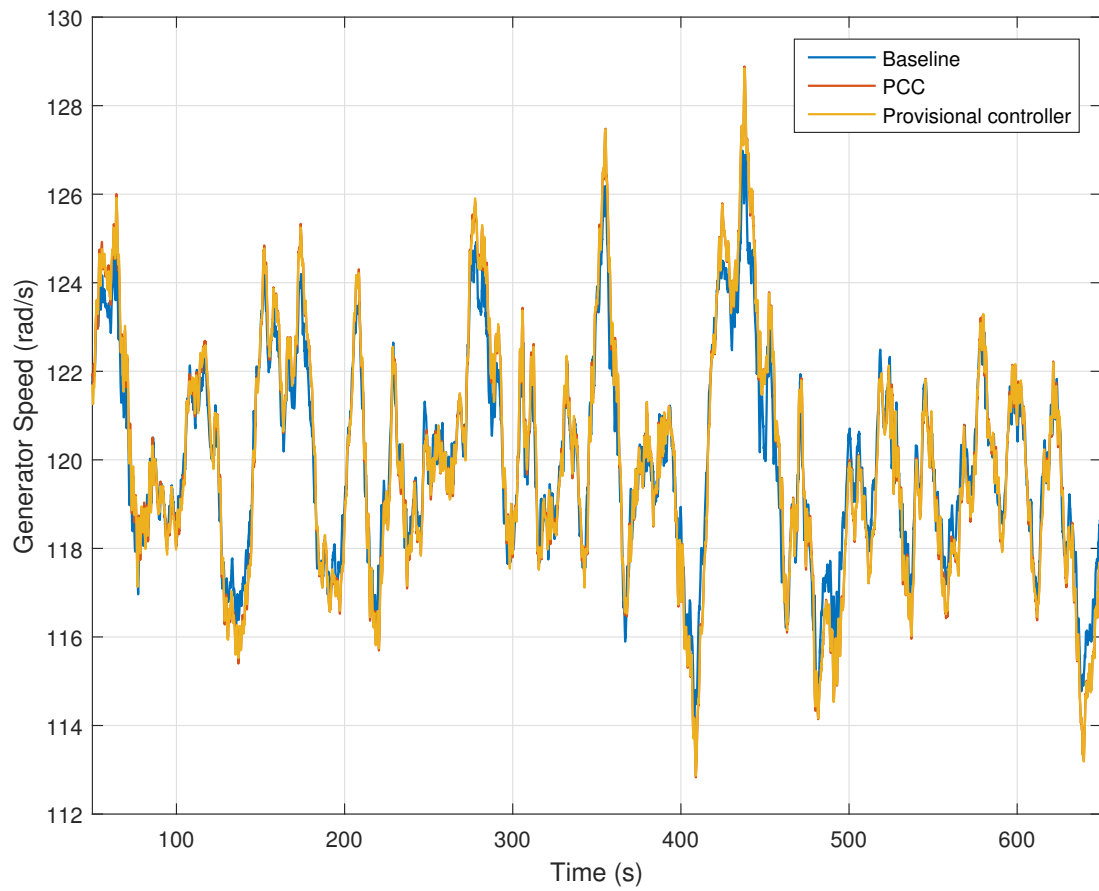


Figure 4.44: Comparison of generator speed for the baseline, PCC and provisional controllers

Similarly, the plot of mechanical power in Figure 4.45 shows negligible difference between the PCC and provisional controllers.

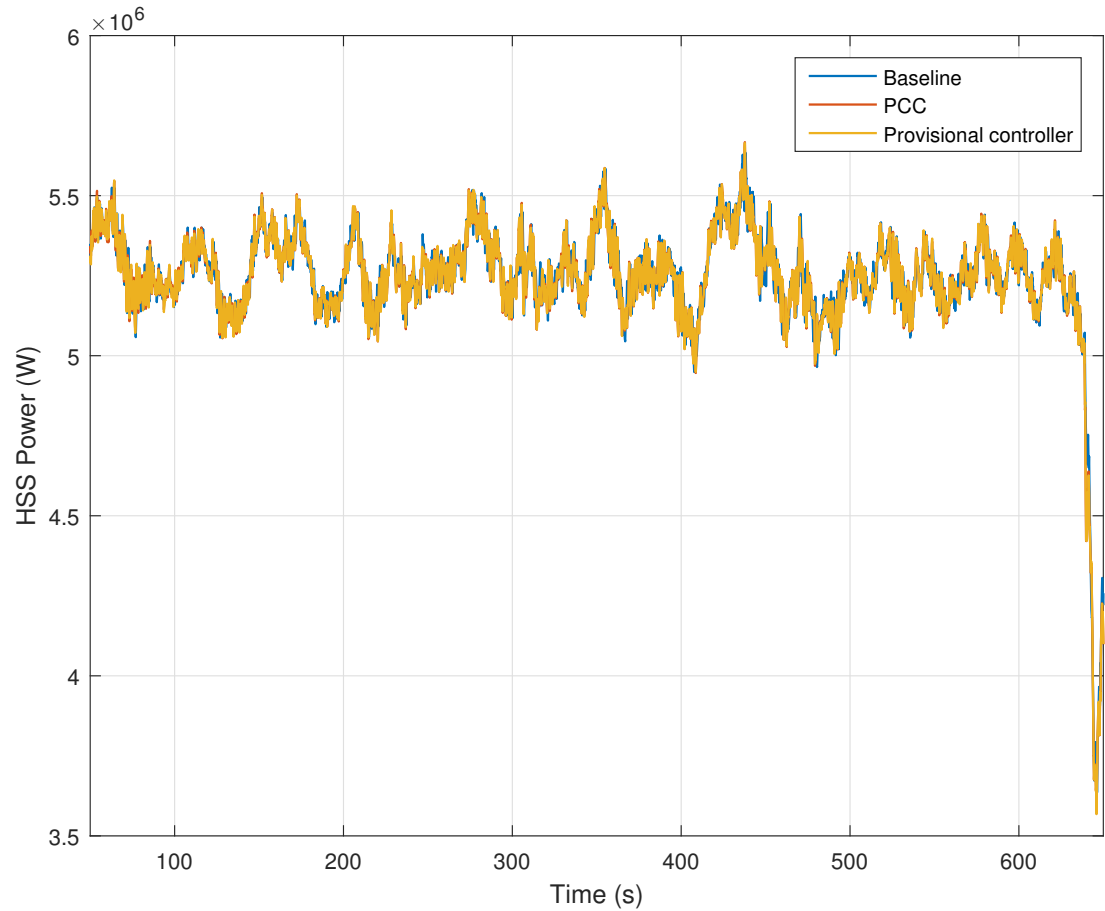


Figure 4.45: Comparison of mechanical power for the baseline, PCC and provisional controllers

The provisional controller increases the gain response at a range of frequencies set by the filter $F(s)$. It is therefore expected to see increased pitch activity at these frequencies and this is shown in the power spectral density plot in Figure 4.46. Increasing pitch activity also has the effect of increasing loads in the tower at these frequencies. The power spectral density of the tower fore-aft moment in Figure 4.47 shows the improvement in this area seen by the introduction of the PCC is removed by the provisional controller, across the frequencies covered by $F(s)$.

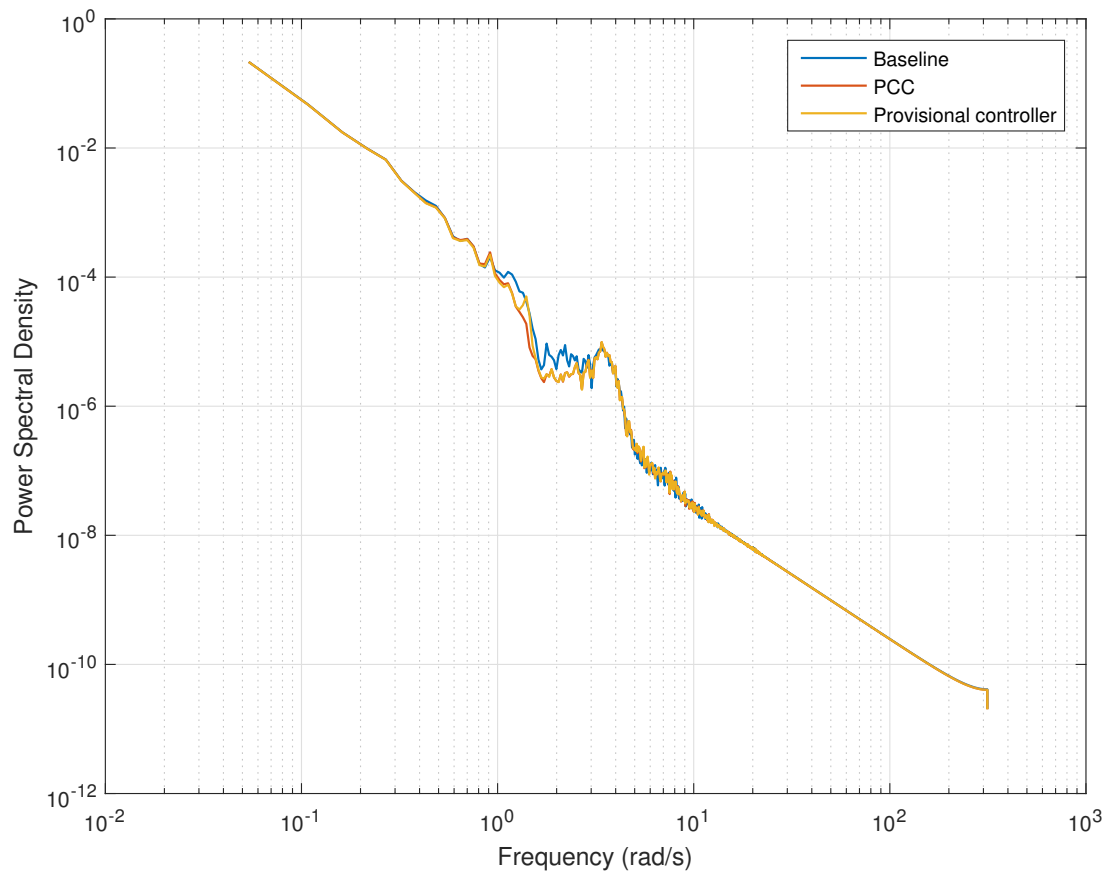


Figure 4.46: Comparison of power spectral densities of blade pitch angle for the baseline, PCC and provisional controllers

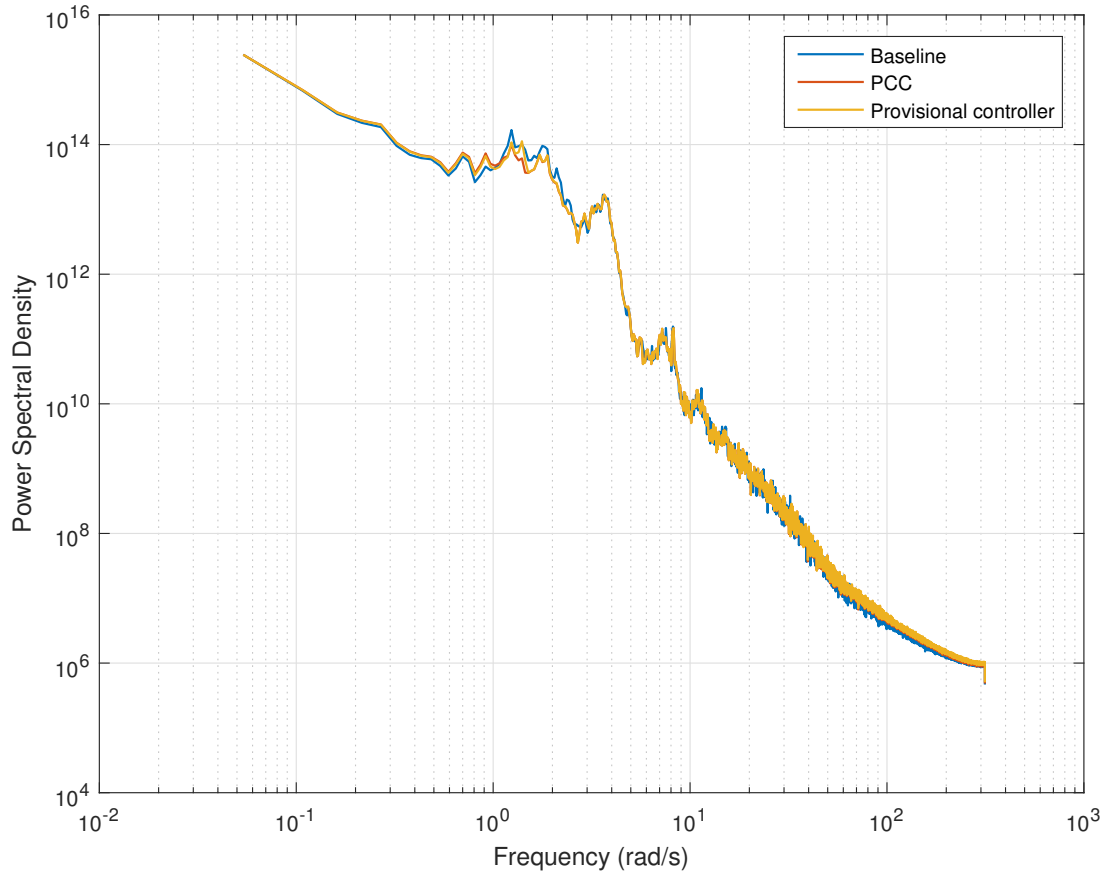


Figure 4.47: Comparison of power spectral densities of tower fore-aft moment for the baseline, PCC and provisional controllers

Simulations with the provisional controller show that a negligible change to speed and power control is achieved at the expense of increased pitch activity and tower loads. This, combined with the risk of introducing instability means that implementation of the provisional controller is not appropriate. Stability may be achieved by introducing a modification to (4.18) where the compensator changes with the wind speed. This would require a complex gain-scheduling implementation, however, and this is not within the scope of this thesis. The following sections in this chapter do not contain the changes made in this provisional controller.

4.5 Concluding Remarks

This chapter presents a controller design which improves controller performance of very large wind turbines by increasing the gain crossover frequency. The change in dynamics due to turbine size is shown to reduce the maximum achievable gain crossover frequency of large wind turbines and therefore impair control performance. Simulations demonstrate an improvement in the control of power output without an unacceptable regression in speed control or tower loads.

It should be noted that only normal operating conditions are considered here with a stochastic wind speed. However, the wind turbine is subject to other disturbances and events such as coherent gusts where the whole rotor sees a sudden change in wind speed. This can cause the wind turbine to over-speed and so be shut down. Increasing the gain crossover frequency makes the controller generally more responsive and so more capable of dealing with these events. Furthermore, fluctuations in generator speed is a reasonable proxy for general controller performance in these circumstances. It is for this reason that the controller performance is assessed here in terms of generator speed fluctuations.

A coordinated controller design (CCD) can be used to reduce tower loads by removing pitch activity at around the frequency of the tower's fore-aft mode. The power coordinated controller (PCC), an extension of the CCD, changes the control objective from generator speed to power output. This removes the greater fluctuations in power which are introduced by the CCD. This design can be further modified to improve the gain crossover frequency of the controller at the expense of the reduction in tower loads from the standard PCC by increasing the overall gain. This increase in gain crossover frequency is especially important for very large wind turbines where the bandwidth of the controller is constricted by a low natural frequency of the tower.

In Chapter 3, the generator speeds for three sizes of wind turbine are com-

pared. Here, two conflicting factors affect how well the wind turbine and the controller can keep the generator speed as close as possible to the set point when operating at above-rated power. Larger wind turbines will see greater averaging of the wind speed across the rotor due to their larger swept area. This has the effect of the wind turbine seeing less variation, particularly at higher frequencies where gusts with a lower length-scale exist. Greater wind speed averaging, if all other factors remain unchanged, would result in smaller excursions in generator speed from the set point. However, as shown in Chapter 3, the generator speed for a larger turbine operating in the same wind field is more variable than a smaller one. This is due to the lower gain crossover frequency in the controller of the larger turbine resulting in poorer speed control under gusts and wind speed changes which are coherent across the whole rotor. The controller design presented in this chapter allows for a higher gain crossover frequency and therefore greater robustness in control of anomalous wind conditions. The area between 0dB and the sensitivity function of the system is indicative of this performance and is directly linked to the gain crossover frequency.

Simulations of the PCC with increased gain show that greater increases in gain crossover frequency can be made in larger wind turbines. These changes result in an improvement in the control of power output by reducing fluctuations from the set point with minimal changes to speed control. Damage equivalent loads at the base of the tower decrease slightly with the design presented in this thesis. These loads can be reduced further by not increasing the overall gain by as much. In this case, the gain crossover frequency will not be increased by as much but damage equivalent loads will also not increase by as much, relative to the baseline. A relationship between the gains in bandwidth and the increase in damage equivalent loads may be a subject for future work.

Chapter 5

Development of a Linear Parameter-varying Wind Turbine Controller

Variable speed, pitch regulated, horizontal axis wind turbines demonstrate highly non-linear dynamics at high wind speeds which can cause difficulties for power regulation. With the trend of wind turbines increasing in size, and the natural frequencies of the major structural components becoming ever lower, it becomes increasingly important to consider this non-linearity in the controller design.

In this chapter a simplistic realisation of a gain-scheduled controller is presented to counter the varying low frequency pole as well as a design of a new controller with a more suitable implementation which offers better performance. This realisation is developed as continuous-time and discrete-time implementations and tested using the same simulation environments as in preceding chapters against a baseline controller. Simulation results demonstrating the improvements of this gain-scheduled controller are presented in the context of varying wind turbine size.

5.1 Non-linearity in the Wind Turbine Plant Dynamics

The dynamics of a pitch regulated wind turbine, when operating at above-rated power, change with the wind speed. Of particular interest is the transmittance between pitch angle demand and rotor speed which has a gain and a pole at low frequency which vary with wind speed. It is standard practice to counteract the varying gain by implementing “gain-scheduling” in the pitch controller, the method for which is discussed in Chapter 3. The low frequency pole, however, is often ignored. Figure 5.1 shows the poles and zeros for the 5MW turbine at a range of wind speeds. The pole can be seen in the left-hand plane, on the imaginary axis at frequencies ranging from about 0.06rad/s for wind speeds of 12m/s up to about 0.6rad/s for wind speeds of 24m/s. The effect of this pole can be seen when the Bode plots of different wind speeds are compared as in Figure 5.2. The gain response is different for different wind speeds up to about 0.6rad/s, which is the frequency that the pole reaches at very high wind speeds. The presence of this non-linearity reduces the open-loop gain of the closed-loop system at low frequency and inhibits the performance of the controller.

Figure 5.1 also shows zeros which are present in the right hand plane. These RHPZs can have a destabilising effect on the system if not adequately dealt with. The pairs of zeros which can be seen between $0s^{-1}$ and $0.2s^{-1}$ on the real axis are due to the dynamics of the tower. A controller to mitigate the effect of these zeros is presented in Chapter 4. The zeros between $0.5s^{-1}$ and $2s^{-1}$ on the real axis are related to the dynamics of the blades. These have frequencies from about 4rad/s to 6rad/s which are much greater than both the gain crossover and phase crossover frequencies and therefore do not have a destabilising effect.

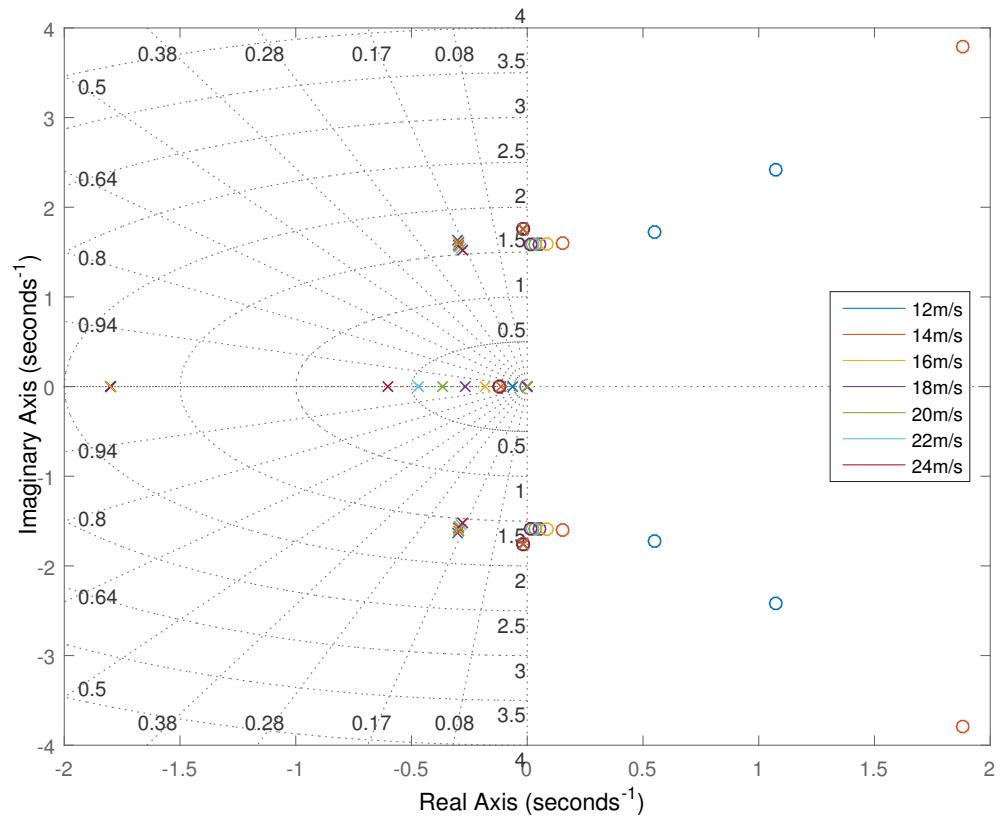


Figure 5.1: Pole-zero map of the open loop system showing a pole on the real axis with a frequency which is a function of wind speed

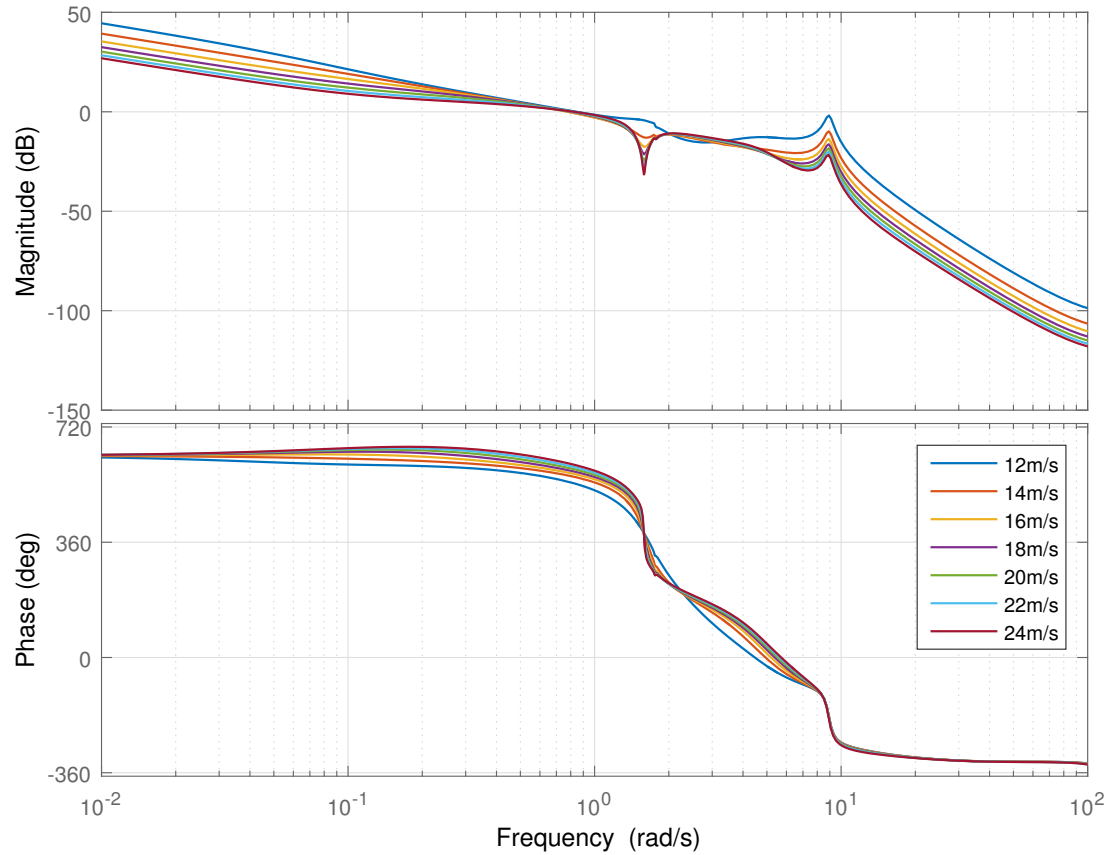


Figure 5.2: Open loop Bode plots of the open loop system showing non-linearity at a low frequency

5.2 Simple Gain-scheduled Controller

If the low frequency pole was considered not to vary with wind speed, it could be countered by including a lead-lag compensator such as (5.1) in the control design. In this example, α would be the frequency of the pole present in the plant. The differential equation of this is (5.2).

$$C(s) = \frac{s + \alpha}{s + k} \quad (5.1)$$

$$\dot{y} + ky = \dot{x} + \alpha x \quad (5.2)$$

To allow the lead-lag compensator to counter a pole which varies with the wind speed, α becomes a function of the wind speed. If the controller is operating properly, the blade pitch angle demand can be used as a reliable proxy for wind speed.

Although the addition of this compensator to the controller would appear to counter the varying pole present in the plant, this particular realisation is not appropriate because (5.2) is not regained from its linearisation. When the system is linearised about an equilibrium point, the differential equation (5.3) becomes (5.4).

$$\dot{y} + ky = \dot{x} + \alpha(\beta_d)x \quad (5.3)$$

$$\Delta\dot{y} + k\Delta y = \Delta\dot{x} + \alpha(\beta_{d_0})\Delta x + \alpha'(\beta_{d_0})x_0\Delta\beta_d \quad (5.4)$$

where:

$$\Delta\beta_d = a\Delta x + b\Delta y \quad (5.5)$$

The constants a and b represent how the scheduling variable relate to the states in the plant, see Section 3.2.3. This is because the pitch demand, β_d , has to be a function of the states of the controller.

The differential equation derived by the linearisation, shown in (5.4), contains terms not present in (5.3). The transfer function of such a linearisation, derived from (5.4) is shown in (5.6).

$$\frac{\Delta y}{\Delta x} = \frac{s + \alpha(\beta_{d_0}) + a\alpha'(\beta_{d_0})x_0}{s + k - b\alpha'(\beta_{d_0})x_0} \quad (5.6)$$

5.2.1 Implementation and Simulations

Standard gain-scheduling based on the realisation in (5.3) is applied to the 5MW turbine to assess its performance and the adequacy of the realisation. For the 5MW turbine, the value of this pole at various wind speeds is shown in Table 5.1. These values are taken from linear models of the plant at different wind speeds.

Wind Speed (m/s)	$\alpha(\beta_d)$ (rad/s)	β (rad)
12	0.0682	0.063
14	0.1534	0.113
16	0.2142	0.182
18	0.2656	0.268
20	0.3117	0.366
22	0.3545	0.470
24	0.3943	0.602

Table 5.1: Frequencies of the variable pole for a selection of wind speeds and blade pitch angles

The data in Table 5.1 can be used to fit a curve and define a polynomial which describes $\alpha(\beta_d)$. The frequencies of the pole are shown in Figure 5.3 overlaid with the polynomial approximation.

$$\alpha(\beta_d) = -0.9177\beta^2 - 1.1659\beta + 0.0179 \quad (5.7)$$

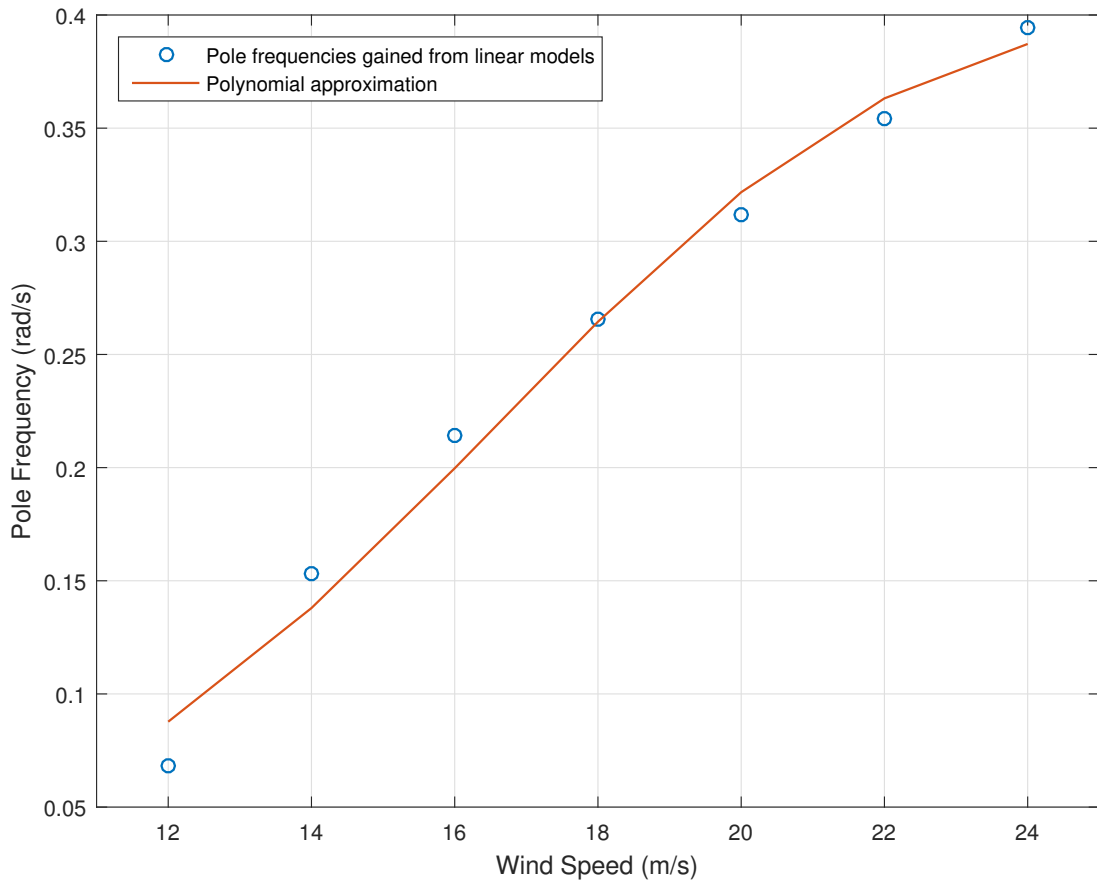


Figure 5.3: Frequencies of the variable pole and polynomial approximation

To ensure smooth switching between below-rated and above-rated operation, the value for $\alpha(\beta_d)$ is held at the same value for all below-rated wind speeds. In the case of the 5MW turbine, this is about 11.4m/s. The value of the fixed pole in the compensator is chosen to be equal to the zero at this minimum point. This means that the compensator is unity for below-rated operation and there is no discontinuity at the switching point.

In Chapter 3 the structure of the baseline controller is outlined. This compensator is included as part of the outer controller, outside the feedback loop which forms part of the switching mechanism. The Bode plot of the system with the simple gain-scheduling implemented, Figure 5.4, shows similar gain responses at low frequencies for all wind speeds. However, these Bode plots are generated

using the compensator in (5.1) with α set to the appropriate value from Table 5.1, so do not account for the nonlinear dynamics introduced through the scheduling variable being dependant on the state of the controller. In reality, this could change the dynamic behaviour of the system considerably from the dynamics shown in Figure 5.4.

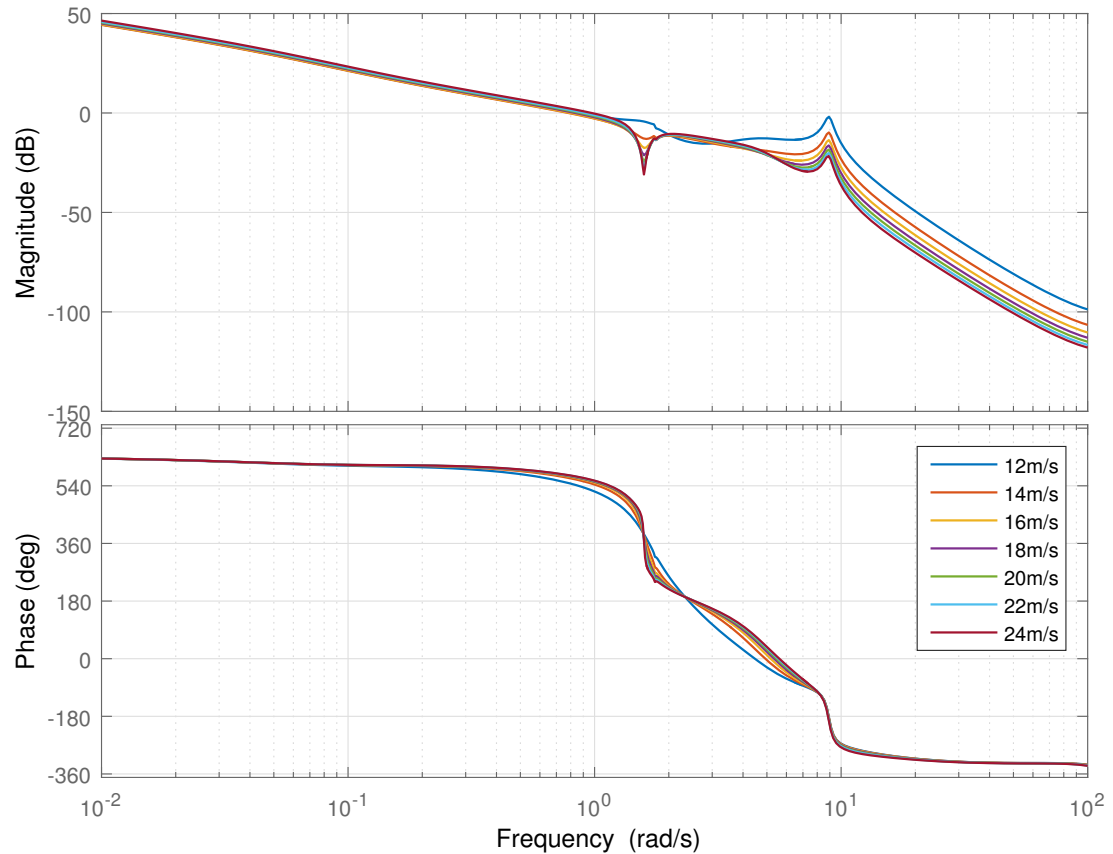


Figure 5.4: Open loop Bode plots of the open loop system with the simple gain-scheduling implementation

Simulations of the above implementation applied to the 5MW turbine show very little difference in speed and power control performance. Figure 5.5 and Figure 5.6 show the generator speed and high speed shaft (HSS) power for a simulation with a 16m/s mean wind speed and a turbulence intensity of about 15%.

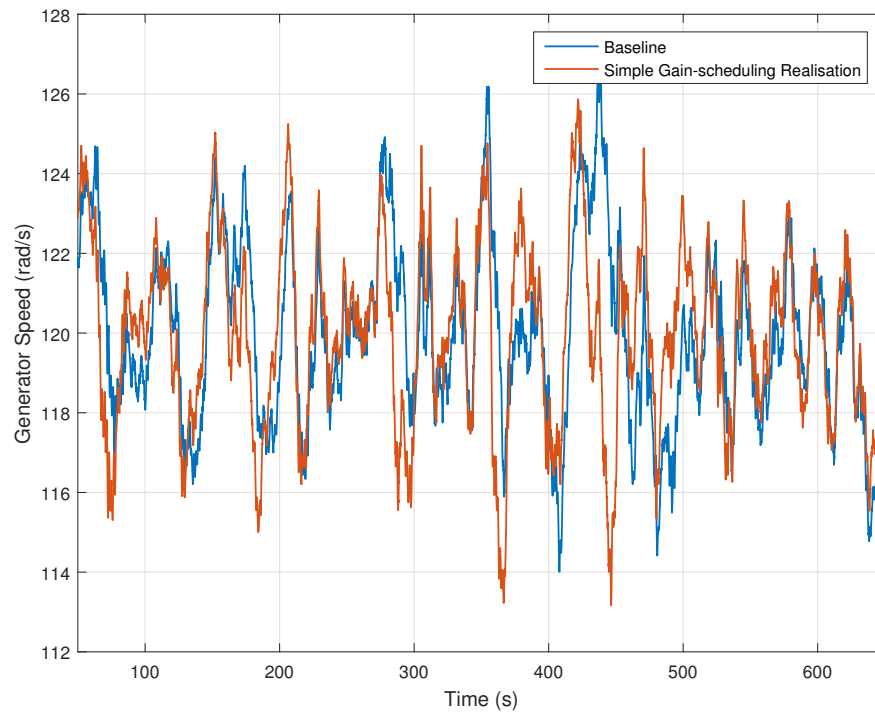


Figure 5.5: Comparison of generator speed for baseline and simple gain-scheduled realisation

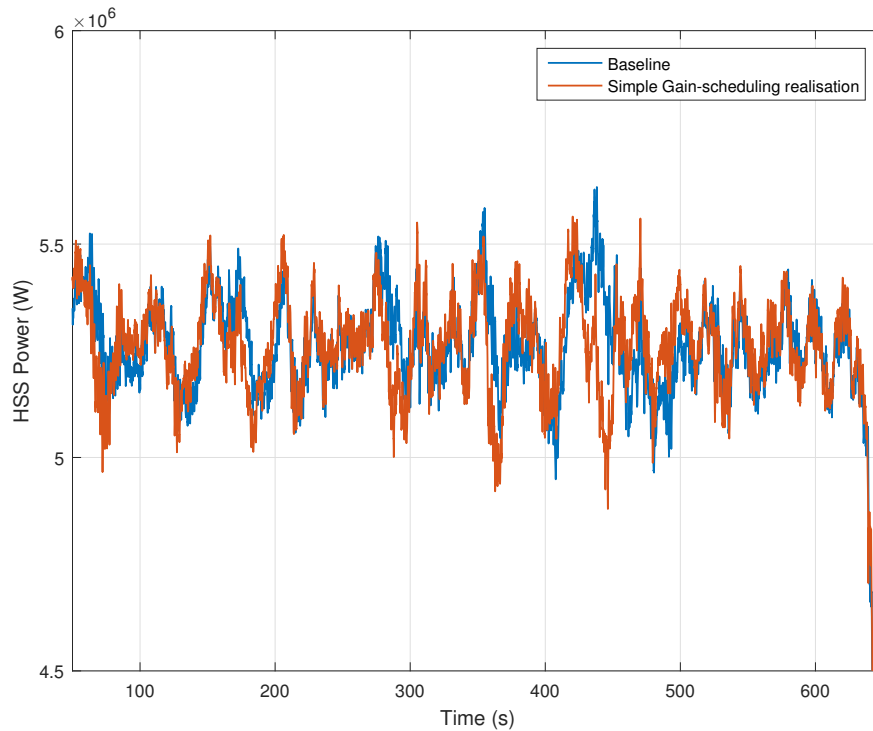


Figure 5.6: Comparison of HSS power for baseline and simple gain-scheduled realisation

Although the magnitude of some excursions in both generator speed and power are reduced, others are increased. The overall effect is that there is no change to performance. The standard deviation of generator speed for the baseline and the simple gain-scheduling realisation are 2.2370 and 2.2577 respectively. For HSS power the standard deviations are 1.8443×10^5 and 1.8726×10^5 . These standard deviations are calculated using a single simulation for each configuration.

This implementation of a gain-scheduled controller performs as it does because of the mismatch of the Taylor Series linearisation of the lead-lag compensator compared to its frozen-time linearisation.

5.3 Extended Local Linear Equivalence

A linear parameter-varying (LPV) controller, continuously interpolating between a series of linear controllers, that satisfies a local linear equivalence (LLE) condition [32] is discussed. LLE controllers have the property that the local controllers obtained by Taylor's Series linearisation regain the original linear controller designed on the basis of the linearised dynamics of the system at the equilibrium operating point. With the local linear equivalence condition, the LPV controller is valid only for regions local to the equilibrium operating points for which the linearised dynamics of the plant and controller are a good representation of the non-linear dynamics. Figure 5.7 illustrates the regions where the local linear equivalence condition is valid. Each dot in Figure 5.7 represents a region of validity for the linearised dynamics at a particular equilibrium point where y is the output and x is a state of the system. In operating conditions with prolonged perturbations, far from the equilibrium points, the linearised dynamics, in general, cease to be a good representation of the non-linear dynamics. In these conditions, this realisation is not adequate.

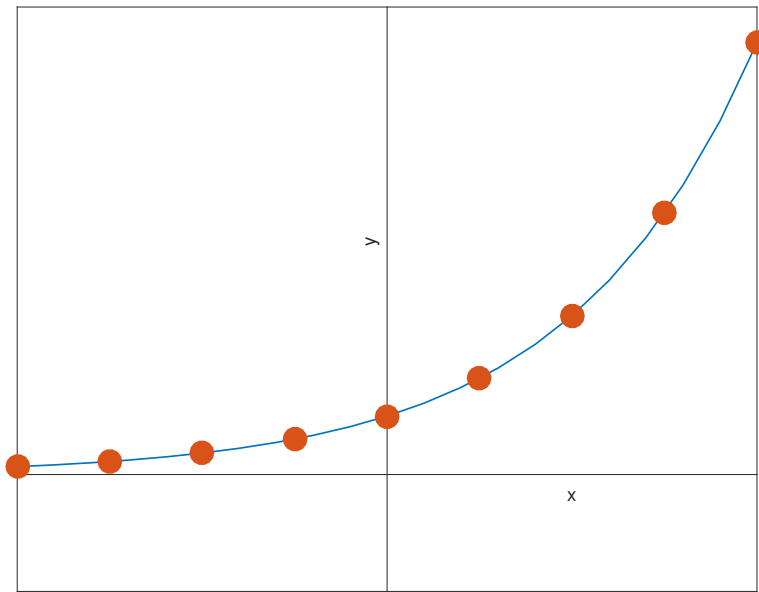


Figure 5.7: LLE condition illustrating locus of equilibrium points

A realisation, in which the region of conditions in Figure 5.7 extend to cover the whole space, satisfies extended local linear equivalence [32]. Figure 5.8 illustrates the extended local linear equivalence condition with the highlighted area showing the extended region where the linearised dynamics are valid for a single equilibrium operating point. The scheduling variable is constant along the dashed lines.

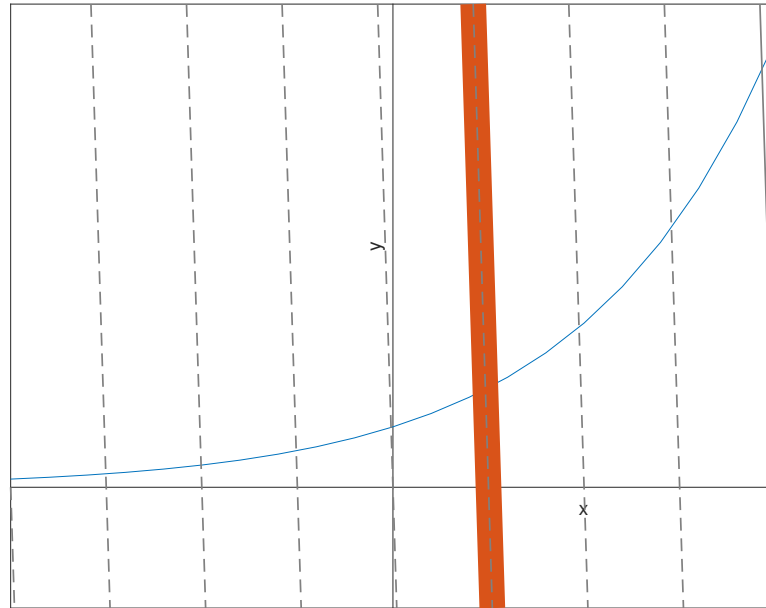


Figure 5.8: ELLE condition illustrating lines of constant β_d

A simple example of a realisation that satisfies ELLE is shown in Figure 5.9.

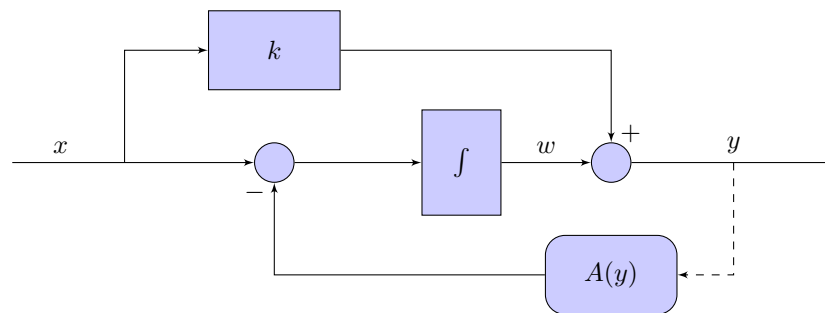


Figure 5.9: A first order realisation of the ELLE condition

The system shown in Figure 5.9 is equivalent to the equation:

$$w = \int (x - A(y)) dt \quad (5.8)$$

$$y = w + kx \quad (5.9)$$

Differentiating (5.8) and (5.9):

$$\dot{w} = x - A(y) \quad (5.10)$$

$$\dot{y} = \dot{w} + k\dot{x} \quad (5.11)$$

Substituting (5.10) into (5.11):

$$\dot{y} = k\dot{x} + x - A(y) \quad (5.12)$$

Applying Taylor's series expansion to (5.12):

$$\Delta\dot{y} = k\Delta\dot{x} + \dot{x} - \alpha(y_0)\Delta y \quad (5.13)$$

Which is equivalent to the transfer function relationship where $\alpha(y) = \frac{dA}{dy}(y)$:

$$\Delta y = \frac{ks + 1}{s + \alpha(y_0)} \quad (5.14)$$

The transfer function system equates to Figure 5.9 has a pole with varying frequency. The scheduling variable in this case is $\rho = y$. The region, for which a linearisation at equilibrium operating points is parameterised by the scheduling variable, ρ , is defined by $y_0 - \epsilon < y < y_0 + \epsilon$ with x at any value. Hence, these regions cover the whole space. The locus of equilibrium operating points is the curve $x = A(y)$.

Suppose that the region in Figure 5.9 is amended by the inclusion of an integrator on the input line as in Figure 5.10. The system is equivalent to (5.8), (5.9) and:

$$x = \int r dt \quad (5.15)$$

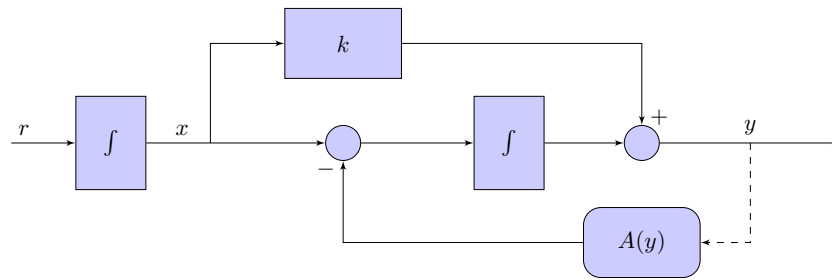


Figure 5.10: A first order realisation of the ELLE condition with an integrator on the input line

If $v = \dot{w}$, (5.10) becomes:

$$v = x - A(y) \quad (5.16)$$

Differentiating (5.16):

$$\dot{v} = \dot{x} - \alpha(y)\dot{y} \quad (5.17)$$

$$= r - \alpha(y)\dot{y} \quad (5.18)$$

In addition, (5.11) becomes:

$$\dot{y} = v + kr \quad (5.19)$$

Hence, Figure 5.10 is equivalent to Figure 5.11.

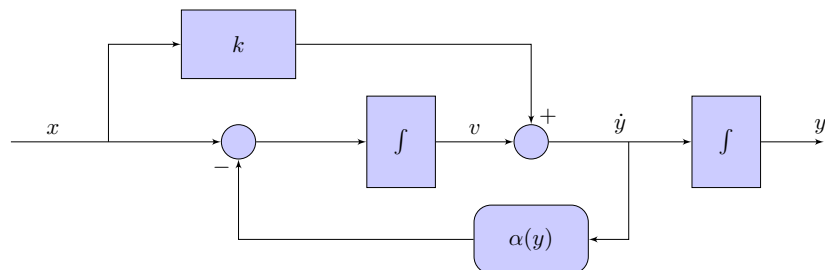


Figure 5.11: A first order realisation of the ELLE condition with an integrator moved to the output

The realisation in Figure 5.11 has a direct relationship to the linearisation shown in (5.15). All that is required is to set the value of the scheduling variable to y_0 when the transfer function for its block diagram is simply (5.15); that is, from linearisation of the non-linear system in Figure 5.11 the local linear dynamics are recovered. Taylor's Series expansion linearisation is not required.

The above example has a single pole with varying frequency. A system with a single zero with varying frequency is not so straight forward to represent in ELLE form and is detailed in the following section.

5.4 An Extended Local Linear Equivalence Controller

The requirement of this controller design is to counter the pole present in the wind turbine dynamics with an LPV controller which satisfies the extended local linear equivalence condition. The example in the preceding section is of a compensator with a variable pole but the present design task requires a controller with a variable zero. A compensator with a variable zero can be approximated by a compensator with a large number of fixed zeros and corresponding variable poles as in (5.20). As the scheduling variable changes, the variable zeroes cancel out different fixed poles, giving the effect of a single variable pole. Here, the scheduling variable is the blade pitch angle demand, β_d , which acts as a proxy for wind speed.

$$\frac{s + \alpha(\beta_d)}{s + k} \approx \frac{(s + \alpha_{\beta_d1})(s + \alpha_{\beta_d2})(s + \alpha_{\beta_d3})(s + \alpha_{\beta_d4})}{(s + k)(s + \psi_1(\beta_d))(s + \psi_2(\beta_d))(s + \psi_3(\beta_d))} \quad (5.20)$$

	β_{d1}	β_{d2}	β_{d3}	β_{d4}
$\psi_1(\beta)$	α_{v2}	α_{v1}	α_{v1}	α_{v1}
$\psi_2(\beta)$	α_{v3}	α_{v3}	α_{v2}	α_{v2}
$\psi_3(\beta)$	α_{v4}	α_{v4}	α_{v4}	α_{v3}

Table 5.2: Values of $\psi(\beta_d)$ at pitch angle demand values of β_{di} ($i = 1, 2, 3, 4$)

In Table 5.2, α_{vi} is the value of $\alpha(\beta_d)$ at the pitch angle β_{di} . Therefore, when $\beta_d = \beta_{di}$, (5.20) reduces to (5.21). For convenience, k can be chosen to be equal to $\alpha_{\beta_{d1}}$, thereby reducing the order.

$$\frac{s + \alpha_{\beta_{di}}}{s + k} \quad (5.21)$$

By expanding the example implementation given in the previous section, a realisation which satisfies the extended local linear equivalence condition for a higher order system is shown in Figure 5.12. The transfer function representing this block diagram is (5.22). It should be noted that the controller in Figure 5.12 has an integral action because this is essential for it to be linearised by freezing the scheduling variable [32].

$$Y(s) = k \frac{b_1 s^n + b_2 s^{n-1} + \dots + b_n s + 1}{s^n + a_1(y) s^{n-1} + \dots + a_{n-1}(y) s + a_n(y)} X(s) \quad (5.22)$$

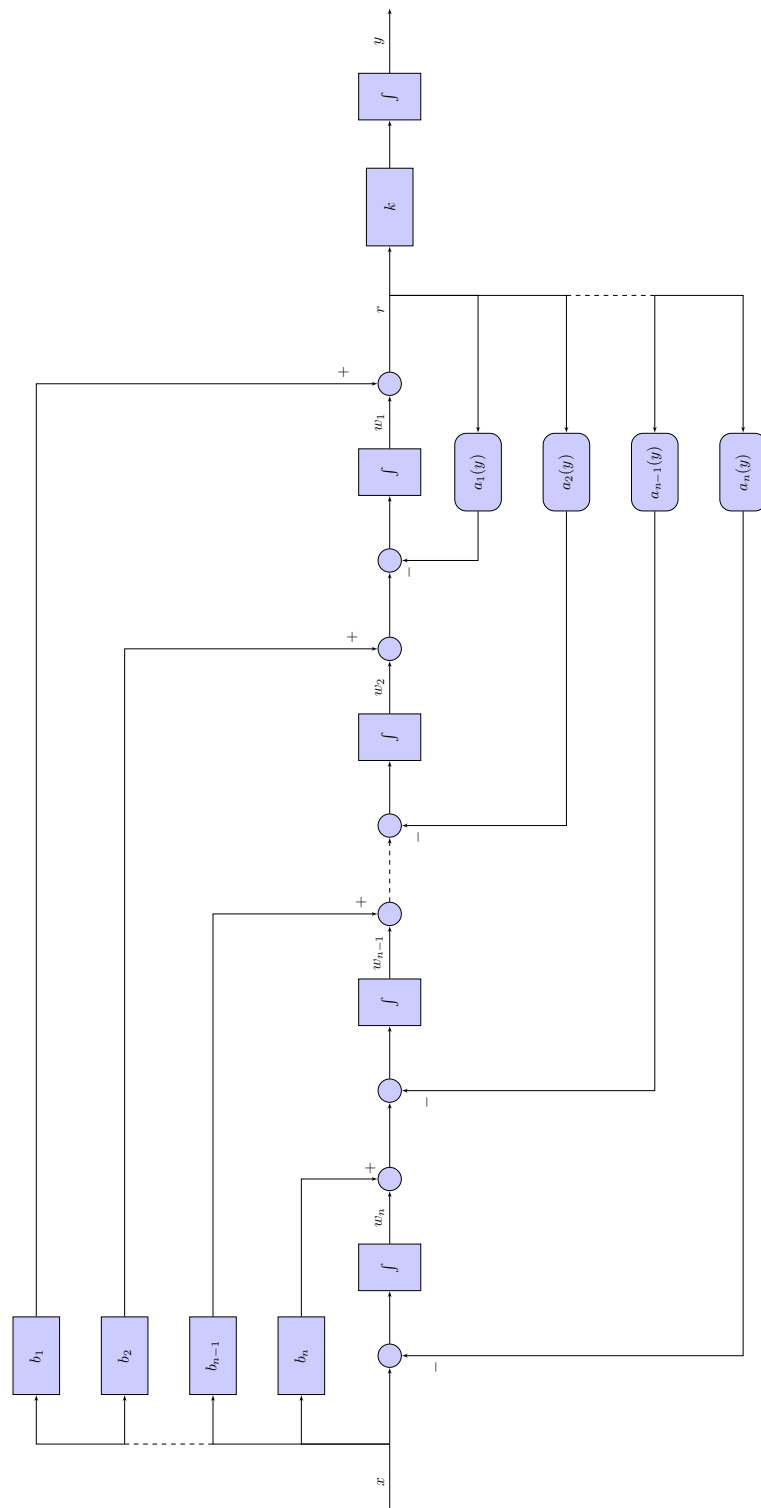


Figure 5.12: Continuous-time implementation of the ELLE condition compensator

5.4.1 Implementation

In the DNV GL Bladed simulation environment, the controller is written in the C programming language as a discrete-time routine. To be implemented in this way, the controller must be rearranged so that there are no algebraic loops present in the system.

There is also a requirement that the controller switches properly between below-rated and above-rated operation and vice versa. When the controller switches to below rated operation, the variable components (indicated in Figure 5.12 by boxes with rounded corners) become constant and the transmittance from x to y becomes unity.

It is a requirement of the realisation shown in Figure 5.12 to have integral action. It is therefore necessary to remove the integrator from the inner controller. As described in Chapter 3, the unmodified inner controller has the form:

$$C_i(s) = \frac{-100(s + a)}{s} \quad (5.23)$$

Removing the integrator from this transfer function would cause the portion of the original inner controller (now without an integrator) to become improper. To ensure that the inner controller is proper in all conditions an additional function, $G_{pre}(s)$, is added between it and the LPV compensator. An appropriate configuration for $G_{pre}(s)$ is shown in (5.24) where ω and ζ are chosen so that the response at lower frequencies are not altered.

$$G_{pre}(s) = \frac{\omega s + \omega^2}{s^2 + 2\zeta\omega s + \omega^2} \quad (5.24)$$

Figure 5.13 shows how the transfer function $G_{pre}(s)$ and the ELLE controller fits into the configuration of the baseline controller as outlined in Chapter 3. Alone, $C_i(s)s$ would be improper because the integrator has been removed to

accommodate the integral action of $GS(s)$. The inclusion of $G_{pre}(s)$ however means that $C_i(s)G_{pre}(s)$ is proper.

When operating below-rated, $GS(s)$ reduces to a pure integrator and the blocks inside the feedback loop previously only occupied by $C_i(s)$ becomes $C_i(s)G_{pre}(s)$. The gains K_o and K_{cp} are calculated from the low frequency gain of $\frac{C_o(s)C_i(s)}{1-C_i(s)}$. Therefore, if $G_{pre}(s)$ is chosen so that the low frequency gain is not changed, then K_o and K_{cp} are also not changed from their baseline values.

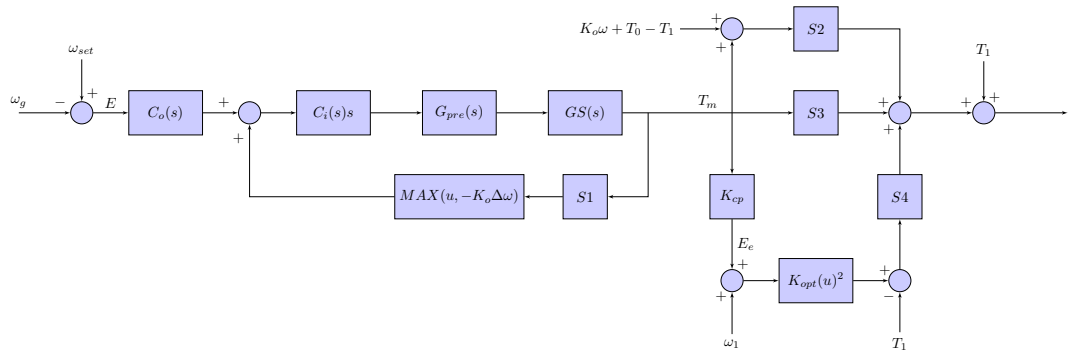


Figure 5.13: Implementation of the ELLE controller in the baseline switching configuration

Additionally, the controller must integrate with the anti-windup loop implemented in the baseline controller. The anti-windup loop prevents the controller from demanding greater blade pitch rates than is achievable. The anti-windup system is discussed in more detail in Section 3.2.5. Implementation of the ELLE controller alongside the anti-windup loop requires that all of the transfer functions in the controller on the direct path between the input and the pitch angle demand are formulated so that they consist of a transfer function, the output of which is solely dependant on the input at the previous time step plus the input at the current time step multiplied by a constant. The formulation of the transfer functions in this way is described in Appendix D.

Rearranging Figure 5.12 to satisfy the above conditions gives Figure 5.14, where T is the time step in seconds. This change is required for implementation

in a discrete-time environment.

The system of equations resulting from Figure 5.14 is (5.25).

$$\begin{bmatrix} t[n] \\ u[n] \\ v[n] \\ w[n] \\ y[n] \end{bmatrix} = \begin{bmatrix} Tx[n-1] - Tc(y[n-1])A + t[n-1] \\ Tx[n-1](b_3 + \frac{T}{2}) + Tt[n-1] - T(b(y[n-1]) + \frac{T}{2}c(y[n-1]))A + u[n-1] \\ Tx[n-1](b_2 + \frac{T}{2}b_3 + \frac{T^2}{4}) + \frac{T^2}{4}t[n-1] + Tu[n-1] - T(a(y[n-1]) + \frac{T}{2}b(y[n-1]) + \frac{T^2}{4}c(y[n-1]))A + v[n-1] \\ TkA + w[n-1] \\ w[n] + \frac{\frac{T}{2}k}{\frac{T}{2}a(y[n]) + \frac{T^2}{4}b(y[n]) + \frac{T^3}{8}c(y[n]) + 1} ((b_1 + \frac{T}{2}b_2 + \frac{T^2}{4}b_3 + \frac{T^3}{8})x[n] + \frac{T^2}{4}t[n] + \frac{T}{2}u[n] + v[n]) \end{bmatrix} \quad (5.25)$$

where:

$$A = \frac{(b_1 + \frac{T}{2}b_2 + \frac{T^2}{4}b_3 + \frac{T^3}{8}b_2)x[n-1] + \frac{T^2}{4}t[n-1] + \frac{T}{2}u[n-1] + v[n-1]}{\frac{T}{2}a(y[n-1]) + \frac{T^2}{4}b(y[n-1]) + \frac{T^3}{8}c(y[n-1]) + 1} \quad (5.26)$$

To calculate the output of the compensator at the current time step a solution for $y[n]$ must be found. This requires that the functions $a(y)$, $b(y)$ and $c(y)$ be linear functions because this only requires a quadratic function to be solved to obtain $y[n]$. If the functions were a higher order, a numerical method would be necessary to solve for y . If a linear approximation for any or all of the three functions was deemed to not be sufficiently accurate, two or more linear function could be switched between using an appropriate value of y as the switching parameter. A hysteresis function may be implemented to avoid chattering across the switch. For the wind turbines considered in this thesis, however, linear functions were found to be adequate.

Testing the Order of the Variable Functions

It is not possible to implement higher order functions for $a(y)$, $b(y)$ and $c(y)$ in a discrete-time environment for the reason outlined above. However, the effect on performance of the order of these functions can be tested in a continuous-time simulation in Simulink. The figures below compare the baseline controller with a

continuous-time implementation of the ELLE controller with $a(y)$, $b(y)$ and $c(y)$ as linear functions and another with quadratic functions. Figures 5.15 and 5.16 show how the linear and quadratic approximations of the variable functions compare to the ideal. The vertical dotted line is the value of y where the controller switches between below-rated and above-rated. For values of y below this, the variable functions are held at constant values.

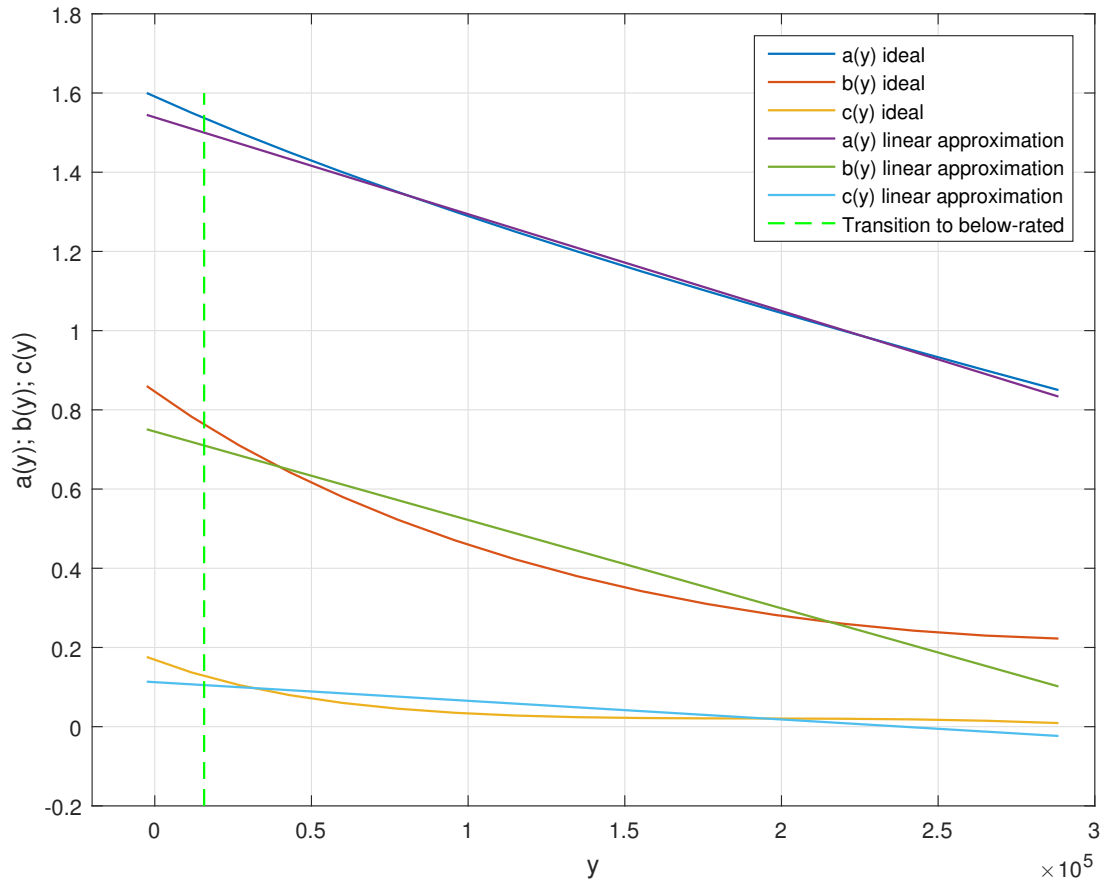


Figure 5.15: Linear approximations for $a(y)$, $b(y)$ and $c(y)$

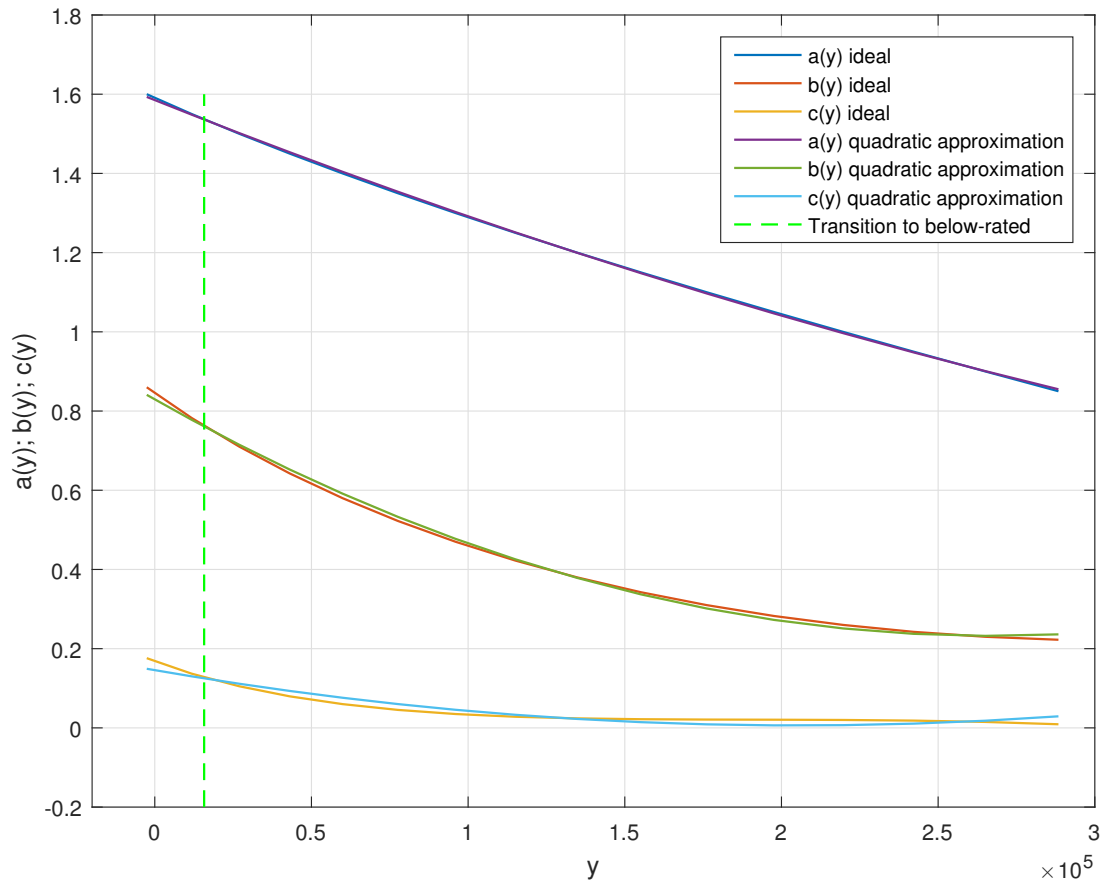


Figure 5.16: quadratic approximations for $a(y)$, $b(y)$ and $c(y)$

Simulations of the 5MW turbine in 16m/s wind with 15% turbulence intensity show a significant drop in the variability of generator speed and power output for both linear and quadratic implementations of the ELLE controller in Figure 5.12. Although the quadratic implementation offers an improvement in performance over the linear implementation, the difference is small. Figure 5.17 shows the generator speed for the baseline and the two ELLE implementations. Figure 5.18 shows the power output for the same simulations. Table 5.3 and Table 5.4 compare the standard deviations for the time series shown in figures 5.15 and 5.16.

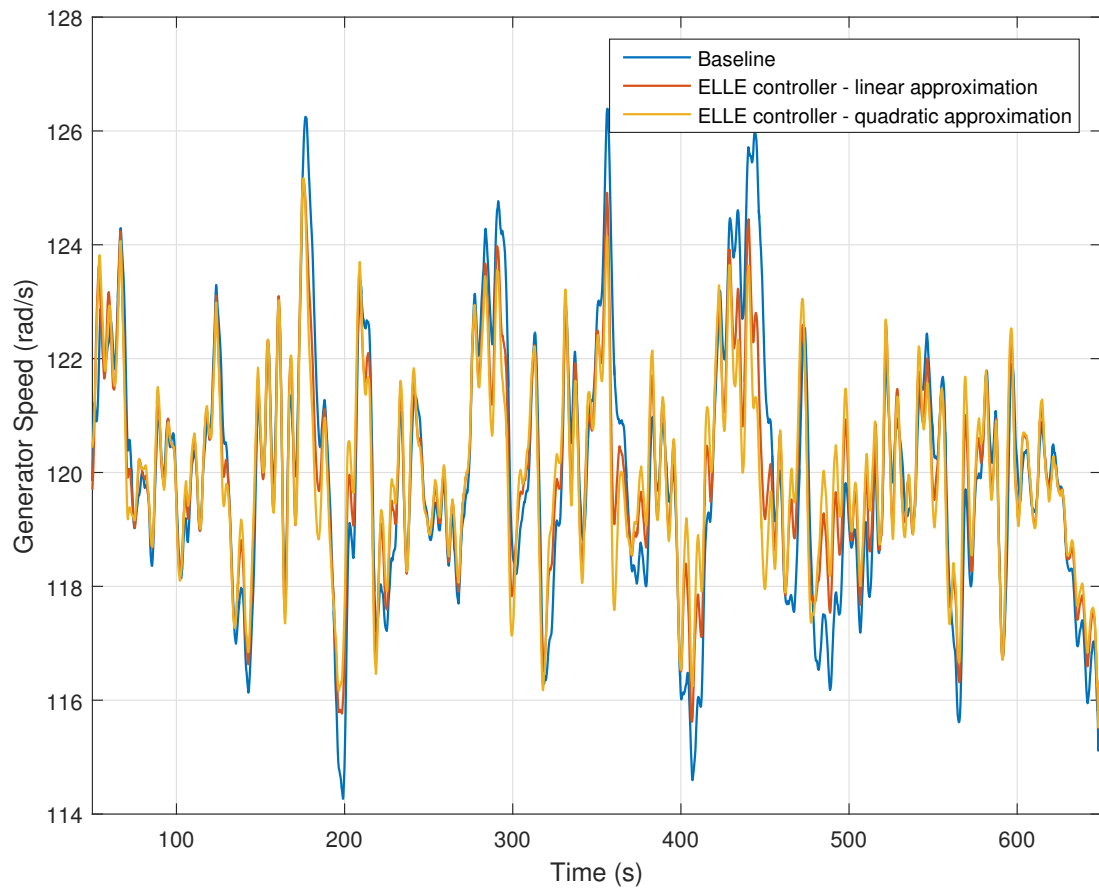


Figure 5.17: Generator speed for the baseline controller and linear and quadratic implementations of the ELLE controller

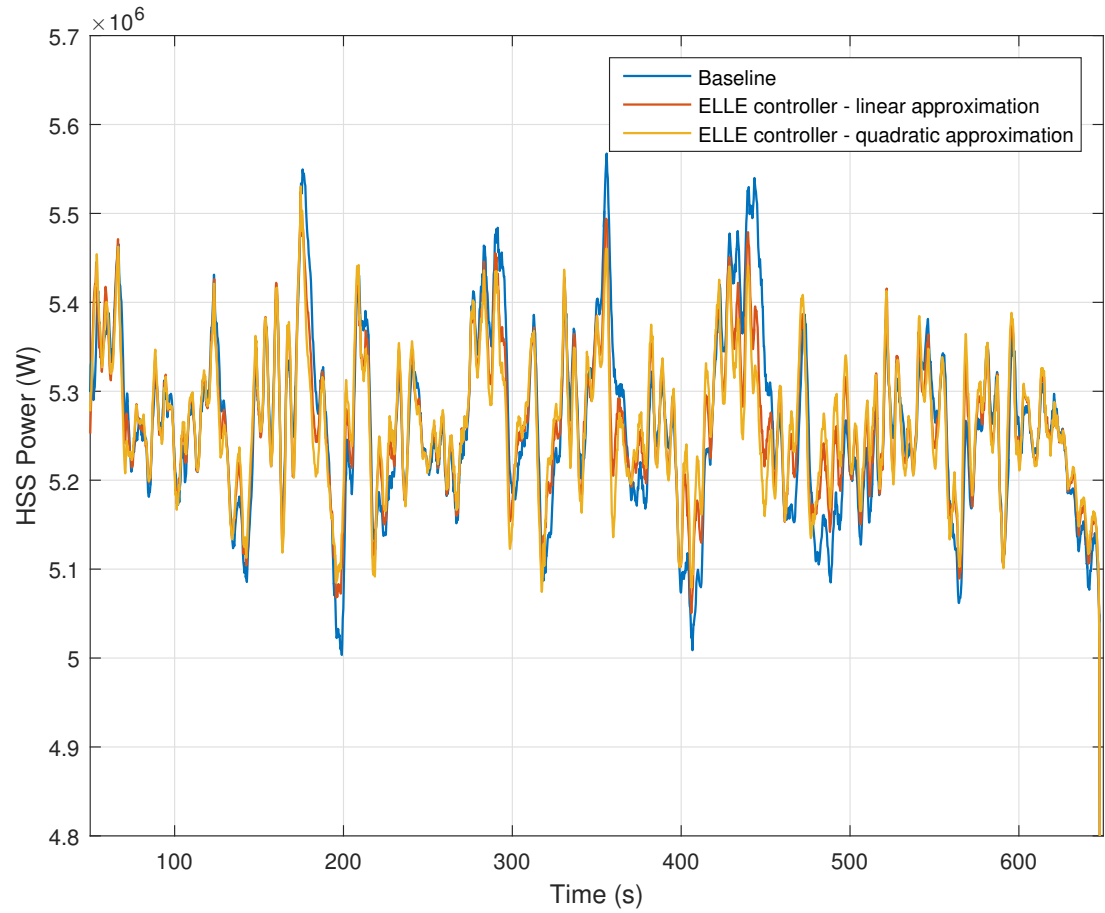


Figure 5.18: HSS power for the baseline controller and linear and quadratic implementations of the ELLE controller

	Standard Deviation	Percentage Difference
Baseline	2.2361	—
Linear approximation	1.7327	22.52%
Quadratic approximation	1.6335	26.95%

Table 5.3: Standard deviations of generator speed for the baseline controller and linear and quadratic implementations of the ELLE controller

	Standard Deviation	Percentage Difference
Baseline	1.0128×10^5	—
Linear approximation	0.7983×10^5	21.18%
Quadratic approximation	0.7593×10^5	25.03%

Table 5.4: Standard deviations of HSS power for the baseline controller and linear and quadratic implementations of the ELLE controller

The tables above show that quadratic approximations for $a(y)$, $b(y)$ and $c(y)$ do offer a small improvement in speed and power control when compared to linear approximations. However, this improvement is small in comparison to the improvement of both over the baseline controller and does not merit the extra complexity that would be required to implement such functions in a discrete-time simulation environment.

Considerations for Implementation in C code

In Chapter 3, the implementation of the switching strategy is described. The inner controller, where the ELLE controller is combined with the existing baseline controller is inside a feedback loop. Therefore, to write a routine in C code to implement the ELLE controller for use in the Bladed simulation environment, specific considerations must be made to ensure this feedback loop functions correctly and the controller can switch between modes properly. The feedback loop is only in use when the controller is operating below-rated and switches based on the output of the inner controller. It is therefore necessary to write the C code in two ‘passes’. The first pass does not contain the variable parts of the LPV controller and is therefore a linear version of the ELLE controller. The output of this pass is used to determine the state of the feedback loop. If the controller is operating above-rated and the feedback loop is inactive, a second pass of the ELLE controller is executed with all the variable parts activated as described in the section preceding this one and the rest of the controller routine is executed

as normal. If the controller is operating below-rated, the feedback loop is active and the a second pass of the ELLE controller is executed where the variable functions are held at their respective below-rated values and the rest of the controller routine is executed as normal.

5MW Implementation

By inspecting linear models of the 5MW turbine for four wind speeds, values for $\alpha(v)$ can be found. Table 5.5 shows the values for $\alpha(v)$ and Table 5.6 shows the polynomials $a(y)$, $b(y)$ and $c(y)$ and the constants b_1 , b_2 , b_3 and k .

Wind Speed (m/s)	$\alpha(v)$ (rad/s)
12	0.063
16	0.182
20	0.366
24	0.602

Table 5.5: Values for α at various wind speeds

$a(y)$	$-1.9965 \times 10^{-6}y + 1.1815$
$b(y)$	$-1.3116 \times 10^{-6}y - 4.1717^{-1}$
$c(y)$	$-1.8505 \times 10^{-7}y + 4.3016^{-2}$
b_1	9.5238
b_2	14.2860
b_3	6.7619
k	0.105.

Table 5.6: Polynomials for the variable components of the compensator

The function, $G_{pre}(s)$, added between the original controller and the compensator is (5.27) for the 5MW turbine.

$$G_{pre}(s) = \frac{18s + 324}{s^2 + 14.4s + 324} \quad (5.27)$$

The effect of the LPV controller can be seen in the Bode plots. With the

baseline controller, shown in Figure 5.19, the gain response for a series of above-rated wind speeds are different at frequencies up to 0.5rad/s. However, the Bode plot for the LPV controller, Figure 5.20, shows all wind speeds have a similar gain response at low frequencies.

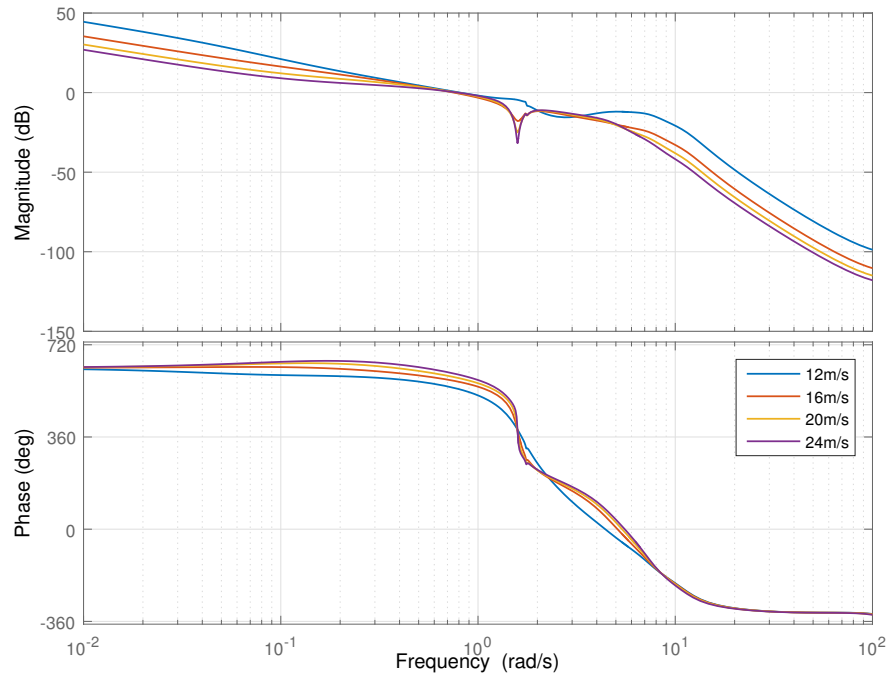


Figure 5.19: Bode plot for the baseline controller at a selection of wind speeds

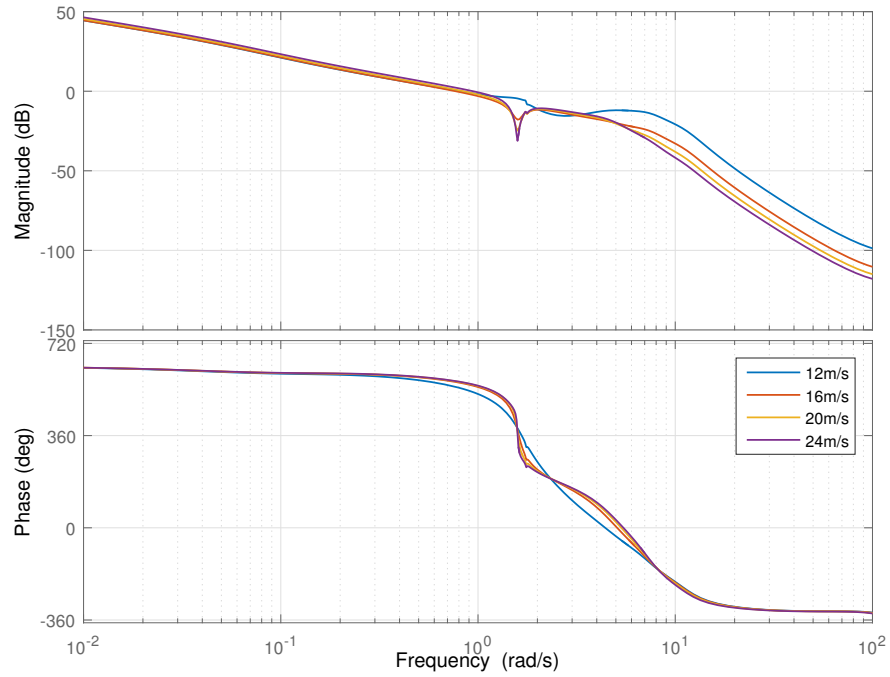


Figure 5.20: Bode plot for the ELLE controller at a selection of wind speeds

Figure 5.21 shows the sensitivity functions for the baseline controller and the gain-scheduled controller operating in a wind speed of 24m/s. If the area between the x-axis (at 0dB) and the gain of the sensitivity function to the left of the gain crossover frequency is indicative of speed control performance, the gain-scheduled controller is better than the baseline at frequencies up to 0.5rad/s.

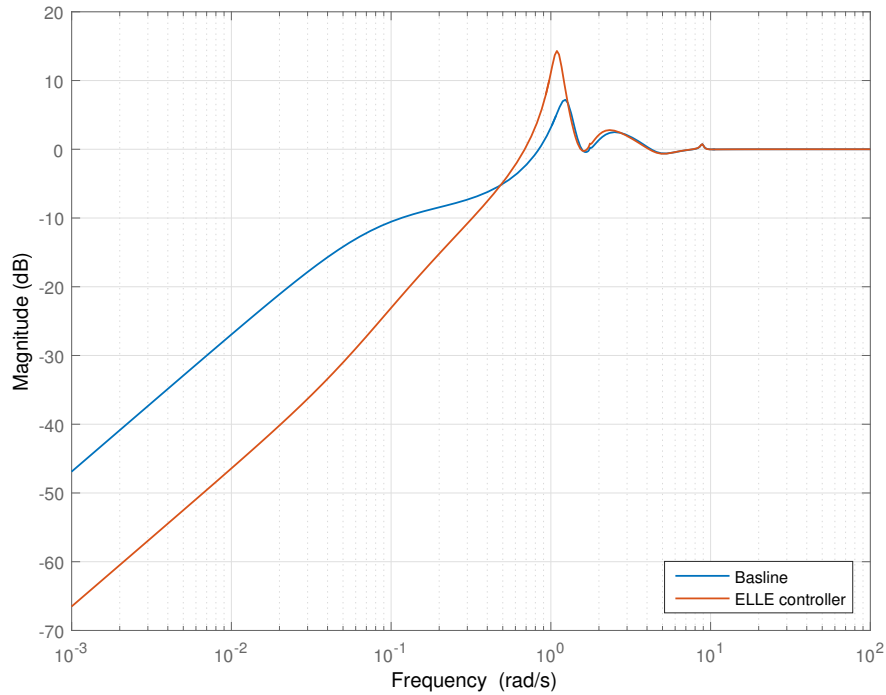


Figure 5.21: Sensitivity functions for the baseline controller and ELLE controller at 24m/s

5.4.2 Simulations

The following figures show the results of simulations of the 5MW turbine operating in a mean wind speed of 16m/s and turbulence intensity of about 15%. With the ELLE controller, the improvements in generator speed control are shown in Figure 5.22. Excursions from the set-point of 120rad/s are decreased across the whole time series. The standard deviation of the generator speed is reduced by 29% from the baseline. Table 5.7 compares the standard deviations of generator speeds for the baseline controller, the simple gain-scheduling realisation and the ELLE controller.

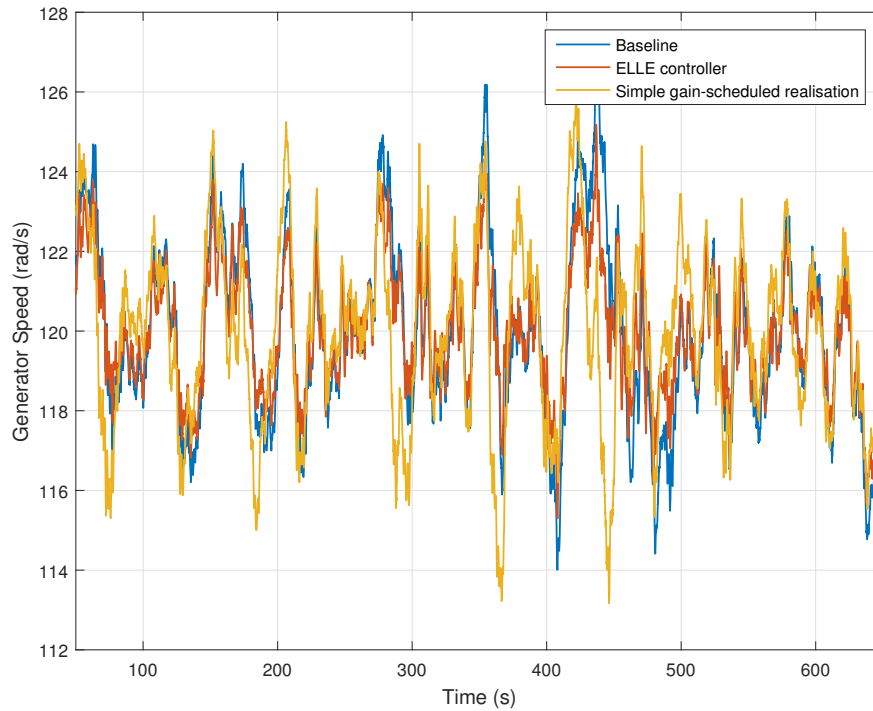


Figure 5.22: Comparison of generator speeds for the baseline controller, the ELLE controller and the simple gain-scheduling realisation

Controller	Std. Dev. of Generator Speed
Baseline	2.2370
Simple Gain-scheduled Realisation	2.2577
ELLE Controller	1.5817

Table 5.7: Standard deviations of generator speed for the baseline controller, the ELLE controller and the simple gain-scheduled controller

The improvements seen in generator speed control are also seen in power output. Figure 5.23 shows a comparison of power output for the baseline controller, the simple gain-scheduling realisation and the ELLE controller. Table 5.8 shows the standard deviations of HSS power for the three controllers.

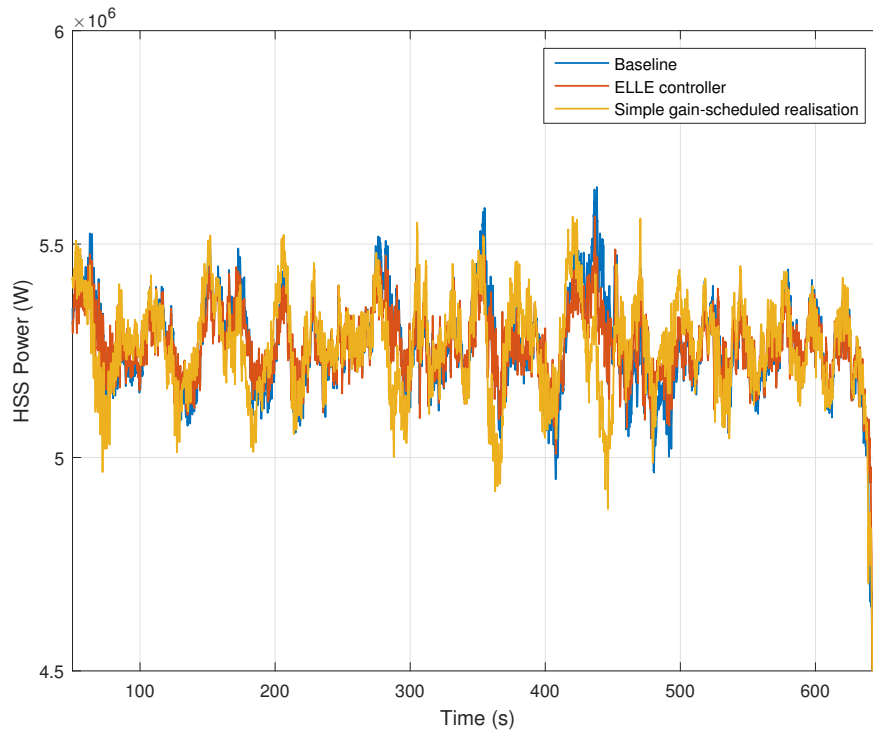


Figure 5.23: Comparison of HSS power for the baseline controller, the ELLE controller and the simple gain-scheduling realisation

Controller	Std. Dev. of HSS Power
Baseline	1.8443×10^5
Simple Gain-scheduled Realisation	1.8726×10^5
ELLE Controller	1.6636×10^5

Table 5.8: Standard deviations of HSS power for the baseline controller, the ELLE controller and the simple gain-scheduled controller

As the sensitivity function in Figure 5.21 shows, the improvements in speed and power control are achieved because the gain of the open-loop system is increased at low frequencies for high wind speeds. This means that pitch activity is increased, as shown by Figure 5.24: the trace for the ELLE controller has

higher peaks and deeper troughs. A consequence of this is an increase in tower loads which can be seen in a plot of the power spectral density of the tower base fore-aft bending moment, Figure 5.25.

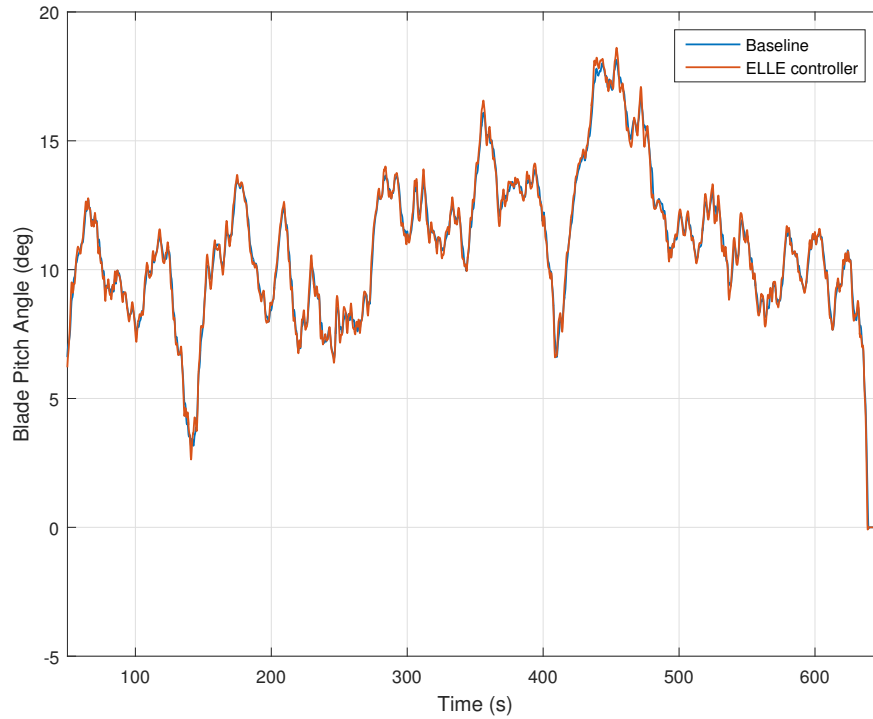


Figure 5.24: Comparison of blade pitch angle for the baseline controller and the ELLE controller

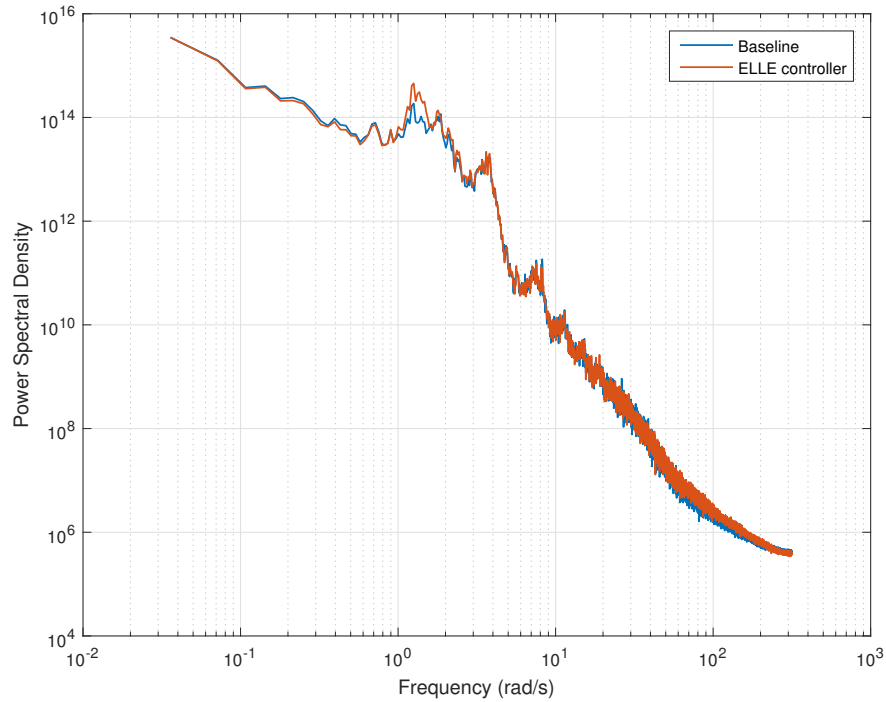


Figure 5.25: Comparison of power spectral densities of the tower base fore-aft bending moment for the baseline controller and the ELLE controller

5.5 Comparison of Turbine Size

The frequency of the variable pole in the plant is driven by the ratio of damping and rotor inertia. As wind turbines increase in size the rotor inertia scales up at a much higher rate than damping. The frequency of the variable pole will therefore reduce as turbine size increases. Table 5.9 show the frequencies for the variable pole at various wind speeds for three sizes of turbine.

Wind Speed (m/s)	5MW $\alpha(v)$ (rad/s)	7.5MW $\alpha(v)$ (rad/s)	10MW $\alpha(v)$ (rad/s)
12	0.063	0.0429	0.0396
16	0.182	0.142	0.118
20	0.366	0.292	0.244
24	0.602	0.489	0.413

Table 5.9: Values for α for three turbines at various wind speeds

In Chapter 4, the effect of turbine size on the achievable gain crossover frequency is discussed. Generally, a larger turbine will have a lower gain crossover frequency. The result of this is that the controller is pulled into operating in a lower range of frequencies where the low-frequency non-linearity is active. Removal of the non-linear effect is therefore more beneficial for these large turbines. Bode plots for a 7.5MW and 10MW turbine are shown in Figure 5.26 and Figure 5.27. In both of these figures, the range of frequencies between the crossover on the right and the non-linearity of the left becomes very small.

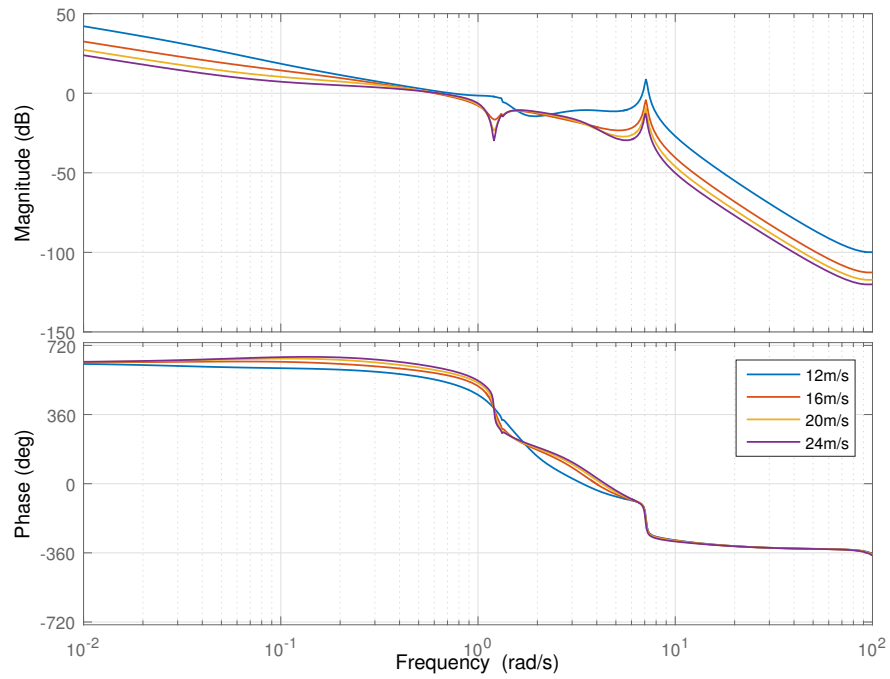


Figure 5.26: Bode plot for the baseline controller at a selection of wind speeds for a 7.5MW turbine

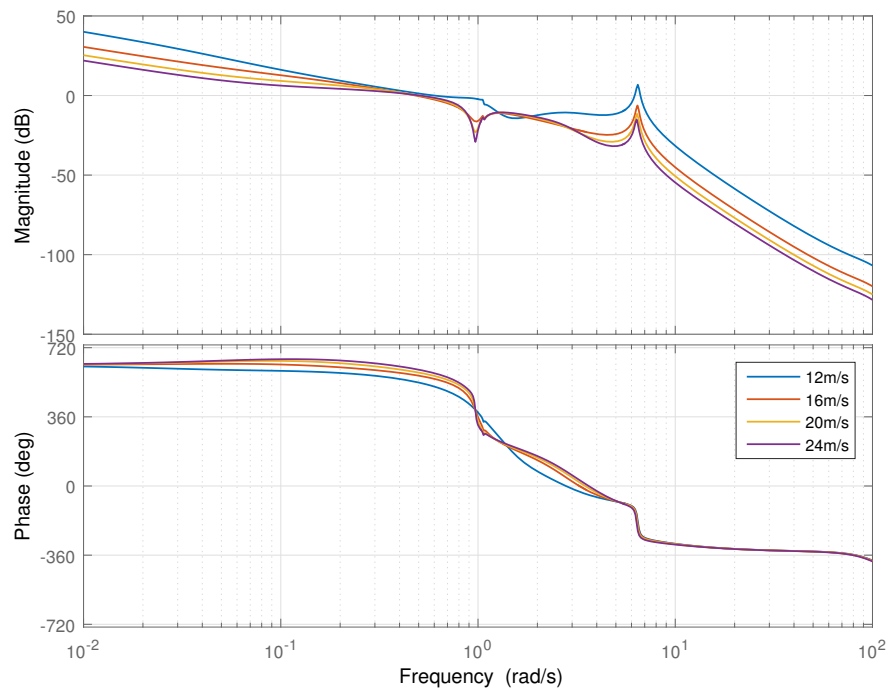


Figure 5.27: Bode plot for the baseline controller at a selection of wind speeds for a 10MW turbine

5.5.1 Simulations

Simulations show a greater improvement in generator speed control as turbine size increases. Figure 5.28 shows the results for the 7.5MW turbine and Figure 5.29 shows the results for the 10MW turbine. The standard deviations of generator speed across three 1500 second simulations for each configuration are shown in Table 5.10 where the difference between the baseline and the ELLE controller increases as turbine size increases.

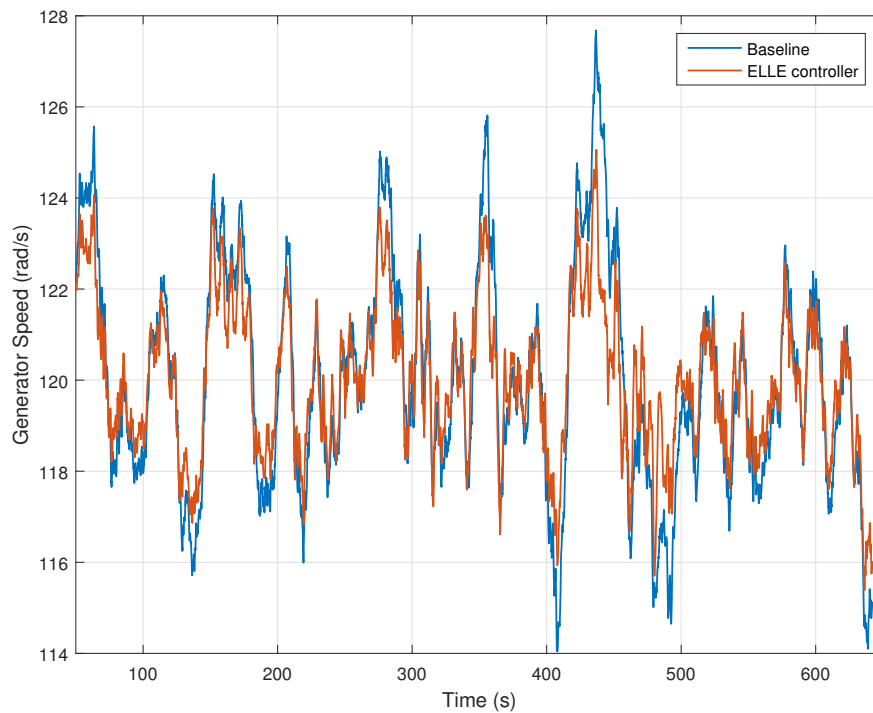


Figure 5.28: Comparison of generator speed for the baseline controller and the ELLE controller for a 7.5MW turbine

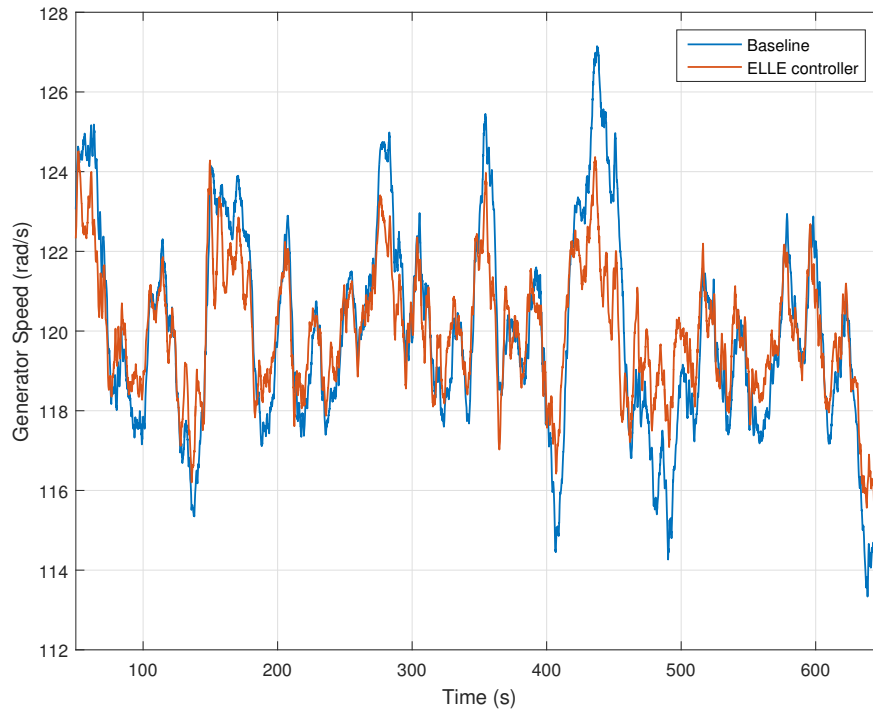


Figure 5.29: Comparison of generator speed for the baseline controller and the ELLE controller for a 10MW turbine

Rated Power (MW)	Baseline	ELLE Controller	Percentage Difference
5	2.2331	1.5941	28.61%
7.5	2.4962	1.6933	32.16%
10	2.6480	1.6385	38.12%

Table 5.10: Standard deviations of generator speed for the baseline controller and the ELLE controller for different sizes of wind turbine at 16m/s

As with the smaller turbines, improvement in speed control also reduces fluctuations in power. Figure 5.30 and Figure 5.31 show the HSS power for a 7.5MW and 10MW turbine in a 16m/s mean wind speed. Table 5.11 shows the standard deviation of HSS power across three 1500 second simulations for each configuration with greater improvement as turbine size increases.

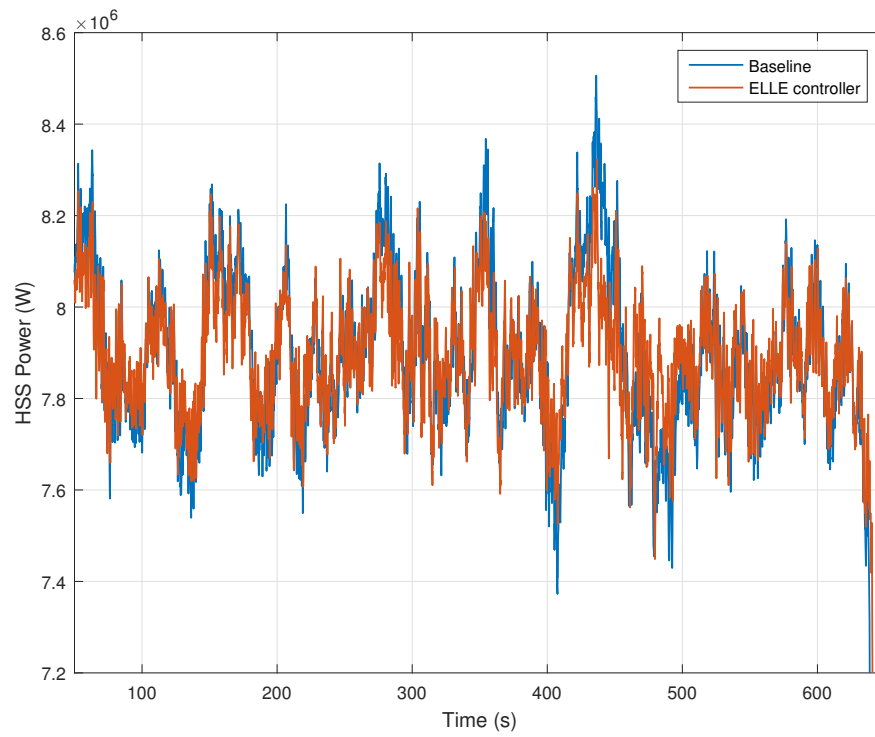


Figure 5.30: Comparison of HSS power for the baseline controller and the ELLE controller for a 7.5MW turbine

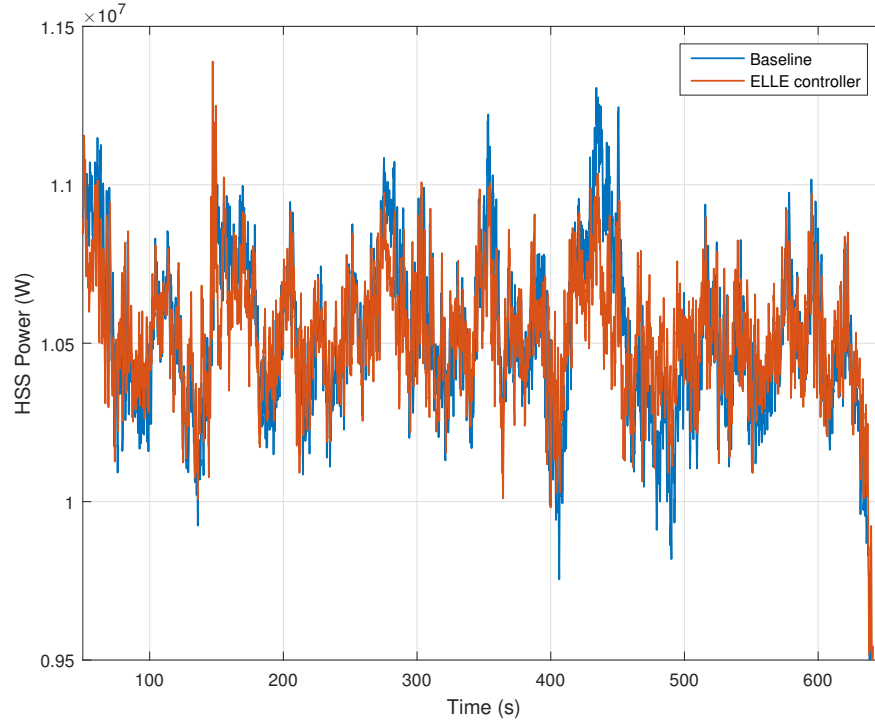


Figure 5.31: Comparison of HSS power for the baseline controller and the ELLE controller for a 10MW turbine

Rated Power (MW)	Baseline	ELLE Controller	Percentage Difference
5	1.8386×10^5	1.7529×10^5	4.66%
7.5	2.9437×10^5	2.7058×10^5	8.08%
10	3.8907×10^5	3.4060×10^5	12.46%

Table 5.11: Standard deviations of HSS power for the baseline controller and the ELLE controller for different sizes of wind turbine at 16m/s

At higher wind speeds, improvements in control of generator speed and HSS power are greater. This is because the frequency of the variable pole in the plant is lower at higher wind speeds and further into the frequency range of the turbulent wind. Table 5.12 and Table 5.13 show standard deviations for generator speed and HSS power for three 1500 second simulations in a turbulent wind with a mean wind speed of 18m/s. For these simulations at a higher wind speed,

greater improvements in speed and power controller can be seen but the greater improvement as size increases.

Rated Power (MW)	Baseline	ELLE Controller	Percentage Difference
5	2.7553	1.7036	38.17%
7.5	3.0684	1.8167	40.79%
10	3.2437	1.7757	45.26%

Table 5.12: Standard deviations of generator speed for the baseline controller and the ELLE controller for different sizes of wind turbine at 18m/s

Rated Power (MW)	Baseline	ELLE Controller	Percentage Difference
5	1.3032×10^5	0.8986×10^5	31.05%
7.5	2.1897×10^5	1.4779×10^5	32.50%
10	3.2378×10^5	2.2186×10^5	31.48%

Table 5.13: Standard deviations of HSS power for the baseline controller and the ELLE controller for different sizes of wind turbine at 18m/s

As with the 5MW turbine, the increase in pitch activity results in an increase in tower loads for the larger turbines too. Figure 5.32 and Figure 5.33 show power spectral density plots for the 7.5MW and 10MW turbines. Across all three sizes of turbine, a small, similarly sized increase in the peak at the tower natural frequency is evident.

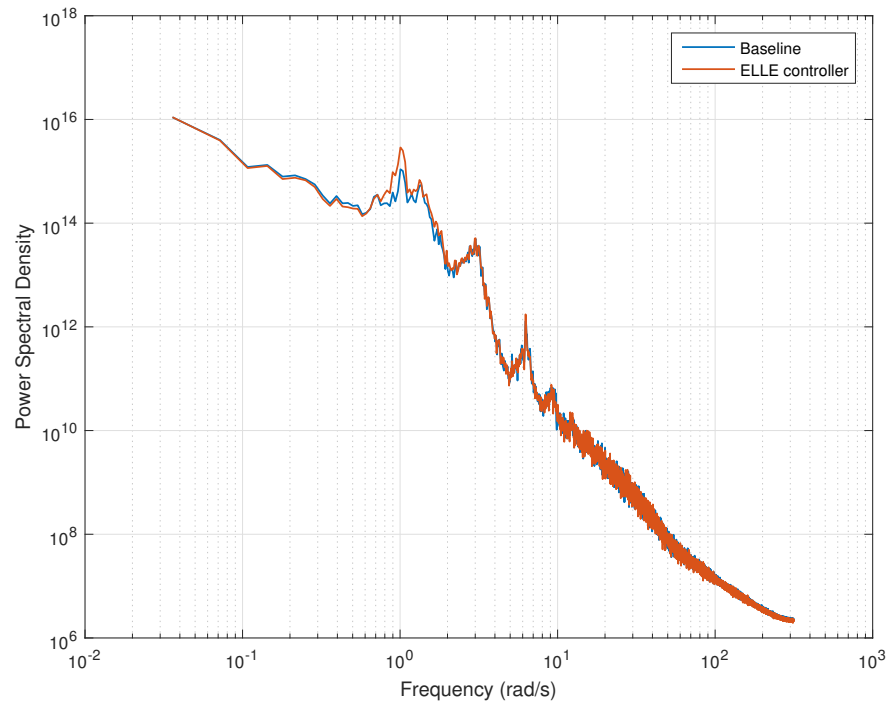


Figure 5.32: Comparison of power spectral densities of the tower base fore-aft bending moment for the baseline controller and the ELLE controller for the 7.5MW turbine

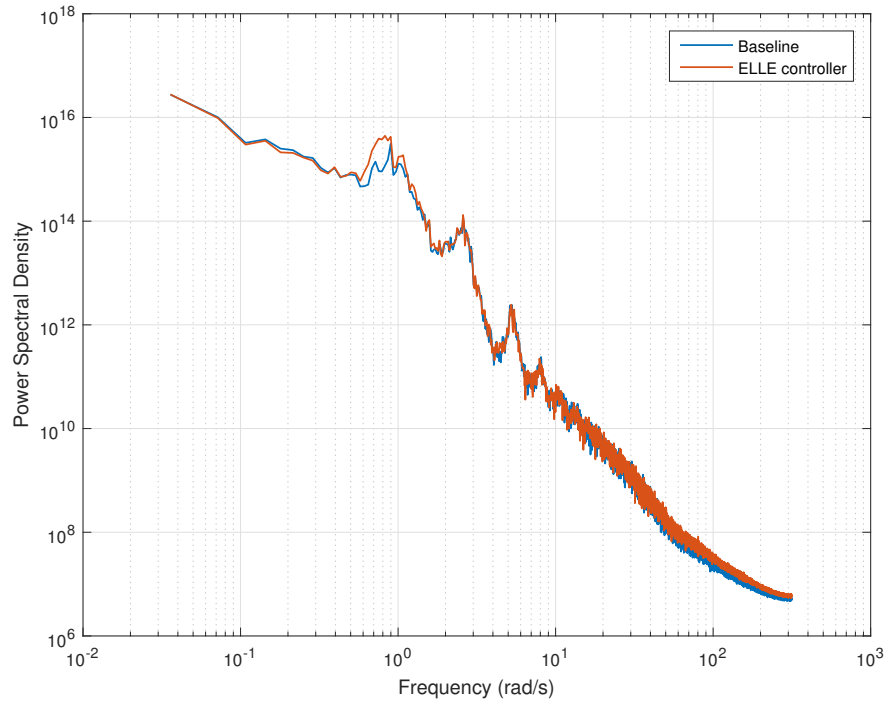


Figure 5.33: Comparison of power spectral densities of the tower base fore-aft bending moment for the baseline controller and the ELLE controller for the 10MW turbine

The levels of damage equivalent loads for the baseline and ELLE controller for all three turbines are shown in Figure 5.34. The plot shows three simulations for each configuration, each with a mean wind speed of 18m/s and IEC class B turbulence. Damage equivalent loads are calculated in the same way as in Chapter 4. The process for this is outlined in Appendix C.

As indicated by time series plots of blade pitch angle and frequency analyses of tower loads, damage equivalent loads are greater with the ELLE controller compared to the baseline.

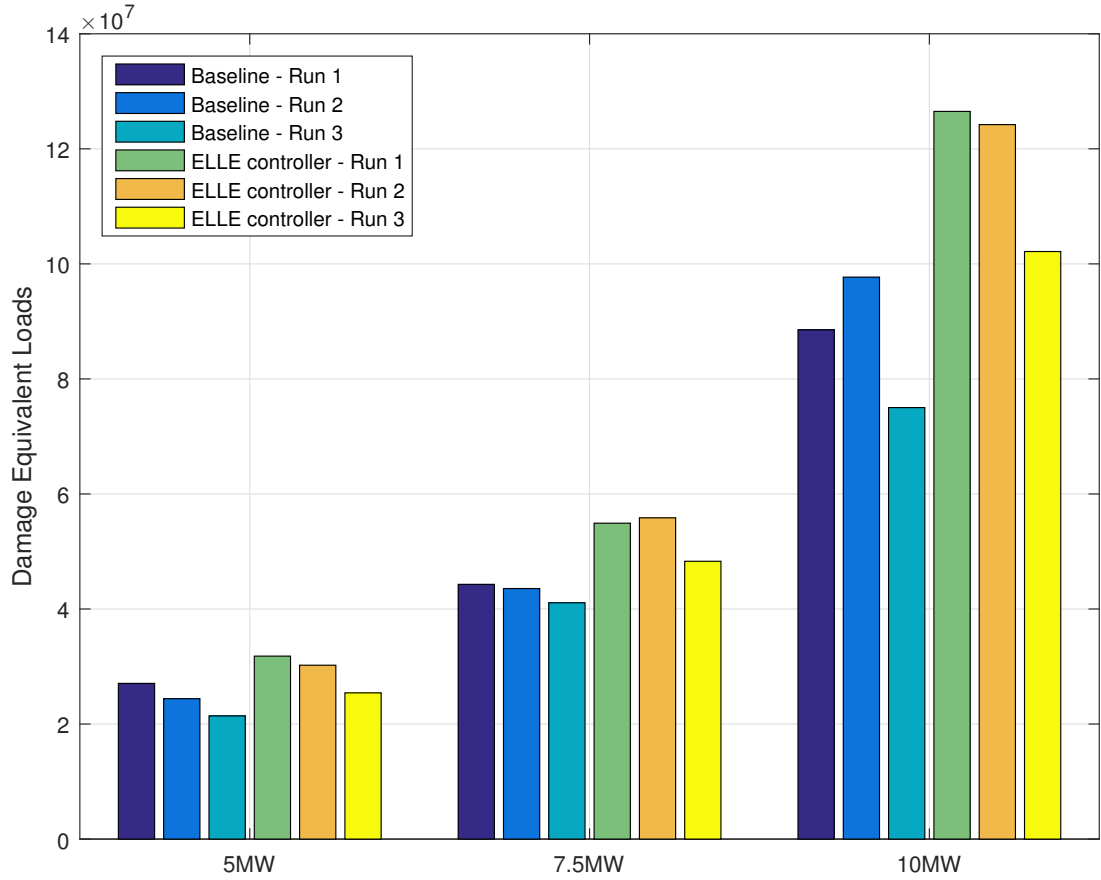


Figure 5.34: Damage equivalent loads at the tower base for the baseline and ELLE controller operating in a turbulent wind with a mean wind speed of 18m/s

Rated Power (MW)	Baseline Controller	ELLE Controller
5.0	2.4297×10^7	2.9153×10^7
7.5	4.2975×10^7	5.3025×10^7
10.0	8.7081×10^7	1.1762×10^8

Table 5.14: Averages of damage equivalent loads across three simulations for the baseline and ELLE controllers

5.6 Concluding Remarks

In this chapter, a controller design is presented which improves the performance of generator speed control by accounting for a non-linearity which is present

in the pitch loop. The realisation of an LPV controller which achieves this is presented with simulations and comparisons to the baseline controller. The affect on performance is demonstrated for a set of differently sized wind turbines.

There is a pole, present in the transmittance from blade pitch angle demand to generator speed, the frequency of which varies with wind speed. To neutralise the effect of this pole on controller performance, a controller with a variable zero to counter the pole could be implemented. Through simulations of such a controller, this chapter shows that the realisation of the LPV controller is important for performance. A controller which satisfies the extended local linear equivalence (ELLE) condition is presented. This requires that the linear equivalent of the controller be an accurate representation of the non-linear system across its whole operating range rather than just in the vicinity of a series of linear approximations. The realisation which satisfies this condition consists of a number of variable poles with corresponding, fixed zeros. Different poles and zeros in the controller cancel each other out, giving the effect of a controller with a variable zero and neutralising the variable pole in the plant.

The controller which satisfies the ELLE condition removes the non-linearity from the controlled system and demonstrates a significant reductions in generator speed and power output fluctuations when operating at high wind speeds. Because of the nature of the non linearity, the improvements of the ELLE controller are especially significant for very large wind turbines. The frequency of the variable pole and the impact of the dynamics of the tower on the control design mean that greater improvements in performance are seen as turbine size increases.

Chapter 6

Mitigating the Restrictions of Wind Turbine Size

In Chapter 4 the effect of the wind turbine tower and the associated non-minimum phase dynamics on controller performance and stability is discussed. In Chapter 5, the non-linearity present at low frequency in the pitch control dynamics is shown to negatively effect controller performance, especially in larger turbines. Both of the issues discussed in these chapters limit controller performance if left unaddressed. The right-half-plane zeros linked to the tower natural frequency put an upper limit on the achievable gain crossover frequency and the non-linearity in the pitch control dynamics reduces performance in the lower frequency range. As wind turbines increase in size, both of these effects worsen. The natural frequency of the tower decreases and pushes the gain crossover frequency lower and the controller is forced to operate in frequency ranges effected by the low-frequency non-linearity.

In this chapter the controller designs presented in Chapter 4 and Chapter 5 are combined. The stability and performance of the resulting controller design is thereby much less sensitive to the effects of turbine size.

6.1 Controller Design

The improved power coordinated controller (IPCC) and the extended local linear equivalence (ELLE) controller both fit into the structure of the baseline controller without interfering with each other. Figure 6.1 shows a block diagram with both of these components in the baseline controller structure. The implementation of the ELLE controller is as in Section 5.4.1 and Figure 5.13. The IPCC is implemented as in Section 4.3 and K_{cc} is the additional gain as described in Section 4.4.

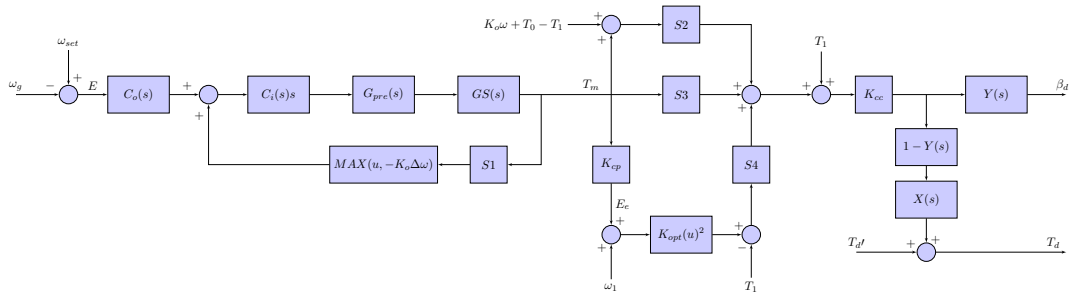


Figure 6.1: Block diagram of the baseline controller structure with the IPCC and ELLE controller implemented

The bode plot representing the block diagram in Figure 6.1 is shown in Figure 6.2 with the IPCC and the ELLE controller. The removal of the right-half plane zeroes from the system can be seen in the phase properties. The effect of the ELLE controller can also be seen in the gain response at low frequencies. The effect of the ELLE controller is better seen in the sensitivity function, shown in Figure 6.3. The area between the x-axis and the line is indicative of speed control in general as well how well the controller can reject the disturbance of wind events such as a coherent gust across the rotor.

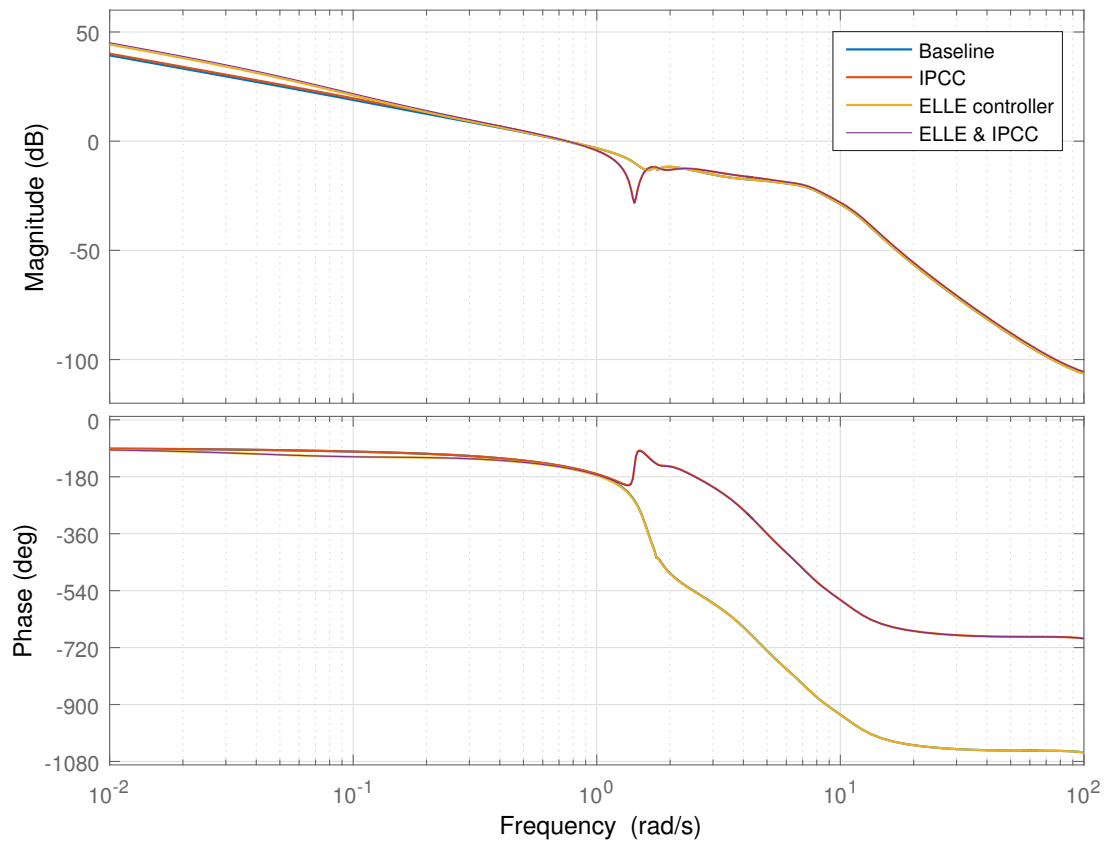


Figure 6.2: Bode plot showing the baseline controller with the IPCC, ELLE controller, and the IPCC & ELLE combined

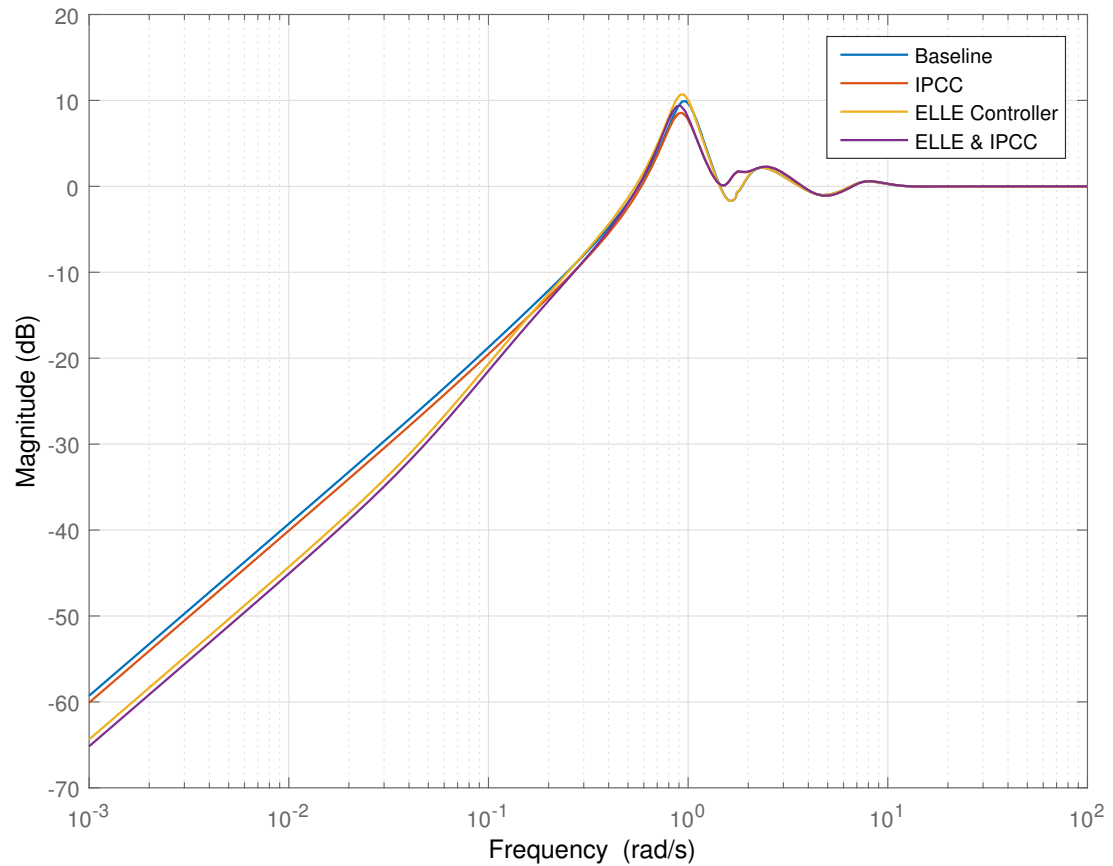


Figure 6.3: Sensitivity function of the baseline controller with the IPCC, ELLE controller, and the IPCC & ELLE combined

The improvements over the baseline are more apparent at higher wind speeds. Where the figures above represent the linearised system operating in a wind speed of 14m/s, Figure 6.4 shows the sensitivity functions for the four controller configurations operating in a wind speed of 22m/s.

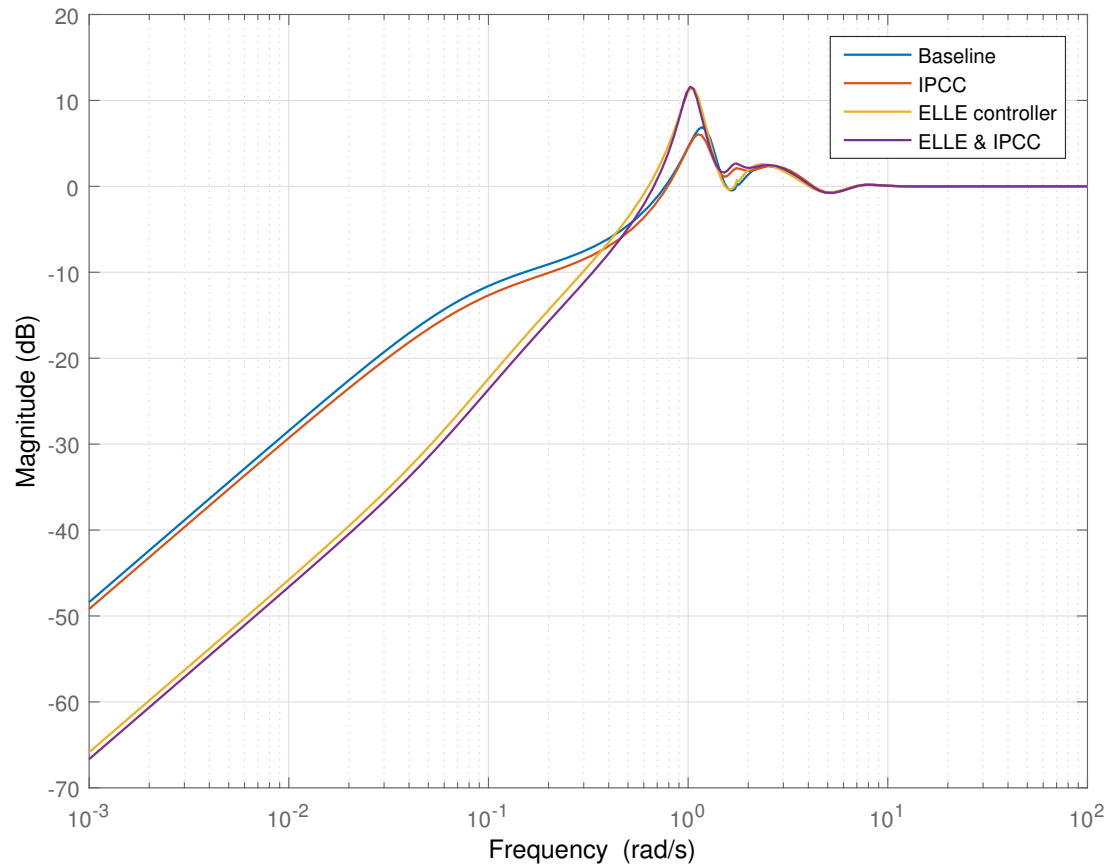


Figure 6.4: Sensitivity function of the baseline controller with the IPCC, ELLE controller, and the IPCC & ELLE combined for the 5MW turbine

As turbines increase in size, the improvements which can be seen in Figure 6.4 are greater. Figures 6.5 and 6.6 show equivalent sensitivity functions for a 7.5MW and 10MW turbine operating in a 22m/s wind speed. The IPCC allows for a greater increase in gain crossover frequency from the baseline controller as turbine size increases. Also, the ELLE controller improves the gain response over a greater range of frequencies when applied to larger turbines. Both of these positive effects are combined when the IPCC and ELLE controller are used together.

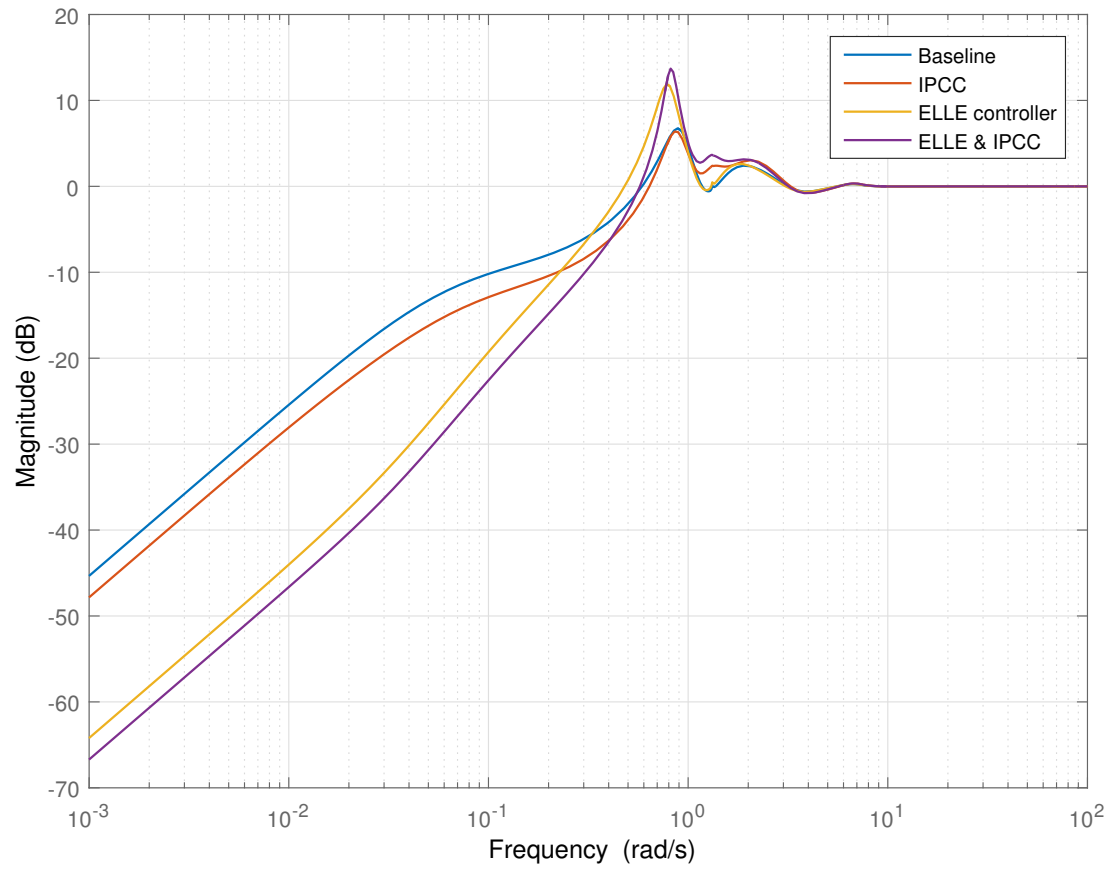


Figure 6.5: Sensitivity function of the baseline controller with the IPCC, ELLE controller, and the IPCC & ELLE combined for the 7.5MW turbine

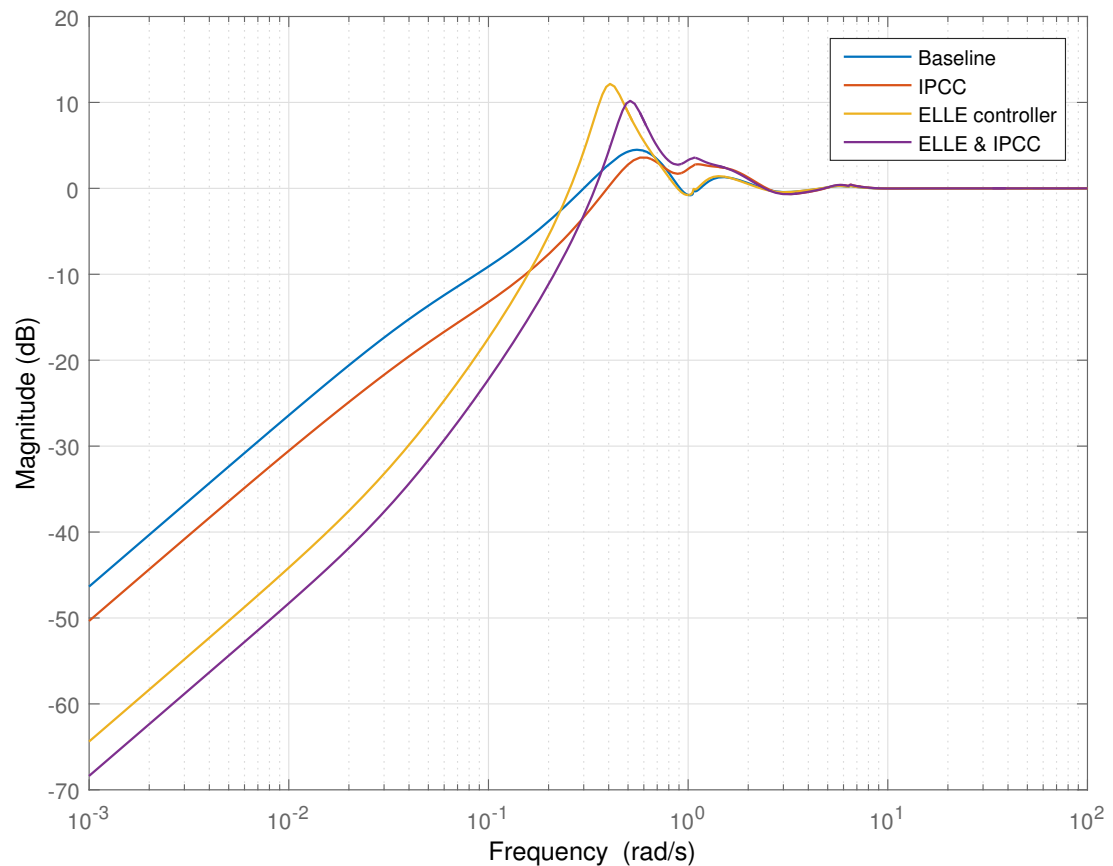


Figure 6.6: Sensitivity function of the baseline controller with the IPCC, ELLE controller, and the IPCC & ELLE combined for the 10MW turbine

6.2 Simulations

In this section, simulations demonstrating the operation of the wind turbine with the IPCC and ELLE controller combined are presented. The effect of the combined controller on speed and power control is presented for a 5MW, 7.5MW and 10MW wind turbine as well as an assessment of the effect of the new controller on loads. The controller is also shown to perform appropriately when switching between below-rated and above-rated operating modes. Finally, the controller function to deal with actuator saturation is demonstrated.

6.2.1 Performance

As with the results when the IPCC and ELLE controller are applied individually, simulations of the combined controller show a significant reduction in excursions from the desired values for both generator speed and mechanical power at the generator.

When applied without the ELLE controller, the IPCC results in a slight increase in excursions from the set point in generator speed as shown in Chapter 4. Conversely, as shown in Chapter 5, the ELLE controller greatly reduces these excursions. When combined, the IPCC and ELLE controller together demonstrate a reduction in the standard deviation of generator speed. With the IPCC alone, the increase in standard deviation of generator speed decreases as turbine size increases because the scope for increasing the overall gain also increases. Similarly, with the ELLE controller alone, the decrease in standard deviation of generator speed is greater as turbine size increases. For simulations of the combined controller, a reduction in standard deviation of generator speed is also seen. Table 6.1 shows the standard deviations of generator speed for the 5MW, 7.5MW and 10MW turbines for the baseline and combined controller. Due to sections of the simulations at this wind speed entering the below-rated operating mode and the controller therefore allowing the generator speed to vary, some sections of data were excluded from the calculation of the results in this table. The data presented is an average of three simulations with different random number seeds for generating turbulent wind fields. Figures 6.7, 6.8 and 6.9 show plots of generator speed against time for the baseline and combined controllers in a mean wind speed of 16m/s.

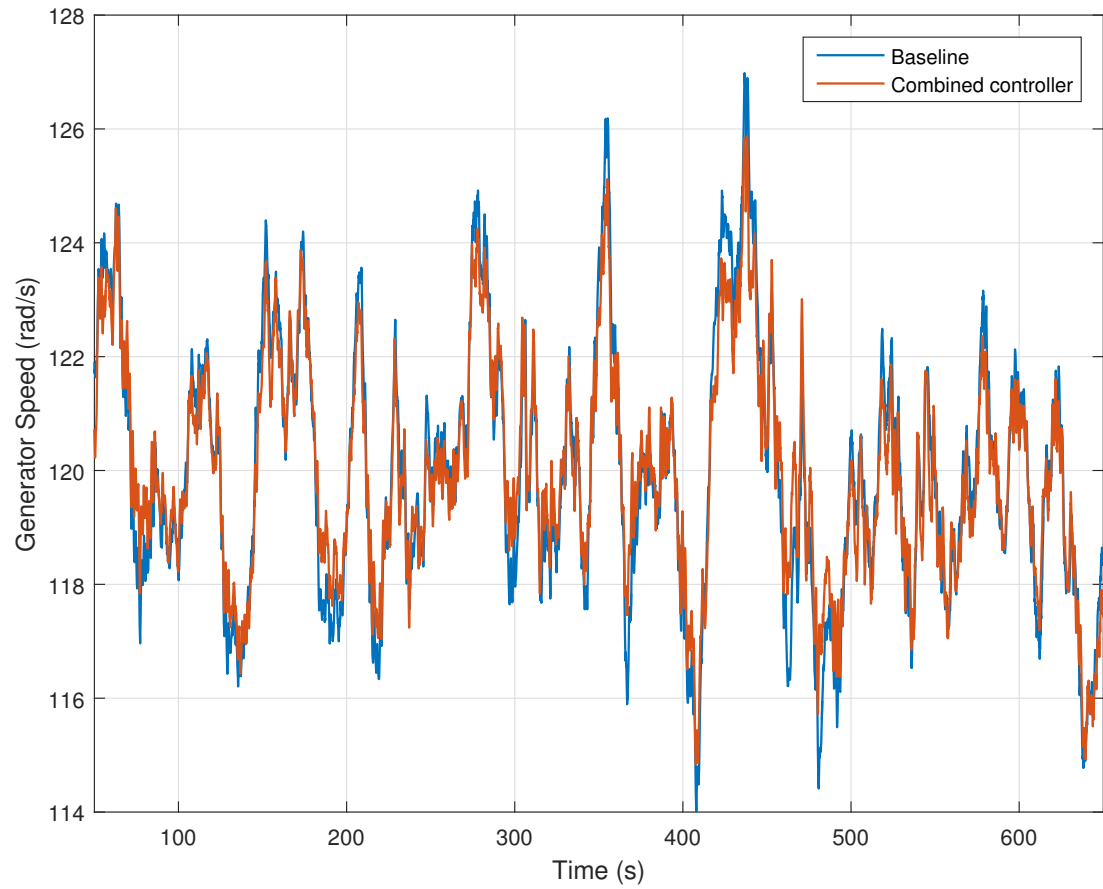


Figure 6.7: Generator speed for the 5MW turbine with the baseline controller and combined controller in 16m/s mean wind speed

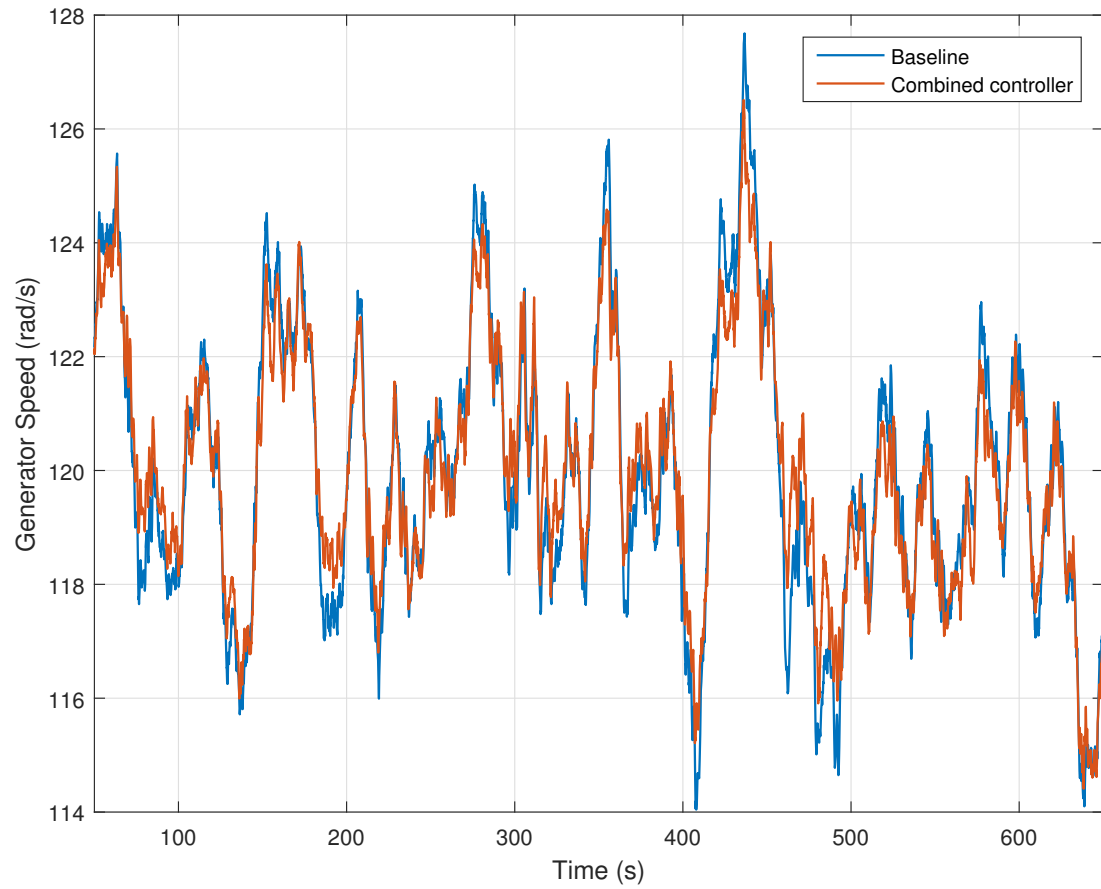


Figure 6.8: Generator speed for the 7.5MW turbine with the baseline controller and combined controller in 16m/s mean wind speed

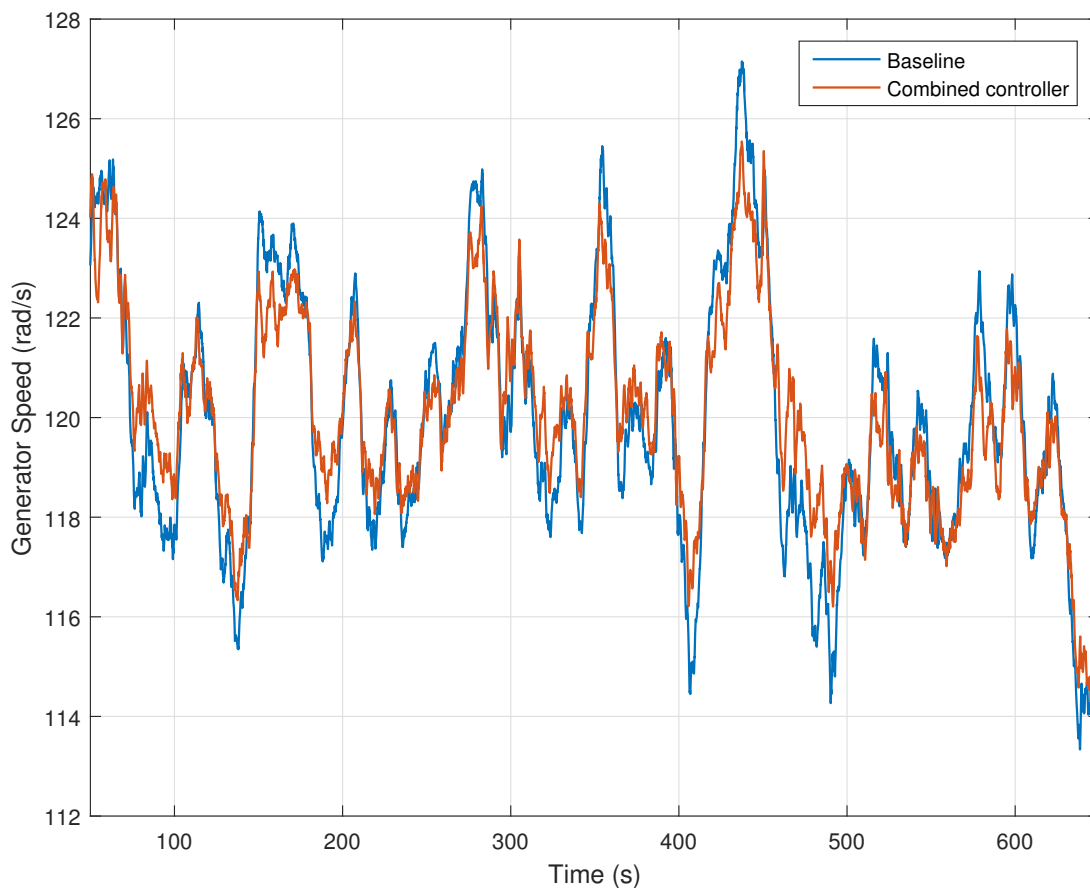


Figure 6.9: Generator speed for the 10MW with the baseline controller and combined controller in 16m/s mean wind speed

Rated Power (MW)	Baseline	Combined Controller	Percentage Difference
5	2.3398	1.9003	18.78%
7.5	2.6160	2.1012	19.68%
10	2.7936	2.0029	28.30%

Table 6.1: Standard deviations of generator speed for the baseline controller and the combined controller for different sizes of wind turbine at 16m/s

Individually, both the IPCC and ELLE controller results in a marked decrease in excursions from the set point in mechanical power at the generator. The combined controller demonstrates significant reductions in the standard deviation of mechanical power ranging from about 30% for the 5MW turbine to about 37%

for the 10MW turbine. As with generator speed, the improvements are greater as turbine size increases. Figures 6.10, 6.11 and 6.12 show time series plots of mechanical power at the generator for the 5MW, 7.5MW and 10MW turbines in a 16m/s mean wind speed. Table 6.2 shows the standard deviations and percentage changes for the three sizes of turbine.

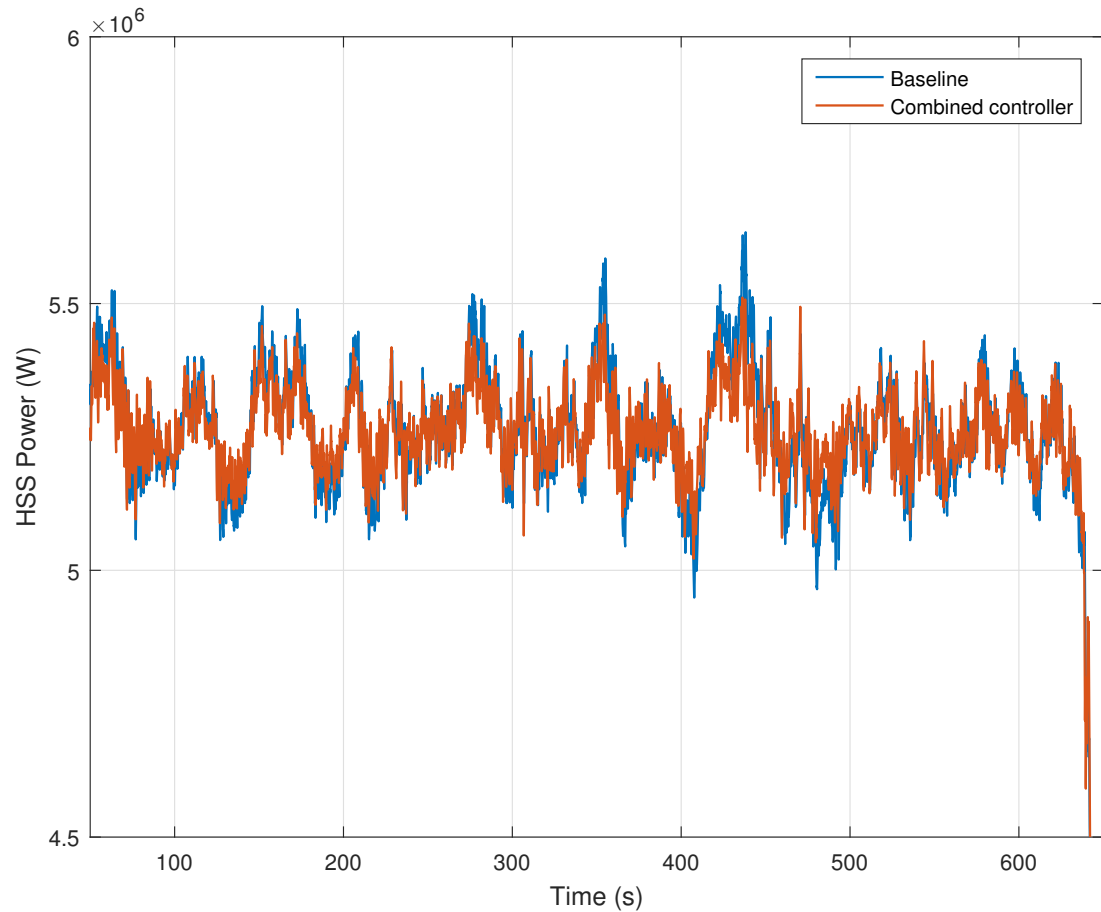


Figure 6.10: Mechanical power at the generator for the 5MW turbine with the baseline controller and combined controller in 16m/s mean wind speed

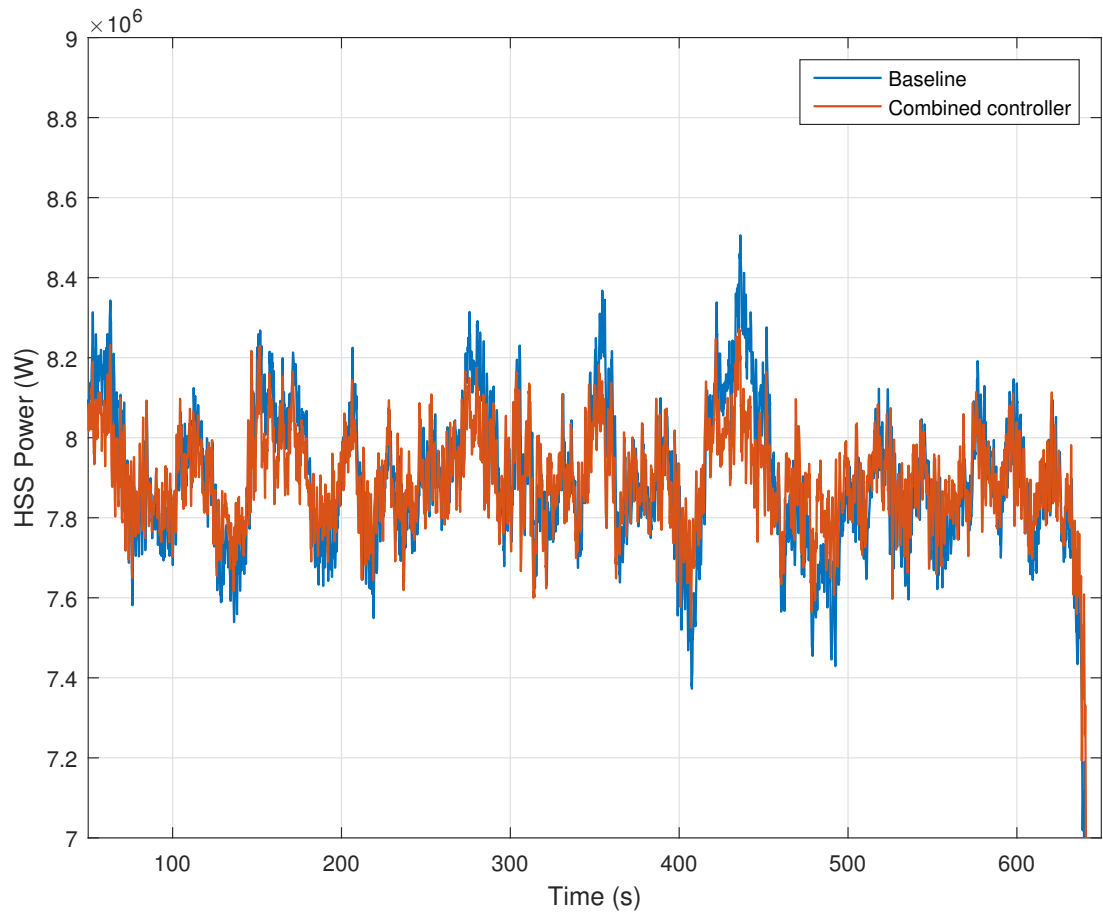


Figure 6.11: Mechanical power at the generator for the 7.5MW turbine with the baseline controller and combined controller in 16m/s mean wind speed

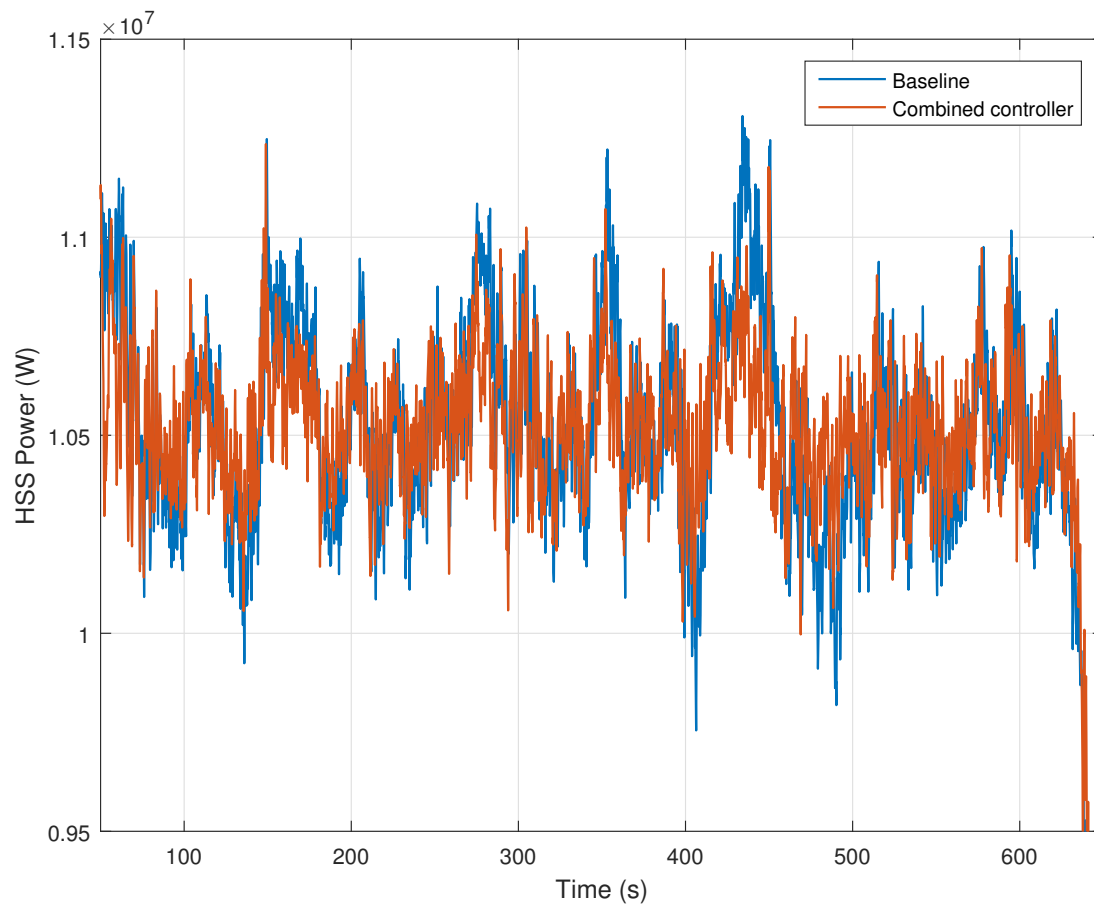


Figure 6.12: Mechanical power at the generator for the 10MW turbine with the baseline controller and combined controller in 16m/s mean wind speed

Rated Power (MW)	Baseline	Combined Controller	Percentage Difference
5	1.1055×10^5	0.7712×10^5	30.24%
7.5	1.8608×10^5	1.1962×10^5	35.71%
10	2.7637×10^5	1.7456×10^5	36.84%

Table 6.2: Standard deviations of mechanical power at the generator for the baseline controller and the combined controller for different sizes of wind turbine at 16m/s

6.2.2 Structural Loads

Tower Base Bending Moments

A comparison of damage equivalent loads with the baseline and combined controllers is shown in Figure 6.13 and Table 6.3. Three different simulations are shown for each controller configuration, all with a mean wind speed of 18m/s.

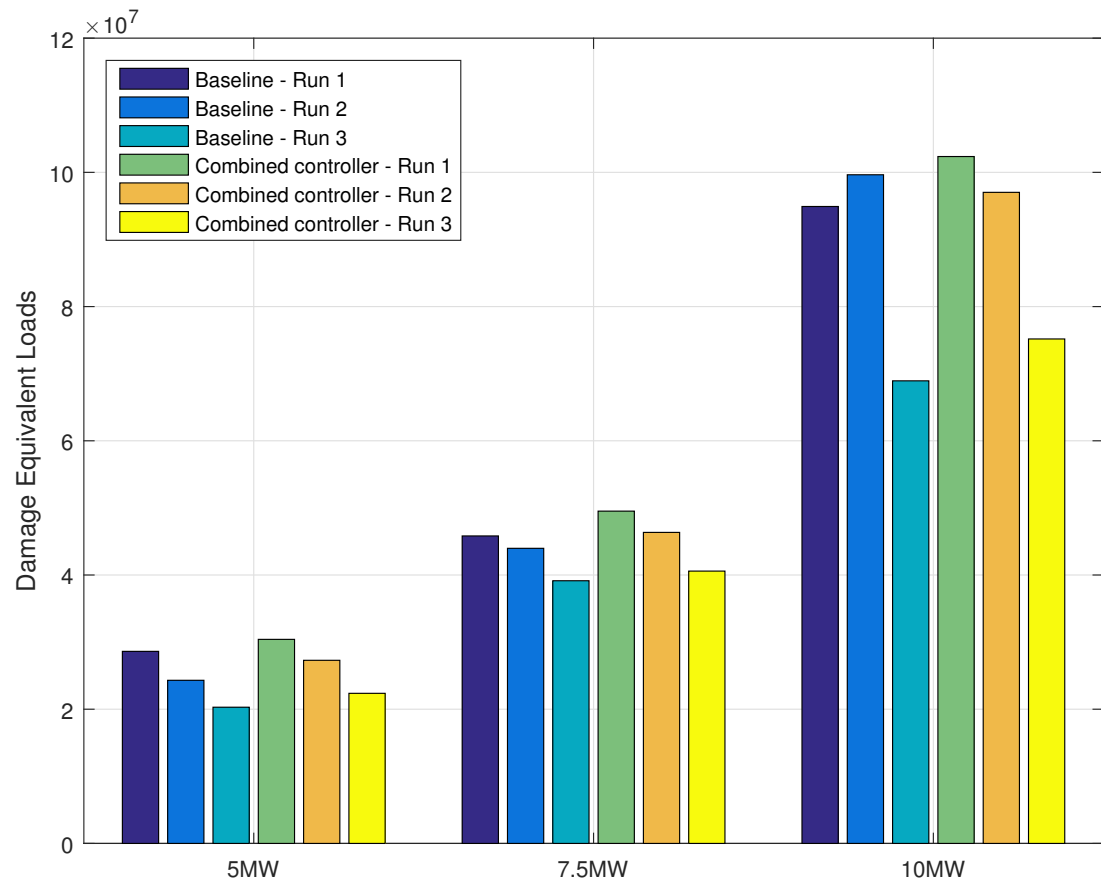


Figure 6.13: Damage equivalent loads at the tower base with the baseline and combined controllers operating in a turbulent wind with a mean wind speed of 18m/s

Rated Power (MW)	Baseline Controller	Combined Controller
5.0	2.4411×10^7	2.6689×10^7
7.5	4.2982×10^7	4.5483×10^7
10.0	8.7831×10^7	9.1518×10^7

Table 6.3: Averages of damage equivalent loads at the tower base across three simulations for the baseline and combined controllers

Individually, the IPCC decreases and ELLE controller increases the damage equivalent loads at the tower base. With the combined controller, the increase in damage equivalent loads over the baseline is much less than with the ELLE controller alone and only slightly greater than the IPCC alone. Table 6.4 compares the values for the percentage change in damage equivalent loads for the different controller configurations. A positive number indicates a decrease in damage equivalent loads.

Rated Power (MW)	IPCC	ELLE Controller	Combined Controller
5.0	3.18%	-19.98%	-9.33%
7.5	5.62%	-19.95%	-5.82%
10.0	10.80%	-29.39%	-4.20%

Table 6.4: Comparison of percentage changes in damage equivalent loads for different controller configurations

Comparing plots of the power spectral densities for the baseline controller and the combined controller, an increase in the size of the peak at the tower frequency is visible. However, if the combined controller is compared to the ELLE controller, there is a reduction in the size of the peak. Figure 6.14 shows the comparison of the baseline and the combined controller and Figure 6.15 shows the comparison of the ELLE controller and the combined controller.

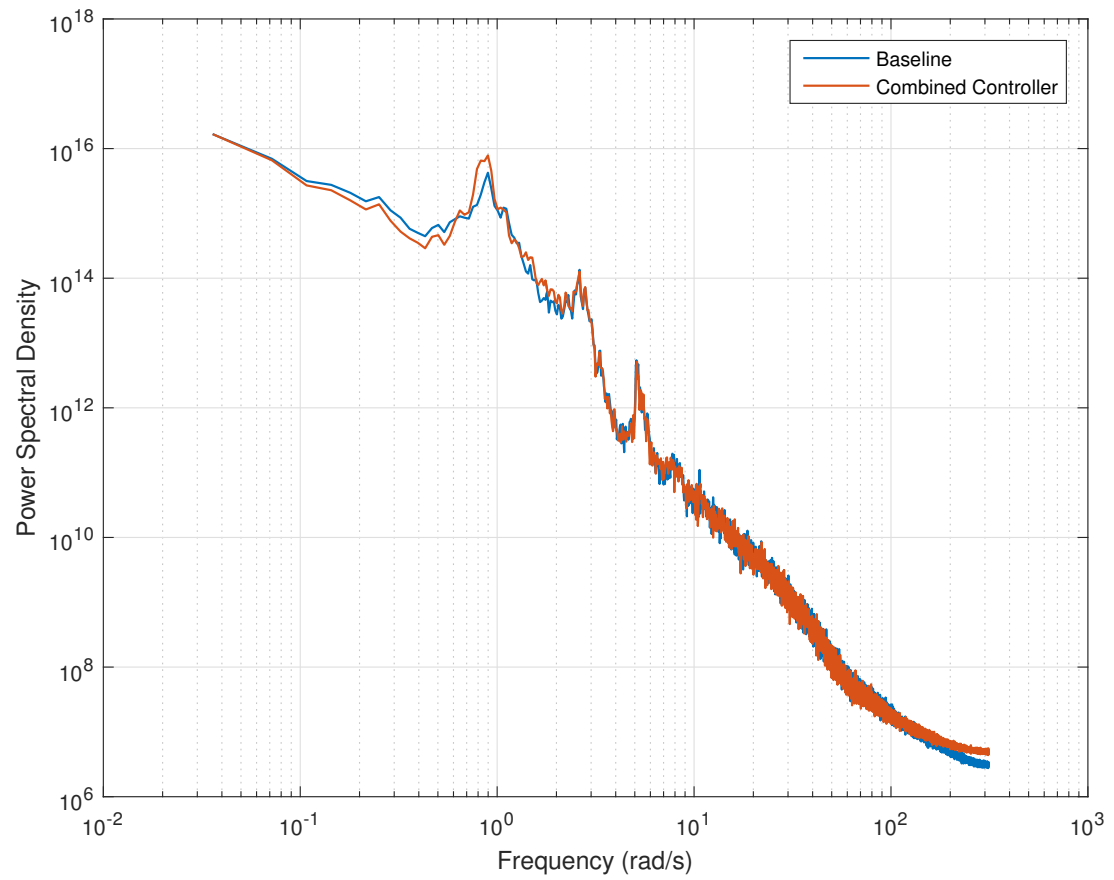


Figure 6.14: Comparison of power spectral densities of the tower base fore-aft bending moment with the baseline and combined controllers for the 5MW turbine in 18m/s mean wind speed

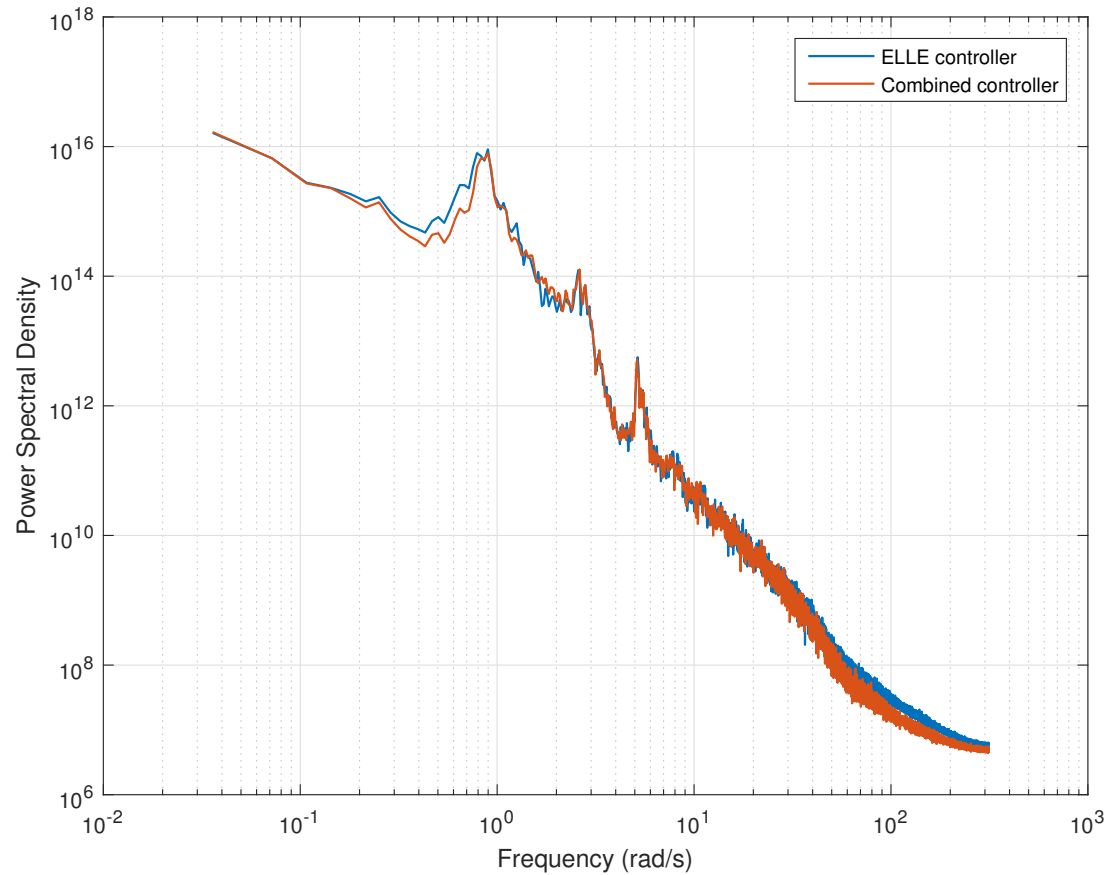


Figure 6.15: Comparison of power spectral densities of the tower base fore-aft bending moment with the ELLE and combined controllers for the 5MW turbine in 18m/s mean wind speed

The change to the power spectral density plot made by the combined controller seen in the 5MW turbine is reflected in the 7.5MW and 10MW turbines, shown in Figure 6.16 and Figure 6.17 respectively.

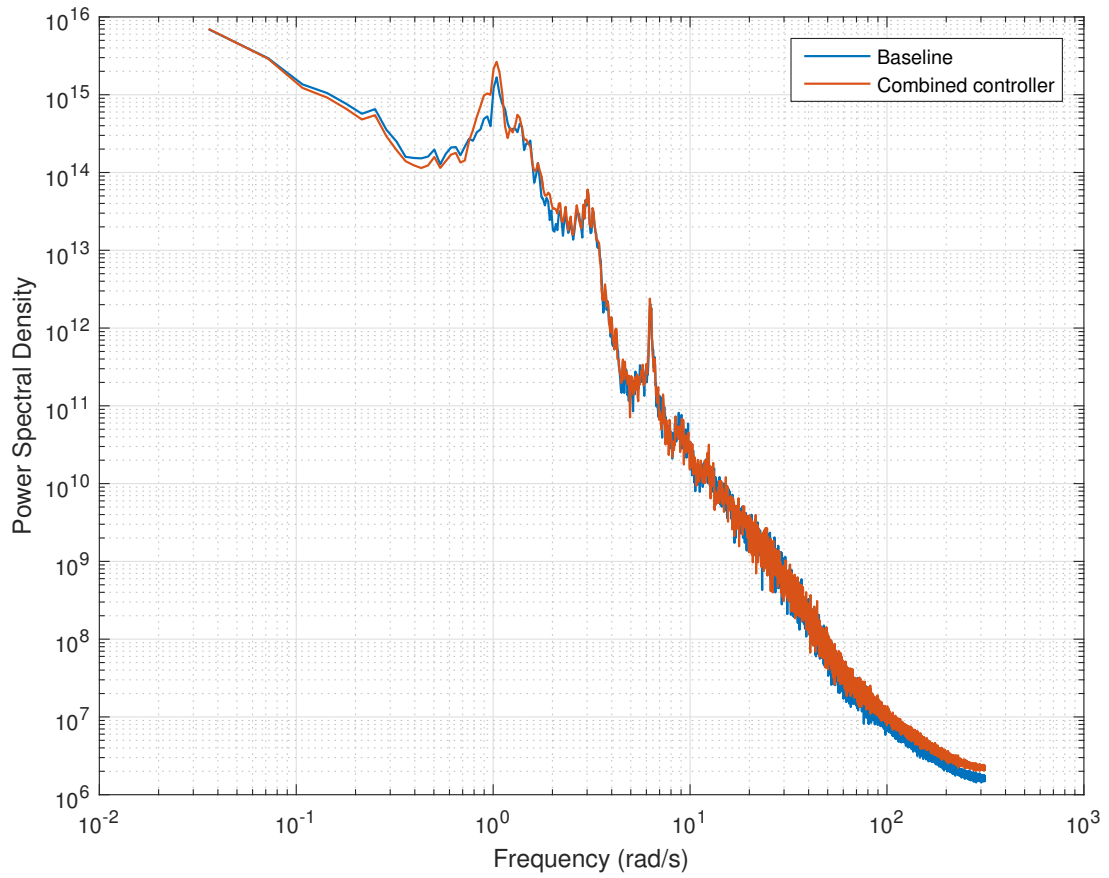


Figure 6.16: Comparison of power spectral densities of the tower base fore-aft bending moment with the baseline and combined controllers for the 7.5MW turbine in 18m/s mean wind speed

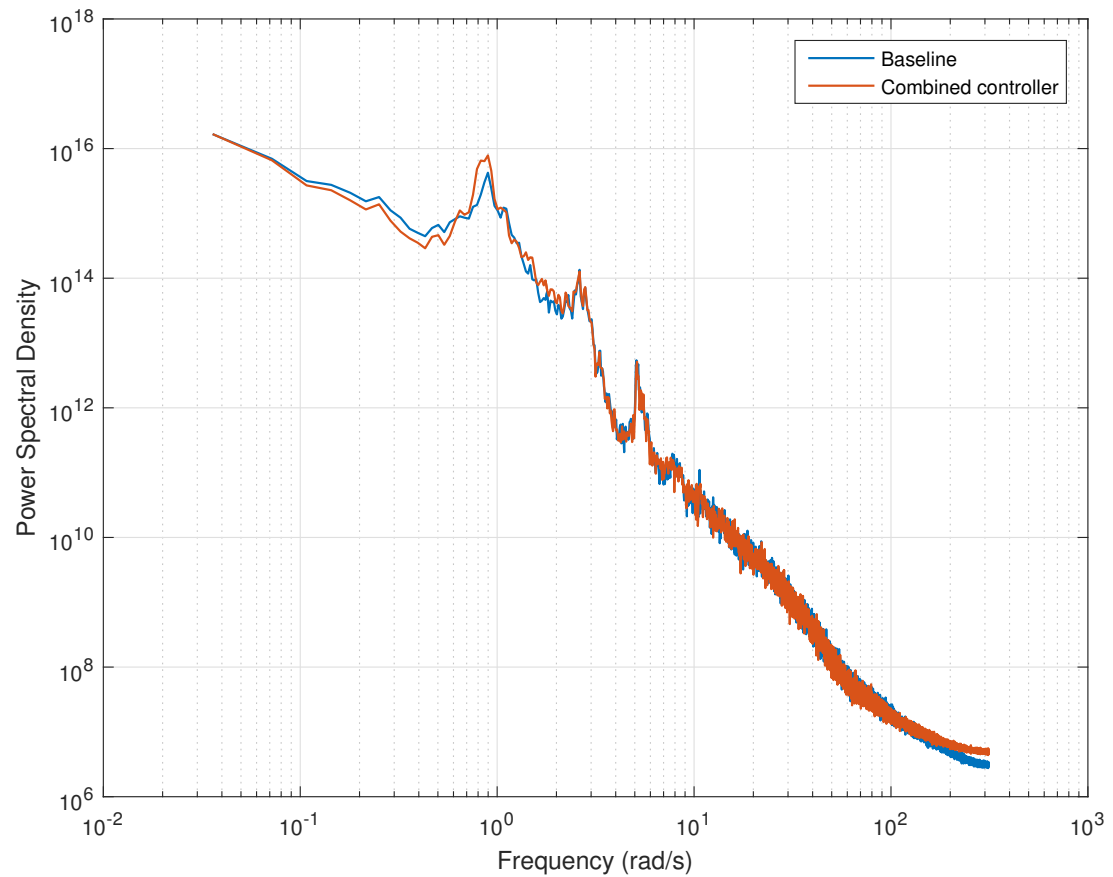


Figure 6.17: Comparison of power spectral densities of the tower base fore-aft bending moment with the baseline and combined controllers for the 10MW turbine in 18m/s mean wind speed

Blade Root Bending Moments

While the application of the combined controller has detrimental effect on tower loads, there is a negligible change to loading on the blades. Figure 6.18 compares the damage equivalent loads at the blade root for three runs with both controller configurations. The average value over the three runs for the combined controller constitutes a change of less than one percentage point over the baseline. These average values are shown in Table 6.5.

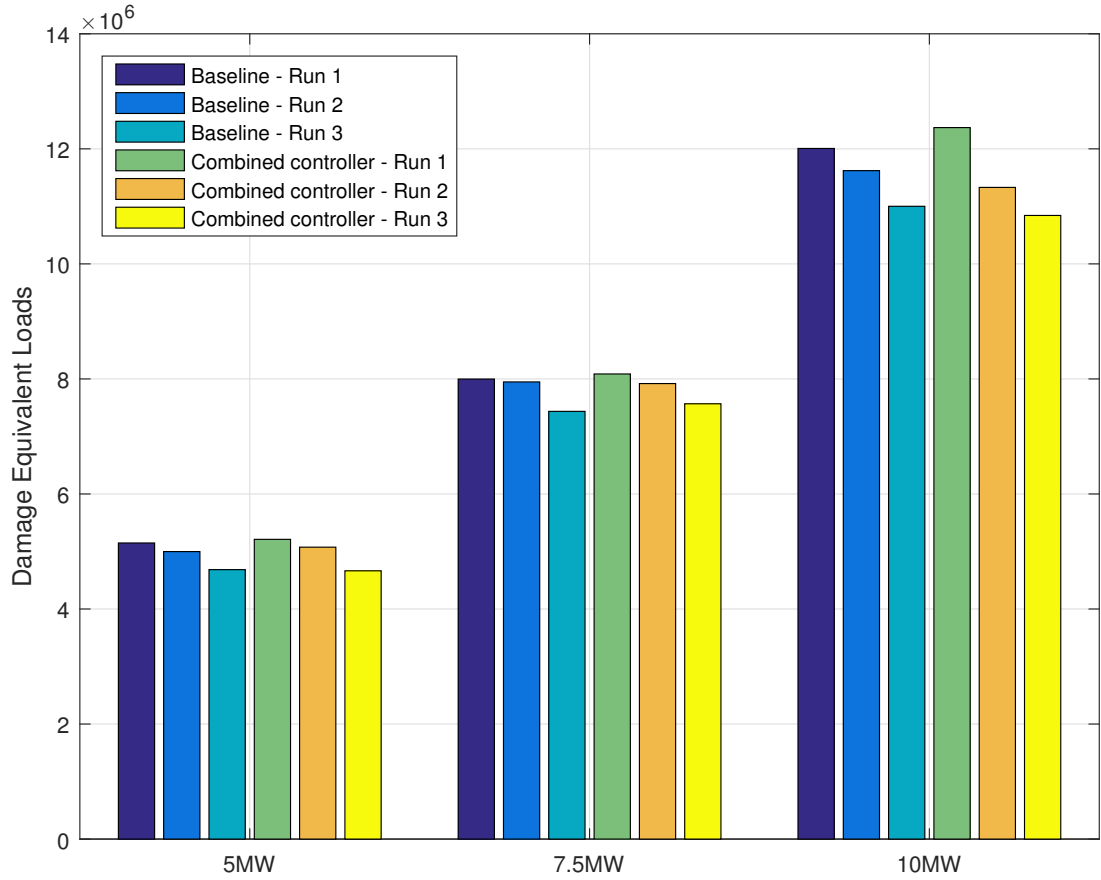


Figure 6.18: Damage equivalent loads at the blade root with the baseline and combined controllers operating in a turbulent wind with a mean wind speed of 18m/s

Rated Power (MW)	Baseline Controller	Combined Controller	Percentage Difference
5.0	0.4944×10^7	0.4983×10^7	-0.79%
7.5	0.7794×10^7	0.7858×10^7	-0.82%
10.0	1.1543×10^7	1.1514×10^7	0.25%

Table 6.5: Averages of damage equivalent loads at the blade root across three simulations for the baseline and combined controllers

Power spectral density plots for the blade root bending moment corroborate the minor changes in damage equivalent loads. Figures 6.19, 6.20 and 6.21 show plots of the power spectral density for the blade root bending moment for the

5MW, 7.5MW and 10MW turbines where there is minimal change to the size and position of the spectral peaks.

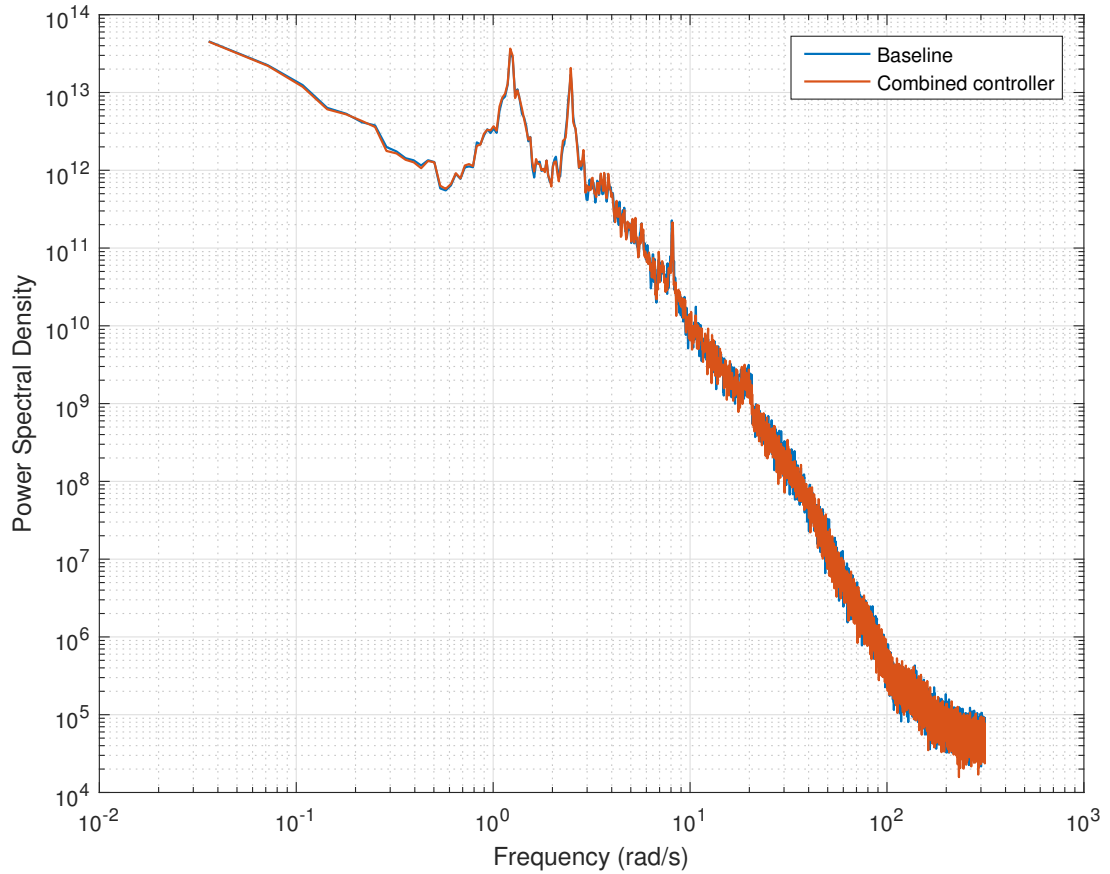


Figure 6.19: Comparison of power spectral densities of the blade root bending moment with the baseline and combined controllers for the 5MW turbine in 18m/s mean wind speed

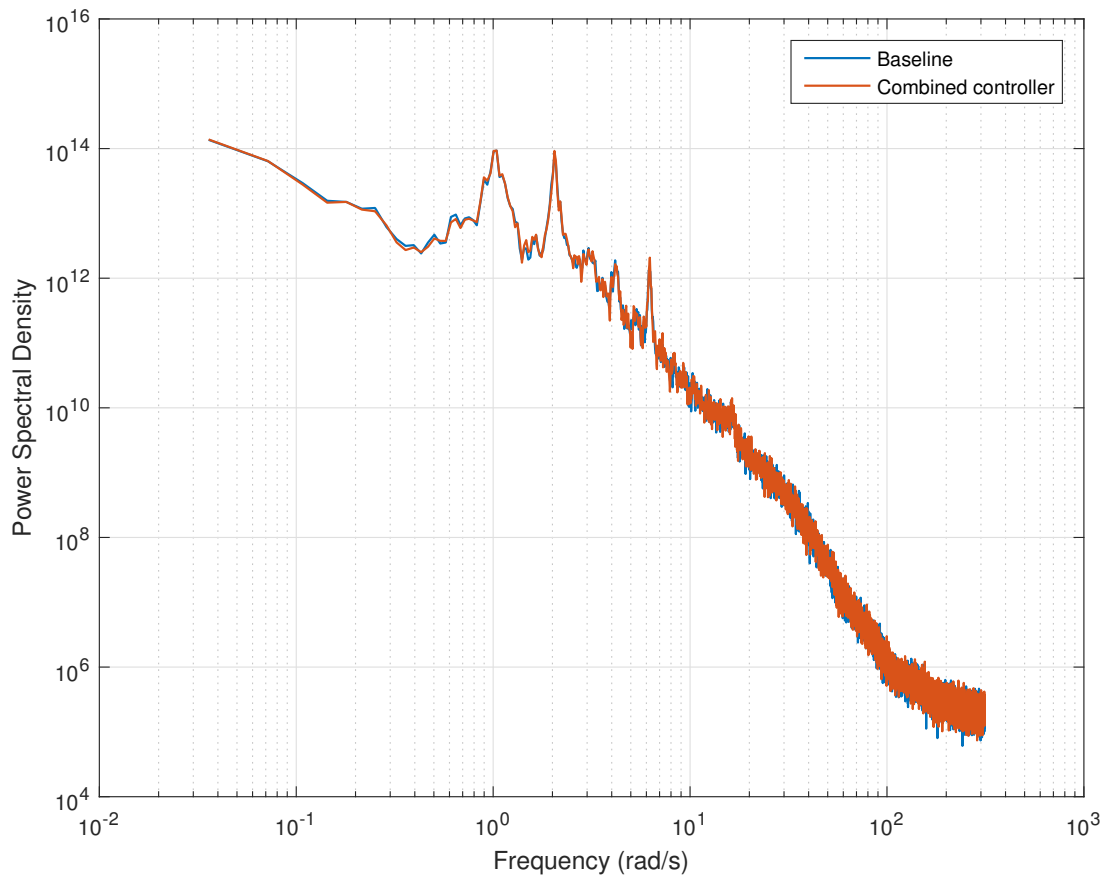


Figure 6.20: Comparison of power spectral densities of the blade root bending moment with the baseline and combined controllers for the 7.5MW turbine in 18m/s mean wind speed

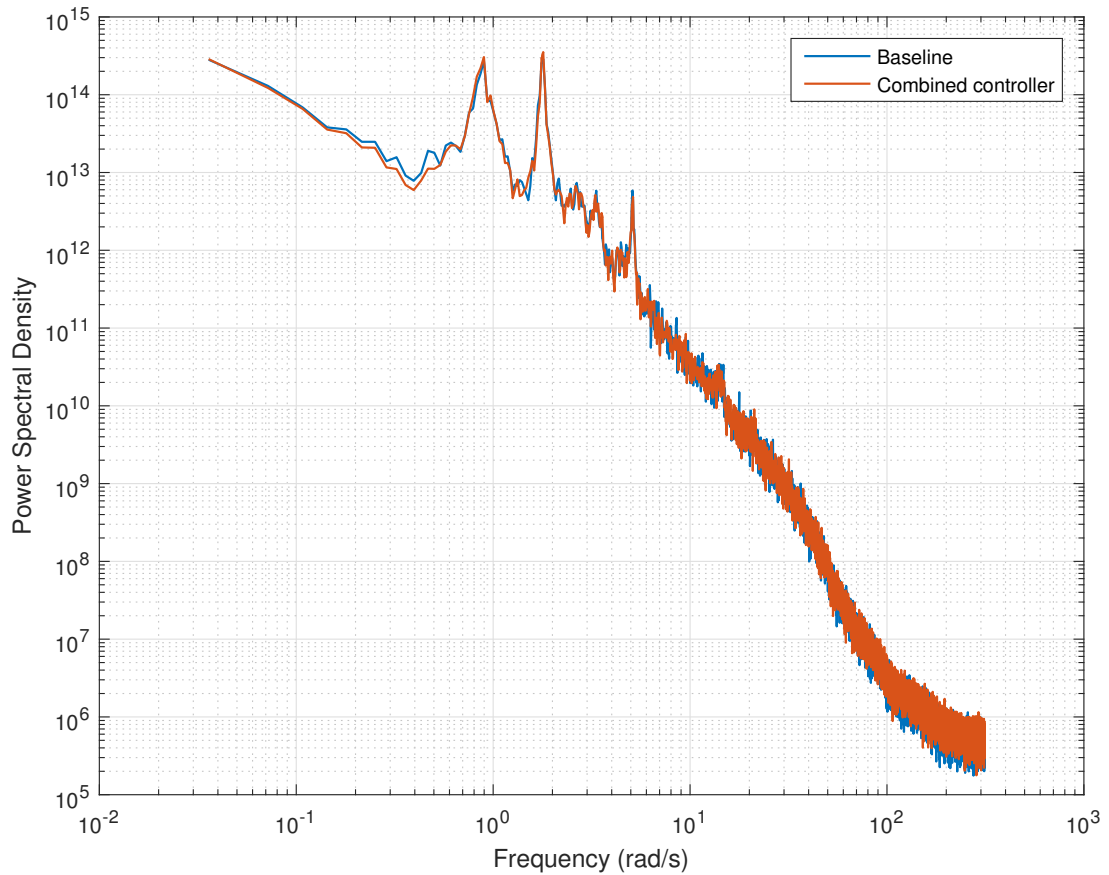


Figure 6.21: Comparison of power spectral densities of the blade root bending moment with the baseline and combined controllers for the 10MW turbine in 18m/s mean wind speed

6.2.3 Switching Between Operating Modes

Simulations of the 5MW turbine in an 11m/s mean wind speed demonstrate how the controller switches between below-rated and above-rated operating modes. Figure 6.22 shows the generator speed held at the above-rated set-point of 120rad/s for the sections of the simulation where the wind speed is above the threshold of about 11m/s and dipping below when it is not. There is no visible discontinuity in the generator speed time series when the controller switches between modes, for example at about 180s, 320s and 550s.

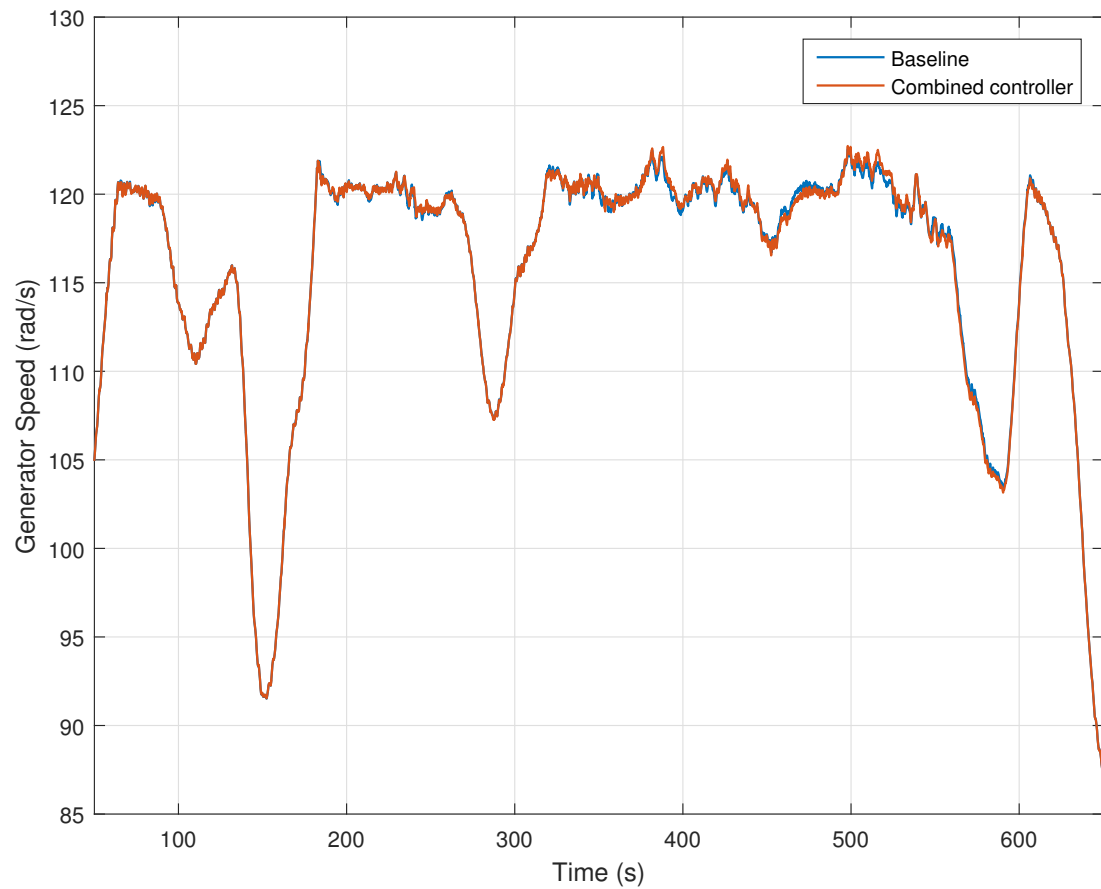


Figure 6.22: Comparison of generator speed with the baseline and combined controllers for the 5MW turbine in 11m/s mean wind speed

For the same simulations with an 11m/s mean wind speed, the plot of blade pitch angle shows a very similar response from the combined controller as with the baseline. Where Figure 6.22 shows the controller switching between tracking C_{Pmax} the upper constant speed mode, Figure 6.23 shows switching between the upper constant speed section and above-rated operation.

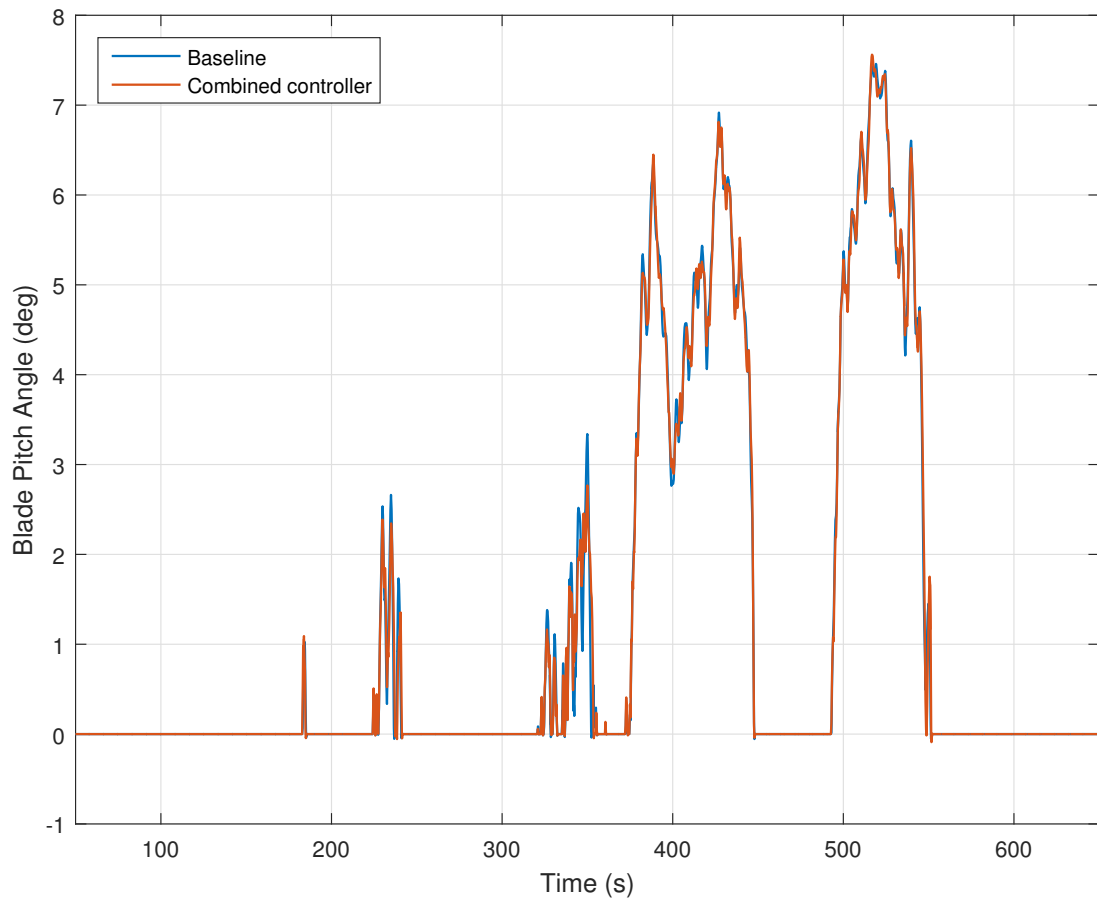


Figure 6.23: Comparison of blade pitch angle with the baseline and combined controllers for the 5MW turbine in 11m/s mean wind speed

6.2.4 Actuator Saturation

In Chapter 5, the ELLE controller is implemented in a way that it is compatible with the anti-windup loop which exists in the baseline controller. Correct function of the anti-windup loop prevents the controller from requesting a pitch angle demand which results in a pitch rate outwith the limits of the actuator or actuators. To demonstrate this, the maximum and minimum pitch rates are set at 1.5deg/s and -1.5deg/s. Figure 6.24 shows a simulation with a 13m/s mean wind speed (chosen because wind speeds just above rated generally result in the greatest pitch rates). The simulation with the anti-windup loop activated shows

the pitch rate is limited to the preset values of $\pm 1.5\text{deg/s}$.

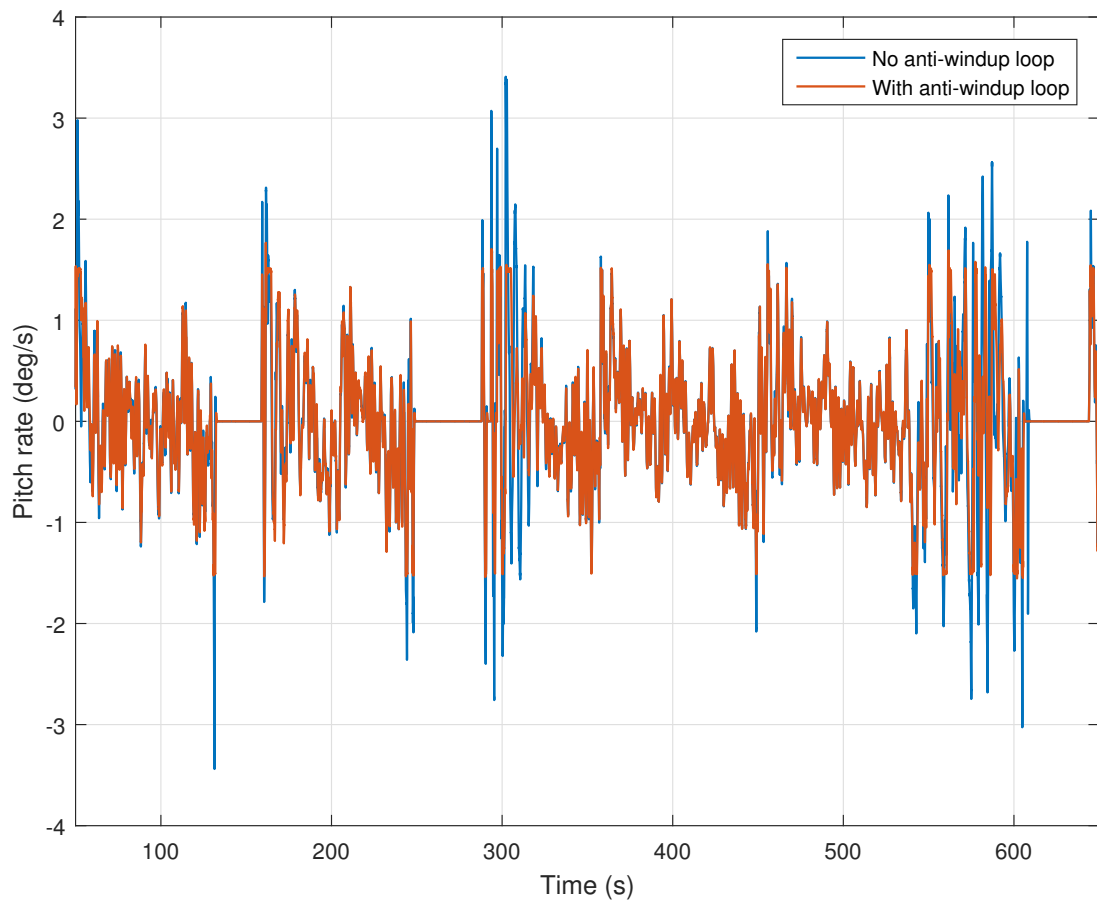


Figure 6.24: Comparison of blade pitch angle rates with and without the anti-windup loop applied and the rate limit restricted to 1.5deg/s

6.3 Concluding Remarks

In this chapter, the combination of the improved power coordinated controller (IPCC) and extended local linear equivalence (ELLE) controller is presented. Simulations show that the combined IPCC and ELLE controller offers better speed and power control at the expense of a small increase in tower loads and no marked change in blade loads.

As wind turbines increase in size, two things change which effect the perfor-

mance of the controller. Firstly, the natural frequency of the first tower fore-aft mode reduces. Secondly, a pole, the frequency of which depends on the wind speed, does not move and therefore has a greater influence on system dynamics as turbine size increases. The result of these two changes is that as wind turbines get bigger, the bandwidth available to the controller is encroached on by the tower fore-aft mode in the high frequencies and the non-linearity due to the variable pole in the lower frequencies. The controller presented in this chapter addresses both of these problems. The IPCC reduces the influence of a lower tower structural mode on the achievable gain crossover frequency by removing a band of frequencies centred on the tower mode from the pitch angle demand and augmenting generator torque demand to maintain accurate control. The ELLE controller removes the non-linearity from the system dynamics by countering the variable pole with a compensator which has the effect of a variable zero. These two individual controller designs are detailed in Chapter 4 and Chapter 5 respectively.

Simulations for three sizes of wind turbine with the combined controller result in reductions in the variation of generator speed and mechanical power at the generator. The IPCC alone is configured to improve the control of power output but also slightly increases excursions from the set point of generator speed. When combined with the ELLE controller, both speed and power control are improved significantly. The standard deviation of generator speed in a 16m/s mean wind speed is reduced by nearly 30% for the largest wind turbine tested and the standard deviation of mechanical power is reduced by about 37%.

When applied alone, the ELLE controller increases loads on the tower. However, when applied in combination with the IPCC, the improvements to speed and power control are retained but tower loads are increased by between 9% to 4% (for the three sizes of turbine tested), rather than 20% to 30%. By modest changes to the tuning of the IPCC, these increases in tower loads may be further

reduced.

While the combined controller improves various aspects as described above, the overall complexity of the controller is increased over that of the baseline. The number of logical steps in the control algorithm is increased as well as the overall order of the controller. However, the simulations presented in this chapter show that this increase in complexity has not introduced any instability to the system. When the code for both the baseline and combined controllers are compiled for use in the Bladed simulation environment, there is no change in size of the resulting file. This means that there would be no additional memory requirement for hardware implementation of the combined controller over the baseline.

Chapter 7

Conclusion

The ever increasing size of wind turbines and the drive to move offshore poses a challenge for control design. In this thesis, these challenges are investigated by simulating three sizes of wind turbine and developing appropriate control solutions. Contributions to knowledge are made in the following areas:

- A framework for producing a set of differently sized wind turbine mathematical models with similarly scaled dynamics has been developed.
- A controller design which mitigates the restriction that the wind turbine tower imposes on control performance and feasibility.
- A controller design which significantly improves performance by countering a non-linearity in the pitch control loop.
- A controller design which combines the two points described above to provide a system which mitigates the negative influence of turbine size.

In Chapter 3 a set of scaling rules are established which allows the construction of three similarly scaled wind turbine models, complete with controllers. The dynamics of these models are such that, while individual parameters like lengths,

masses, and inertias are scaled appropriately, the dynamics also demonstrate behaviour which shows a clear pattern in relation to size. This is especially evident in the bode plots and plots of the sensitivity functions of the three machines, where a pattern of reducing natural frequencies and poorer speed and power control is evident. In Chapter 3, the following points are established.

- The frequency of the first fore-aft mode of the tower reduces as turbine size increases. This reduction in frequency forces a lower gain crossover frequency which has a detrimental effect on controller performance.
- The effect of wind speed averaging across the rotor is greater with larger rotors. The variation in the effective wind speed is therefore reduced as rotor size increases.
- Although the above two points counteract each other, the net result is that speed and power control performance is reduced as wind turbine size increases.

In Chapter 4, a controller is developed which helps to counter the limiting effect that the first fore-aft mode of the tower has on controller performance. Due to the increased influence that this property has on larger turbines, this controller design is especially applicable as turbine size increases.

Previous research used a coordinated controller design (CCD) to reduce loads on the tower by filtering pitch activity around the tower frequency and augmenting the torque control loop to maintain the dynamics. This is further developed, with the power coordinated controller (PCC) to reduce fluctuations in torque and improve power control at the expense of speed control. In Chapter 4, the structure of the PCC is used to counter the right-half-plane zeros (RHPZs) which have the negative effect on controller performance identified in Chapter 3. With the effect of the RHPZs eliminated, the controller gain can be increased to increase

the gain crossover frequency, therefore improving control performance. In addition to this, it is found that as wind turbine size increases, the improvements seen by applying the improved power coordinated controller (IPCC) also increase.

In Chapter 5, a controller is developed which greatly improves controller performance by countering a low-frequency non-linearity in the plant. A pole, the frequency of which varies with wind speed is present in the transmittance between blade pitch angle demand and generator speed. This non-linearity which is evident by comparing bode plots of the system at different wind speeds, has a detrimental effect on the performance of the controller.

Previous research describes the concept of extended local linear equivalence (ELLE) and how it applies to gain-scheduled controllers. In Chapter 5, a controller which satisfies the ELLE condition is designed and applied to the three models developed in Chapter 3 in order to counter the non-linearity described above. Application of this controller sees reductions in the standard deviation of generator speed of 20% to 40%. The improvements are found to be greater with bigger wind turbines. While the issues described in Chapter 4 deal with the high frequency end of the controller bandwidth, the cancellation of this non-linearity increases available bandwidth in the low frequency range.

In Chapters 4 and 5, two problems affecting controller performance and stability are identified and addressed. Simulations of three sizes of wind turbine with these controllers applied demonstrate that these solutions are more effective as turbine size increases. In Chapter 6, the IPCC and the gain-scheduled ELLE controller are combined to produce a controller which is much more robust to the influence of turbine size. The available bandwidth of the combined controller is increased from that of the baseline controller at high frequencies by the IPCC and at low frequencies by the ELLE controller. When applied to a range of wind turbine sizes, the combined controller demonstrates a greater improvement in performance with larger turbines. This is because, as the size of a wind turbine

increases, the natural frequency of the tower in the fore-aft mode decreases and restricts the maximum achievable gain-crossover frequency. The frequency range covered by the low-frequency pole introduced by the aerodynamic non-linearity also decreases with turbine size, but not at the same rate as the tower frequency. The result of this is a restriction of available bandwidth as turbine size increases.

The combined controller demonstrates a reduction in the standard deviation of generator speed by up to 30% and mechanical power by up to 37%. Where the ELLE controller alone increases damage equivalent loads at the tower base by 20% to 30%, the combined controller only increases them by 4% to 9%. While the IPCC does decrease damage equivalent loads somewhat, the combination of the IPCC and the ELLE controller is better than the sum of its parts in this respect.

While the changes made in the combined controller does increase the complexity somewhat, relative to the baseline, simulations presented in Chapter 6 show that stability is not effected.

Future Work

Potential areas for future work based on the research presented here are as follows:

- In Chapter 3, the influence of the tower frequency on controller performance is identified. It is also noted that as wind turbines increase in size, the averaging of the wind speed across the rotor acts to improve speed control performance. Further work may investigate whether very large rotors have different requirements in terms of an ideal gain-crossover frequency and what this means for the feasibility of controllers for very large wind turbines.
- In the implementation of the IPCC presented in this thesis, the gain is increased to maintain the same gain and phase margins as with the baseline controller so that a reasonable comparison may be made. As it is known

that tower loads are increased by increasing the gain in such a way, future work may establish whether this relationship will limit the usefulness of the IPCC when applied to wind turbines bigger than those tested here.

- The PCC and IPCC introduces a dip in the gain response in above-rated control around the tower frequency. In Chapter 4, a method for rectifying this and returning to the dynamics of the baseline controller is investigated. It was concluded that a simple filter was insufficient so a more complex approach may be the subject of future work.

References

- [1] “Blyth’s wind turbine.” [Online]. Available: <http://www.taplondon.co.uk/bwea30/pdf/Closing{ }PeterMusgrove-web.pdf>
- [2] R. W. Righter, *Wind energy in America : a history*. University of Oklahoma Press, 1996.
- [3] H. Pettersen and Statoil, “Havvindparken Sheringham Shoal.” [Online]. Available: <https://www.flickr.com/photos/nhd-info/8033151828/>
- [4] T. F. Stocker, Q. Dahe, G.-K. Plattner, L. V. Alexander, S. K. Allen, N. L. Bindoff, F.-M. Bréon, J. A. Church, U. Cubash, S. Emori, P. Forster, P. Friedlingstein, L. D. Talley, D. G. Vaughan, and S.-P. Xie, “Technical Summary,” *Climate Change 2013: The Physical Science Basis. Contribution of Working Group I to the Fifth Assessment Report of the Intergovernmental Panel on Climate Change*, pp. 33–115, 2013.
- [5] R. P. Core Writing Team and L. M. (eds.), *IPCC, 2014: Climate Change 2014: Synthesis Report. Contribution of Working Groups I, II and III to the Fifth Assessment Report of the Intergovernmental Panel on Climate Change*, 2014. [Online]. Available: <http://ebooks.cambridge.org/ref/id/CBO9781107415324>

REFERENCES

- [6] United Nations Framework Convention on Climate Change, “Paris Agreement,” 2015. [Online]. Available: <https://treaties.un.org/doc/Publication/MTDSG/VolumeII/ChapterXXVII/XXVII-7-d.en.pdf>
- [7] UNFCCC. Conference of the Parties (COP), “Paris Climate Change Conference–November 2015, COP 21,” Tech. Rep., 2015. [Online]. Available: <http://unfccc.int/resource/docs/2015/cop21/eng/l09r01.pdf>
- [8] T. J. Price, “James Blyth - Britain’s first modern wind power pioneer,” *Wind Engineering*, vol. 29, no. 3, pp. 191–200, may 2005. [Online]. Available: <http://wie.sagepub.com/lookup/doi/10.1260/030952405774354921>
- [9] Project Upwind, “Design Limits and Solutions for Very Large Wind Turbines,” Tech. Rep., 2011.
- [10] “Joint Statement to further the deployment of offshore energy in Europe,” London, 2017. [Online]. Available: <https://windeurope.org/wp-content/uploads/files/policy/topics/offshore/Offshore-Wind-Statement-of-Intent-signed.pdf>
- [11] P. Jamieson, *Innovation in Wind Turbine Design*, 2011.
- [12] S. Hogg and C. J. Crabtree, *UK Wind Energy Technologies*. Taylor and Francis, 2016.
- [13] V. W. Neilson, “Individual Blade Control for Fatigue Load Reduction of Large-scaled Wind Turbines : Theory and Modelling,” no. March, 2010.
- [14] A. P. Chatzopoulos, “Full Envelope Wind Turbine Controller Design for Power Regulation and Tower Load Reduction,” *University of Strathclyde*, no. August, 2011.
- [15] I. Van der Hoven, “Power Spectrum of Horizontal Wind Speed in the Frequency Range From 0.0007 To 900 Cycles Per Hour,” pp. 160–164, 1957.

- [16] DNV GL, “Bladed Theory Manual,” no. 1, pp. 1–5, 2014.
- [17] T. Burton, D. Sharpe, N. Jenkins, and E. Bossanyi, *Wind Energy Handbook*, 2001.
- [18] D. Robb and W. Leithead, “Derivation and Validation of Simple Correlated Wind Speed Models,” 1995.
- [19] W. E. Leithead and M. C. M. Rogers, “Drive-train Characteristics of Constant Speed HAWTs: Part I - Representation by Simple Dynamic Models,” *Wind Engineering*, vol. 20, no. 3, pp. 175–201, 1996.
- [20] —, “Drive-train Characteristics of Constant Speed HAWTs: Part II - Simple Characterisation of Dynamics,” *Wind Engineering*, vol. 20, no. 3, pp. 175–201, 1996.
- [21] C. Gonzalez, “SgurrControlBox theory manual March 2014,” no. March, pp. 1–86, 2014.
- [22] K. Dykes, A. Platt, Y. Guo, A. Ning, R. King, T. Parsons, D. Petch, and P. Veers, “Effect of Tip-Speed Constraints on the Optimized Design of a Wind Turbine Effect of Tip-Speed Constraints on the Optimized Design of a Wind Turbine,” no. October, 2014.
- [23] D. J. Leith and W. E. Leithead, “Survey of Gain-Scheduling Analysis & Design,” *International Journal of Control*, vol. 73, no. 11, pp. 1001–1025, 2000.
- [24] W. E. Leithead, D. J. Leith, F. Hardan, and H. Markou, “Global Gain-Scheduling control for variable speed wind turbines,” *EWEC-Conference*, vol. 44, pp. 853–856, 1999.

REFERENCES

- [25] D. J. Leith and W. E. Leithead, "Implementation of wind turbine controllers," *International Journal of Control*, vol. 66, no. 3, pp. 349–380, 1997. [Online]. Available: <http://www.tandfonline.com/doi/abs/10.1080/002071797224621>
- [26] W. E. Leithead and B. Connor, "Control of variable speed wind turbines: Design task," *International Journal of Control*, vol. 73, no. 13, pp. 1189–1212, jan 2000. [Online]. Available: <http://www.tandfonline.com/doi/abs/10.1080/002071700417849>
- [27] W. Leithead and S. Dominguez, "Active regulation of multi-MW wind turbines: an overview," *Power Systems Technology*, vol. 31, no. 20, pp. 24–34, 2007.
- [28] IEC 61400-1, "Wind turbines - Part 1: Design requirements," Tech. Rep., 2005.
- [29] W. E. Leithead, S. Dominguez, and C. Eee, "Coordinated Control Design for Wind Turbine Control Systems," *Proceedings of the EWEC*, 2006.
- [30] S. Dominguez and W. E. Leithead, "Size Related Performance Limitations on Wind Turbine Control Performance," *Proceedings of the European Wind Energy Conference*, 2006.
- [31] M. Sidi, "Gain-bandwidth limitations of feedback systems with non-minimum-phase plants," *International Journal of Control*, vol. 67, no. 5, pp. 731–744, jan 1997. [Online]. Available: <http://www.tandfonline.com/doi/abs/10.1080/002071797223974>
- [32] D. J. Leith and W. E. Leithead, "Appropriate realization of gain-scheduled controllers with application to wind turbine regulation," *International Journal of Control*, vol. 65, no. 2, pp. 223–248, 1996.

REFERENCES

- [33] C. Plumley, “The Smart Rotor Wind Turbine,” Ph.D. dissertation, University of Strathclyde, 2016.
- [34] G. Freebury and W. Musial, “Determining equivalent damage loading for full-scale wind turbine blade fatigue tests,” *2000 ASME Wind Energy Symposium*, no. February, p. 12, 2000. [Online]. Available: <http://arc.aiaa.org/doi/abs/10.2514/6.2000-50>

Appendix A

Parameters for Upscaled Wind Turbines

The following tables contain parameters for 5MW, 7.5MW, and 10MW wind turbines and their respective controllers. Parameters for the 7.5MW and 10MW turbines are gained by scaling up those from the 5MW turbine. The method used to upscale these parameters are in Chapter 3. Sections A.1 and A.2 contain transfer functions and parameters for the wind turbine plant. Sections A.3 and A.4 contain transfer functions and parameters for the controllers.

For transfer functions, the numerator and denominator are defined separately in MATLAB. For example, the pitch actuator transfer function is G_{pac} , the numerator is G_{pacNum} and the denominator is G_{pacDen} .

A.1 Plant Transfer Functions

Pitch actuator, G_{pac} :

5MW	7.5MW	10MW
$\frac{64}{s^2+11.2s+64}$	$\frac{42.25}{s^2+9.1s+42.25}$	$\frac{32.49}{s^2+7.98s+32.49}$

A.2 Plant Parameters

Parameter	Symbol	5MW	7.5MW	10MW
Gain to shape nP spectral peaks	$Ka3p$	7.41×10^{-6}	7.41×10^{-6}	7.41×10^{-6}
Gain to shape nP spectral peaks	$Kb3p$	5.54×10^5	5.54×10^5	5.54×10^5
Rotor radius	R	63	75.88	87.61
Blade effective length	L	45	54.20	62.58
Rotor inertia	J	23047500	69441000	163311000
Cross-coupling inertia	Jc	98196435	248840000	510670000
Tower fore-aft inertia	Jt	2.4039×10^9	6.0917×10^9	1.2502×10^{10}
Tower fore-aft damping	Bt	8.3980×10^7	1.6153×10^8	2.6706×10^8
Blade edgewise stiffness	Ke	1.0652×10^9	1.8388×10^9	2.8000×10^9
Blade flapwise stiffness	Kf	4.2073×10^8	7.2709×10^8	1.1104×10^9
Tower fore-aft stiffness	Kt	7.3344×10^9	1.0708×10^{10}	1.4262×10^{10}
Low speed shaft inertia	ILs	12439926	3.8808×10^7	9.3096×10^7
Low speed shaft damping	gls	150000	277360	461100
Low speed shaft stiffness	$KLsb$	445000000	1.1277^9	2.3142×10^9
High speed shaft stiffness	KHs	1×10^{10}	2.5341×10^{10}	5.2005×10^{10}
Low speed shaft material damping	$g1s$	4200000	5935900	7756200

APPENDIX A. PARAMETERS FOR UPSCALED WIND TURBINES

High speed shaft material damping	$g2s$	1000	1000	1000
Gearbox ratio	n	97	117	135
High speed shaft inertia	IHs	539.1160×10^2	1.3662×10^3	2.8037×10^3
High speed shaft damping	ghs	5	5	5
Tower side-to-side inertia	Jts	2.8350×10^9	7.1842×10^9	1.4744×10^{10}
Tower side-to-side stiffness	Kts	8.7747×10^9	1.2628×10^{10}	2.2799×10^{10}
Tower side-to-side damping	Bts	9.9753×10^7	1.9050×10^8	3.6668×10^8
Hub height	h	90	108.39	125.16

A.3 Controller Transfer Functions

Outer controller, Co :

5MW	7.5MW	10MW
$\frac{117.432}{(s+1.8)}$	$\frac{165.270}{(s+1.5)}$	$\frac{139.330}{(s+1.3)}$

Inner controller, $Ciazs$:

5MW	7.5MW	10MW
$\frac{-0.06012s-12.02}{s}$	$\frac{-0.04383s-8.766}{s}$	$\frac{-0.03624s-7.249}{s}$

Preceding transfer function to keep ELLE controller proper, $Gpre$:

5MW	7.5MW	10MW
$\frac{-1800s^2-3.262 \times 10^4 s-3896}{s^2+14.4s+324}$	$\frac{-1800s^2-3.256 \times 10^4 s-2840}{s^2+14.4s+324}$	$\frac{-1800s^2-3.253 \times 10^4 s-2349}{s^2+14.4s+324}$

Phase advance, Pa :

5MW	7.5MW	10MW
$\frac{s+0.6}{s+1.6}$	$\frac{s+0.6}{s+1.6}$	$\frac{s+0.6}{s+1.6}$

Notch filter for coordinated controller, Y_{cc} :

5MW	7.5MW	10MW
$\frac{s^2+0.3s+3.051}{s^2+0.9s+3.051}$	$\frac{s^2+0.3s+1.758}{s^2+0.9s+1.758}$	$\frac{s^2+0.3s+1.141}{s^2+0.9s+1.141}$

$(1 - Y_{cc})$, Y_{1cc} :

5MW	7.5MW	10MW
$\frac{0.6s}{s^2+0.9s+3.051}$	$\frac{0.6s}{s^2+0.9s+1.758}$	$\frac{0.6s}{s^2+0.9s+1.141}$

Coordinating function for the power coordinated controller and the improved power coordinated controller, X_{1cc} :

5MW	7.5MW	10MW
$\frac{-1 \times 10^8}{(s+0.035)(s+5)(s+50)(s+120)}$	$\frac{-3.7 \times 10^7}{(s+0.0245)(s+3.5)(s+35)(s+84)}$	$\frac{-1.3 \times 10^7}{(s+0.0175)(s+2.5)(s+25)(s+60)}$

Drivetrain filter, G_{dtr} :

5MW	7.5MW	10MW
$\frac{2000s}{0.1119s^2+s+8.94}$	$\frac{3000s}{0.1125s^2+s+5.688}$	$\frac{8000s}{0.1548s^2+1s+6.46}$

A.4 Controller Parameters

Parameter	Symbol	5MW	7.5MW	10MW
Above-rated generator speed set point	WSET	120	120	120
Gain paired with Ciazs (See Appendix D)	a_0	-100.06012	-100.04	-100.04
Gain for ELLE controller	b_1	24.9374	9.5238	76.1900

APPENDIX A. PARAMETERS FOR UPSCALED WIND TURBINES

Gain for ELLE controller	b_2	28.6780	14.2860	57.1430
Gain for ELLE controller	b_3	9.8879	6.7619	13.5240
Gain for ELLE controller	k_{gs}	4.0100×10^2	0.105	0.013125
Parameter for ELLE controller variable function	$Ay(1)$	-1.9965×10^{-6}	-1.1872×10^{-6}	-1.1634×10^{-6}
Parameter for ELLE controller variable function	$Ay(2)$	1.1815	0.9144	0.7641
Parameter for ELLE controller variable function	$By(1)$	-1.3116×10^{-6}	-6.4325×10^{-7}	-5.1346×10^{-7}
Parameter for ELLE controller variable function	$By(2)$	0.4172	0.2678	0.1837
Parameter for ELLE controller variable function	$Cy(1)$	-1.8505×10^{-7}	-8.2817×10^{-8}	-5.2421×10^{-8}
Parameter for ELLE controller variable function	$Cy(2)$	4.3016×10^{-2}	2.5005×10^{-2}	0.0138
Torque to define control strategy	T_0	8692.2	14096	19397
Torque to define control strategy	T_1	27340	42791	58136
Above-rated generator torque	$TQSET$	43860	65789	87719

APPENDIX A. PARAMETERS FOR UPSCALED WIND TURBINES

Gain for mode switching	K_o	65.24	62.069	75.305
Gain for mode switching	K_{cp}	0.0153	0.0161	0.0133
Gain defining $C_{p_{max}}$ tracking	$GainOpt$	2.0731	3.1046	4.1475
Generator speed range	DW	50	50	50
Above-rated gain	K_p	1.4679×10^{-5}	1.7751×10^{-5}	1.4232×10^{-5}
Gain for the IPCC	k_{cc}	1.0965	1.3335	3.8000
Parameter for global gain scheduling matches G_{pac}	b	11.2	9.1	7.98
Parameter for global gain scheduling matches G_{pac}	c	64	42.25	32.49
Parameter defining global gain scheduling	$dslope$	42	51.09	51.3
Parameter defining global gain scheduling	$dcons$	1	1	1
Minimum blade pitch angle	$PITMIN$	0	0	0

Appendix B

State Space Model

The following is a state space model of the wind turbine. It is split into two parts; one containing the rotor dynamics and another containing the drivetrain dynamics. Figure B.1 shows the split and the inputs and outputs of each part [14].

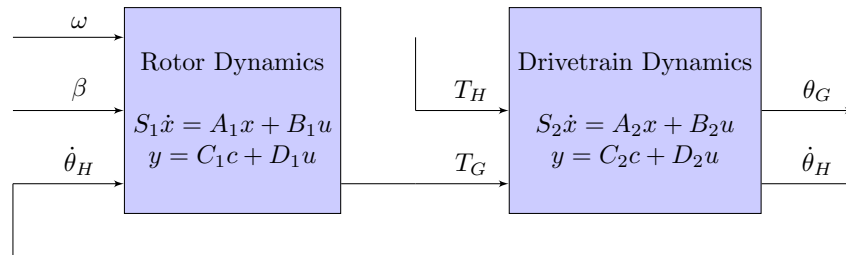


Figure B.1: Rotor dynamics and drivetrain dynamics in the state space model

In this appendix θ refers to a degree of freedom in-plane with the rotor and ϕ refers to a degree of freedom out-of-plane with the rotor. The subscript R refers to the rotor, H refers to the hub, T refers to the tower, G refers to the generator, E refers to the blade edgewise direction, and F refers to the blade flapwise direction. All symbols are defined in the nomenclature section at the start of this thesis.

B.1 Rotor Dynamics

The state space variables for the rotor dynamics are:

$$x_1 = \theta_R - \theta_H \quad x_2 = \phi_R \quad x_3 = \phi_T \quad x_4 = \dot{\theta}_T \quad x_5 = \dot{\phi}_R \quad x_6 = \dot{\phi}_T$$

$$u_1 = \omega \quad u_2 = \beta \quad y = T_H$$

And the state space model is as follows:

$$\dot{x}_1 = x_4 - \dot{\theta}_H$$

$$\dot{x}_2 = x_5$$

$$\dot{x}_3 = x_6$$

$$\begin{aligned} \dot{x}_4 = & -(\omega_E^2 \cos^2 \beta_0 + \omega_F^2 \sin^2 \beta_0)x_1 + (\omega_E^2 - \omega_F^2) \sin \beta_0 \cos \beta_0 x_2 \\ & -(\omega_E^2 - \omega_F^2) \sin \beta_0 \cos \beta_0 x_3 \\ & + \frac{1}{J} \frac{\partial F_1}{\partial \theta_R} x_4 - \frac{L}{J} \frac{\partial F_1}{\partial \omega} x_5 - \frac{h}{J} \frac{\partial F_1}{\partial \omega} x_6 + \frac{1}{J} \frac{\partial F_1}{\partial \omega} u_1 + \frac{1}{J} F_{1\beta} u_2 \end{aligned}$$

$$\begin{aligned}
 \frac{1 - \frac{J_c^2}{J_T J}}{1 + \frac{J_c}{J}} \dot{x}_5 &= (\omega_E^2 - \omega_F^2)x_1 - (\omega_E^2 \sin^2 \beta_0 - \omega_F^2 \cos^2 \beta_0)x_2 \\
 &+ (\omega_E^2 \sin^2 \beta_0 - \omega_F^2 \cos^2 \beta_0 + \frac{J_c K_T}{J(J_T + J_c)})x_3 + \frac{J_T}{J(J_T + J_c)} \frac{\partial F_2}{\partial \dot{\theta}_R} x_4 \\
 &- L \frac{J_T}{J(J_T + J_c)} \frac{\partial F_2}{\partial \omega} x_5 - \frac{J_T}{J(J_T + J_c)} \left(h \frac{\partial F_2}{\partial \omega} - \frac{J_c}{J_T} B_T \right) x_6 \\
 &+ \frac{J_T}{J(J_T + J_c)} \frac{\partial F_2}{\partial \omega} u_1 + \frac{J_T}{J(J_T + J_c)} F_{2\beta} u_2
 \end{aligned}$$

$$\begin{aligned}
 \frac{1 - \frac{J_c^2}{J_T J}}{1 + \frac{J_c}{J}} J_T \dot{x}_6 &= -(\omega_E^2 - \omega_F^2) \sin \beta_0 \cos \beta_0 x_1 - (\omega_E^2 \sin^2 \beta_0 + \omega_F^2 \cos^2 \beta_0)x_2 \\
 &- \left(\omega_E^2 \sin^2 \beta_0 + \omega_F^2 \cos^2 \beta_0 + \frac{K_T}{J + J_c} \right) x_3 - \frac{J_c}{J(J + J_c)} \frac{\partial F_2}{\partial \dot{\theta}_R} x_4 \\
 &+ L \frac{J_c}{J(J + J_c)} \frac{\partial F_2}{\partial \omega} x_5 - \frac{1}{J + J_c} \left(h \frac{J_c}{J} \frac{\partial F_2}{\partial \omega} - B_T \right) x_6 \\
 &- \frac{J}{J(J + J_c)} \frac{\partial F_2}{\partial \omega} u_1 - \frac{J}{J(J + J_c)} F_{2\beta} u_2
 \end{aligned}$$

$$\begin{aligned}
 y &= J(\omega_E^2 \sin^2 \beta_0 + \omega_F^2 \cos^2 \beta_0)x_1 - (\omega_E^2 - \omega_F^2) \sin \beta_0 \cos \beta_0 x_2 \\
 &+ (\omega_E^2 - \omega_F^2) \sin \beta_0 \cos \beta_0 x_3 + \left(\frac{\partial F_1}{\partial \beta} - F_{1\beta} \right) u_1
 \end{aligned}$$

B.2 Drivetrain Dynamics

The state space variables for the drivetrain dynamics are:

$$y_1 = x_1 \quad y_2 = x_6$$

$$u_1 = T_H \quad u_2 = T_G$$

And the state space model is as follows:

$$\dot{x}_1 = \frac{1}{I_{LS}}(u_1 - \gamma_{LS}x_1 - \bar{x})$$

$$\dot{x}_2 = \bar{K}_{LS} \left(x_1 - \frac{n-1}{n}x_3 + \frac{1}{n\gamma_2^*}x_5 - \frac{1}{n}x_6 - \frac{1}{n^2\gamma_2^*}\bar{x} \right)$$

$$\dot{x}_3 = \frac{1}{J_{TS}} \left(\frac{n-1}{n}\bar{x} - B_{TS}x_3 - x_4 \right)$$

$$\dot{x}_4 = K_{TS}x_3$$

$$\dot{x}_5 = \frac{K_{HS}}{\gamma_2^*} \left(\frac{\bar{x}}{n} - x_5 \right)$$

$$\dot{x}_6 = \frac{1}{I_{HS}} \left(\frac{1}{n}\bar{x} - \gamma_{HS}x_6 - u_2 \right)$$

where:

$$\bar{x} = \left(\frac{n^2\gamma_2^*}{\gamma_1^* + n^2\gamma_2^*} \right) \left(\gamma_1^*x_1 + x_2 - \frac{n-1}{n}\gamma_1^*x_3 + \frac{\gamma_1^*}{n\gamma_2^*}x_5 - \frac{\gamma_1^*}{n}x_6 \right)$$

Appendix C

Calculation of Damage Equivalent Loads

Damage equivalent loads are calculated using a rainflow counting method, the S-N curve for the material and Miner's rule as described in [33] and [34]. Load cycles calculated using rainflow counting are converted to stresses, S , as in (C.1). Where M is the bending moment about the neutral axis, y is the distance from the neutral axis to the point of maximum stress. In this case, this is the outer radius of the tower at the base. I_x is the second moment of area as calculated by (C.2).

$$S = \frac{M \times y}{I_x} \quad (\text{C.1})$$

$$I_x = \frac{\pi}{4}(r_2^4 - r_1^4) \quad (\text{C.2})$$

The number of cycles to failure for the given load case, N can then be calculated from the stress cycles using the S-N curve described by (C.3). S_D is the endurance limit of the material, N_D is the number of cycles to failure at the en-

durance limit and m is the Wholer exponent. In the case of a steel wind turbine tower, the endurance limit is assumed to be 200Mpa at 10^6 cycles with a Wohler exponent of 5.

$$N = N_D(S_D/S)^m \quad (\text{C.3})$$

The damage from each load case can be calculated using Miner's rule as in (C.4). Where D is the total damage, i is the load case number, j is the number of load cases, n_i is the number of cycles for load case i and N_i is the number of cycles to failure for load case i .

$$D = \sum_{i=1}^j \frac{n_i}{N_i} \quad (\text{C.4})$$

Appendix D

Formulation of Transfer Functions for the Anti-windup Loop

The anti-windup loop requires that transfer functions in the path from the controller input to the pitch angle demand be formulated so that their output is solely dependant on the input from the previous time step. The output of this is added to the input at the current time step multiplied by a constant [25].

The process is described below:

$$F(s) \rightarrow F_z(z) = \frac{n(z)}{d(z)} = \frac{a_n z^{-n} + a_{n-1} z^{-(n-1)} + \dots + a_1 z^{-1} + a_0}{b_m z^{-m} + b_{m-1} z^{-(m-1)} + \dots + b_1 z^{-1} + 1} \quad (\text{D.1})$$

$$F_z(z) - a_0 = z^{-1} \frac{m(z)}{d(z)} = z^{-1} G_z(z) \quad (\text{D.2})$$

So, a function, F , at a time step t is equal to the output of function G at the time step $t - 1$ plus a constant, a_0 multiplied by the input at time step k :

APPENDIX D. FORMULATION OF TRANSFER FUNCTIONS FOR THE ANTI-WINDUP LOOP

$$f_t = g_{t-1} + a_0 u_t \quad (\text{D.3})$$

The MATLAB code below calculates $G(s)$ and a_0 for a given $F(s)$ and time step size T .

```
1 function [G,a0] = disca0(F,T,FLAG_DELAY)
2 % DISCA0 Calculate G(s) and a0 from F(s)
3 % F(s) may be up to third order
4 % T is the time step
5 % FLAG_DELAY {1,0} sets whether a time delay, z^-1, should be
   included in
6 % G(s)
7 %
8 % [G,a0] = disca0(F,T,1) calculates G where G(s) = (F(s)-a0)z^-1
9 % [G,a0] = disca0(F,T,0) calculates G where G(s) = (F(s)-a0)
10
11 if nargin < 2
12     T=0.01;
13 end
14 if nargin < 3
15     FLAG_DELAY=1;
16 end
17
18 [Fn,Fd]=tfdata(F,'v');
19
20 if (numel(Fn)==2)
21     Fn(3)=Fn(2);
22     Fn(2)=Fn(1);
23     Fn(1)=0;
24 end
25
26 if (numel(Fd)==2)
27     Fd(3)=Fd(2);
```

APPENDIX D. FORMULATION OF TRANSFER FUNCTIONS FOR THE ANTI-WINDUP LOOP

```
28     Fd(2)=Fd(1);
29     Fd(1)=0;
30 end
31
32 A=Fn(1);
33 B=Fn(2);
34 C=Fn(3);
35 D=Fd(1);
36 E=Fd(2);
37 F=Fd(3);
38
39 a0=(4*A+2*T*B+T^2*C)/(4*D+2*T*E+T^2*F);
40
41 if FLAG_DELAY
42     GNum1=a0*D-A;
43     GNum2=((2*A-2*a0*D)/-T)+((T*C-T*a0*F)/2);
44 else
45     GNum1=A-a0*D;
46     GNum2=B-a0*E;
47 end
48 GNum3=C-a0*F;
49 GDen1=D;
50 GDen2=E;
51 GDen3=F;
52 GNum=[GNum1 GNum2 GNum3];
53 GDen=[GDen1 GDen2 GDen3];
54 G=tf(GNum, GDen);
55
56 end
```